Thesis for the Degree of Doctor of Philosophy

Investigation of Metal Oxide Thin Films and Nanofibers by Electron Emission Spectroscopy

by

Juyun Park

Department of Chemistry

The Graduate School

Pukyong National University

February 2015

Investigation of Metal Oxide Thin Films and Nanofibers by Electron Emission Spectroscopy

(전자 방출 분광기를 이용한 금속산화물 박막과 나노섬유의 연구)

Advisor: Prof. Yong-Cheol Kang

by
Juyun Park

A thesis submitted in partial fulfillment of the requirements
for the degree of

Doctor of Philosophy

in Department of Chemistry, The Graduate School,
Pukyong National University

February 2015

Investigation of Metal Oxide Thin Films and Nanofibers by Electron Emission Spectroscopy

A Dissertation
by
Juyun Park

Approved by:

(Chairman) Ju Chang Kim

(Member) Kang-Lyeol Ha

(Member) Yeong Il Kim

(Member) Eungsun Byon

(Member) Yong-Cheol Kang

February 27, 2015

CONTENTS

LIST OF FIGURES

LIST OF TABLES

Investigation of Metal Oxide Thin Films and Nanofibers by Electron Emission Spectroscopy

Juyun Park

Department of Chemistry, The Graduate School,

Pukyong National University

Abstract

In this thesis, the results of surface characteristics of CuO_x, MoO_xN_y, MoS_x, and various metal oxide thin films investigated with electron emission spectroscopy (EES) were reported. In order to study of the surface properties of the thin films, EES and sputter chambers were built and modified. The EES chamber was equipped with X-ray photoelectron spectroscopy (XPS), Auger electron spectroscopy (AES), and ultraviolet photoelectron spectroscopy (UPS). The oxidation state of the elements on the films was determined after peak deconvolution process. We verified that the ratio of chemical species with different oxidation states is one of crucial factors of the characteristics of the films.

CHAPTER I. Introduction

1.1 Material System

In this research, a variety of metal oxide systems and conductive polymers were examined by means of electron emission spectroscopy, those material systems have been widely used in a number of application fields including solar cell, semiconductors, photovoltaic devices, and electrochromic devices. The material systems investigated in this research are copper oxide (CuO_x) thin films [1.1-1.3], copper oxide (CuO_x) nanofibers [1.4], molybdenum oxide (MoO_x), oxynitride (MoN_xO_y), and sulfide thin films [1.5,1.6], hafnium aluminum oxide ($HfAlO_3$) thin films [1.7], gallium zinc tin oxide (GZTO) thin films [1.8,1.9], fluorine doped SnO_2 (FTO) thin films [1.10], and poly(3,4-ethylenedioxythiophene) (PEDOT) thin films [1.11].

Cuprous oxide (Cu_2O) is a p-type semiconductor with a direct band gap in the range between 2.0 and 2.6 eV [1.12-1.14] and is suitable for photovoltaic devices [1.15,1.16], while band gap of cupric oxide (CuO) is 1.2-1.5 eV [1.17]. Although Cu_2O has great advantages for the applications in optical photovoltaic devices, the difficulty of growth of single phase Cu_2O without CuO mixing still remains. Mo oxides have become an important material system for application in electrochromic and photochromic devices in the solar cell industry [1.18,1.19], active and selective catalysts [1.20,1.21], and gas sensors [1.22]. The organic optoelectronic devices have been

interested in the demand of flexible devices. One promising material system is poly(3,4-ethylenedioxythiophene) (PEDOT) which is a conductive polymer with work function between 4.7 and 5.1 eV, high transparency in visible light region, and excellent chemical stability.

To fabricate the thin films, which were investigated in this work, various techniques were applied including radio frequency magnetron sputtering, direct current sputtering, magnetron co-sputtering, electrospinning, and spin coating. The chemical environment and the oxidation state of the elements on the surface region of the fabricated thin films are key factors to understand the physicochemical and electrical properties of the thin films. In order to focus on the surface region of the material systems, surface sensitive technique was needed. In this aspect, X-ray photoelectron spectroscopy (XPS), ultra-violet photoelectron spectroscopy (UPS), and Auger electron spectroscopy (AES) are suitable techniques. However, due to the small number of photoelectrons from the surface of the thin films, interference free environment was required to analyze. For this purpose, we constructed ultra-high vacuum (UHV) electron emission spectroscopy (EES) system based on ESCALab MKII system. The details of the EES system and standard operating procedures of a variety of surface analysis techniques will be described in Chapter 1.2 and Appendices A-H, respectively. Figure 1.1 shows the conceptual diagram of the approach used in this research. In the figure, photoelectrons can be ejected by various excitation sources such as X-ray and ultra violet light. And Auger electrons can be emitted commonly by

electron beam. The energy of emitted electrons from the sample surface was analyzed with an electron energy analyzer and those techniques are called as XPS, UPS, and AES.

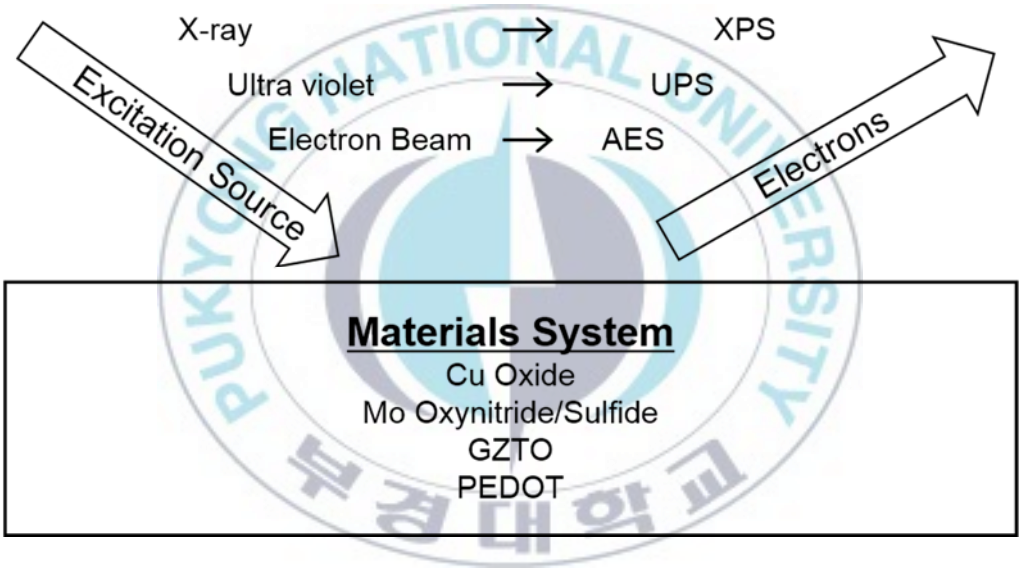

Figure 1.1 Conceptual illustration of the EES used in this research.

1.2 Electron Emission Spectroscopy System

The schematic diagram of electron emission spectroscopy (EES) chamber has been built for this research is shown in Fig. 1.2. The EES chamber is a modified model based on ESCALab MK II (VG, UK) for versatile uses. The modified EES ultrahigh vacuum (UHV) chamber is consisted of three chambers: analysis chamber, sample preparation chamber, and rf sputter chamber. Each chamber is connected with a manual gate valves for isolation of the chambers at different pressures. The detailed illustrations of the three chambers are shown in Fig. 1.3-1.5.

The signal from most surface sensitive techniques is weak in general, therefore EES analysis requires interference-free environment. The interference-free condition can be made by vacuum system. The UHV (10^{-10} Torr range) condition of EES chamber has been achieved with a rotary vane pump (RP), a turbo molecular pump (TMP), two ion pumps (IPs) with different pumping speed (360 and 720 L/s), and a Ti-sublimation pump (TSP) as shown in Fig 1.2. Whenever the EES chamber was vented to atmosphere, the EES chamber should be pumped with a RP until the pressure reaches to low vacuum (LV, ~10^{-3} Torr). After the pressure reached to LV, TMP pumped the chamber to reach high vacuum (HV, ~10^{-8} Torr). Then IP and TSP can evacuate the chamber to UHV.

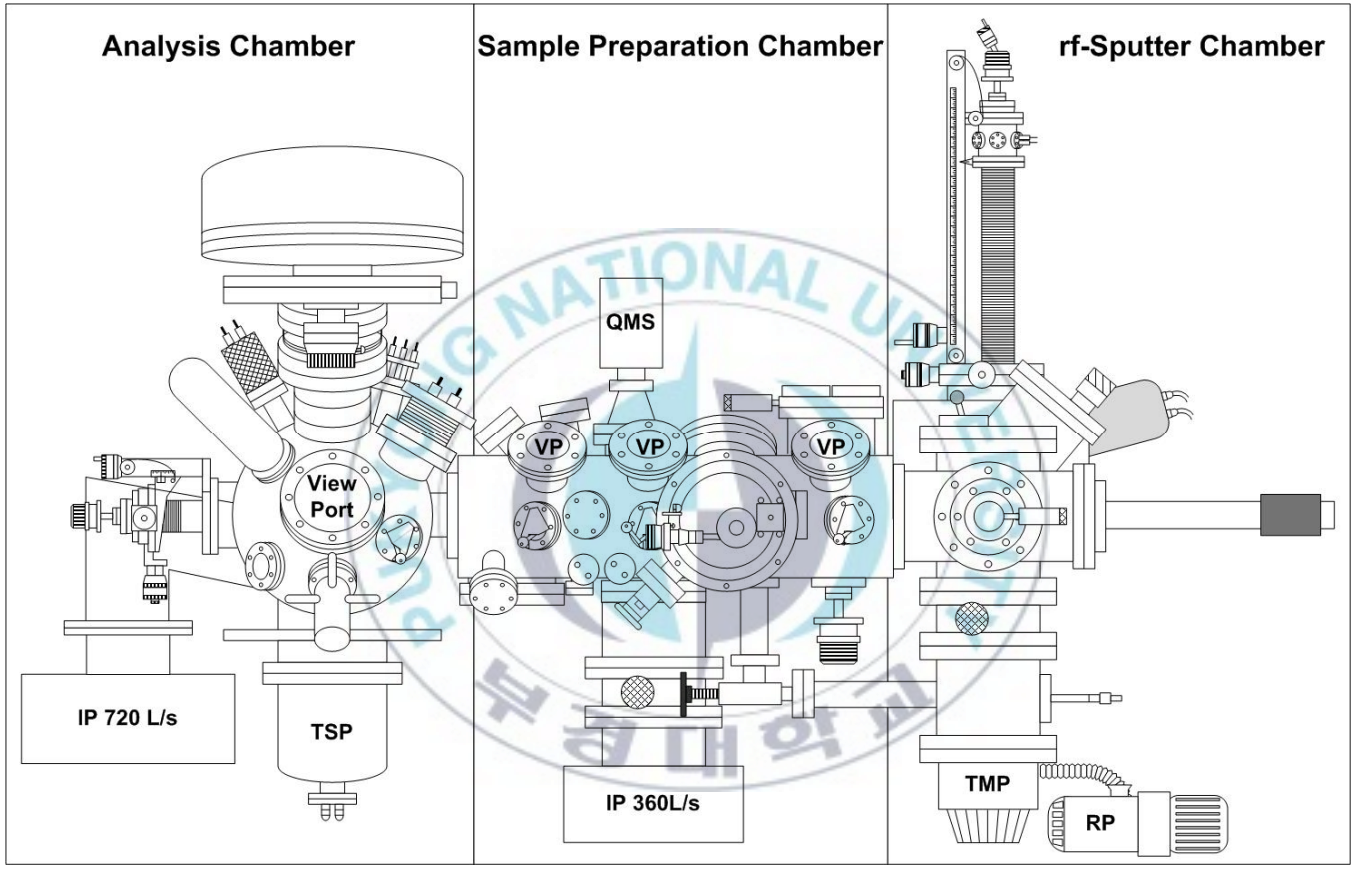

Figure 1.2 Schematic diagram of electron emission spectroscopy (EES) chamber.

1.2.1 Analysis Chamber

Most of surface analysis tools are mounted on the analysis chamber as shown in Fig 1.3. In the figure, **A** is a concentric hemispherical electron energy analyzer (CHA) which is equipped with a channeltron for the detection of photoelectrons. **B** is an ultra-violet (UV) energy source for ultra-violet photoelectron spectroscopy (UPS) which is activated by He gas discharge. **C** is a dual anode (Mg and Al) X-ray source for X-ray photoelectron spectroscopy (XPS). The Mg Kα X-ray has 1253.6 eV of photon energy with 0.7 eV of full width at half maximum (FWHM) and Al Kα X-ray has 1486.6 eV of photon energy with 0.85 eV of FWHM [1.23]. The advantage of the usage of the dual anode source is that it can differentiate between XPS and Auger electron spectroscopy (AES) peaks. **D** is a precision sample manipulator for sample positioning which moves the sample with four directions (x, y, z, and θ) to desired position for analysis. Charge coupled device (CCD) camera is used for exact position of sample. **E** is an Ar-ion sputter gun with low intensity for sample cleaning which removes the contaminant layer formed in atmosphere. **F** is a high flux electron gun for AES, **G** is a wobble stick for transferring a sample from a rack and pinion to sample manipulator, **H** is an Ar-sputter gun with high intensity for depth profile study. The base pressure of the analysis chamber is ~10^{-10} Torr range achieved by IP and TSP. The standard operating procedures of the surface analysis techniques are in Appendices.

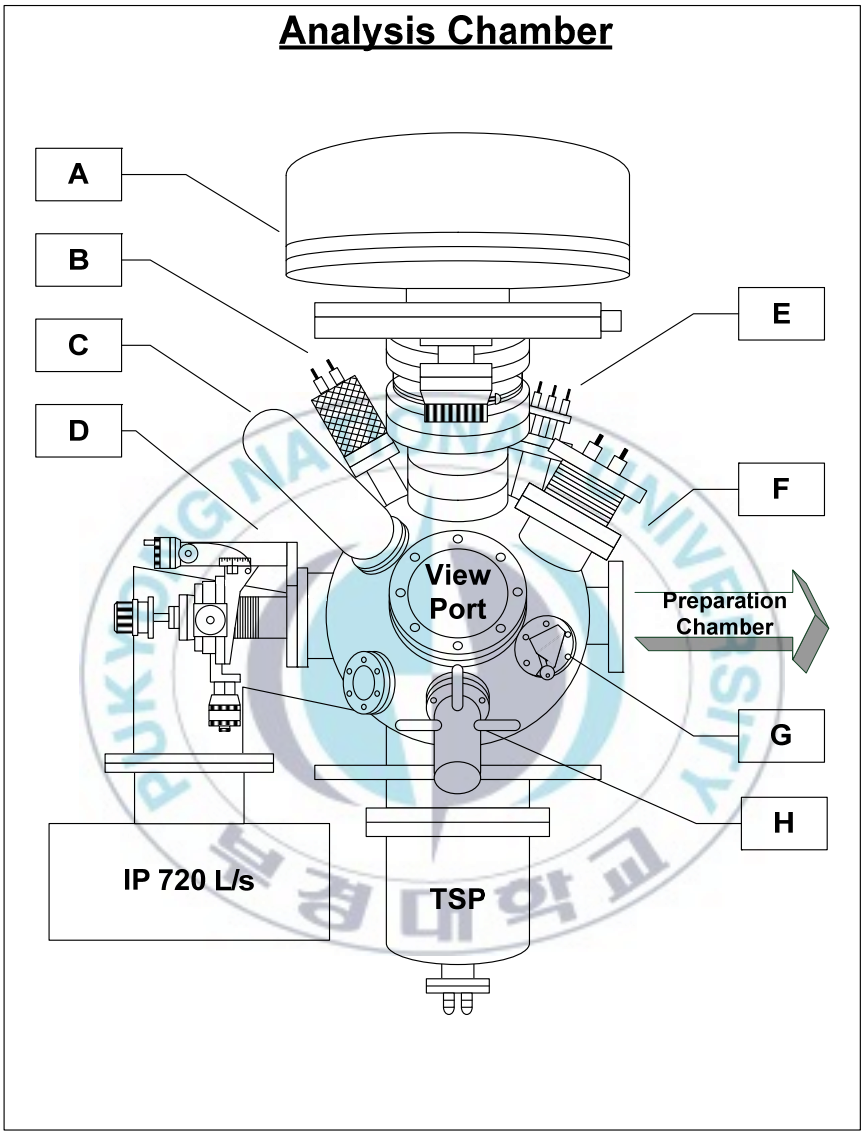

Figure 1.3 Schematic diagram of analysis chamber. **A** is CHA, **B** is an UV source, **C** is a dual anode X-ray source, **D** is a manipulator, **E** is an Ar-ion gun for AES, **F** is an electron gun for AES, **G** is a wobble stick, and **H** is an Ar-ion gun for depth profile.

1.2.2 Sample Preparation Chamber

The sample preparation chamber is consisted of two parts: sample transferring part and sample load-lock part. The illustration of sample preparation chamber is shown in Fig 1.4. In the figure, **I** is a wobble stick for transferring the sample holder from a carousel to a rack and pinion. The sample holders are made with stainless steel, titanium, and copper. The diameter of the sample holder is 8 mm and the height is 10 mm with several notches to manipulate. **J** is a carousel for storing sample holders which can store 10 holders. **K** is control knobs of the rack and pinion system. **L** is sample load-lock chamber to install the sample from atmosphere. **L** is needed to be vented or pre-pumped before installing the sample or surface analysis, respectively. After the sample was pre-pumped the sample can be transferred into the sample transferring part. In order to check the contaminants in the UHV chamber, quadrupole mass spectrometer (QMS) was housed in the sample preparation chamber. **M** is a low energy electron diffraction (LEED) and AES system for investigation of single crystal. **N** is a wobble stick for transferring the sample between a carousel and the rack and pinion system. **O** is a carousel storing sample which can store 12 holders. **P** is an angle valve which connects the load-lock chamber and TMP to pre-pump after sample installation. The parts denoted as **VP**s are view ports. The sample transferring part of the sample preparation chamber was pumped by IP with 360 L/s of pumping speed.

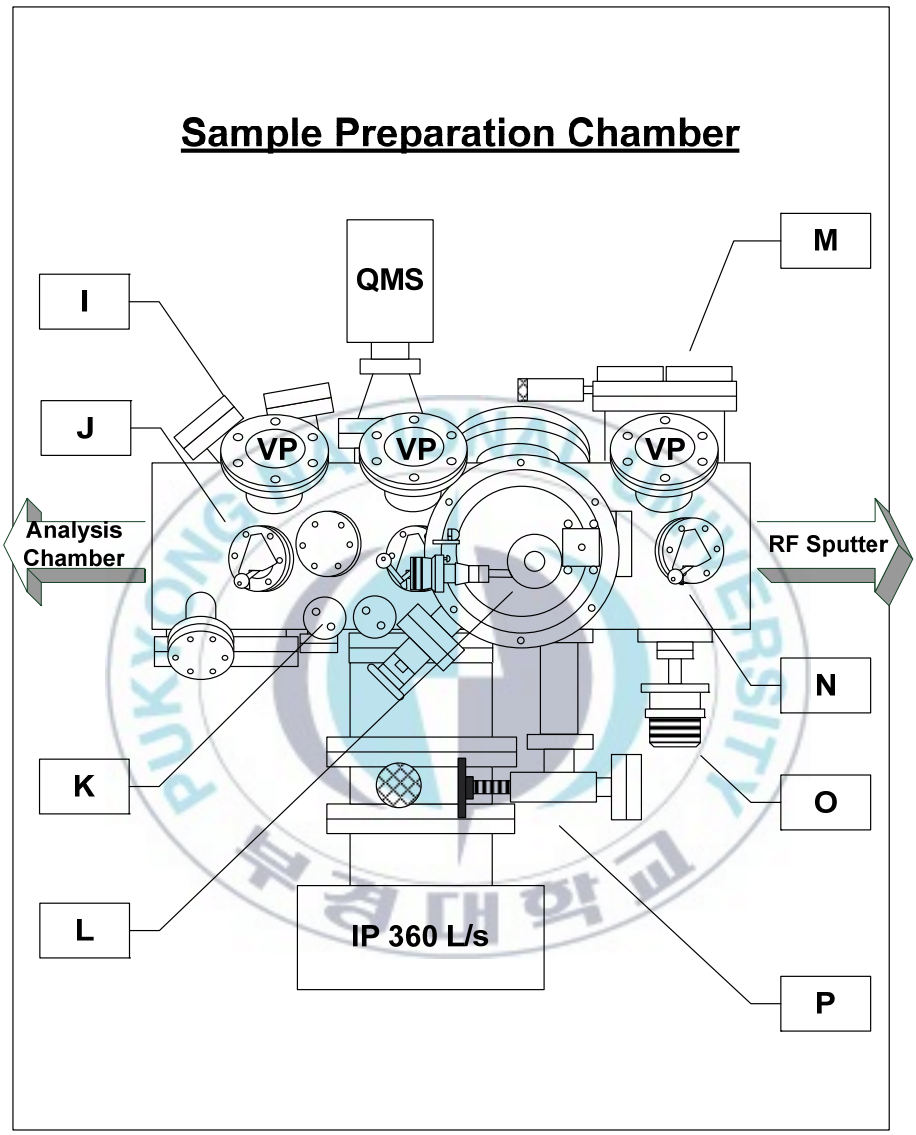

Figure 1.4 Schematic diagram of sample preparation and load-lock chamber. **I** is a wobble stick, **J** is a carousel, **K** is control knobs of the rack and pinion system, **L** is sample load-lock chamber, **M** is LEED and AES, **N** is a wobble stick, **O** is a carousel, **P** is an angle valve, and **VP**s are view ports.

1.2.3 rf Sputter Chamber

rf sputter chamber was built for fabrication of thin films without air contamination. In order to study the thin film fabricated in this chamber in situ, the rf sputter chamber was clustered with the analysis chamber. The schematic diagram of radio frequency (rf) sputter chamber is shown in Fig. 1.5. In the figure, **Q** is a wobble stick. **R** is a molecular beam doser (MBD) to control the number of gas to react with the sample. The detailed designs for MBD and MBD gas line are shown in Fig. 1.6 and Fig. 1.7, respectively. Calibration of the MBD was required to figure out the exact number of impinging gas. We calibrated the MBD using N_2 gas as a reference applying pin-hole conductance equation [1.24]. The pin-hole conductance is given as below;

$$\frac{dn}{Pdt} = -\frac{V}{kT}\left[\frac{d\ln(P/P_0)}{dt}\right],$$

where (dn/Pdt) is pin-hole conductance, V is the volume of dosing gas storage, P is the pressure in the dosing gas storage which is read by a convectron pressure gauge as shown in Fig. 1.7, T is the temperature of the gas storage in Kelvin unit, k is Boltzmann's constant. The slope of the plot of $\ln(P/P_0)$ versus t was given as following and the plot is shown in Fig. 1.8;

$$\text{slope} = \frac{dn}{Pdt}\left(-\frac{kT}{V}\right).$$

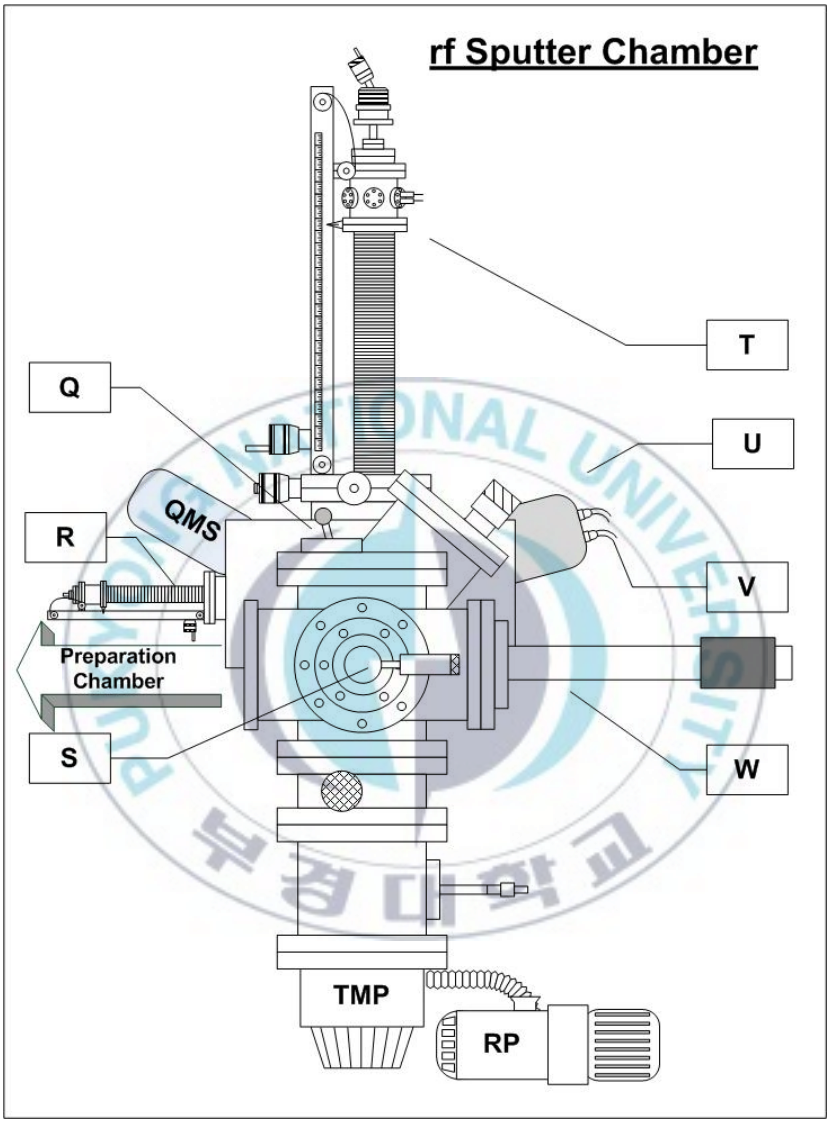

Figure 1.5 Schematic diagram of UHV rf sputter chamber. **Q** is a wobble stick, **R** is a molecular beam doser, **S** is a sample transfer rod, **T** is a manipulator, **U** is a UHV rf sputter target, **V** is cooling line, and **W** is a sample transfer rod.

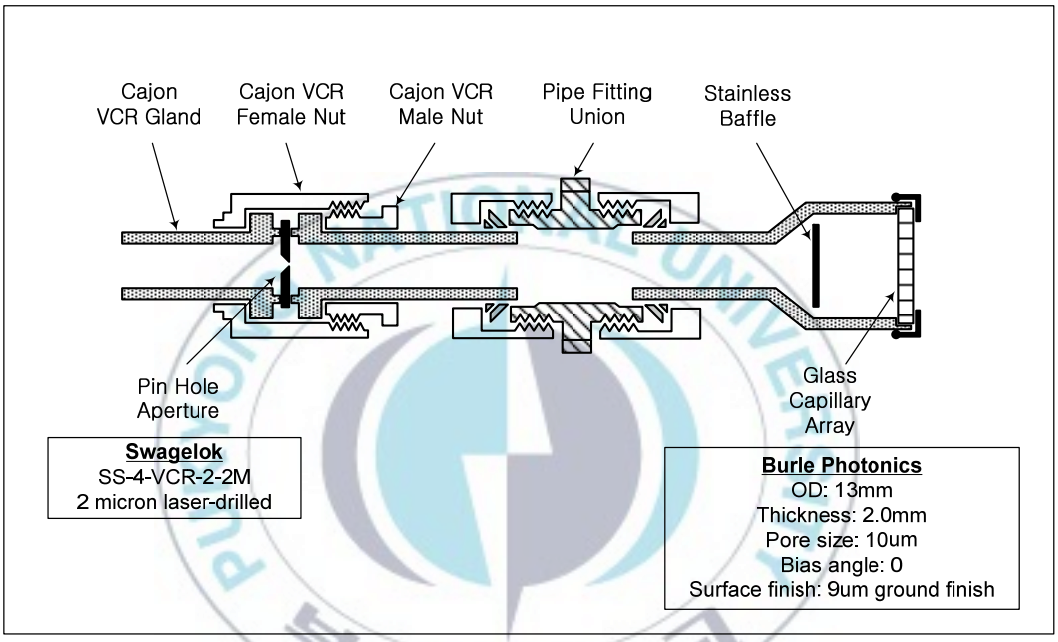

Figure 1.6 Design for a molecular beam doser.

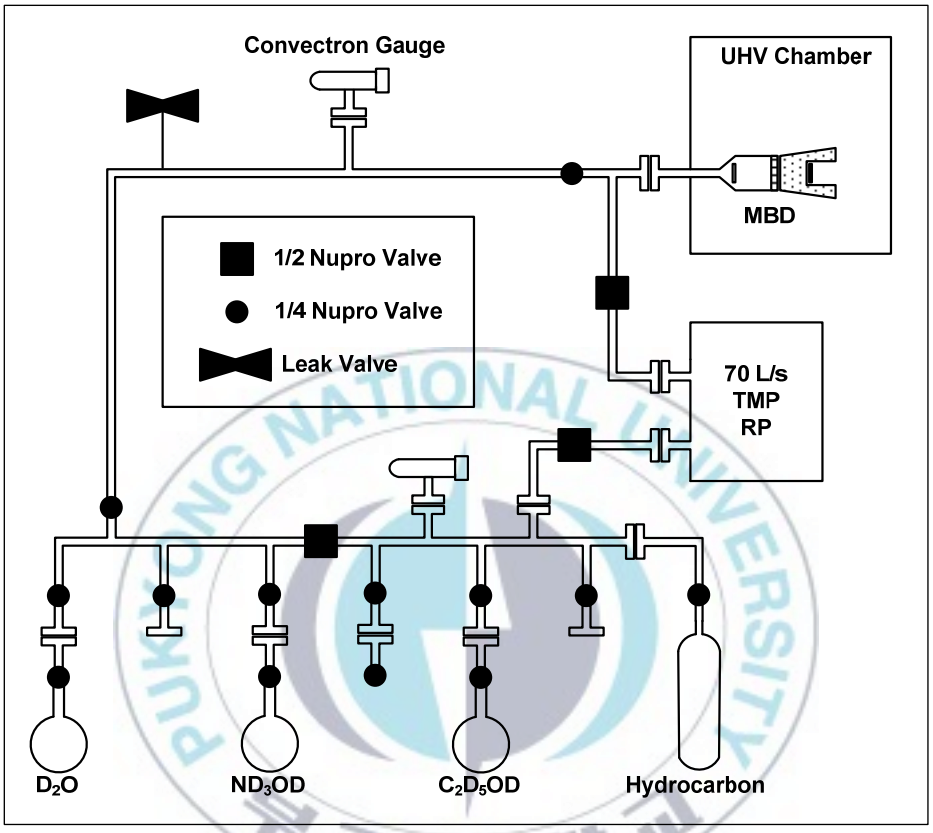

Figure 1.7 Schematic diagram of gas manifolds for a molecular beam doser.

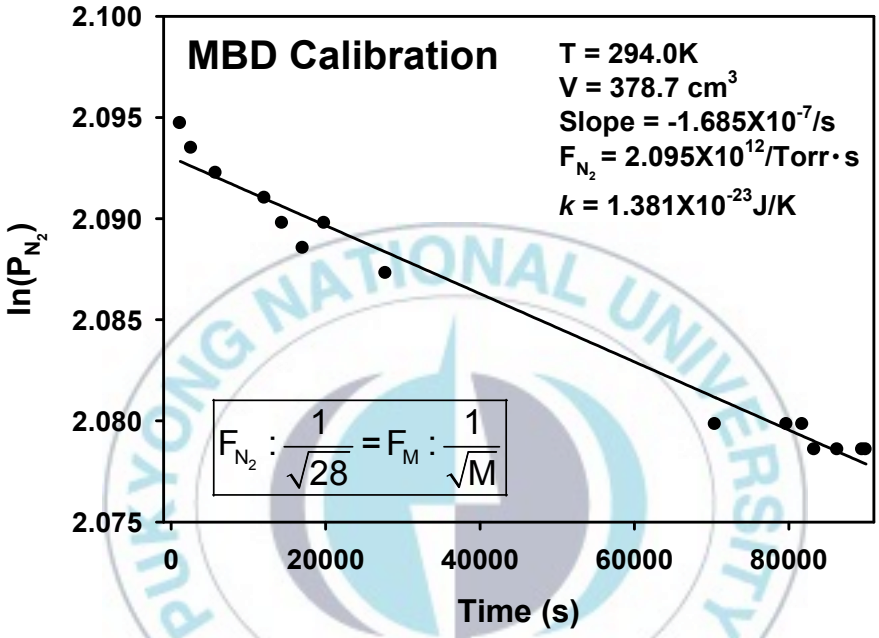

Fig. 1.8 Calibration result of a molecular beam doser.

From the relationship above, pin-hole conductance of N_2, F_{N_2}, was determined. The number of N_2 gas was figured out with F_{N_2}. The number of molecules delivered by MDB is given as below;

$$\text{The number of gas} = \left(1.109 \times 10^{13}\right) \frac{P(Torr) \times t(s)}{\sqrt{M(g/mol)}}.$$

The MBD is useful to study about the kinetics between the sample and desired gas by temperature programmed desorption (TPD). **S** is a sample transfer rod for transferring the sample between the sample preparation chamber and rf sputter chamber. **T** is a precision sample manipulator with five directions (x, y, z, θ_1, and θ_2) for positioning the sample. **U** is a UHV rf sputter target for deposition. Gas manifolds for rf sputter target are shown in Fig 1.9. **V** is cooling line for cooling the rf target. **W** is a sample transfer rod for transferring the sample between the rack and pinion and rf sputter chamber. The purity of the sputter gas was monitored with a QMS. The QMS is also used for TPD. The rf sputter chamber was evacuated independently with a RP, a TMP, an IP, and TSP. The base pressure of the rf sputter chamber is kept in ~10^{-9} Torr range. During rf sputtering process, the working pressure (WP) is controlled with a manual gate valve and the WP is kept in mTorr range. The detailed rf sputter process is described in Appendix M.

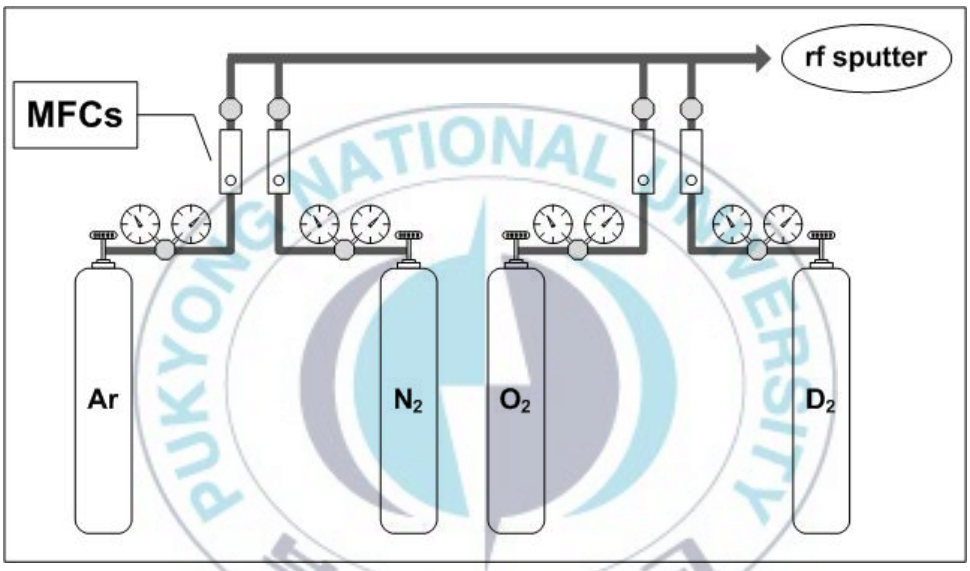

Figure 1.9 Schematic diagram of gas manifolds for rf sputter.

CHAPTER II. Theories

2.1 X-ray Photoelectron Spectroscopy (XPS)

X-ray photoelectron spectroscopy (XPS), also known as an electron spectroscopy for chemical analysis (ESCA), is a widely used technique for surface analysis since 1970. In these days, surface analysis is crucial to evaluate and improve the performance of devices, such as solar cells, semiconductors, and light emitting devices (LED) in fundamental level and commercial field. The number of publications per year in each of the last five years is shown in Fig. 2.1 and it indicated that the frequency in the use of XPS is gradually increased. The theory of XPS is based on the photoelectric effect. After introducing the characteristic X-ray with a sufficient energy on the sample, electrons at core and/or valence levels could be ejected from the sample and these are called as photoelectrons. Fig. 2.2 shows the process about generation of photoelectron. The ejected photoelectrons are moved to analyzer and collected at channeltron. Finally the number of electrons is converted to current and XPS spectra which are represented by binding energy versus counts per seconds (cps) were obtained. The inset in Fig. 2.2 is the survey XPS spectrum of Ag standard, the first spectrum obtained with our modified EES system. The notation of photoelectron is determined by the core level where the emitted electron was located. The binding energy of electrons, E_b is calculated by the following equation.

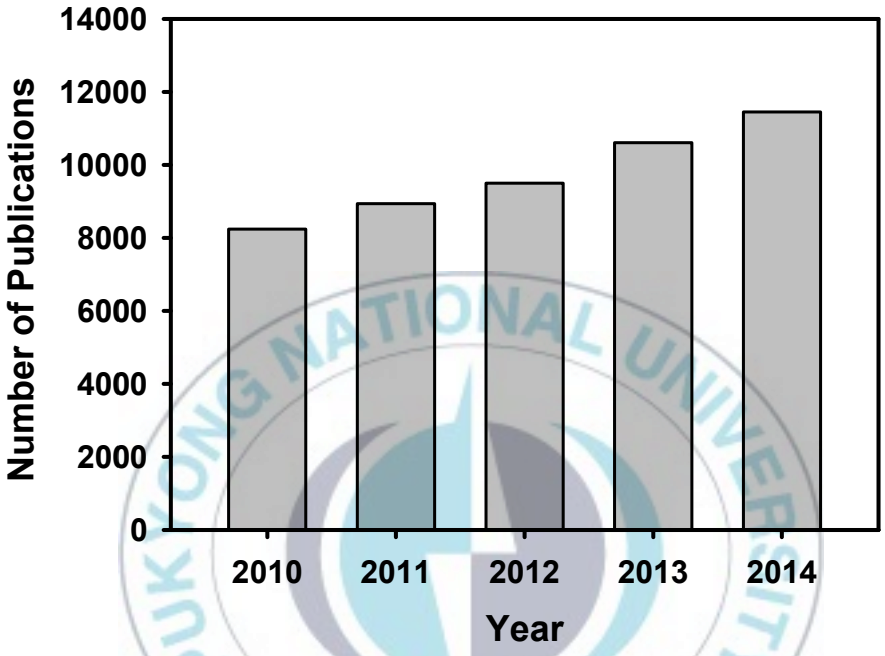

Fig. 2.1 The number of publications using XPS from 2010 to 2014. It is resulted from the database with the searching keywords of XPS in Scifinder website.

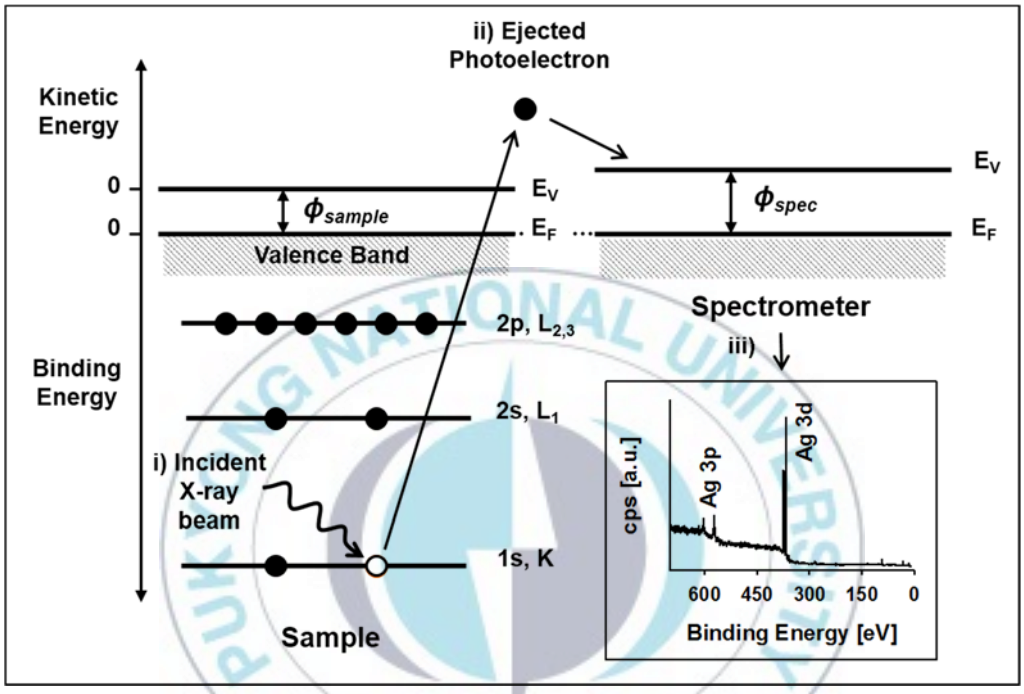

Fig. 2.2 The process of generation of photoelectron and the first XPS spectra obtained using Ag sample in our EES system.

$$E_b = h\nu - E_k - \phi_{spec}$$

where, $h\nu$: energy of X-ray,

E_k : kinetic energy of photoelectron,

ϕ_{spec} : work function of spectrometer.

The energy of X-ray and the work function of spectrometer are known and the kinetic energy of photoelectrons can be measured by electron energy analyzer, so the binding energy of photoelectrons can be determined.

XPS instrument is composed with X-ray source, electron energy analyzer, and detector at least. In this chapter, X-ray source and electron energy analyzer will be mentioned.

To be a proper X-ray source, two conditions should be satisfied to be used as an X-ray anode. The first requirement is an effective bandwidth. From the high resolution XPS spectra, we can obtain the information, such as oxidation state of elements and the surrounding environment of atom. If the effective bandwidth of the X-ray line is broad, the resulted XPS spectra are also broad and it makes difficult to analyze. In general, X-ray line with narrow bandwidth less than 1.0 eV is suitable for an X-ray source. In the Table 2.1, the photon energy and bandwidth of characteristic X-ray lines for many metals are listed [2.1]. Among the various metals, 5 metals have potential to be used as an X-ray anode. As shown in Table 2.1, the energy of Y Mζ and Zr Mζ is very lower than those of Mg Kα, Al Kα, and Si Kα. At this point, the second requirement is considered and it is X-ray energy. As

Table 2.1 Energy and effective bandwidth of some characteristic lines.

Line	Energy [eV]	Bandwidth [eV]
Y Mζ	132.3	0.47
Zr Mζ	151.4	0.77
Nb Mζ	171.4	1.21
Mo M ζ	192.3	1.53
Ti Lα	395.3	3.00
Cr Lα	572.8	3.00
Ni Lα	851.5	2.50
Cu Lα	929.7	3.80
Mg Kα	1253.6	0.70
Al Kα	1486.6	0.85
Si Kα	1739.5	1.00
Y Lα	1922.6	1.50
Zr Lα	2042.4	1.70
Ti Kα	4510.0	2.00
Cr Kα	5417.0	2.10
Cu Kα	8048.0	2.60

we mentioned above, X-ray with sufficient energy can eject electrons from core levels out to the vacuum level. If the energy of X-ray is lower than the binding energy of electrons, photoelectrons could not be produced. Thus Y and Zr are not suitable materials for an X-ray anode. Because Si is a semiconductor, Si has poor heat conduction characteristics. Mg and Al are better to use as an X-ray anode material considering the above criteria.

X-ray can be generated by the bombardment of highly energetic electron to anode. When the electron produced from the filament has sufficient kinetic energy, emission of X-ray is started from the surface of Mg or Al anode. As the energy of electron is increased, the flux of X-ray is increased and finally saturated. Thus the filament voltage is usually maintained in the range from 9 to 15 kV during XPS measurement. The maximum power of X-ray source is about 1 kW in compact design (external diameter of shield is about 35 mm). When the power is increased, X-ray source is more heated. If the X-ray source is overheated, inter-diffusion of Al and Mg is occurred and dual excitation is produced. More severe case leads to agglomeration between Al and Mg and then XPS peaks from Cu Lα radiation will appear. To prevent these problems, X-ray source should be cooled by water, in general 3.5 L/min of a flow rate and 3.5 bar of a working pressure, during operating.

The schematic diagram of dual anode X-ray source used in this work is shown in Fig. 2.3 [2.2]. The X-ray anode is composed of Cu and the end of anode is stepped. Two sides are deposited with Al and Mg with the

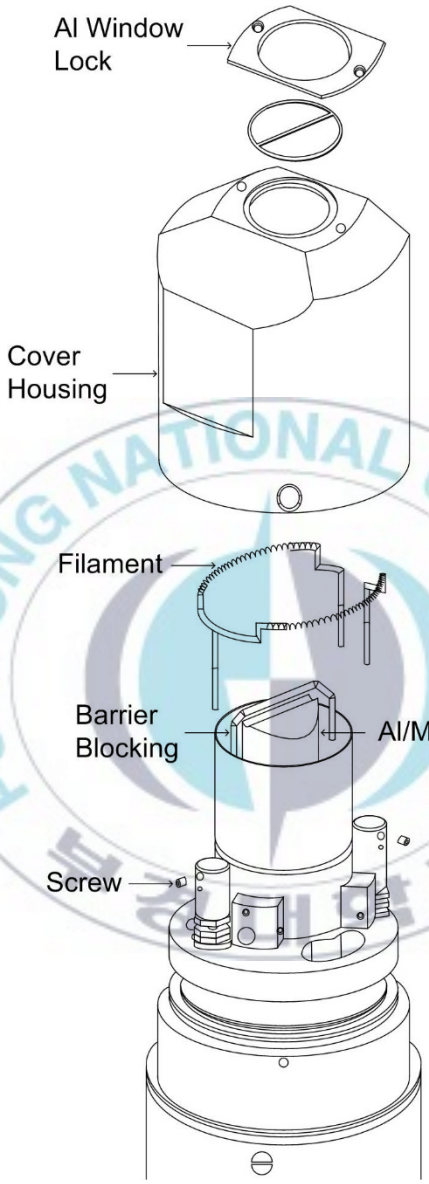

Fig. 2.3 Schematic of dual anode X-ray source RS 40B1 made by Prevac.

thickness of 10 μm, respectively. A semi-circular filament is located near the each anode and the center of the filament is grounded. The electrons produced from filament are accelerated by high voltage and bombarded to anode. To prevent the bombardment of undesired side, barrier blocking is positioned at the middle of anode. The selection of anode between Al and Mg is simple. The thin Al window is installed at the end of cover housing. It protects the exposure to stray electrons from electron energy analyzer and contamination from X-ray anode. Also the Al window is separated the space of main chamber and X-ray source.

To obtain XPS spectra, the kinetic energy of emitted photoelectrons should be detected and analyzed. For higher resolution spectra, electron energy analyzer is the most important component in XPS instrument. Many electron energy analyzers are developed and two analyzers, cylindrical mirror analyzer (CMA) for AES and concentric hemispherical analyzer (CHA) for XPSs are mostly used in these days. In this chapter, the details of CHA will be discussed (CHA is also used for AES analysis in our group).

The schematic diagram of CHA with electrostatic lens systems is shown in Fig. 2.4. To remove the effect of magnetic field which can cause the change of path way of photoelectrons, Mu metal is used for the material of UHV chamber. The ejected photoelectrons are entered to electron energy analyzer through the transfer lens. CHA is consisted of two hemispheres, outer and inner. They have same center and applied with negative voltages. The absolute value of the voltage applied in outer heisphere is larger than that

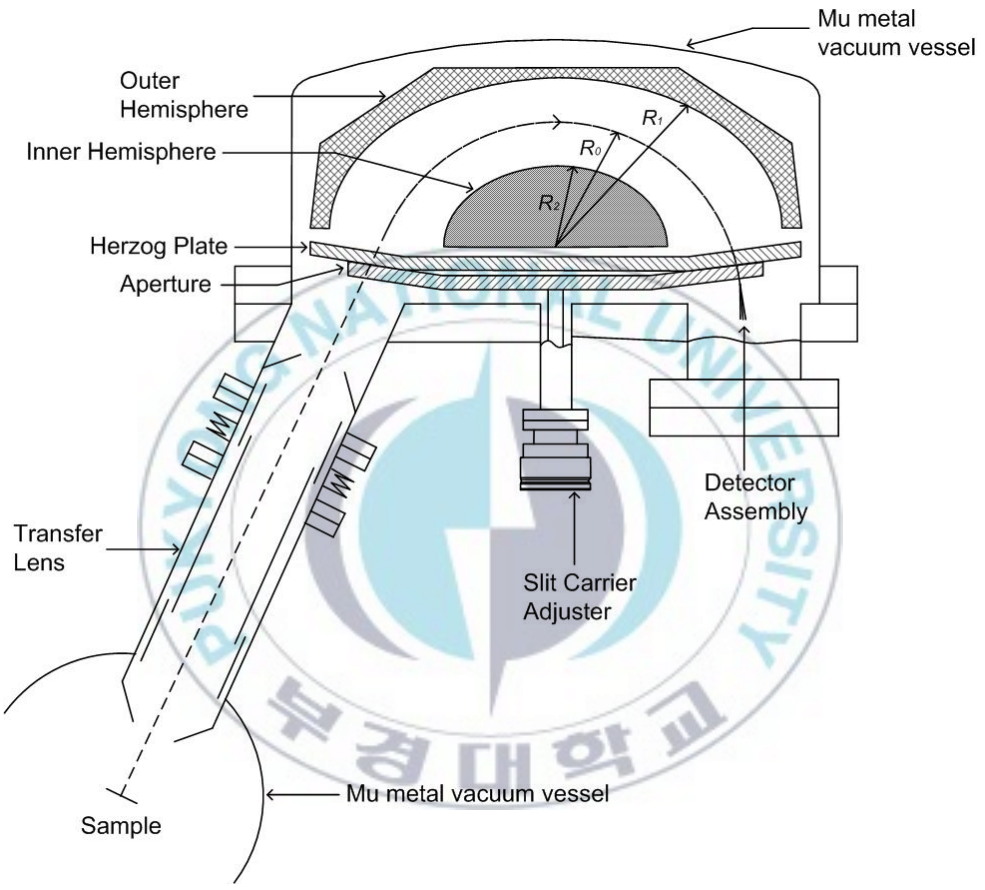

Fig. 2.4 Schematic diagram of CHA with standard input lens systems installed in ESCALab MK II made by VG.

in inner hemisphere. After the introduction of photoelectrons to analyzer, they should pass the curved path under the electric field to reach the detector. Electrons with high kinetic energy is moved in high speed and they are difficult to change the travel path in the CHA, thus electrons removed by the collision to outer hemisphere. Electrons with low kinetic energy is moved in the analyzer with low speed and collapsed to the inner hemisphere. Finally, electrons which have specific kinetic energy are only arrived at the exit slit and collected into the channeltron. The reached electrons can be controlled using their kinetic energy and applied voltage.

$$V_0 = \frac{V_1 R_1 + V_2 R_2}{2R_0}$$

The applied voltages of curved path, outer, and inner hemispheres are V_0, V_1, and V_2, respectively. The radii betwen the center and curved path, outer, and inner hemispheres are R_0, R_1, and R_2, respectively. Therefore, the electrons with the kinetic energy of eV_0 could only be detected.

To detect the electrons, CHA is operated in one of two modes, constant analyzer energy (CAE) and constant retarding ratio (CRR). In the CAE mode, the applied voltages of two hemispheres are fixed. The analysis of electrons is perfomed by varying the retarding voltage. Before the electrons were entered the entry slits, the retarding voltage is applied and then the kinetic energy of entered electrons are adjusted. For example, let's assume that only electrons with 100 eV of kinetic energy can be arrived at the exit slit and the kinetic energies of emitted electrons from sample are 50, 100,

and 150 eV. For electrons with kinetic energy of 50 eV, positive retarding voltage is applied and then changed their kinetic energy like 100 eV. For electrons with higher kinetic energy, negative voltage is applied and enalbes electrons to reach the channeltron. In the CRR mode, the retarding ratio (the ratio of retarding voltage and analyzer voltages) is constant and the analyzer voltages are vaired in accordance with the kinetic energy of electrons. Herzog plate in the Fig. 2.4 contains the entry and exit slits and the retard plates are applied at this plate. Because CAE and CRR modes are considered to constant energy resolution and constant resolving power, CAE and CRR mode are commonly used for XPS and AES, respectively.

2.2 Auger Electron Spectroscopy (AES)

Auger electron spectroscopy (AES) is one of the surface analysis techniques. It provides qualitative and semi-quantitative determination of elements and information of surface phenomena such as adsorption, desorption, and diffuse in to/out from the bulk.

The principle of generation of Auger electrons is shown in Fig. 2.5. It consists of three steps, ionization, relaxation, and emission of Auger electrons. The electrons in core level are ionized by the incident X-ray beam (in the case of AES, electron beam). The ejected electrons are called as photoelectrons and analyzed in XPS. After ionization, further steps can be occurred to be stabilized. The electrons at upper states are naturally filled up the hole and the energy difference between two levels is emitted. This process is called as relaxation process. The relaxation process can be either radiative or non-radiative process. In radiative relaxation, the energy difference can be emitted as the characteristic X-ray photon, fluorescence. In non-radiative process, the energy difference used for ejection of electron at same or upper level (L_1 or $L_{2,3}$ in Fig 2.5) and this electron is called as an Auger electron. The processes of between emission of X-ray and generation of Auger electron are competed. The detailed notation of Auger electron is determined by the sequence of generating holes. In this case, the first hole is generated in K level, the next hole is in L_1 level, and the last hole is in $L_{2,3}$ level. Thus, this Auger electron is called as $KL_1L_{2,3}$ electron. In some cases, the alphabet V is used for denote an Auger electron. The letter V means

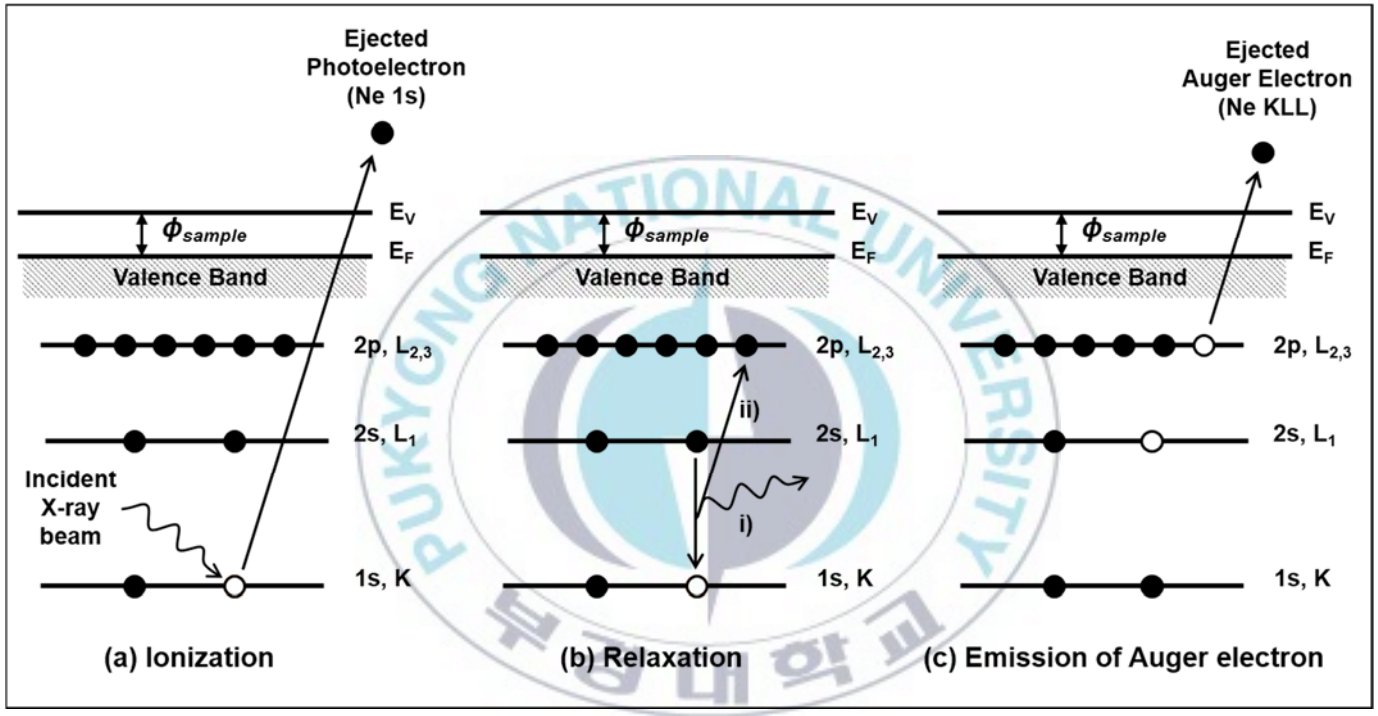

Fig. 2.5 Production of Auger electron: (a) ionization, (b) relaxation, and (c) emission of Auger electron.

valence band.

The kinetic energy of Auger electron can be calculated by

$$E_k = E_K - E_{L_1} - E_{L_{2,3}} - \phi$$

As shown in the equation above, the kinetic energy of Auger electron is independent of the incident energy. It is used to distinguish two electrons, Auger electrons and photoelectron. The binding energy of Auger electrons is constant despite changing the X-ray source, while that of photoelectrons is changed. The other difference between AES and XPS is the beam size and the intensity in spectrum. Usually, the beam size of AES is smaller than that of XPS and can be controlled by electric field, local area of sample can be analyzed by AES. The intensity in spectrum of AES is lower than that of XPS, the interpretation of spectrum of AES is performed using derivative spectrum, instead of original spectrum because the intensity of AES is weak as mentioned above.

AES instrument is similar to the XPS instrument, it is composed of electron source, electron energy analyzer, and detector. Electron sources can be divided to two types, thermionic and field emission electron source. It resulted from the different method to generate the electron from the filament. When the filament is heated sufficiently, the electron is emitted by overcoming the work function of filament material. The relationship between thermionic current and temperature is presented by Richardson equation [2.3] given as below,

$$J = A(1-\bar{r})T^2 \exp\left(-\frac{e\phi}{kT}\right) \qquad [\mathrm{A/cm^2}]$$

where, J = current density,

A = Richardson constant, whose ideal value is 120 A/(cm^2 deg^2),

but which varies with material,

$\bar{r}$ = zero-field electron reflection coefficient,

T = absolute temperature,

$e\phi$ = work function.

The higher temperature leads to increase the amount of emitted electrons.

Field emission is based on the tunneling effect. The reduction of the height of the work function barrier is occurred by high electrostatic field and then electrons come out from the filament even at room temperature. The field emitted electron current is deduced from following equation, Fowler-Nordheim expression [2.4] given as following,

$$J = \frac{1.55\times10^{-6}E^2}{e\phi}\exp\left(-\frac{6.86\times10^{7}(e\phi)^{3/2}\theta(x)}{E}\right) \qquad [\mathrm{A/cm^2}]$$

where, E = Field strength,

$\theta(x)$ = Nordheim elliptic function, in which $x = 3.62\times10^{-4}\,E^{1/2}/e\phi$.

It means that the current density is dependent on the field strength and work function. As field strength is increased, work function is decreased and then current is increased and electrons are easily escaped the filament material. Thus, the work function of material is important factor for selection of filament in the electron source. Usually, W filament and filament coated with

LaB_6 is commonly used for electron source. Adsorption of impurities on the filament is also considered, because it could be increase the work function. Thus, increasing the filament current slowly is needed to remove the residual gases and UHV environment is equipped to prevent the increase of the work function.

Fig. 2.6 shows the diagram of LEG200 electron gun installed in our EES system [2.5]. It is thermionic electron source and the V-shaped tungsten filament is in the extraction electrode, Wehnelt cylinder. The end of filament and the hole of Wehnelt is aligned by a jigging arrangement or optical means. After the alignment of filament, the path of emitted electron beam from the filament is controlled by alignment screws and bellows. There are two condenser lenses and an objective lens. Among the two condenser lenses, one has the variable potential for controlling the spot size and the other has the constant potential. To focus the electron beam, the potential of objective lens is changed. And the stigmator poles are corrected any astigmatism. The scanning poles which are located at the end of gun are used for scanning the electron beam.

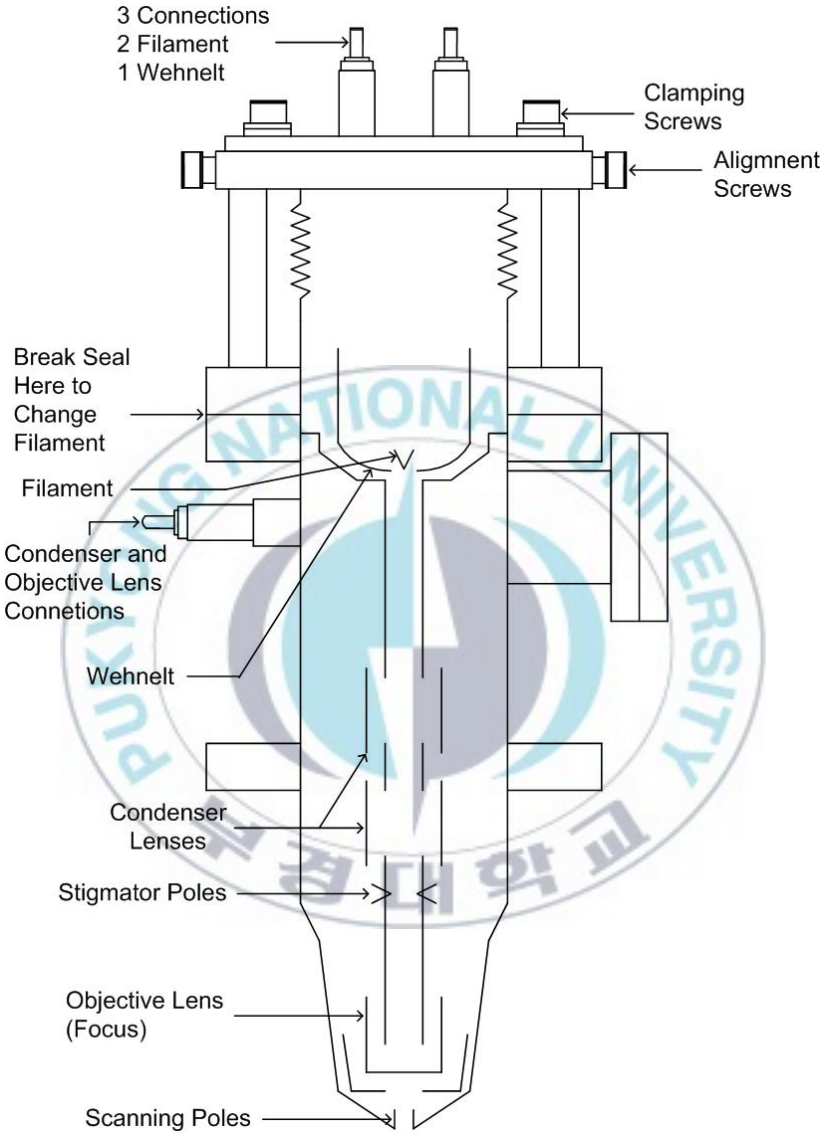

Fig. 2.6 LEG200 electron gun.

2.3 Ultraviolet Photoelectron Spectroscopy (UPS)

Ultraviolet photoelectron spectroscopy (UPS) is one of the surface analysis techniques in the photoemission spectroscopy (PES). XPS is also one of the PES techniques. The schematic diagram of PES is shown in Fig. 2.7. The spectroscopy where the X-ray photon with sufficient energy is used to eject the electron in core level is XPS and the spectroscopy achieved with UV is UPS. Because the energy of UV is lower than that of X-ray, the detected electrons are coming from valence band rather than core levels in UPS as shown in Fig. 2.7 (a). Normally, electrons with the kinetic energy in the range from 10-1000 eV is escaped from the solid during photoemission experiment, some electrons are collided with other electrons and lost their kinetic energy. This process is inelastic scattering and the lowest kinetic energy of inelastically scattered electrons is 0 eV. From the figure, the work function of sample, ϕ_{sample}, is calculated by

$$\phi_{sample} = h\nu - (\text{Fermi edge - Secondary edge}) .$$

The detection of Fermi edge is much easier in UPS than XPS, UPS is used to obtain the work function of sample usually. Fig. 2.7 (b) shows the UPS spectrum without any bias on the sample and it revealed the Fermi edge and secondary electrons, no peaks from core levels. Because the work function of detector is commonly lower than that of sample, secondary electrons of sample and detector are overlapped and the secondary edge of sample is not clearly observed. It can be corrected by application of bias on the sample and

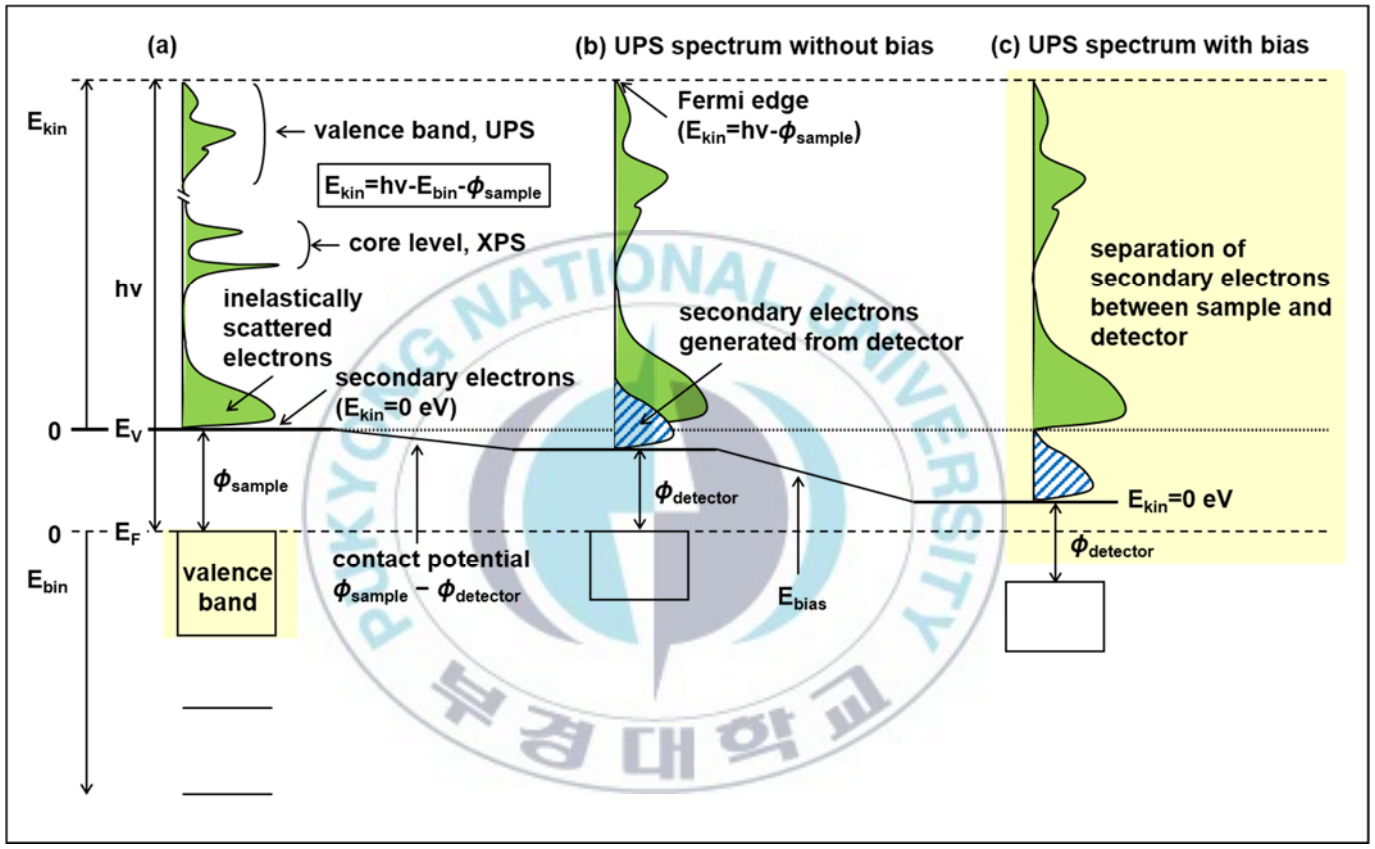

Fig. 2.7 Schematic diagram of photoemission spectroscopy process and UPS spectrum.

the result is shown in Fig. 2.7 (c).

Generally, UV source is a gas discharge lamp. After the introduction of inert gas into the inner of lamp with a suitable pressure and application of voltage about 2 kV, the discharge is occurred and the UV light is obtained. The gas pressure of the UV lamp is higher than the pressure of analysis chamber, the pressure difference is maintained by differential pumping using the combination of RP and TMP. The energy of UV source is determined by the gas in the discharge lamp. Helium gas is commonly used to generate the UV light, the energy of He I source is 21.2 eV and it has high photon yield and stable for a long time [2.6]. While He II source has 40.8 eV, greenish color, and low intensity, it works in low pressure. The other gases used for UV sources are Ne I (16.8 e), Ne II (26.9 eV), and Xe (8.437 eV) [2.6].

CHAPTER III. Copper Oxide Thin Films

3.1 Introduction

There are two different copper oxide (CuO_x) with different oxidation states, CuO (cupric oxide or tenorite) and Cu_2O (cuprous oxide or cuprite). Out of these Cu oxides, Cu_2O is an attractive material to researchers because Cu_2O is a p-type semiconductor with a direct band gap of 2.0-2.6 eV [3.1-3.3] suitable for photovoltaic devices [3.4,3.5], while that of CuO is 1.2-1.5 eV [3.6] and CuO is occasionally considered as an n-type semiconductor. In addition, Cu_2O has highly optical transparency in visible light region, nontoxicity, and low cost for productivity. Besides, Cu_2O thin film has high recombination energy of exciton and theoretical power conversion efficiency of 20% based on radiative recombination mechanism under air mass 1 (AM1) condition [3.7]. These advantages make Cu_2O thin film possible to apply in optical photovoltaic devices such as inorganic solar cells [3.7-3.9] and organic solar cells (OSCs) [3.10,3.11]. Although Cu_2O has great advantages for the applications in optical photovoltaic devices, the difficulty of growth of single phase Cu_2O without CuO contamination still remains. Various deposition methods for the formation of Cu_2O have been attempted such as electrodeposition [3.12], sol-gel techniques [3.13], pulsed laser deposition [3.14], thermal and chemical oxidation [3.15,3.16], spraying [3.17], plasma evaporation [3.18], and sputter deposition [3.19,3.20]. The physical and

chemical properties of the films are affected by the deposition method as well as its conditions. In addition, it can also be influenced on the electrical properties, for example, band gap. Therefore these large variations can make CuO_x films suitable for many applications. Among a variety of deposition methods, radio frequency (rf) magnetron sputtering is the most commonly used method to synthesize films with splendid quality.

Chapter 3.2 is focused on the control of the compositional ratio of cuprous to cupric oxide and preferential phase in CuO_x films deposited on flexible polyethyleneterephthalate (PET) substrates by varying rf power and O_2 gas ratio during rf sputtering process. Studies about the quantitative assignment of compositional ratio of metallic Cu and Cu^+ by X-ray photoelectron spectroscopy (XPS) are very sparse because of the complexity due to the final state effect on Cu^0 and Cu^+. Therefore the assignment of the ratio of Cu species with different oxidation states were applied by X-ray induced Auger electron spectroscopy (XAES) peak analysis.

The study about CuO_x thin films prepared by reactive rf magnetron sputtering on p-type Si(100) substrate at various substrate temperatures were introduced in the chapter 3.3. The substrates were annealed in the range from room temperature to 573K during deposition. The effect of substrate temperature on the structural, physical, chemical, and wetting properties of the CuO_x thin films was investigated.

3.2 Effect of rf Power and Oxygen Gas Ratio

3.2.1 Experimental

In this research, we examined the CuO_x thin films deposited by rf magnetron sputtering with different rf power and O_2 gas ratio. In order to check the feasibility of CuO_x for flexible photovoltaic devices, CuO_x thin films were deposited on flexible polyethyleneterephthalate (PET) substrates. The distance between metallic Cu target (3 inches in diameter) and PET substrate (125 μm in thickness) was fixed at 11 cm and the substrate was rotated during deposition with a constant speed. The base pressure of the sputtering chamber was maintained at 2.4×10^{-6} Torr by a rotary vane pump and a turbo molecular pump and the working pressure was kept at 1.1 mTorr by mass flow controllers. Ar and O_2 gases were used to obtain the CuO_x thin films as a sputter and reactive gas, respectively. The flow rate of Ar gas was fixed at 30 sccm and that of O_2 gas was varied in the range of 0-10 sccm. The detailed sputtering condition was listed in Table 3.1. Furthermore, various rf powers (200, 300, and 400 W) were employed to investigate the formation of cuprous and cupric oxide thin films. In order to exclude the temperature effect on the flexible substrate, the substrate was cooled at 20°C by a chiller during the sputtering process. The surface resistance was evaluated by four-point probe method (Mitsubishi Chemical Corp., Loresta-GP (MCP-T600), Japan). X-ray diffraction (XRD, PANalytical, X'Pert Pro, Netherlands) experiments were performed for phase identification with the

diffraction patterns. The scanning electron microscopy (SEM, JEOL, JSM-6700F, Japan) was performed for investigation of the surface morphology of the films. The chemical nature of the films was examined by XPS (VG, MultiLab 2000, UK). To assign the oxidation state of Cu species in CuO_x films, high resolution XPS spectra and XAES were deconvoluted using XPSPEAK software (version 4.1). For the detailed information about the equipment was posted in the published papers [3.21,3.22].

3.2.2 Results and Discussion

The surface resistance of CuO_x films was measured and shown in Fig. 3.1. In case of the films obtained at 200 and 300 W of rf power, the surface resistance increased as the O_2 gas ratio increased up to 14.3%. Because the conductivity of Cu_2O is lower than that of CuO, the increase of surface resistance indirectly proved the formation of Cu_2O [3.23]. After that, the resistance of the film obtained at 25.0% of O_2 decreased about 10 folds in magnitude. It is worth to note the propensity of surface resistance of the films obtained at 400 W of rf power. The monotonic increase of the resistance as a function of O_2 gas ratio implies that the formation of Cu_2O. Therefore the compositional ratio of CuO in the CuO_x films obtained at 25.0% of O_2 deposited at 400 W is not as significant as the films obtained at 200 and 300 W.

Table 3.1 O_2 gas flow rate and the ratio of O_2 gas in the sputter gas.

flow rate [sccm]	0.0	0.1	0.3	0.5	0.7	1.0	2.0	3.0	5.0	10.0
ratio [%]	0.0	0.3	1.0	1.6	2.3	3.2	6.3	9.1	14.3	25.0

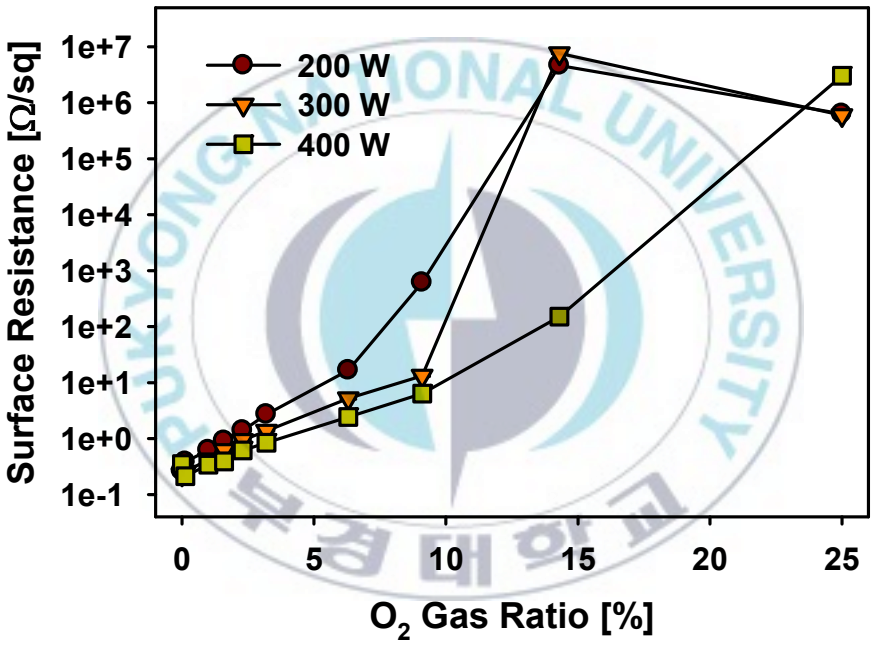

Fig. 3.1 Surface resistance of CuO_x films as a function of O_2 gas ratio increased from 0.0 to 25.0% at various rf power.

The effect of O_2 gas ratio and rf power on the crystallinity of the CuO_x films was investigated with XRD. The XRD patterns of the CuO_x films obtained at 200, 300, and 400 W of rf power with various O_2 gas ratios are shown in Fig. 3.2. The peak for PET at 46.6° was detected that could be caused from the defect sites of the CuO_x films. Metallic cubic Cu(111) phase and Cu(200) were observed at 43.3° and 50.4° from all the films obtained at 0.0% of O_2 gas ratio regardless of rf power [3.24,3.25]. The decrease of Cu(111) peak intensity, when the O_2 gas ratio increased from 0.3% (200 W) and 0.0% (300 and 400W) to 3.2%, maybe resulted from the oxidation of Cu. This indirectly explains the formation of CuO_x films. At the oxygen gas ratio of 1.6% with 200 W, evolution of features at 36.4° and shoulder at 42.3° was detected which could be assigned to cubic Cu_2O(111) and Cu_2O(200) [3.25]. Further increase of O_2 gas ratio to 6.3% with 300 and 400 W of rf power also caused Cu_2O formation. Noticeably, the films obtained at 200 W showed CuO(202) peak at 58.4° and CuO(022) peak at 65.8° with 14.3% of O_2 gas ratio while that at 300 and 400 W showed only Cu_2O features. When the O_2 gas ratio increased to 25.0%, all Cu_2O peaks decreased and monoclinic CuO peaks were dominant from the CuO_x films obtained with 200 and 300 W of rf power [3.26]. The Cu_2O(111) peak, however, did not decreased but increased when the rf power was 400 W. Comparing the XRD peaks of the CuO_x films obtained at 25.0% of O_2 gas ratio with different rf powers, the dominant phases were monoclinic CuO obtained at 200 and 300 W and cubic Cu_2O obtained at 400 W for the CuO_x films, respectively. And the

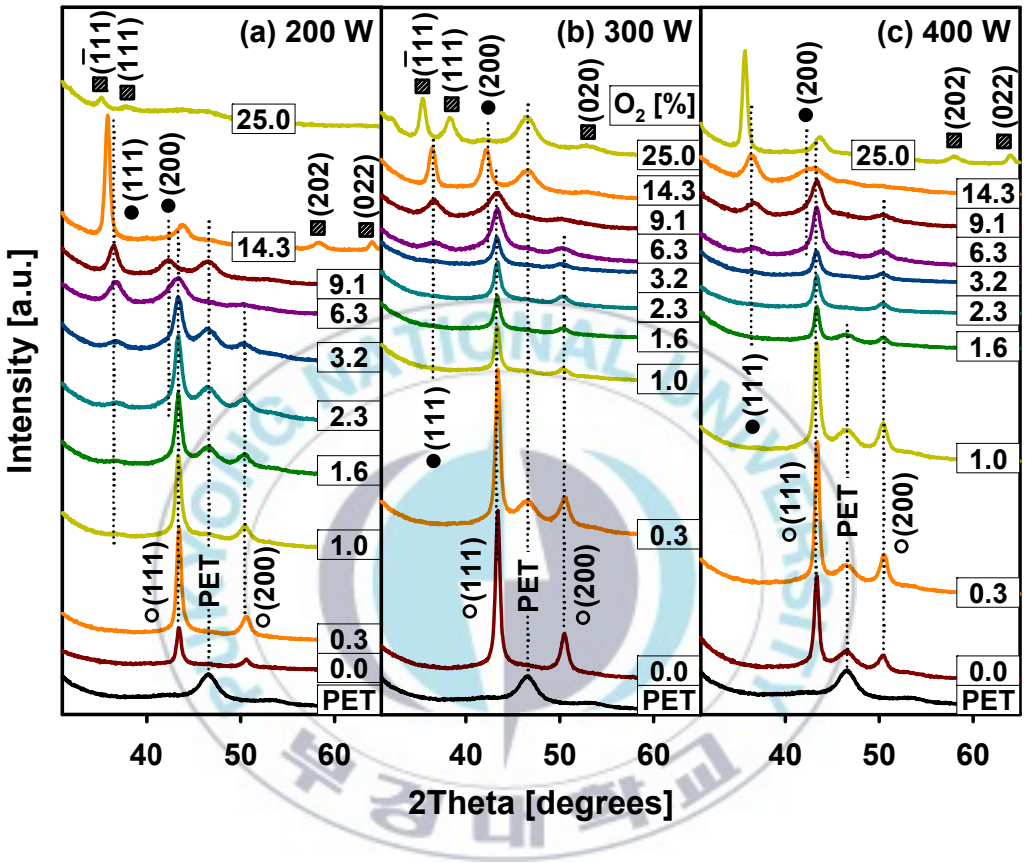

Fig. 3.2 XRD patterns of CuO_x films obtained at various O_2 gas ratios with (a) 200 W, (b) 300 W, and (c) 400 W of rf power. The hollow circles represent for metallic Cu, the filled circles represent for Cu_2O, and the shaded squares represent for CuO. The number in the box shows the O_2 gas ratio.

preferential crystal phase of CuO_x was changed from cubic Cu(111) through cubic Cu_2O(111) to monoclinic CuO($\bar{1}$11) by increase of oxygen gas ratio.

Fig. 3.3 shows the representative SEM images of CuO_x films obtained at 200, 300, and 400 W of rf power. At the O_2 gas ratio was 0.0%, the aggregated granular morphologies were observed for all CuO_x films. When the O_2 gas ratio was increased to 9.1%, the shape of CuO_x films were not noticeably changed. However, the filed flake shape was observed from the films obtained at 14.3% of O_2 gas ratio with 200 W of rf power. The films fabricated at 14.3% of O_2 gas ratio with 300 and 400 W were maintained the granular morphologies. Further increase of O_2 gas ratio to 25.0%, the granular shape was disappeared at 300 W and the filed flake shape was barely observed at 400 W. From the XRD results, cubic crystal phases were dominant up to 9.1% of O_2 gas ratio with 200 W, 14.3% of O_2 gas ratio with 300 W and then monoclinic CuO was superior in the CuO_x films. The difference of the morphology; granule vs. flake, could be dependent with the dominant phase of the CuO_x films; cubic vs. monoclinic. It could be confirmed that the films deposited at 14.3% of O_2 gas ratio with 200 W and 25.0% of O_2 gas ratio with 400 W were shown the similar XRD peaks and SEM images.

Interestingly, the sizes of granule and flake were noticeably changed depending on the O_2 gas ratio and rf power. The size of granule of the sample obtained at 0.0% of O_2 gas ratiowas decreased with increasing the rf power. When the O_2 gas ratio was 9.1%, the size of granule for all CuO_x

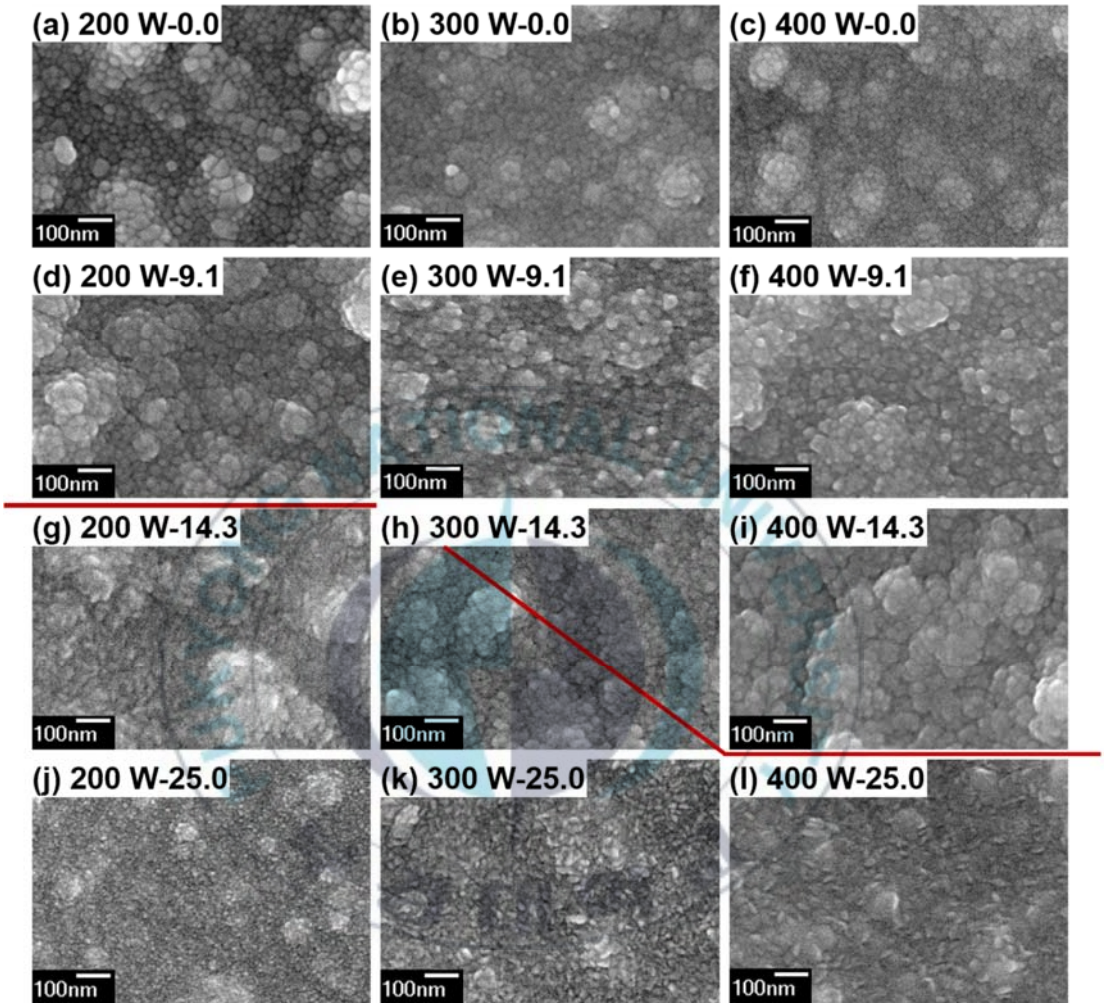

Fig. 3.3 Representative SEM images of CuO_x films obtained at various rf powers and O_2 gas ratios.

films was almost similar and it indicates that the size was independent on the rf power at about 9.1% of O_2 gas ratio. The size of granule at 14.3% of O_2 gas ratio deposited at 400 W was significantly increased while that at 300 W was not changed. The O_2 gas ratio was increased to 25.0%, the size of flake was extremely small at 200 W and then increased with increasing the rf power. The difference of the size of granule and/or flake between 200 and 400 W at 25% of O_2 gas ratios was the largest among the various O_2 gas ratios. As the O_2 gas ratio increased, the size of granule and/or flake decreased with lower rf power while that increased with higher rf power. Therefore the growth of granule and/or flake showed the different propensity with various rf power. It concludes that the phase and morphology of CuO_x could be manipulated by O_2 gas ratio and rf power.

Fig. 3.4 (a), (b), and (c) show the high resolution XPS spectra of Cu 2p core level of CuO_x films obtained at 200, 300, and 400 W of rf power, respectively. The charge accumulation effect of all spectra shown here was corrected with an aliphatic carbon at 284.6 eV [3.27]. In Fig. 3.4 (a), the sharp Cu $2p_{3/2}$ peak centered at 933 eV and the peak Cu $2p_{1/2}$ centered at 953 eV were increased up to 9.1% of O_2 gas ratio. This means that the Cu_2O and/or metallic Cu was grown with negligible formation of cupric oxide CuO except for 200 W. The noticeable CuO formation was observed when the O_2 gas ratio was 14.3% by evolution of satellite peaks at 942-946 eV, which is the characteristic satellite peak of Cu^{2+} [3.28]. The peak measured from the films obtained at 14.3% of O_2 gas ratio with 200 W is broader than those with

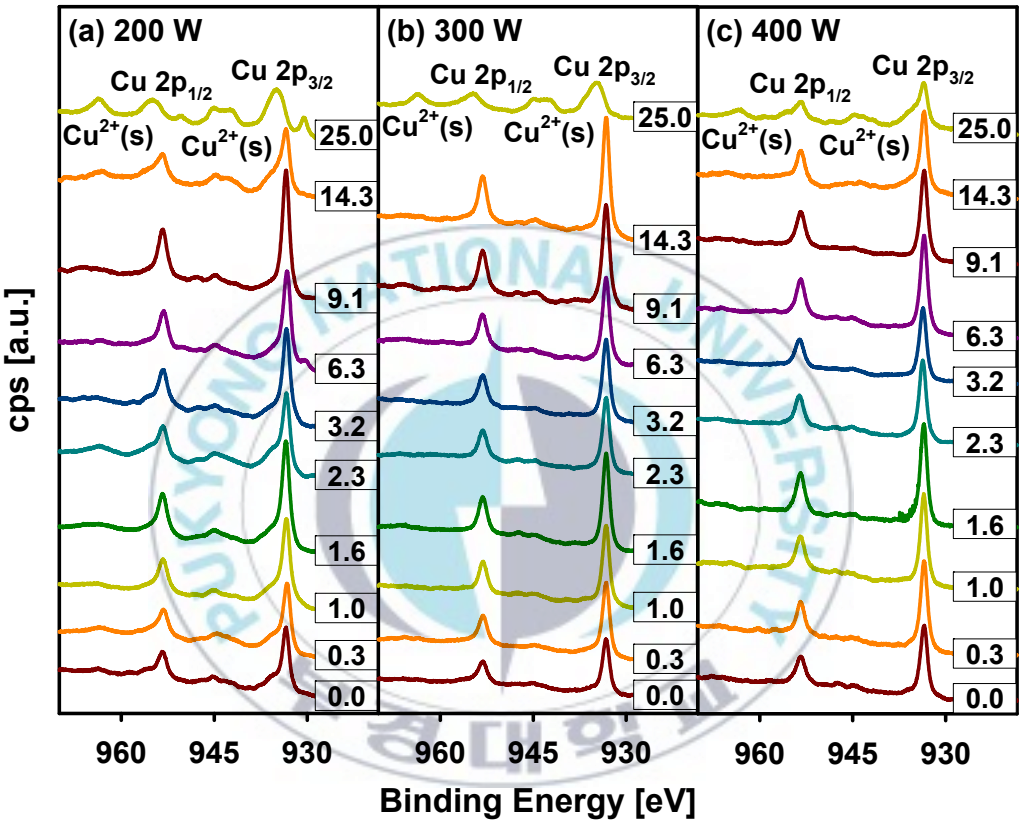

Fig 3.4 High resolution XPS spectra of Cu 2p region of CuO_x films obtained at various O_2 gas ratios at 200 W in (a), 300 W in (b), and 400 W of rf power in (c). The number in the box represents O_2 gas ratio.

300 and 400 W. It revealed that the lower rf power leads to more rapid oxidation of metallic Cu. And then the Cu $2p_{3/2}$ peak maximum shifted towards the higher binding energy and distinct satellite peaks evolved over 14.3% of O_2 gas ratio at 200 and 300 W of rf power. This implies that the compositional ratio with different oxidation states of Cu changed. The characteristic satellite peaks of Cu corresponding to Cu $2p_{3/2}$ and Cu $2p_{1/2}$ were shifted to higher binding energy side as well [3.29]. When the CuO_x films were synthesized at 25% of O_2 gas ratio with 400 W, the peak profile is not broad and the development of satellite was not remarkable. It means that the films were not fully oxidized in this deposition conditions. However, it is difficult to differentiate between Cu^0 and Cu^+ by the XPS spectra of Cu 2p, which were overlapped each other, due to the final state effect [3.30]. In order to differentiate the oxidation states of Cu, XAES of Cu LMM was performed [3.31] and the change of the oxidation state of Cu was clearly observed with XAES spectra

Fig. 3.5 shows the high resolution XAES spectra of Cu LMM. As the O_2 gas ratio increased, the LMM Cu^0 peak decreased while those for Cu^+ and Cu^{2+} increased until 9.1% of O_2 gas ratio with 200 W. Further increase of O_2 gas ratio to 25.0% promoted oxidation of Cu species from Cu^+ to Cu^{2+} therefore the LMM of Cu^{2+} was dominant at 25.0% of O_2 gas ratio with 200 W shown in Fig. 3.5 (a). In 300 W, the peak profile of Cu LMM region at 14.3% of O_2 gas ratio was similar to that at 9.1% of O_2 gas ratio with 200 W. And the LMM Cu^+ peak was not decreased comparing with the spectrum at 25%

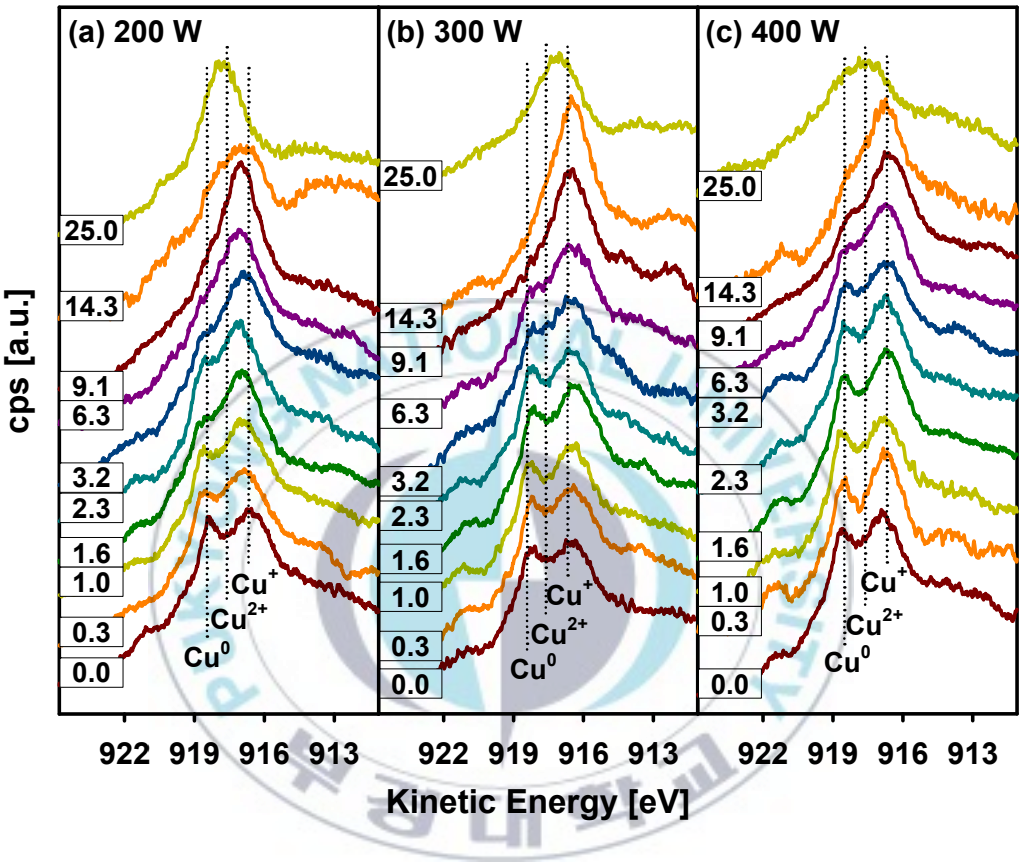

Fig. 3.5 High resolution XAES spectra of Cu LMM region of CuO_x films obtained at various O_2 gas ratios with (a) 200, (b) 300, and (c) 400 W of rf power. The number in the box represents O_2 gas ratio.

with 200 W. From the films obtained with 400 W, the LMM Cu^0 peak was remained at 14.3% of O_2 gas ratio therefore we can conclude that the oxidation process of 200 W during increasing the O_2 gas ratio was slower than that of 200 and 300 W.

Fig. 3.6 shows the representative deconvoluted XAES spectra of Cu LMM of CuO_x films deposited at 200, 300, and 400 W of rf power in (a), (b), and (c), respectively. From the XAES results shown in Fig. 3.6 (a) and (b) for 200 and 300 W of rf power, as the O_2 gas ratio increased, the peak intensity of Cu^+ (916.7±0.1 eV) increased as the Cu^0 state (918.5±0.1 eV) converted to the Cu^+ state. In addition, as the O_2 gas ratio increased up to 14.3% then the major Cu species was changed from Cu^+ to Cu^{2+} (917.7±0.1 eV) at 25.0% of O_2 gas ratios. The dominant Cu moiety, however, of CuO_x films deposited at 25.0% of O_2 gas ratio and 400 W of rf power, shown in Fig. 3.6 (c), was Cu^+. This result is consistent with the results of electric property measurement and XRD experiment. The more Cu^{2+} species, the lower surface resistance and the higher portion of crystalline phase with lower oxidation states of Cu.

Fig. 3.7 shows the compositional ratio of Cu species with different oxidation states in CuO_x films deposited at different condition deduced from XAES of Cu LMM peak. When the O_2 gas ratio was less than 10% (Region 1 in Fig. 3.7), Cu^+ and Cu^{2+} increased as the Cu^0 species converted to these two species and the Cu^+ seemed to be saturated near 10% of O_2 gas ratio regardless of the rf power. In Region 1, stepwise oxidation reaction of Cu

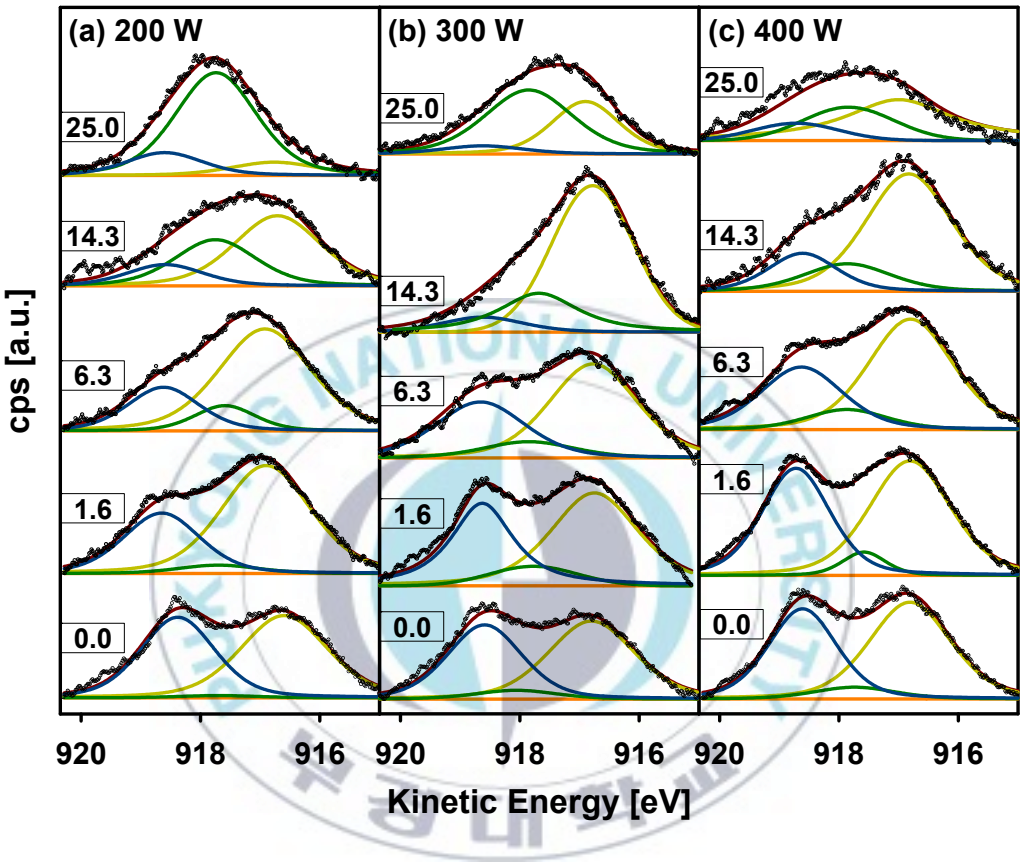

Fig. 3.6 Representative deconvoluted XAES spectra of Cu LMM region of CuO_x films obtained at various O_2 gas ratios with (a) 200, (b) 300, and (c) 400 W of rf power.

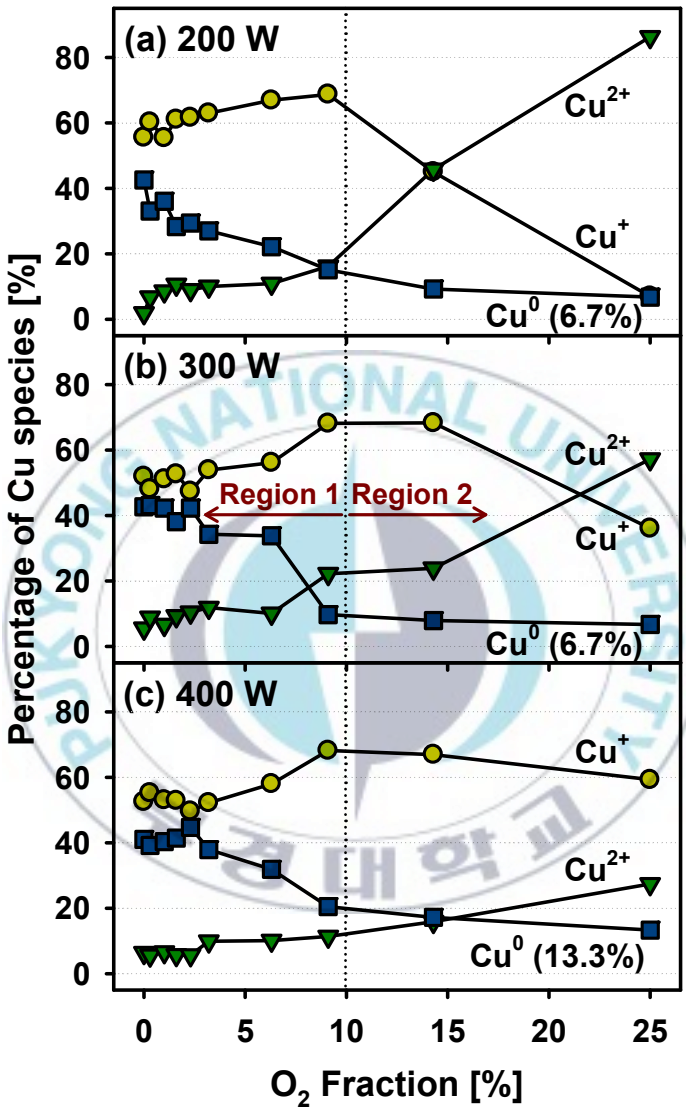

Fig. 3.7 Percentage of Cu species of CuO_x films obtained with various O_2 gas ratios and rf power determined with XAES of Cu LMM peaks.

could be dominant as following reactions; $4Cu + O_2 \rightarrow 2Cu_2O$ and $2Cu_2O + O_2 \rightarrow 4CuO$. Most of the Cu sputtered from the target oxidized to Cu_2O and the Cu_2O oxidized further to CuO as O_2 gas ratio increased. Therefore the content of Cu^0 decreased and those of Cu^+ and Cu^{2+} increased. When more than 10% of O_2 was employed (Region 2 in Fig. 3.7), the Cu^0 ratios were 6.7, 6.7, and 13.3% for the films deposited with 200, 300, and 400 W, respectively, at 25% of O_2 gas ratio but the profiles of Cu^+ and Cu^{2+} ratios were changed as the O_2 gas ratio increased. The profiles of increase in Cu^{2+} ratio and decrease in Cu^+ ratio were dependent with the rf power in Region 2. In this region, disproportionation reaction of Cu_2O is dominant as following reaction; $Cu_2O \rightarrow Cu + CuO$. By this reaction, more Cu^0 species sputtered at higher rf power which shifts the equilibrium to the left by Le Châtelier's principle. Therefore the content of Cu^+ increased in CuO_x films deposited at high rf power while that of Cu^{2+} decreased. Therefore the higher rf power applied during the sputtering, the less Cu^{2+} formed.

3.2.3 Conclusion

CuO_x thin films were deposited on PET substrates with various rf power and O_2 gas ratio to manipulate the compositional ratio of Cu_2O to CuO and the preferential crystalline phase in CuO_x films to apply in OSCs. XRD study revealed that the preferential CuO_x phase could be controlled by O_2 gas ratio in the sputtering gas and rf powers as well. The dominant crystalline

phase of CuO_x films changed from metallic cubic Cu(111) through cubic Cu_2O(111) to monoclinic CuO($\bar{1}$11) as the O_2 gas ratio increased to from 0.0 to 25.0%. The preferential phase change indirectly confirmed by SEM images. Surface resistance increased up to 14.3% of O_2 gas ratio and then decreased about ten folds in magnitude of the films obtained at 200 and 300 W of rf powers with 25.0% of O_2 gas ratio. Which means that compositional ratio of CuO is higher than that of CuO in the films because the surface resistance of CuO is lower than cuprous oxide. XAES analysis revealed that the compositional ratio of CuO increased up to 9.1% of O_2 gas ratio in the films regardless of rf power. Above 14.3% of O_2 gas ratio, the amounts of CuO decreased while the contents of CuO increased with different profiles depending on rf power. This phenomenon had good agreement with the result of electrical property of CuO_x thin films. From the findings described above, we can possibly control the compositional ratios of CuO and CuO and preferential phase of CuO_x films by varying rf power and the oxygen gas ratio.

3.3 Effect of Substrate Temperature

3.3.1 Experimental

CuO_x thin films were synthesized with metallic Cu target (99.9%, 2 inches in diameter) on p-type Si(100) wafer, which was cleaned by the HF cleaning process to remove the surface oxide, using rf magnetron sputtering method. The deposition chamber was evacuated using a rotary vane pump and a turbo molecular pump to achieve 1.0×10^{-7} Torr of base pressure. Highly pure Ar (99.99%) gas for sputtering of Cu target and O_2 (99.99%) as a reactive gas were used for CuO_x deposition. The introduced gases were controlled by mass flow controllers, separately. The total gas flux was kept at 20 sccm and the gas mixing ratio (O_2/O_2+Ar) was 50%. In order to clean the Cu target and stabilize the plasma, pre-sputtering was performed for 1 hr while the substrate was shielded. The deposition of CuO_x thin films was performed with a rf power of 40 W for 3 hrs after pre-sputtering process and the working pressure was 50±0.5 mTorr. In our work, CuO_x thin films were obtained at different substrate temperatures from room temperature to 573K.

The thickness of the CuO_x thin films was measured by cross-sectional images of field emission scanning electron microscopy (FE-SEM, JEOL, JSM-6700F, Japan). Another method to analyze the thickness of films was spectroscopic ellipsometry (SE, J. A. Woollam, M- 2000D, USA) for cross check. In addition, the SE data were used to determine the surface roughness and direct band gap. The surface morphology of CuO_x thin films was

investigated using an atomic force microscopy (AFM, Veeco, Multimode Digital Instruments Nanoscope IIIα, USA) in contact mode. The root mean square (rms) values were used to determine the roughness of the films. The crystalline phase of CuO_x thin films was investigated by XRD (PANalytical, X'Pert MPD, Netherlands) with Cu Kα radiation in normal mode. The chemical analyses of CuO_x thin films were carried with XPS (VG, MultiLab 2000, UK). The detailed parameters for XPS analysis are described in elsewhere [3.32]. The water contact angles of CuO_x thin films were measured with a customized contact angle analyzer to investigate the hydrophilicity of CuO_x films with 0.2 μL of water droplet. The measurement of contact angle was performed in static contact mode and the contact angle of obtained image was determined by Motic images analysis program (ver. 2.0).

3.3.2 Results and Discussion

The thickness of CuO_x thin films was measured by FE-SEM images. Fig. 3.8 shows the cross-sectional views of Cu-rt, Cu-373, Cu-473, and Cu-573, respectively. The sample notation used here such as Cu-573 means that the substrate temperature was 573K during CuO_x deposition. As shown in Fig. 3.8, the thickness of thin films is relatively constant about 180 nm and the columnar structure was grown normal to the surface of Si substrate. The thickness measured using SE analysis is listed in Table 3.2 for comparison. There is a slight discrepancy between the thicknesses obtained by FE-SEM and SE. This caused because the thickness measured from the FE-SEM

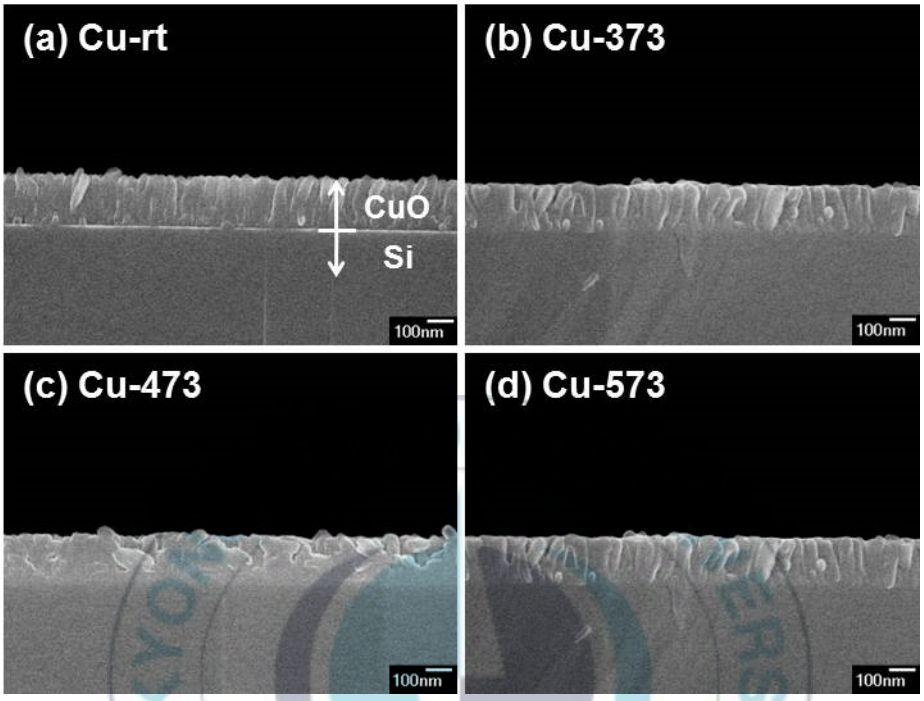

Fig. 3.8 The cross-sectional SEM images of CuO_x thin films obtained at different substrate temperatures: (a) Cu-rt, (b) Cu-373, (c) Cu-473, and (d) Cu-573.

Table 3.2 The parameters of CuO_x films obtained at different substrate temperatures.

	Cu-rt	Cu-373	Cu-473	Cu-573
Thickness [nm], SE	154.8±1.4	176.1±6.3	189.9±5.1	183.9±6.2
d-spacing [Å], XRD	2.544	2.538	2.533	2.527
Grain size [nm], AFM	44.9±6.3	55.5±4.9	70.1±7.3	89.6±6.7
Roughness [nm], SE	0.07±0.04	15.9±0.4	19.2±1.3	27.5±1.5

images was ambiguous due to the surface roughness. The relatively constant film thickness caused by the constant mixing ratio of sputter gas. Thus, the film thickness was not affected by the substrate temperature in this study.

The crystal structure of CuO_x films was characterized by XRD and shown in Fig. 3.9. The diffraction angles of CuO_x films were matched with the monoclinic CuO [3.26]. The characteristic diffraction peaks of CuO of (110), ($\bar{1}$11) and/or (002), and (111) phases were observed. All the CuO_x films obtained at different substrate temperatures possessed relatively weaker intensity of (110) than other phases. The intensity of ($\bar{1}$11) and/or (002) was increased up to 473K and then decreased with high preference. The peak intensity of (111) phase was increased at 573K. It could be certain that the preferential growth of CuO changed from ($\bar{1}$11) and/or (002) to (111) phase above 473K of substrate temperature. It is interesting to note that the peak position shifted to higher diffraction angle by annealing during deposition. It indicates that CuO crystals formed more packed crystal by highly mobile active species and have a smaller lattice parameter as summarized in Table 3.2. The crystal size of CuO was calculated by using the Scherrer's equation to verify the crystal size of the thin films. The crystal sizes obtained from peak were 13.74, 16.77, 16.79, and 16.45 nm for Cu-rt, Cu-373, Cu-473, and Cu-573, respectively. This phenomenon was observed in microwave dielectric ceramic thin films by Shi *et al.* [3.33]. The results of the investigation of the polycrystalline CuO_x films annealed below 873K were reported that the

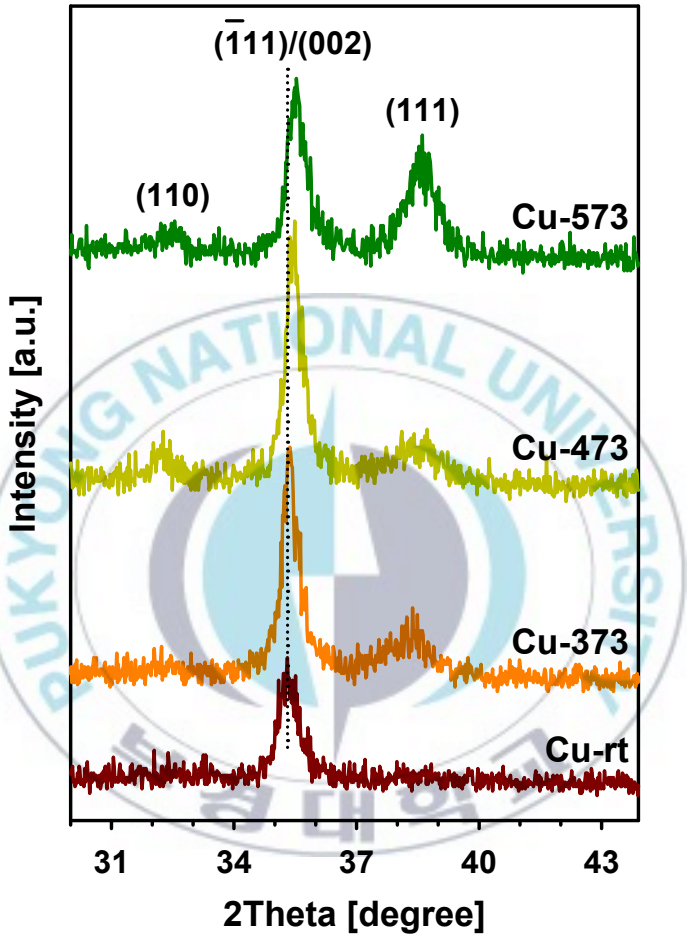

Fig. 3.9 XRD patterns of the CuO_x thin films as a function of substrate temperature.

polycrystalline phases were converted to single crystalline or continuously existed as mixing phases of Cu_2O and CuO [3.34,3.35] According to the equilibrium phase diagram of the Cu-O system, CuO is the stable phase up to 573K even at low oxygen partial pressure [3.36]. Therefore the formation of CuO phase was reasonable and the substrate temperature affected on the quality of crystal, preferential orientation, not the crystal phase in CuO_x thin films synthesized by rf magnetron sputtering. The kinds of crystal structure were not affected but the preferential orientation was affected by annealing temperature.

Fig. 3.10 shows AFM images and the roughness (R_{rms}) values of CuO_x films. The average grain sizes of CuO_x thin films are summarized in Table 3.2. The grain size increased as the substrate temperature increased. This can be explained by the thermal energy, which is supplied by annealing process, used for filling the micro-voids or defects among columnar structures by active species. So the grain size increased by annealing and this caused the increase of roughness. This phenomenon shows agreement with the previous study about the relationship between roughness and grain growth [3.37,3.38].

The chemical analysis, which extensively focused on the oxidation state of elements, was performed by XPS. The high resolution Cu 2p XPS spectra are shown in Fig. 3.11 (a) and the representative deconvoluted Cu $2p_{3/2}$ peaks for Cu-rt and Cu-573 are shown in Fig. 3.11 (b) and (c), respectively. The XPS spectra of Cu 2p showed characteristic doublet peaks with 20 eV of

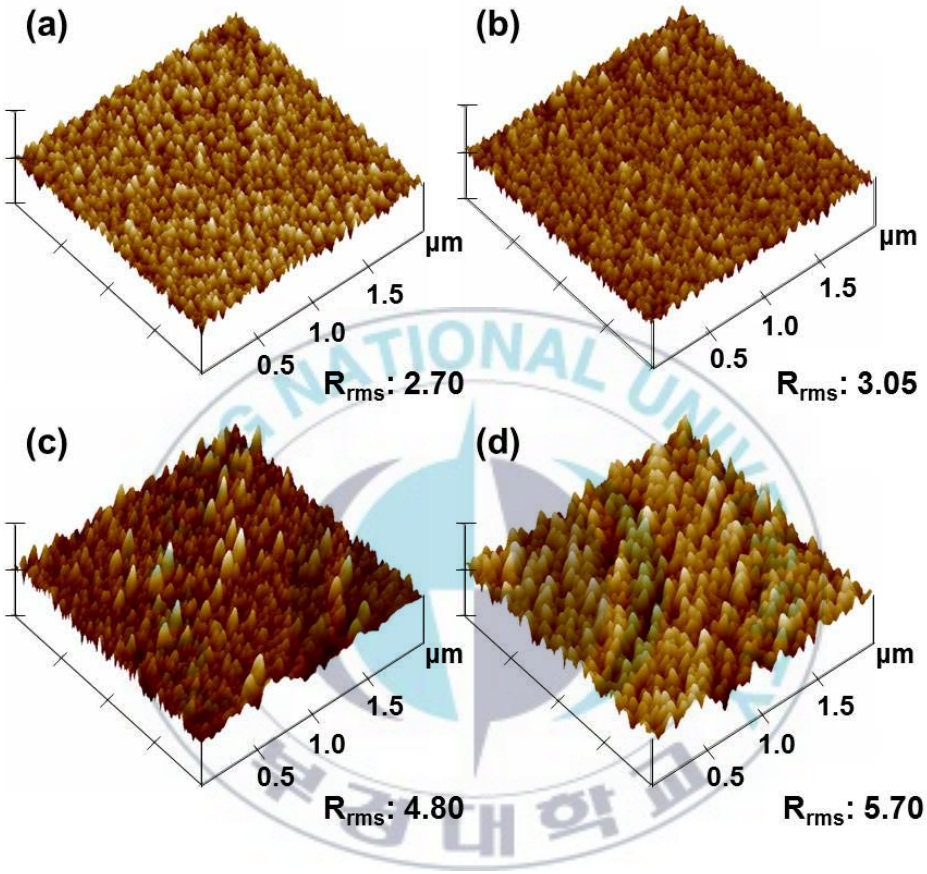

Fig. 3.10 AFM images of CuO_x thin films deposited at different substrate temperature (a) rt, (b) 373, (c) 473, and (d) 573K. X scale is 2 μm and Z scale is 40 nm for the images. The surface roughness (R_{rms}) was 2.70, 3.05, 4.80, and 5.70 nm in (a), (b), (c), and (d), respectively.

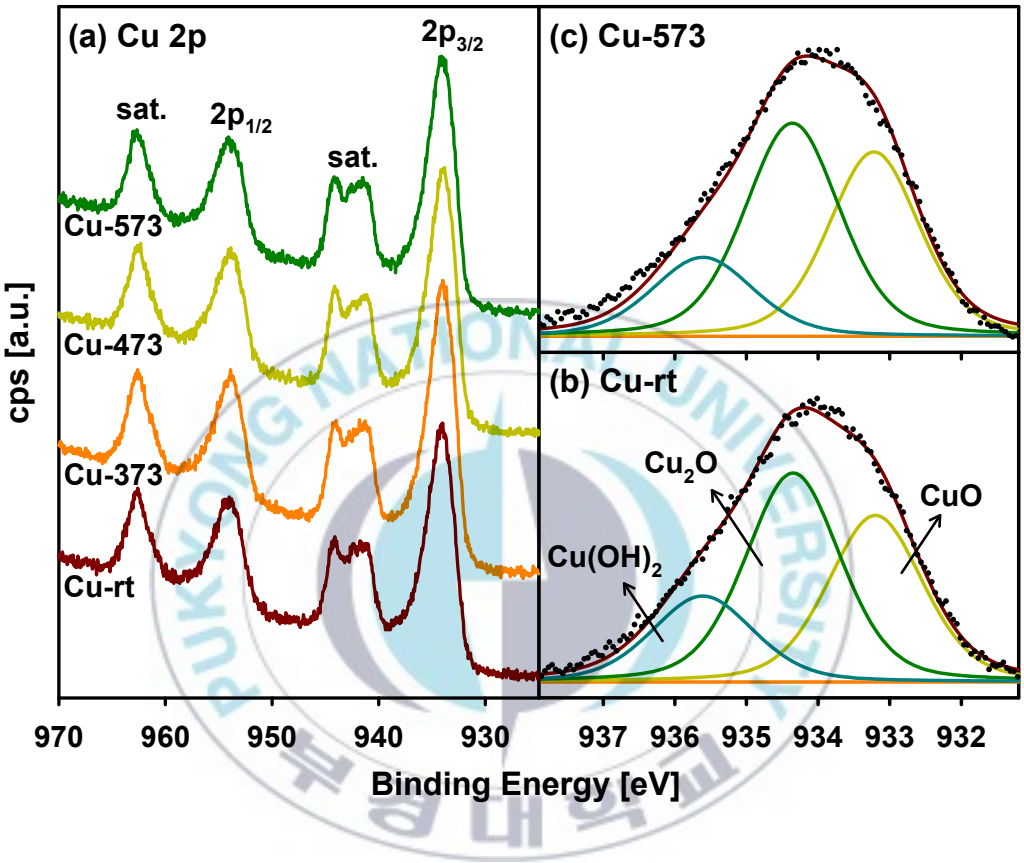

Fig. 3.11 (a) High resolution XPS spectra of Cu 2p of CuO_x thin films obtained at different substrate temperature, sat. means the satellite shake up peak of CuO. The deconvoluted spectra of Cu $2p_{3/2}$ at (b) Cu-rt and (c) Cu-573.

spin orbit splitting (SOS) and the shake-up satellite peaks were observed at about 7 and 9 eV of binding energies higher than that of Cu 2p peak [3.32]. The existence of satellite peaks indirectly indicates the formation of CuO [3.28]. These results are cross matched with the results of XRD. The Cu $2p_{3/2}$ peaks were curve fitted with three species corresponding to Cu_2O (933.20 eV, FWHM: 1.56 eV), CuO (934.34 eV, FWHM: 1.56 eV), and $Cu(OH)_2$ (935.61 eV, FWHM: 1.67 eV) [3.36,3.40]. As shown in Fig. 3.11 (a), no significant difference was detected in the Cu 2p XPS spectra of CuO_x films. As mentioned previously, only the crystalline CuO peak was detected from the CuO_x films in XRD study, however the coexistence of CuO and Cu_2O was confirmed by XPS investigation. From the above observation, it may be concluded that Cu_2O existed as an amorphous phase and CuO grew preferentially in monoclinic crystal phase. In addition, the oxidation of Cu was almost independent of the substrate temperature and Cu_2O and CuO were coexisted with constant mixing ratio (Fig. 3.11 (b) and (c)).

In the high resolution XPS spectra of O 1s region (Fig. 3.12), the deconvoluted O 1s peaks were assigned for three species, O-Cu bond (529.56 eV, FWHM: 0.95 eV), O-C bond (531.07 eV, FWHM: 1.17 eV), and surface oxygen (O-Surf., 531.85 eV, FWHM: 1.27 eV) from low to high binding energy (Fig. 3.12 (b) and (c)). Even though the deposition was carried in high vacuum condition, the residual carbon contaminants in the deposition chamber were attributed to the formation of carbonyl species [3.41]. The third species, surface oxygen, indicated that hydroxide species caused by the

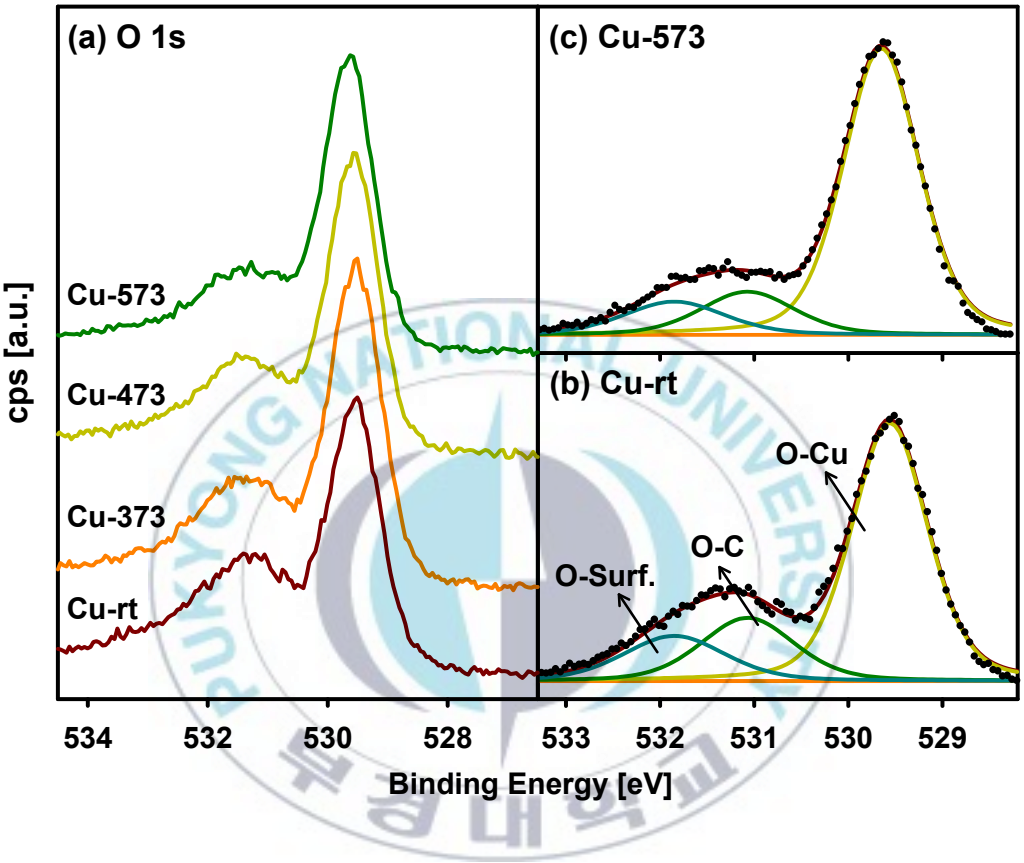

Fig. 3.12 (a) High resolution XPS spectra of O 1s from CuO_x thin films obtained at different substrate temperature. (b) The deconvoluted spectra of O 1s in CuO_x films obtained at rt and (c) at 573K.

residual hydrogen species such as water in the deposition chamber and adsorbed on the surface to form $Cu(OH)_2$ [3.42]. The ratio of $Cu(OH)_2$ calculated from O 1s XPS spectra decreased with increase of the substrate temperature and it is consistent with the result of Cu 2p XPS spectra. This means that the ratio of CuO_x increased as the substrate temperature increased and the transformation between Cu_2O and CuO was undetectable below 573K.

The contact angles of CuO_x thin films were measured to check hydrophilicity of the CuO_x films and the images for all CuO_x films are shown in Fig. 3.13. CuO_x thin films obtained at high substrate temperature have more hydrophobic surface than that obtained at low temperature, confirmed by the higher degree of the contact angle of water on the CuO_x films. This observation is opposite with the common Wenzel's model [3.43] which is good model for homogeneous wetting surface, the contact angle decreased as the roughness of the surface increased. This could be explained by lotus effect [3.44]; the surface wettability is changed from hydrophilic to hydrophobic as the roughness increased. The wettability is attributed to the composition and roughness of the surface. From the XPS results, the composition of CuO_x thin films was not the major factor of the increase of contact angle. Therefore the contact angle in this study was affected by the surface roughness and grain size. According to the AFM and SE results, the roughness and grain size increased as a function of substrate temperature. As a result, the contact angle was significantly dependent on the substrate temperature.

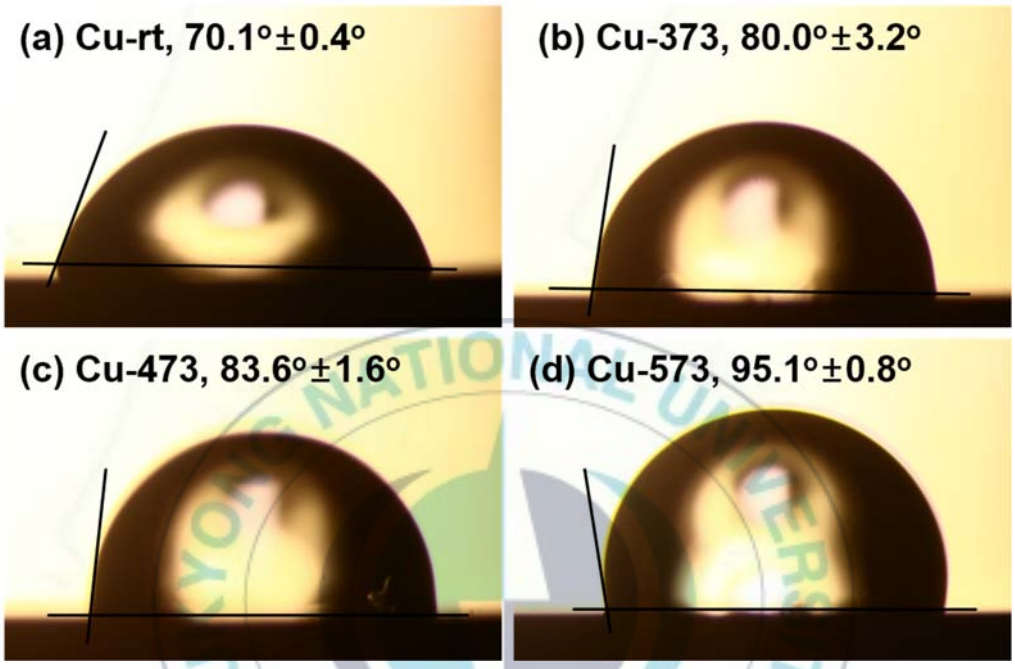

Fig. 3.13 The images of contact angle measurement for Cu-rt in (a), Cu-373 in (b), Cu-473 in (c), and Cu-573 in (d). The numbers in the figure indicate the measured contact angles.

To investigate the optical properties of CuO_x thin films, SE measurement was performed on the CuO_x thin films. SE measurement was based on the change in the state of polarization of light. A polarized beam of monochromatic or quasi-monochromatic light is incident on a sample, the reflected light which is polarized in an unknown state is examined. The analysis of the incident and reflected states of polarization was performed to adjust the calculated spectrum which is matched the measured spectrum. The calculated spectrum was created in the construction on the model of sample, where the structure and composition of sample was expressed as the model. By controlling the model parameters, we can obtain the well matched calculated spectrum with the measured spectrum. Finally, the information such as thickness, surface roughness, refractive index, and etc. were collected from SE.

Two experimental parameters (Ψ, Δ) were obtained from SE. The Ψ is defined as the arctangent of the amplitude ratio of the decrease of the field intensity of the parallel and senkrecht waves and Δ is defined as a phase difference of the two waves [3.45]. In this research, only Ψ spectra was considered and the plot of Ψ values versus photon energy presents in Fig. 3.14. The data points were reduced to 1/5 to easily detect the samples. The optical model of CuO_x thin films was composed by three layers. The bottom layer is a Si wafer which is set to 1 mm for thickness, the middle layer is a genosc layer described the oscillators, and the top layer is a surface roughness of CuO_x thin films. As shown in the Fig 3.14, the peak shape of CuO_x thin

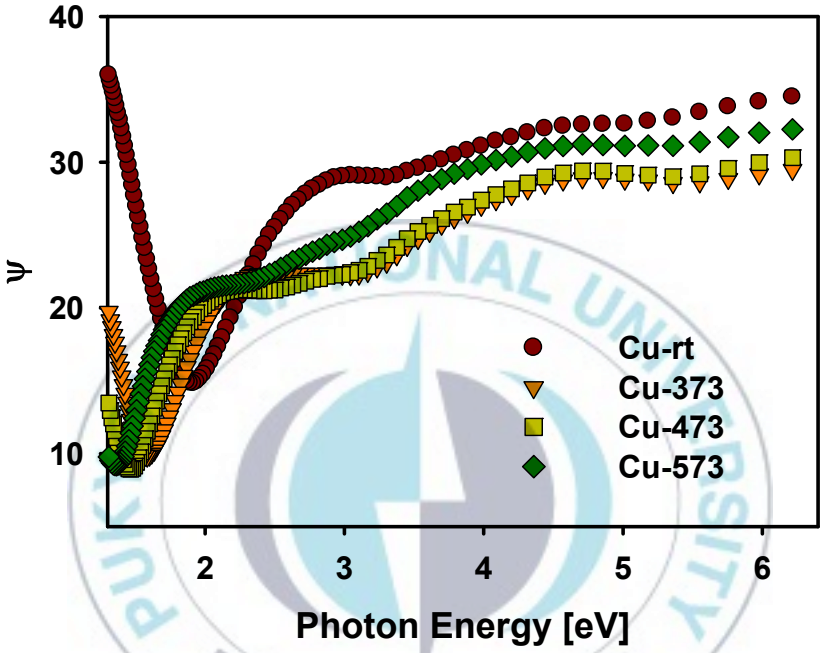

Fig. 3.14 The calculated Ψ spectra for CuO_x thin films with different substrate temperature.

films deposited at rt was different with that obtained at higher substrate temperature. And the maximum peak position was shifted to lower photon energy with increasing the substrate temperatures. This means that the thickness of thin films was decreased and an accurate thickness and roughness of CuO_x thin films were listed in Table 3.2.

The optical parameters obtained from SE, such as refractive index (n), extinction coefficient (k), and dielectric constants (ε_1, ε_2) were shown in Fig. 3.15. Fortunately SE provides dielectric constants and two constants (ε_1, ε_2) can be calculated by [3.46],

$$\varepsilon_1 = n^2 - k^2, \quad \varepsilon_2 = 2nk$$

where ε_1 is the real part and ε_2 is the imaginary part of the dielectric constant. These four graphs showed the similar results with the Ψ spectra. The Cu-rt spectra are distinct from Cu-373, 473, and 573. Entirely, the refractive index was decreased with increasing the photon energy. In the graph of extinction coefficient, the number of peak maximum is one for Cu-rt at about 2.4 eV and that is two for other films at about 2.4 and 3.9 eV. Especially the peak maximum at about 3.9 eV was shifted to lower photon energy with increasing the substrate temperature. As shown in Fig. 3.15 (c) and (d), these spectra are almost coincident with Fig. 3.15 (a) and (b), respectively.

The other important information from SE is absorption coefficient (α). This parameter was usually calculated from the following relationship from UV-vis spectra [3.47]

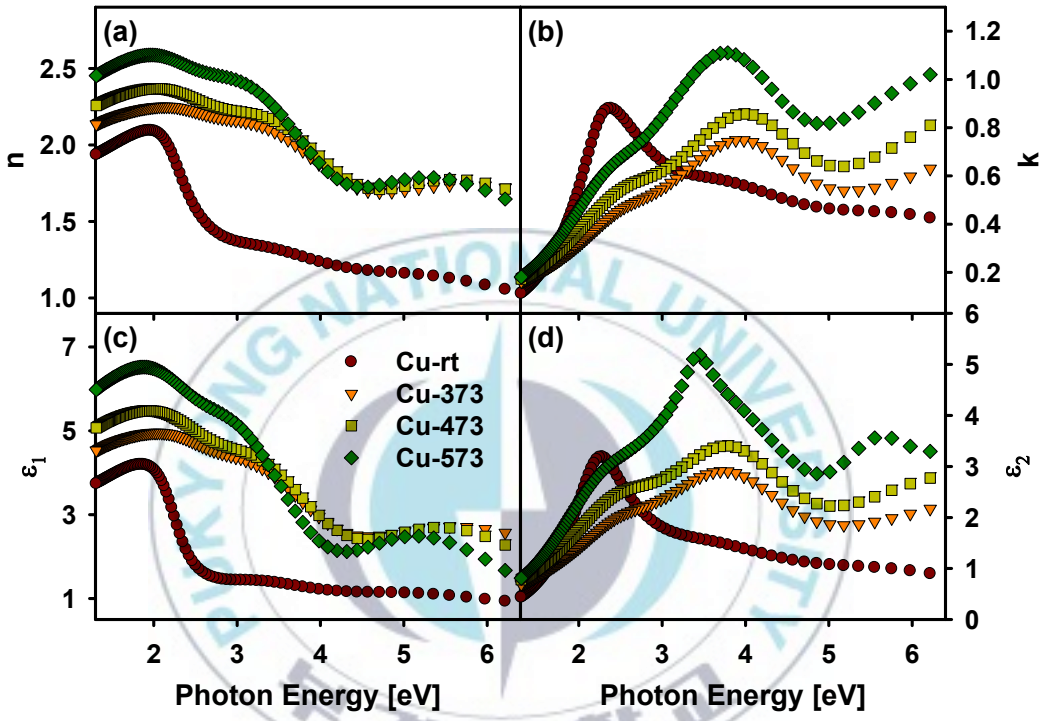

Fig. 3.15 The variation of (a) refractive index, (b) extinction coefficient, (c) real parts of the dielectric coefficient, and (d) imaginary parts of the dielectric coefficient with photon energy.

$$\alpha = \frac{1}{t} \ln\left(\frac{1-R^2}{T}\right).$$

where t is the thickness, R is the reflectance, and T is the transmittance of the films. In this study, the absorption coefficient was figured out using following relationship [3.48],

$$\alpha = \frac{4\pi k}{\lambda}.$$

The absorption coefficient as a function of photon energy is shown in Fig. 3.16. Similarly other optical results, the absorption coefficient spectrum of Cu-rt has different propensity with those of other films. The absorption coefficient of all films was gradually increased to 2.4 eV. And the broad peak was observed in the Cu-rt. However the spectra of samples obtained at higher substrate temperature than rt seemed to be continuously increased and the value of absorption coefficient reaches to 3.67×10^{-2} m^{-1} at 3.45 eV for Cu-573.

The optical absorption spectra are commonly divided in three regions, absorption tail, exponential edge, and high absorption region [3.46,3.48]. The first, absorption tail is contained the region below 1.7 eV of photon energy and it shows the quality of amorphous and crystalline films, for example, the observation of long tail and its related peaks in the absorption tail region could be caused from the defects and impurities in the films [3.49]. The second, exponential edge is strongly connected with the structural randomness of the sample. And the final, exponential edge uses to obtain the optical band gap.

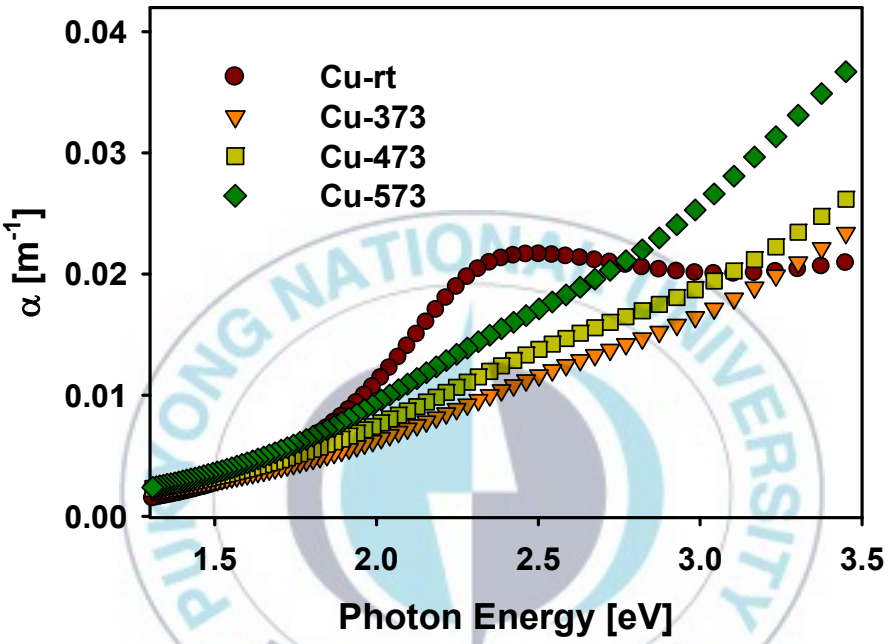

Fig. 3.16 The absorption coefficient with photon energy for CuO_x thin films with different substrate temperature.

In the absorption tail and exponential edge region, Urbach energy, E_u, or the width of band tails of the localized states was determined by Urbach law [3.46,3.48],

$$\alpha = \alpha_0 \exp\left(\frac{h\nu}{E_u}\right),$$

where α_0 is a constant depending on the photon energy. The above relationship is applied to logarithm, the plot of ln α as a function of photon energy gives the value of Urbach energy from slope. The graph of ln α versus photon energy is shown in Fig. 3.17. The region from 1.25 to 2.10 eV contains two distinct regions, where two different slopes exist. Two Urbach energies, E_{u1} for absorption tail region and E_{u2} for exponential edge region were calculated from the slope of the tangent. The resulted values of Urbach energies for different substrate temperatures are given in Table 3.3 and those were increased up to Cu-473 and then decreased.

The most important purpose to use the SE is the estimation of the optical band gap, E_g, of the thin films using the plot of the absorption coefficient versus the photon energy. The analysis of the optical band gap is based on the equation as Pankove [3.47]

$$\alpha h\nu = B(h\nu - E_g)^p,$$

where B is a constant depending on the transition probability, P is an index that indicates the optical absorption process and is theoretically equal to 1/2, 2, 3/2, and 3 for direct allowed, indirect allowed, direct forbidden, and indirect

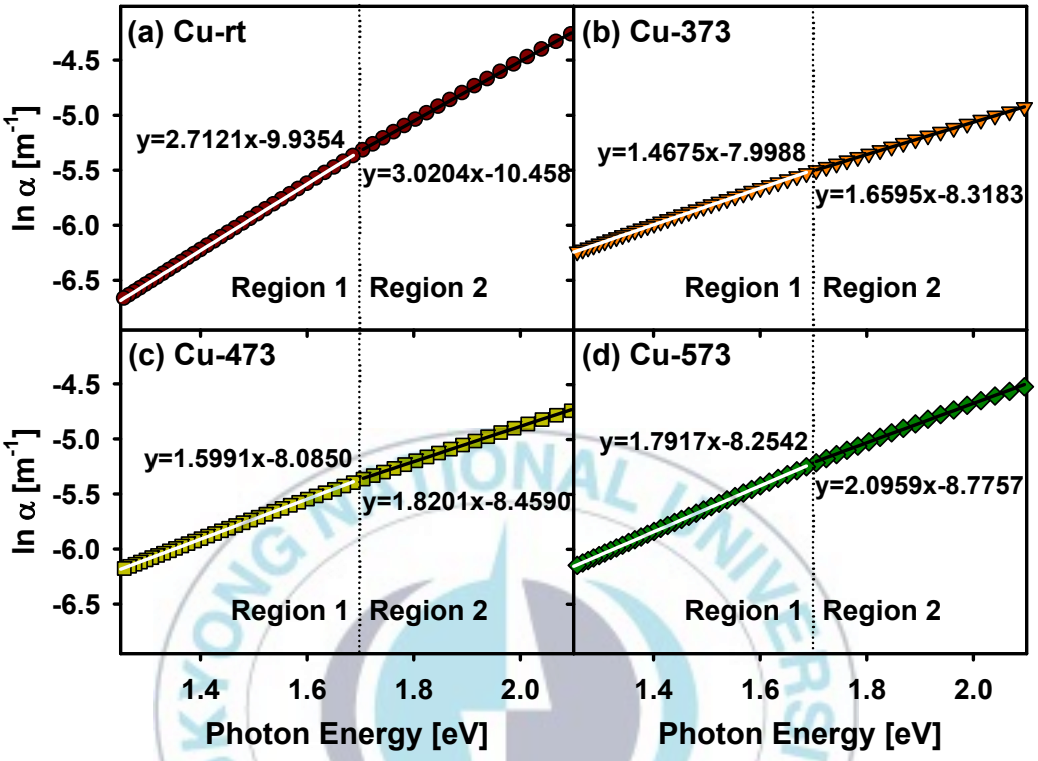

Fig. 3.17 The plot of ln α versus photon energy for (a) Cu-rt, (b) Cu-373, (c) Cu-473, and (d) Cu-573.

Table 3.3 The optical parameters of the CuO_x thin films obtained at different substrate temperature.

	Cu-rt	Cu-373	Cu-473	Cu-573
E_g [eV]	2.30±0.17	2.98±0.04	3.06±0.03	2.93±0.05
E_{u1} [meV]	403.01±61.43	673.98±6.75	624.64±1.14	554.74±3.82
E_{u2} [meV]	368.35±78.04	609.42±7.71	542.90±5.72	458.94±12.94
B [$eV^{1/2}$ m^{-1}]	0.0048 ±0.0005	0.0143 ±0.0003	0.0201 ±0.0003	0.0333 ±0.0054

forbidden transitions, respectively. Using the equation, four spectra were plotted and the best plot which has linear portion of CuO_x thin films was the direct allowed transition spectra. The direct allowed band gap, shown in Fig. 3.18, was determined by the x-intercept of the extrapolating line of tangent line. The obtained direct band gap values showed blue shift up to 473K and then red shift was observed. This phenomenon was also reported in CuO_x thin films deposited by thermal oxidation of metallic Cu films between 373 and 723K [3.50]. The optical band gap was determined by several parameters such as the grain growth, crystallinity, and stress of the films. It is well known that the increase of grain size could cause the red shift [3.51]. In this study, the grain size of CuO_x films monotonically increased with increasing the substrate temperature from AFM result. This implies that the grain size was not the dominant factor to change the direct band gap. To understand the effect of crystallinity on the variation of direct band gap, the physical model of the CuO_x thin films should be considered. All samples have monoclinic CuO and amorphous CuO_2 and $Cu(OH)_2$. This propensity of the band gap change, blue shift then red shift, is the same as the intensity change of the peak of monoclinic CuO. The intensity was increased with increasing the substrate temperature up to 473K then decreased at 573K. In order to verify the final factor, stress, it is reported that the stress was decreased with increasing the film thickness [3.52]. In this study, the thickness of CuO_x thin films analyzed by SE data was slightly increased up to 473K and then decreased at 573K (Table 3.2). It is helpful to think that the

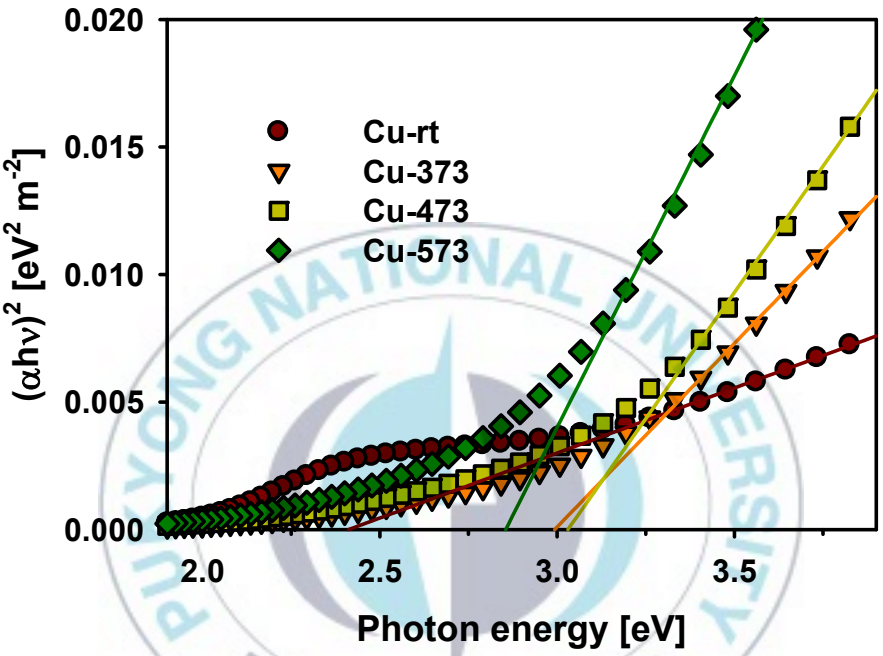

Fig. 3.18 Plots of $(\alpha h\nu)^2$ versus photon energy of the CuO_x films under various substrate temperature. The tangent lines were calculated from the data points.

stress of the films decreased and then increased at 573K. If the shift of the direct band gap was attributed to the stress in the CuO_x thin films, the band gap should be red shifted then blue shifted. However, our band gap measurement shows opposite propensity with the film thickness. Therefore we can conclude the band gap shift is strongly affected by the preferential growth in phase. We should note the $(\alpha h\nu)^2$ values at about 2.5 eV of photon energy on Cu-rt. This may be caused by lack of perfectness of the CuO_x films or more than one direct band gap states exist in the CuO_x sample.

3.3.3 Conclusion

The CuO_x thin films were synthesized by reactive rf magnetron sputtering from metallic Cu target. During the deposition process, the sputter gas mixing ratio maintained in constant level, but the substrate temperature increased from rt to 573K. According to the XRD and XPS results, the CuO_x films consist of monoclinic CuO and amorphous Cu_2O and $Cu(OH)_2$. The phases of CuO_x were not affected by substrate temperature, while the roughness of films increased with increase of the substrate temperature. The crystal size and contact angle increased as the substrate temperature increased. The increase of the roughness was depending on the grain growth. The hydrophobic character of the CuO_x films was detected by increase of substrate temperature. The direct band gap shift was observed initiating blue shift up to 473K and then converted to red shift.

CHAPTER IV. Molybdenum Oxynitride Thin Films

4.1 Introduction

Transition metal oxynitride thin films are attractive materials for a wide range of applications due to the superior properties of metal oxynitrides which have a dielectric oxide and metallic nitride compound. Despite the superb characteristics of metal oxynitride, most studies have focused only on either oxide or nitride films. In particular, group VI elements have attracted less attention than other transition metals, such as titanium [4.1,4.2], zirconium [4.3,4.4], and iron [4.5].

In the last decade, Mo oxides have become an important material system for applications in electrochromic and photochromic devices in the solar cell industry [4.6,4.7], active and selective catalysts [4.8,4.9], and gas sensors [4.10]. Moreover, Mo nitride has been considered as an excellent material for wear and corrosion resistant coatings [4.11,4.12], diffusion barriers in semiconductors [4.13], and catalysts for reactions, including hydrodenitrogenation and dehydrogenation [4.14,4.15]. Therefore, Mo oxynitride (MoN_xO_y) is a potential material system which has both characteristics of Mo oxides and nitrides. Shen and Mai reported residual stress and structural properties of DC-sputtered MoN_xO_y for diffusion barrier applications [4.16]. The crystal structure of DC-sputtered MoN_xO_y films was studied by Rivière's group [4.17]. The as-deposited MoN_xO_y thin film

showed meta-stable phase, hexagonal δ-MoN, and cubic δ-Mo_2N structures; after annealing at 873K the substrate peaks dominated. In this work, MoN_xO_y thin films were deposited on a p-type Si(100) substrate by a reactive rf magnetron sputtering method, which is one of the most commonly applied methods for the preparation of thin films. We focused here on the effect of the N_2 gas ratio on the physical and chemical properties of MoN_xO_y films.

4.2 Experimental

MoN_xO_y thin films were deposited on a p-type Si(100) substrate by reactive rf magnetron sputtering using a metallic Mo (99.95%, Tasco) target with a diameter of 50 mm and a thickness of 5 mm. The deposition chamber was evacuated with a turbo molecular pump backed by a rotary vane pump to achieve 4.0×10^{-7} Torr of base pressure. The water cooled target was installed at the bottom of the chamber and the substrate was cooled by a chiller. The Si(100) wafer was cleaned with 2% HF solution and then it was blown with dry N_2 gas before introduction into the sputtering chamber. The target was pre-sputtered for 1 hr with rf (13.56 MHz) power of 30 W to stabilize the plasma and clean the target while the substrate was shielded by a stainless steel shutter. The preparation of the films was carried out with rf power of 30 W for 4 hrs. The substrate was kept at room temperature and the sputtering gases of high-purity argon (99.99%) and nitrogen (99.99%) were controlled by independent mass flow controllers. The introduced N_2 gas ratio was calculated by dividing the N_2 flow rate by the total flow rate of argon and nitrogen (N_2/Ar+N_2). The working pressure was maintained at about 48 mTorr and was monitored by a convectron gauge during the deposition process.

The thickness of the thin films was measured by FE-SEM (JEOL, JSM-6700F, Japan). The surface morphology of the MoN_xO_y thin films was investigated by AFM (Veeco, Multimode Digital Instruments Nanoscope IIIα, USA) in contact mode. The images of the MoN_xO_y thin films were obtained

in two data types, deflection and height type and the 3D images shown here were converted from the deflection-type data. The surface roughness of the thin films was obtained from AFM images as well. XRD (PANalytical, X'Pert-MPD, Netherlands) was used to analyze the crystal structure of the films. Cu Kα (λ=1.5406 Å) radiation and a 0.02° step size were applied for the XRD study. Chemical analysis was performed with XPS (VG, MultiLab 2000, UK) [4.18]. The X-ray source was monochromatic Al Kα (1486.6 eV). The base pressure of the XPS chamber was kept at 2×10^{-10} Torr. The survey XPS spectra were taken with a pass energy of 50 eV, a dwell time of 50 ms and an energy step of 0.5 eV. High-resolution XPS spectra such as Mo 3d, O 1s, N 1s, and the valence band region were taken at a pass energy of 20 eV and other parameters were kept the same as the survey spectra.

4.3 Results and Discussion

The thickness of the MoN_xO_y thin films was examined by FE-SEM shown in Fig. 4.1. The thickness of MoN-0 was about 1000 nm and a columnar structure was observed. The sample notation used here, such as MoN-50, refers to the MoN_xO_y films obtained at 50% ratio of N_2 in the sputtering gas. As the N_2 gas ratio increased, the thickness decreased to about 75 nm in MoN-100. This phenomenon agreed with previous results found by our group [4.19]. As the ratio of Ar gas (which acted as sputter gas) decreased, the sputter yield decreased. Therefore, the film thickness of MoN_xO_y decreased.

The surface morphology of the MoN_xO_y thin films was investigated with AFM in contact mode as shown in Fig. 4.2. Note the z scales of the AFM images. The diameter of the column of regularly packed MoN-0 was about 110 nm, obtained by cross-sectional images. At MoN-7, the diameter of the column increased to 155 nm with irregular arrangement. Fig. 4.3 shows the roughness of the MoN_xO_y films obtained at various N_2 gas ratios in root-mean-squared (rms) value. The roughness of MoN-7 was larger than that of MoN-0 and the degree of roughness between MoN-3 and MoN-13 was relatively constant. The roughness of MoN-27 was similar to that of MoN-0. After this point, the roughness dramatically decreased in MoN-50. The MoN_xO_y films that had low roughness values seemed to have few voids as shown in Fig. 4.2 (c).

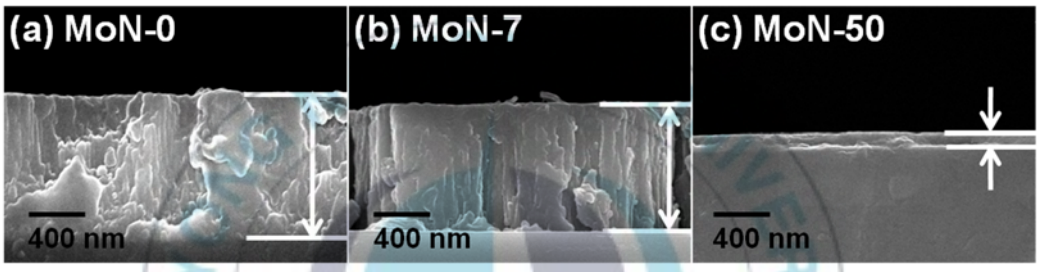

Fig. 4.1 Representative FE-SEM cross-sectional images of MoN_xO_y thin films.

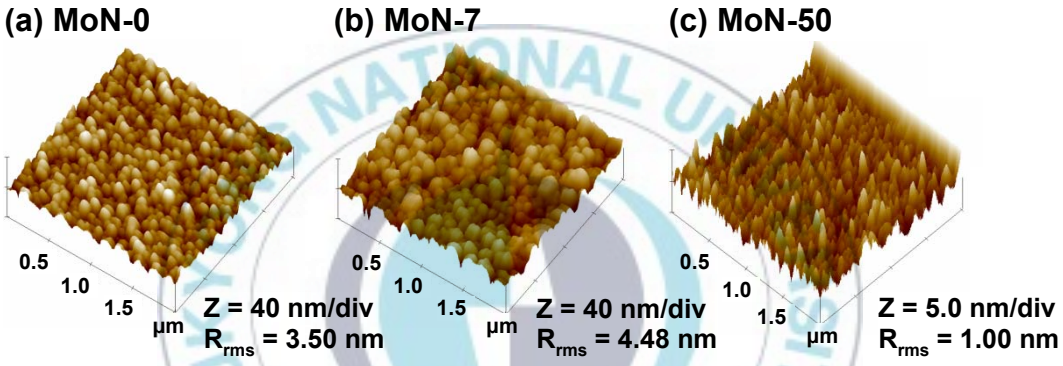

Fig. 4.2 AFM images and roughness (rms) of MoN-0, MoN-7, and MoN-50 films in (a), (b), and (c), respectively.

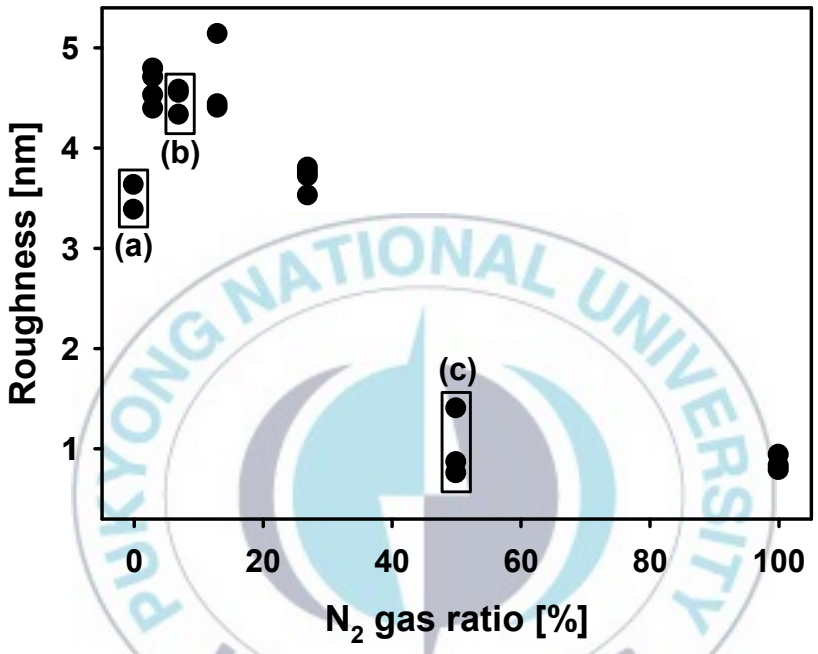

Fig. 4.3 The roughness (rms) of MoN_xO_y thin films obtained at various N_2 gas ratios. The boxes are used to emphasize the selected samples used for characterization, (a) MoN-0, (b) MoN-7, and (c) MoN-50.

At low N_2 gas ratios, the films were formed with preferential growth of MoN_xO_y grain with micro-voids by rf sputtering process. When the N_2 gas ratio was higher than 13%, enhanced energetic particles bombarded the MoN_xO_y films. The bombardment by energetic particles during deposition caused a relatively strong resputtering effect and increased the renucleation rate at the void sites. This leads to denser and smoother films with fewer voids. Therefore, the surface roughness in MoN-27 was lower than that of MoN-7 and it continuously decreased until MoN-50 and then remained almost constant. Similar results were reported by Tsai *et al*. about (TiVCrZrY)N coatings with variation of the N_2 flow ratio [4.20]. Xiao *et al*. reported that the bombardment may decrease the surface energy that forms a smooth surface on the films [4.21]. The influence of the resputtering and redeposition effect on the MoN_xO_y thin films was also confirmed by SEM images. In this research, a columnar structure of the MoN_xO_y thin films was observed in the SEM images of MoN-0 and 7, but it disappeared in MoN-50.

The XRD patterns of the MoN_xO_y thin films are shown in Fig. 4.4. Cubic Mo (c-Mo) (110) phase appeared in MoN-0 with 13.48 nm of the crystalline size calculated by Scherrer's equation. When nitrogen gas was introduced into the sputter chamber, the c-Mo(110) peak decreased and the γ-Mo_2N (200) phase evolved. The γ-Mo_2N structure is a NaCl type structure which has FCC sites occupied with Mo atoms and 50% of octahedral sites occupied with N atoms [4.22]. Thus, the remaining vacancies of octahedral sites in the thin films were occupied by incorporated oxygen atoms. Even

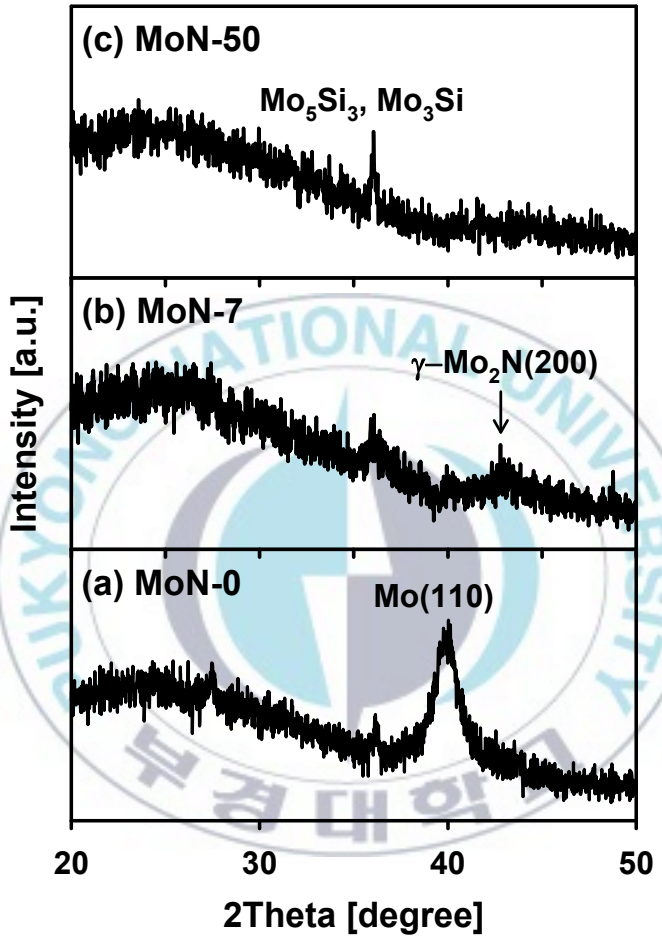

Fig. 4.4 XRD patterns of MoN_xO_y thin films: (a) MoN-0, (b) MoN-7, and (c) MoN-50.

when an oxygen free environment was applied during the sputtering process, the residual oxygen in the sputter chamber, such as H_2O and CO_2, contributed to the formation of Mo oxynitride. This observation will be discussed in the XPS results. In MoN-50, only a hexagonal Mo silicate (Mo_5Si_3(002) or Mo_3Si(200)) [4.19] peak was observed and it indicates that no other crystallite structures involving Mo and nitrogen appeared; moreover, the MoN_xO_y film was thin at high N_2 ratio. Note the intensity of XRD peaks of MoN-7. The intensity of the γ- Mo_2N (200) peak was weaker than that of the Mo silicate peak in MoN-50. This indicates that the MoN_xO_y thin films have weak crystallinity and/or form amorphous phase at nitrogen ratios above 7%. However, the formation of amorphous films at higher N_2 gas ratio is inconsistent with the previous research on the MoN_xO_y thin films deposited by DC reactive magnetron sputtering [4.23]. Barbosa *et al*. reported that γ-Mo_2N or c-MoN_x and δ-MoN phases were formed at low or high N_2 flow rates with low oxygen concentration. They also concluded that amorphous phase was obtained for high oxygen content, 18 at.% of oxygen. From our XPS analysis, the atomic percentage was calculated using atomic sensitivity factors: 2.750 for Mo 3d, 0.660 for O 1s, and 0.420 for N 1s. The obtained oxygen contents on the surface of the MoN_xO_y thin films were 40.3 for MoN-0, 39.8 for MoN-7, and 41.5 at.% for MoN-50. This indicates that the content of oxygen on the surface region of the films obtained with various N_2 gas ratios is almost constant. Shen and Mai reported that about 48 at.% oxygen existed in the surface region and about 16-18 at.% oxygen remained in the bulk region

of $Mo_{55}O_{19}N_{26}$ film. The surface composition of about 40 at.% oxygen on MoN_xO_y thin films could be reasonable. For more accurate XRD analysis, further investigation about the bulk composition of MoN_xO_y thin films will be required.

Fig. 4.5 (a) shows the Mo 3d core-level high-resolution XPS spectra of the MoN_xO_y films. Comparing the spectra before and just after (MoN-3) introduction of N_2 gas, the peak shape of the Mo 3d spectra was quite different due to the pronounced Mo 3d peak in the high binding energy region. This implies that several oxidation states of Mo 3d were formed in the MoN_xO_y thin films. With further increase of the N_2 gas ratio, no other significant change was observed except the shape of the shoulder in the low binding energy region. For better understanding of the chemical environment of the films, a peak deconvolution process was performed; representative deconvoluted XPS spectra of MoN-0, MoN-7, and MoN-50 are shown in Figs. 4.5 (b), (c), and (d), respectively. The Mo 3d spectra were decomposed to 6 doublet peaks with 3.15 eV of spin-obit splitting (SOS). The lowest and highest binding energies of Mo $3d_{5/2}$ are centered at 227.9 and 233.0±0.1 eV, respectively. These binding energies were corresponded to Mo^0 and Mo^{6+} [4.24]. The other four peaks were assigned to $Mo^{\delta+}$ ($0<\delta<3$), Mo^{3+}, Mo^{4+}, and Mo^{5+} from low to high binding energy. Further introduction of N_2 gas promoted oxidation of Mo species which resulted in metallic Mo and $Mo^{\delta+}$ being oxidized to a higher oxidation state of Mo, such as Mo^{6+}. The portion of Mo^{3+} and Mo^{4+} in MoN-7 was dramatically increased up to about 50%, but

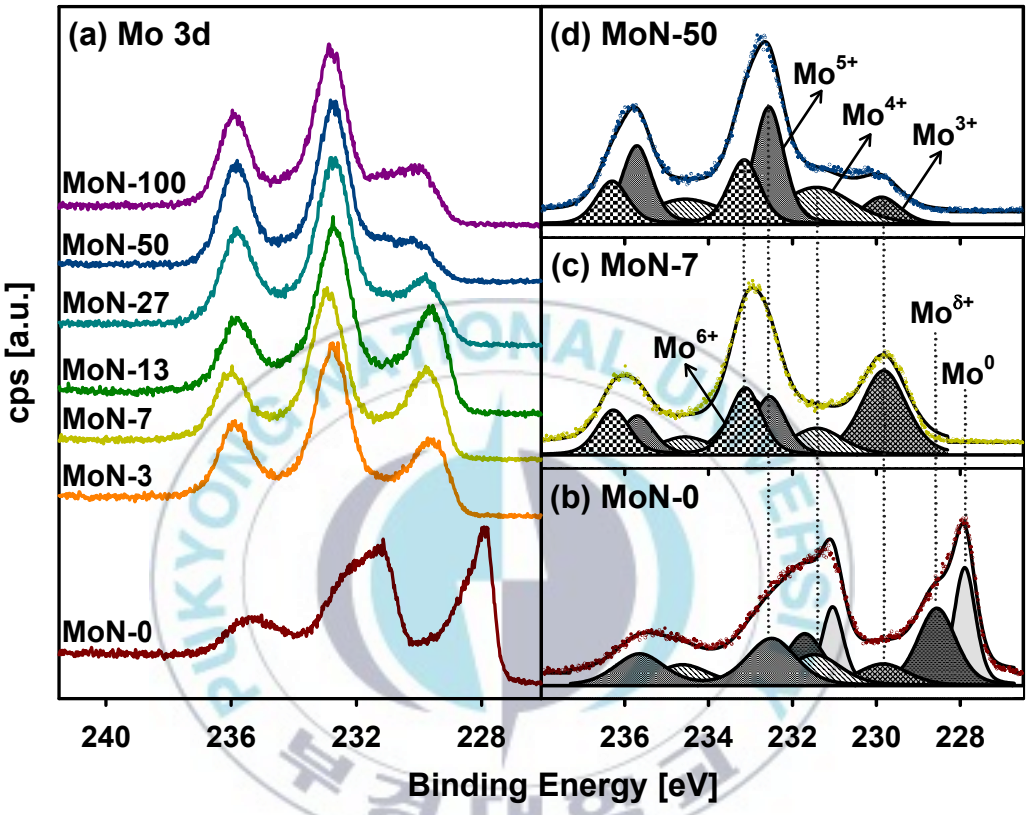

Fig. 4.5 XPS spectra of Mo 3d region in (a) and deconvoluted Mo 3d XPS spectra of MoN-0, MoN-7, and MoN-50 in (b), (c), and (d), respectively. The dots in the spectra represent the raw data and the lines represented the sum of each Mo species. The vertical dotted lines are added to emphasize the agreement of peak positions for MoN-0, MoN-7, and MoN-50 samples.

that of Mo^{5+} did not change noticeably. In MoN-50, the major Mo species was Mo^{5+} and the portions of other oxidation states, Mo^{3+}, Mo^{4+}, and Mo^{6+} decreased or remained almost constant. According to these results, we could confirm that the major oxidation states of Mo changed from low oxidation states (Mo^0 and $Mo^{\delta+}$) to Mo^{5+} through Mo^{3+} and Mo^{4+} with increased N_2 gas ratio. These Mo species, from $Mo^{\delta+}$ to Mo^{5+} were attributed to MoN_xO_y phase [4.25]. Notably, the lower oxidation states vanished after nitrogen gas was introduced. This indicates that the introduction of nitrogen gas effectively promoted oxidation of Mo species with low oxidation states. On the other hand, Mo^{6+} was immediately formed in nitrogen atmosphere, the portion was not dependent on the N_2 gas ratio. This Mo species could exist in the form of Mo oxide and/or Mo oxyhydroxides.

To investigate the effect of N_2 gas on the MoN_xO_y thin films, the N 1s region was monitored. Because the binding energies of N 1s and Mo $3p_{3/2}$ overlap, deconvolution is necessary in this region as well. Curve fitting for N 1s was conducted after deconvolution of the Mo 3p spectra based on the result of deconvolution of the Mo 3d XPS spectra. Peak deconvolution of the Mo 3p spectra was performed with 17.2-17.4 eV of SOS. Fig. 4.6 shows the XPS spectra of the N 1s and Mo 3p regions (a) and representative deconvoluted spectra of MoN-0 (b), MoN-7 (c), and MoN-50 (d). The N 1s peak was detected and the intensity of nitrogen increased in MoN-7 and MoN- 50. The N 1s peak located at 397.6±0.1 eV is attributed to the Mo-N bond [4.26]. This reveals that the MoN_xO_y thin films were formed by the introduction of N_2

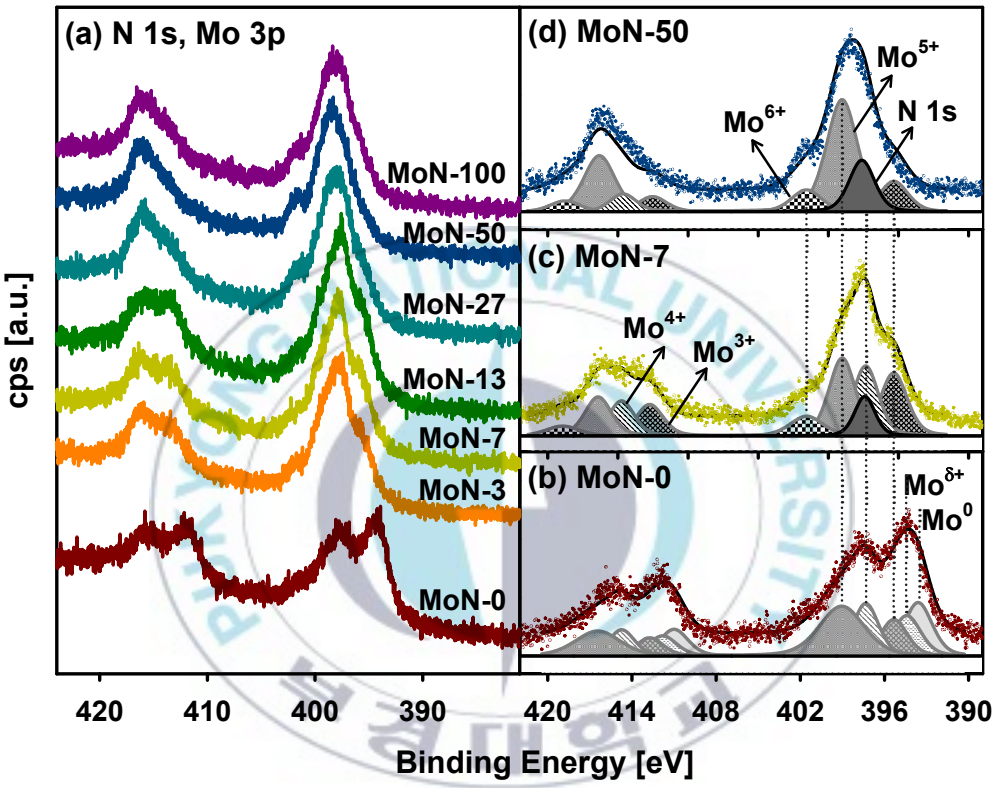

Fig. 4.6 XPS spectra of N 1s and Mo 3p regions in (a) and deconvoluted N 1s and Mo 3p XPS spectra of MoN-0, MoN-7, and MoN-50 in (b), (c), and (d), respectively. The gray lines indicate the Mo 3p spectra and the line filled black indicates the N 1s peak.

gas.

The high-resolution XPS spectra of the O 1s region was stacked in Fig. 4.7 (a) and the representative deconvoluted spectra of MoN-0, MoN-7, and MoN-50 are presented in Figs. 4.7 (b) to (d). As shown in Fig. 4.7, the asymmetric O 1s peak was observed from all of the films and the peak profile became sharp with increasing N_2 gas ratio. The O 1s spectra were decomposed with three different components: lattice oxygen (O^{2-}), surface-adsorbed oxygen, denoted as O^- and OH^-, and water molecules [4.26,4.27]. The deconvoluted peaks of O 1s showed that the thin films contained oxygen species which could be originated from an oxide layer on the surface produced naturally due to residual oxygen. Agouram *et al*. mentioned that the O 1s peak positioned at 531.5±0.1 eV could indicate the existence of ON^- in thin films [4.28]. Our XPS result agrees with their result that the binding energies centered at 531.6±0.1 eV could be attributed to the ON bond in MoN_xO_y films and this oxygen species increased with increasing the N_2 gas ratio. However, a small amount of O 1s at this binding energy was detected in the MoN-0 spectra. This could be originated from O^- and/or OH^-. Therefore, the O species at 531.6±0.1 eV in our study could be mainly contributed by O^-, OH^-, and ON^-. Interestingly, the peak intensity of ON^- was not dominant at any stage, even at a 50% N_2 gas ratio. This implies the formation of the ON^- bond was difficult with N_2 introduction under mild conditions, which is a hurdle to the formation of MoN_xO_y films incorporating a high atomic percentage of nitrogen. This might cause the discrepancy in terms of the

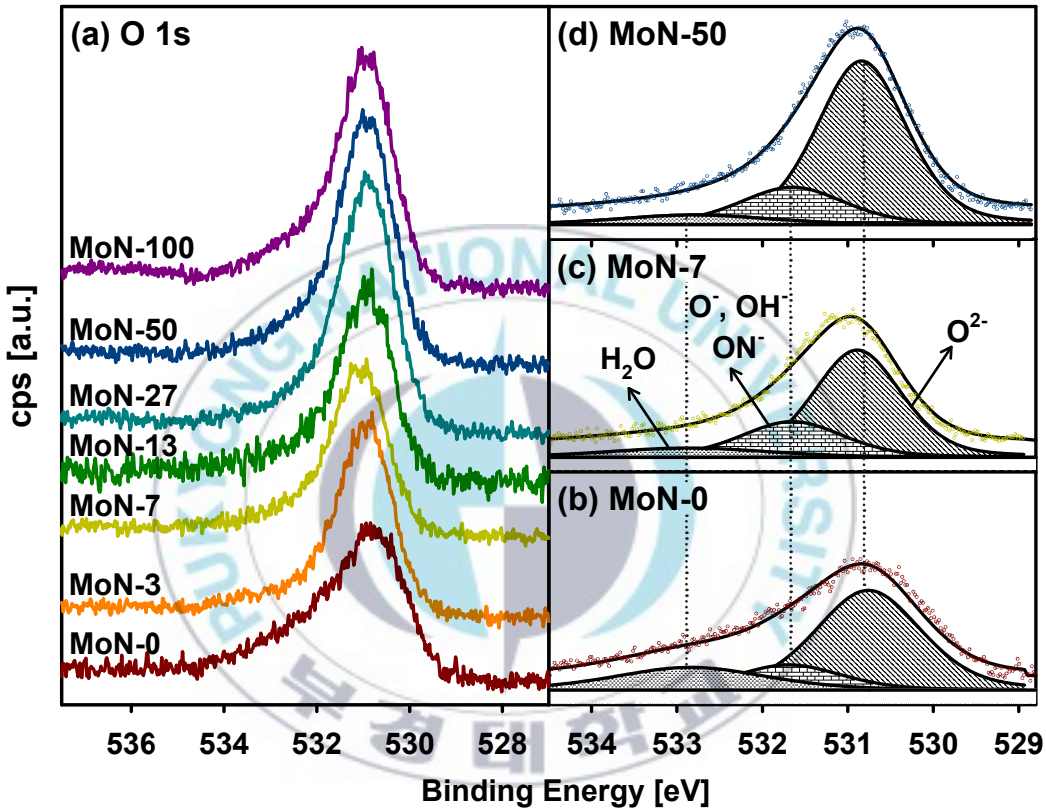

Fig. 4.7 XPS spectra of O 1s region in (a) and deconvoluted O 1s XPS spectra of MoN-0, MoN-7, and MoN-50 in (b), (c), and (d), respectively.

crystallinity of MoN with the results of Barbosa's work discussed in relation to XRD analysis. As the N_2 gas ratio increased, the peak intensities of O_2^- and O^- and/or OH^- increased; however, that of H_2O was decreased.

Fig. 4.8 shows the valence band region XPS spectra of the MoN_xO_y thin films. The peak at around 2 eV corresponds to the Mo 4d orbital and that at 4-10 eV is attributed to the N 2p and/or O 2p orbitals observed in the valence band region XPS spectra of the MoN_xO_y thin films. At MoN-0, the intensity of the Mo 4d band was stronger than that of O 2p band and the density of state (DOS) near the Fermi edge was relatively sharp compared with other films. This means that the metallic Mo was dominant among Mo species and this result agreed well with the XPS results of Mo 3d and 3p. In particular, the intensity of the Mo 4d band decreased, while that of the O 2p and/or N 2p increased with the introduction of N_2 gas. As the N_2 gas ratio increased, the oxidation state of Mo changed from low to high, resulting in an increase of the valence band maximum (VBM) of about 0.65 eV by the vanishing of Mo 4d level.

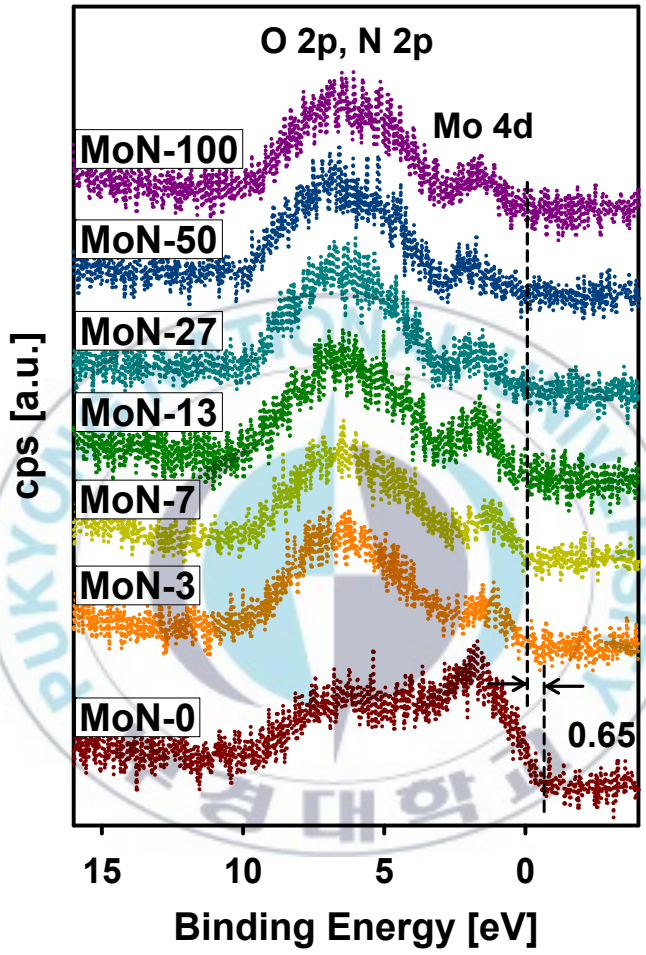

Fig. 4.8 Valence band region XPS spectra of Mo oxynitride thin films.

4.4 Conclusion

MoN_xO_y thin films were deposited on a p-type Si(100) wafer by rf magnetron sputtering at various N_2 gas ratios. The thickness decreased to 70 from 1000 nm with an increasing N_2 gas ratio. AFM images revealed that the roughness of the films increased up to an N_2 gas ratio of 7% and then significantly decreased. The XRD results showed that the crystal structure of the film changed from metallic c-Mo through γ-Mo2N to Mo silicate phase. The XPS results confirmed that the oxidation state of Mo and the VBM increased and N 1s peak appeared with an increasing N_2 gas ratio.

CHAPTER V. Molybdenum Sulfide Thin Films

5.1 Introduction

Single-layered Mo disulfide (MoS_2) is a two dimensional layered material that is included in the family of VIA transition metal dichalcogenides. A monolayer of this material is composed of S-Mo-S triple layers and the bulk comprises these triple layers stacking on top of one another due to a relatively weak interaction known as the van der Waals force being present in between each set of S-Mo-S triple layers. Due to this unique 2D structure, which is also observed in graphene and hexagonal boron nitride, MoS_2 is characterized with a low friction coefficient which consequently led the material being utilized in applications of solid lubrication [5.1]. For the same matter, researches have been done on tribological study for MoS_2 films [5.2-5.4]. Recently, MoS_2 has been redrawing the attention in the scientific community as the electronic bandgap can be widely tuned by controlling the film thickness. Single-layered MoS_2 films exhibit a direct bandgap of 1.8 eV while bulk MoS_2 films exhibit an indirect bandgap of 1.2 eV [5.5,5.6]. This fascinating property of MoS_2 films make them an attractive candidate material for flexible electronic devices including organic solar cells [5.7,5.8] and field effect transistors [5.9,5.10].

Mo sulfide (MoS_x) thin films have been synthesized by various methods, such as atomic layer deposition [5.11], electrodeposition [5.12],

vapor phase sulfurization [5.13], dc magnetron sputtering [5.14], and rf magnetron sputtering [5.15]. Among these techniques, the rf sputtering method has advantages such as the formation of thin films with high quality and independence on the kinds of the sputter targets whether those are conductive or not. To adapt the MoS_x thin films in a variety of application fields, controlling the film properties is crucial and it can be tuned by deposition conditions, such as sputtering pressure, substrate temperature, rf power, and substrate bias. The researches of Mo sulfide thin films deposited by sputtering with changing not only deposition conditions [5.1,5.16] but also film thickness [5.11] and different substrate [5.14] had been done. However a detailed relationship between rf power and the chemical composition of MoS_x thin films have not been extensively investigated, especially surface analysis of MoS_x thin films. In this research, MoS_x thin films on the ITO substrate were synthesized by reactive rf magnetron sputtering in ultra high vacuum chamber. The study about dependence of rf power on the MoS_x thin films were conducted with a surface profiler, a 4-point probe, contact angle measurements, X-ray diffraction (XRD), and X-ray photoelectron spectroscopy (XPS).

5.2 Experimental

MoS_x thin films were deposited by reactive rf magnetron sputtering. The sputter target equipped with a water cooling system was MoS_2 (2 inches in diameter, 99.95%, Thifine) and the substrate was ITO glass (10 Ohms/sq) cleaned by sonication in acetone which was then rinsed with distilled water. After confirming the purity of Ar (99.99%) by a quadrupole mass spectrometer (QMS, shown in Fig. 5.1), Ar was used as a sputter gas and the flow rate was fixed at 7 sccm by a mass flow controller. The working pressure was maintained constant at about 45 mTorr during sputtering. Before deposition of MoS_x thin films on the ITO glass, pre-sputtering was performed for 5 min as the target was covered with a stainless steel shield. The rf power was changed from 100 to 200 W and MoS_x thin films were deposited for 10 min. The MoS_x thin film obtained at X W of rf power will be referred as MoS-X throughout this report.

The chemical properties of MoS_x thin films were investigated by X-ray photoelectron spectroscopy (XPS, VG, ESCALAB MKII, UK). In this study, Mg Kα X-ray source (1253.6 eV) was used to obtain XPS spectra. Survey spectra were collected with 20 mA of beam current, 14 kV of acceleration voltage, 0.5 eV of energy step, 100 ms of dwell time, and 2500 V of channeltron voltage. High resolution XPS spectra were obtained at 0.05 eV of step size and other conditions were the same as the survey spectra. To deconvolute XPS spectra, XPSPEAK program (ver. 4.1), Shirley background, and 30-70% Lorentzian-Gaussian ratio were applied for Mo 3d and S 2p XPS

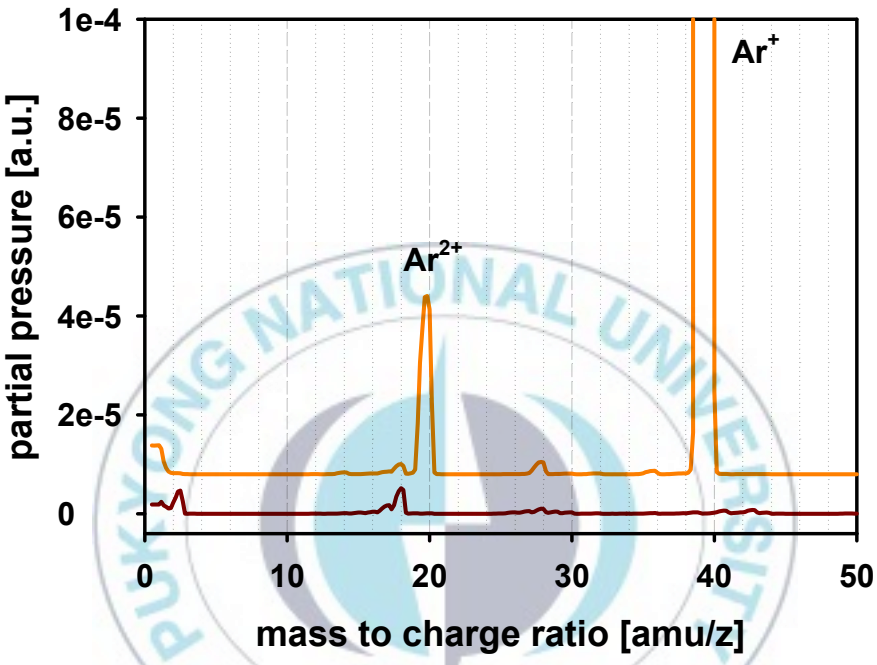

Fig. 5.1 Purity of Ar gas checked by QMS. The bottom spectrum showed that the background of rf sputter chamber. The top spectrum was obtained after introducing the Ar gas into the chamber.

spectra.

The crystallinity of MoS_x thin films was analyzed with X-ray diffraction (XRD, PANalytical, X-Pert pro, Netherlands) with Cu Kα (λ = 1.5406 Å) radiation and a 0.05 degree of step size. Contact angles were measured to identify the surface free energy of MoS_x films with distilled water (DW) and ethylene glycol (EG). Electrical properties of the MoS_x films were examined with a 4-point probe (Mitsubishi Chemical Co., Loresta-GP (MCP-T610), Japan). The thickness of thin films was measured with a surface profiler (Tenco, Alpha-Step 500, USA) and the average thickness of each films was determined after validation with Q-test under 90% of confidence level.

5.3 Results and Discussion

The thickness of MoS_x thin films obtained at different rf power was measured by a surface profiler and the thickness of the thin films was found to be 100.1±8.9, 172.2±11.5, and 240.9±16.8 nm for MoS-100, 150, and 200, respectively. It indicated that the thickness increases with increasing rf power. This phenomenon is consistent with the results of previous studies [5.17]. As the rf power was increased, the ionization rate of sputter gas increases, thus the sputter yield also increases. Therefore, the higher rf power leads to the formation of thicker films. Fig. 5.2 shows the deposition rate of MoS_x thin films as a function of rf power. The plot indicates that the deposition rate linearly increased with rf power. The slope in the plot represents the deposition rate, 1.41 nm/W and the y-intercept represents the sputter efficiency, −40.3 W [5.18].

The chemical environment of MoS_x thin films was analyzed with XPS. High resolution XPS spectra of Mo 3d and S 2s region are shown in Fig. 5.3. Unfortunately, the binding energies of electrons in Mo 3d and S 2s are too close to distinguish Mo 3d and S 2s peaks. In order to obtain the chemical information of Mo species, both S 2s as well as Mo 3d spectra were put into consideration. It is found that the peak shape of Mo 3d and S 2s with different rf power was similar and no other significant difference was observed. However Mo species have numerous oxidation states, such as Mo^0, $Mo^{\delta+}$, Mo^{4+}, Mo^{5+}, and Mo^{6+} [5.19]. To obtain the specific information about rf power effect on the oxidation state of Mo, Mo 3d and S 2s peaks were

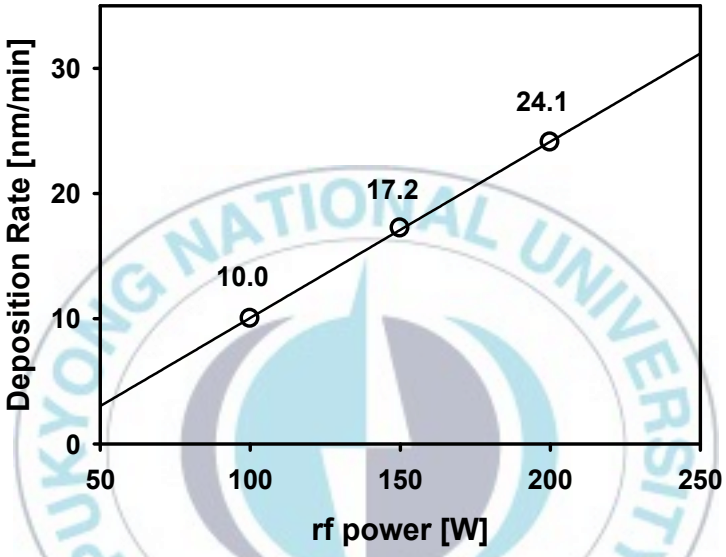

Fig. 5.2 Deposition rate of MoS_x thin films with different rf power.

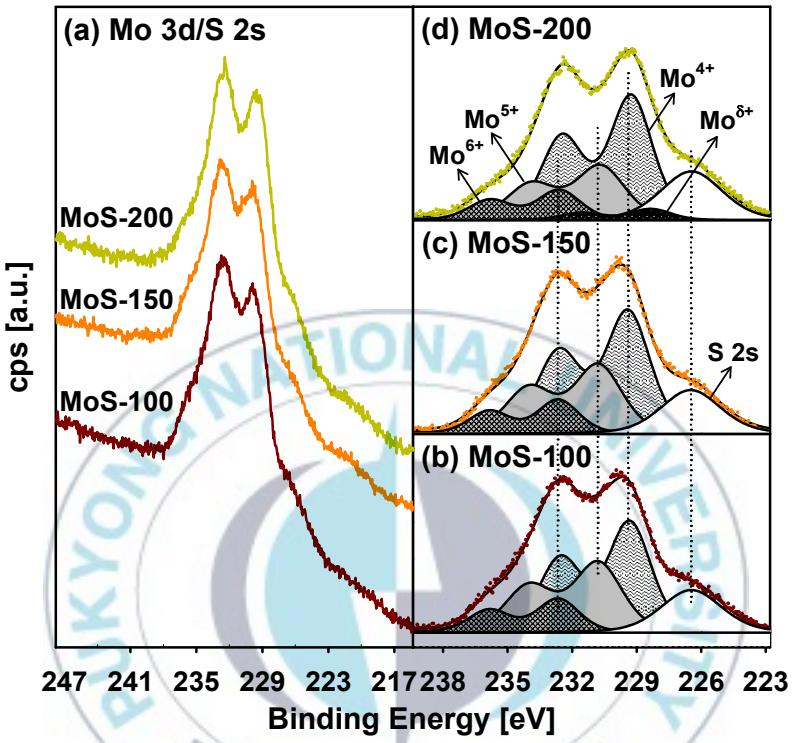

Fig. 5.3 High resolution XPS spectra of Mo 3d/S 2s in (a) and deconvoluted XPS spectra of Mo 3d/S 2s region in (b), (c), and (d) for MoS-100, MoS-150, and MoS-200, respectively.

deconvoluted. The deconvoluted Mo 3d and S 2s XPS spectra are shown in Fig. 5.3 (b), (c), and (d) for MoS-100, 150, and 200, respectively. As shown in Fig. 5.3 (b), three doublet peaks and one singlet peak are apparent in Mo 3d and S 2s spectra in MoS-100. The doublet peaks with 3.2 eV of spin-orbit splitting (SOS) represent Mo 3d peaks and the singlet peak represents the S 2s peak. It indicated that different oxidation states of Mo coexisted in MoS_x thin films. The binding energies of 226.5±0.1 eV (white singlet peak), 229.3±0.1 eV (grey doublet peak with dashes), 230.8±0.1 eV (gray doublet peak), and 232.6±0.1 eV (gray doublet peak with cross lines) are assigned to S 2s [5.12], Mo^{4+}, Mo^{5+}, and Mo^{6+} [5.20,21], respectively. The intensities of Mo 3d and S 2s are almost identical with increasing rf power. Interestingly, the ratio of Mo species with different oxidation states is noticeably changed by varying rf power. The intensities of Mo^{6+} and Mo^{5+} decreased while that of Mo^{4+} increased. In addition, the peak centered at 228.4 eV evolved in MoS-200. This peak corresponds to $Mo^{\delta+}$ ($0<\delta<3$). The relative ratio of Mo species calculated from the results of deconvoluted Mo 3d spectra is shown in Fig. 5.4. Since Mo^{6+} is the most stable oxidation state among Mo species with different oxidation states, the decreasing ratio is larger in Mo^{5+} than in Mo^{6+} with increasing the rf power. It means that the higher rf power leads to a high deposition rate (shown in Fig. 5.2) and this causes kinetically controlled deposition of MoS_x films to be dominant over thermodynamically controlled deposition [5.22].

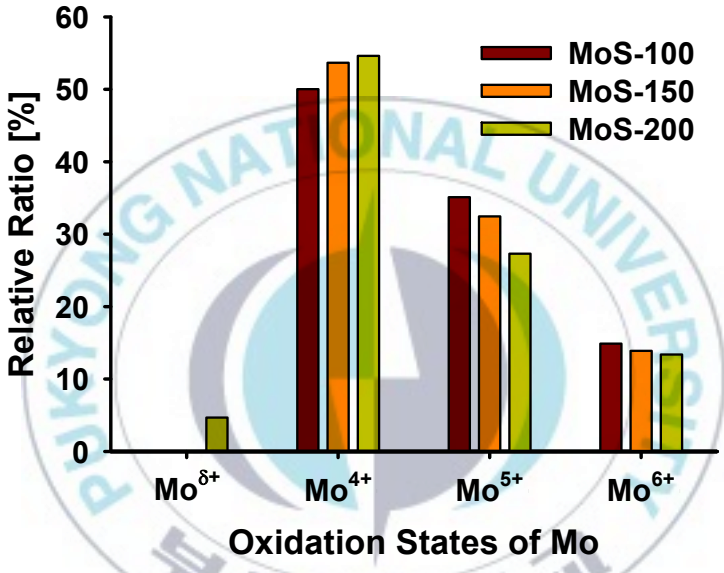

Fig. 5.4 Relative ratio of various Mo species with various oxidation states with different rf power. MoS-100 (red), MoS-150 (orange), and MoS-200 (yellow).

High resolution S 2p spectra with respect to various rf powers are shown in Fig. 5.5. Similarly, the shape and intensity of the Mo 3d and S 2s spectra, showed little to no difference with varying rf power. The deconvoluted S 2p XPS spectra are shown in Fig. 5.5 (b), (c), and (d) for MoS-100, 150, and 200, respectively. The three spectra are fitted with one peak with 1.18 eV of SOS. The dotted line shows the peak maximum centered at 162.4 eV of S $2p_{3/2}$ and it concurs with the binding energy of S^{2-} species [5.12,5.23]. This provides a concrete proof that MoS_x thin films were successfully deposited by rf sputtering. The atomic ratios of S/Mo are calculated with the results of deconvoluted Mo 3d and S 2p spectra and which are 2.15, 2.10, and 2.27 for MoS-100, Mo-150, and Mo-200 films, respectively. It means that the sputter yield of MoS_2 target and the amounts of S and Mo species are independent on the rf power, however the oxidation state of Mo is influenced by the rf power described above.

XRD analysis was performed to verify the crystallinity of the MoS_x films obtained at different rf power. As mentioned above, the film growth rate increased as rf power increased. Due to the fast growth rate of the MoS_x thin films, amorphous phase was formed (not shown here) [5.22].

Contact angles (CAs) of DW and EG on MoS_x thin films were measured at 23°C and shown in Fig. 5.6. The inset images in Fig. 5.6 are CAs of DW and EG on MoS-200 thin film on the left and right, respectively.

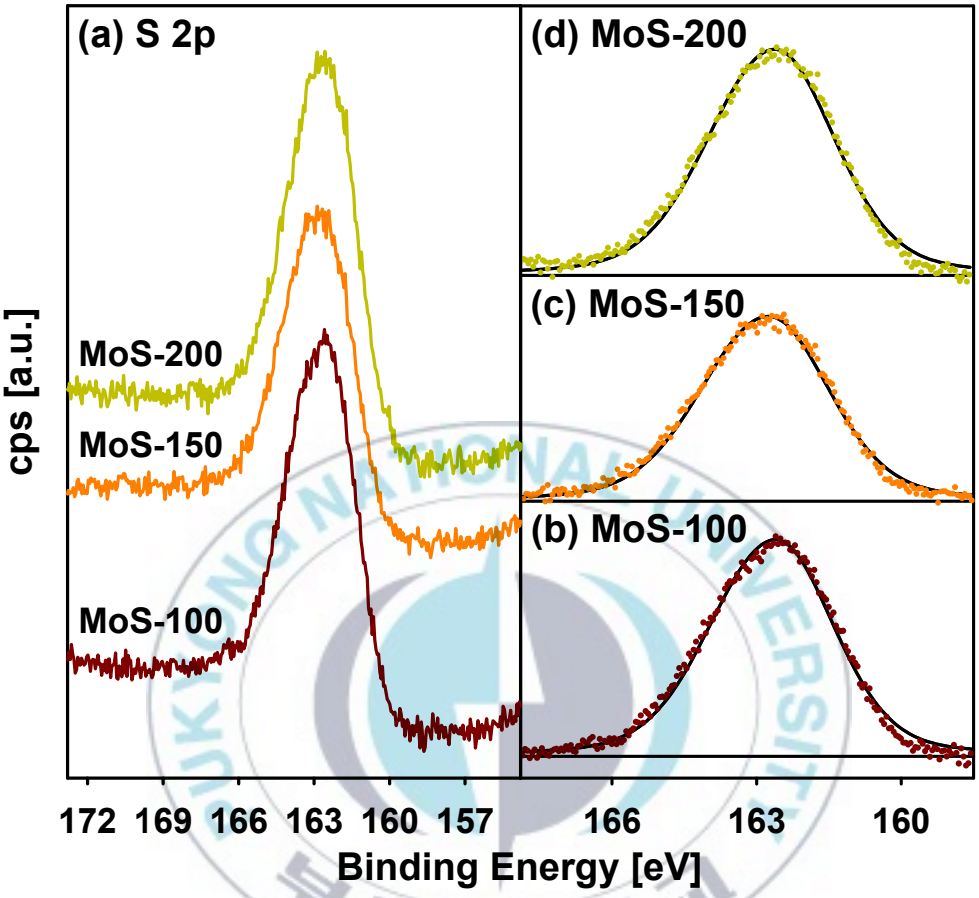

Fig. 5.5 High resolution XPS spectra of S 2p in (a) and deconvoluted XPS spectra of S 2p region in (b), (c), and (d) for MoS-100, MoS-150, and MoS-200, respectively.

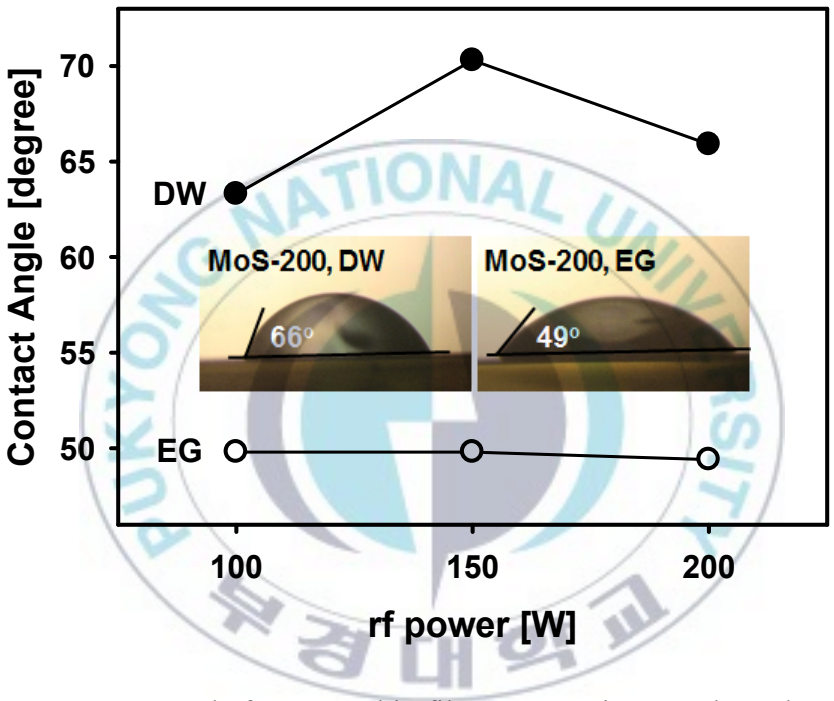

Fig. 5.6 Contact angle for MoS_x thin films. Inset images show the contact angle of MoS-200 films with DW and EG.

When EG was used as a test liquid, the CAs were relatively constant at around 49 degrees with varying rf power, while the CAs of DW were varied as the rf power increased. In order to estimate the surface free energy (SFE) of the MoS_x films, the Young's equation was employed:

$$\gamma_L \cos\theta = \gamma_S - \gamma_{SL},$$

where θ is a contact angle, γ_L is the surface tension of pure liquid, γ_S is the SFE of the solid, and γ_{SL} is the solid-liquid interfacial energy at equilibrium [5.24]. The surface tension for DW is estimated with the following equation [5.25]

$$\gamma_L = 235.8\left(\frac{374-T}{647.15}\right)^{1.256}\left[1-0.625\left(\frac{374-T}{647.15}\right)\right],$$

where T (°C) is the water temperature. The surface tension for EG is estimated with the following equation [5.26]:

$$\gamma_L = 48.97 - \frac{T}{15},$$

where T (°C) is the EG temperature. The Young's equation is modified after inclusion of hydrogen bond effects between the surface of the solid and liquid [5.27] and the concept that the total SFE is consisted of two components: the dispersive and polar components [5.28]. The modified Young's equation is:

$$\gamma_L\left(1+\cos\theta\right) = 2\sqrt{\gamma_S^d \gamma_L^d} + 2\sqrt{\gamma_S^p \gamma_L^p},$$

where γ_S^d and γ_S^p are the SFE of dispersive and polar part of MoS_x films, respectively. The SFEs of MoS_x films were calculated with the modified

Young's equation and are shown in Fig. 5.7. The total SFE was 38.3 mN/m for MoS-100 and then changed as the rf power varied. The contribution of polar SFE is larger than dispersive SFE to the total SFE for all MoS_x films obtained at different rf power. The changing propensity of polar SFE is similar to the total SFE.

The electrical properties of MoS_x thin films were investigated by a 4-point probe system and the surface resistance and conductivity with varying rf power are shown in Fig. 5.8. The surface resistance was 356.2, 401.1 Ω/sq for MoS-100 and MoS-150 and increased to 2006 Ω/sq for MoS-200. The conductivity gradually decreased with increasing the rf power. Therefore, MoS_x thin films with different chemical and electrical properties were controlled by varying rf power.

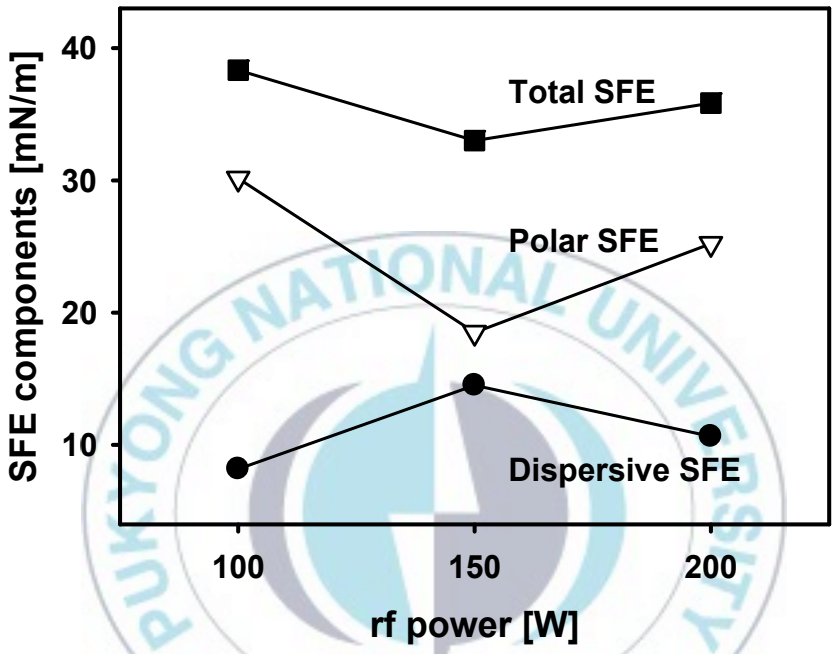

Fig. 5.7 SFE components for MoS_x thin films. Total SFE, polar SFE, and dispersive SFE are represented by filled squares, hollow triangles, and filled circles.

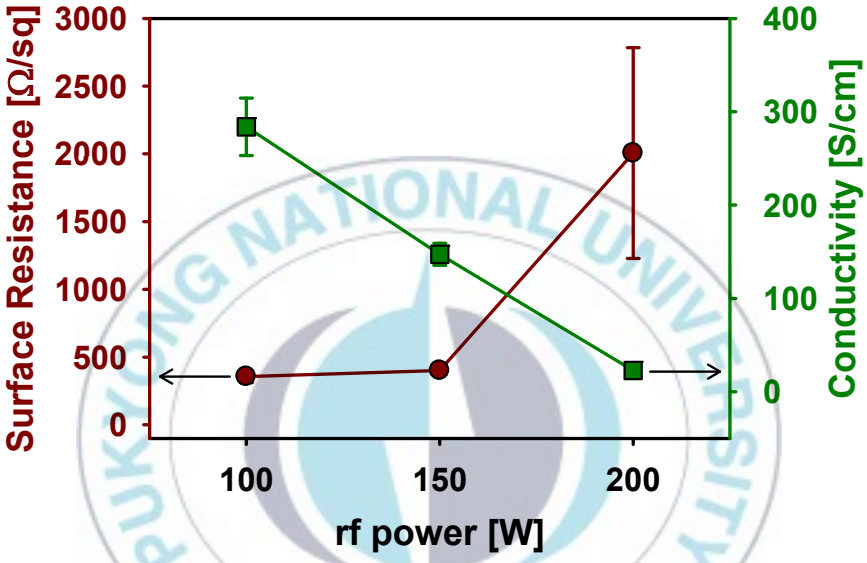

Fig. 5.8 Electrical properties of MoS_x thin films.

5.4 Conclusion

MoS_x thin films at different rf power were obtained successfully by reactive rf magnetron sputtering. The film thickness of MoS_x increased from 100 through 170 to 240 nm at 100, 150, and 200 W of rf power, respectively. The surface resistance increased from 356 to 2006 Ω/sq with increasing rf power. The oxidation state of Mo changed while the intensity of Mo and S were constant as the rf power was increased. The amorphous phase of MoS_x thin films was confirmed by XRD. The total SFE varied from 38.3 through 33.0 to 35.8 mN/m at 100 and 200 W of rf power, respectively. The polar SFE dominantly contributed to the total SFE and the changing trend of polar SFE is similar to that of the total SFE.

CHAPTER VI. Copper Oxide Nanofibers

6.1 Introduction

One dimensional (1-D) nanostructures, such as nanobelts, nanotubes, nanowires, and nanofibers have been receiving great attention because of their unique morphologies, physical, optical, and electronic properties. The Cu oxide nanowires and nanotubes were obtained by thermal oxidation process [6.1,6.2] and annealing of Cu nanowires [6.3], respectively. Out of the many 1-D nanostructures, nanofibers have attracted a great deal of attention for adaption to filters, photocatalysts [6.4], sensors [6.5], solar cells [6.6], and mechanical fields [6.7-6.9]. Nanofibers have been synthesized by several techniques including electrodeposition, a self-catalytic mechanism [6.10], a dielectric-barrier discharge plasma [6.11], and electrospinning [6.12].

In particular, the electrospinning method is commonly used to prepare ultrafine nanofibers because it is convenient and a low-cost method. Electrospinning requires three main components: a high voltage power supply, a syringe pump, and a collector. The syringe contains polymeric solution having proper viscosity to synthesize bead-free nanofibers. A high voltage is applied to the needle of the syringe and the collector is grounded. Thus, the solution ejected from the needle produces Taylor cones [6.13] and nanofibers are collected to various collectors such as a plate, a disc, a ring, and a drum [6.14].

Cu is a material that readily reacts with oxygen to form Cu oxides. Cu oxides have been intensely investigated because several kinds of Cu oxides exist such as Cu_2O, Cu_3O_2, Cu_3O_4, and CuO. These materials have different physical, optical, and electronic properties. Among them, cuprous oxide (Cu_2O) and cupric oxide (CuO) are the more popular ones to be utilized in various applications. Cu_2O is a p-type semiconducting material with a band gap of 2.0-2.6 eV and is in cubic phase [6.15]. On the other hand, CuO is an n-type semiconducting material with a band gap of 1.3-2.1 eV and is in monoclinic phase [6.16]. The formation of Cu_2O was reported by Vasilevich *et al.* under low temperatures (~373K) and pressures (~10^{-3} Pa) [6.17]. High temperatures and pressures may lead to a mixture of the various Cu oxides mentioned above. The chemical reactions of the formation of Cu oxides can be explained by the following equilibrium reactions [6.18]:

$$4Cu + O_2 \rightarrow 2Cu_2O,$$

$$2Cu_2O + O_2 \rightarrow 4CuO.$$

Therefore, phase transformation is speculated to be the cause of the change from Cu to CuO through Cu_2O [6.2,6.18,6,19]. Xu *et al.* reported that Cu oxide mixtures were formed with high contents of Cu_2O and low contents of CuO in wet air environment. However, only Cu_2O and CuO phases were obtained in N_2 and pure O_2 atmosphere, respectively [6.1]. Hsu *et al.* showed that thermal decomposition from CuO to Cu_2O was achieved at 723K [6.20]. These previous results showed that the phase of Cu oxide was controlled by

several heating conditions, for example, different gas environment, temperature, and time.

In this study, Cu oxide/polyvinyl alcohol (PVA) nanofibers were fabricated using sol-gel and electrospinning method and Cu oxide nanofibers were obtained after calcination of Cu oxide/PVA nanofibers. The Cu oxide nanofibers prepared at different calcination temperatures were characterized to investigate their morphology, physical, and chemical properties.

6.2 Experimental

Cu oxide nanofibers were obtained by sol-gel and electrospinning method. Two chemicals were used to fabricate Cu oxide nanofibers. Copper (II) sulfate pentahydrate ($CuSO_4 \cdot 5H_2O$, MW: 249.69, Junsei Chemical Co., Ltd.) was used for the Cu source and the polymer, which has proper viscosity to make nanofibers via electrospinning, was polyvinyl alcohol (PVA, $(CH_2CHOH)_x$, MW: ~22000, Junsei Chemical Co., Ltd). The Cu sulfate pentahydrate, PVA, and distilled water were mixed at the ratio of 1.0:1.9:18.6 and stirred for 3 hrs at 353K. The mixed solution was subsequently stirred for 1 hr at room temperature to stabilize. The viscosity of the obtained electrospinning solution was about 180 cP at room temperature measured with a viscometer (A&D, SV-10, Japan). The parameters employed in this work were 16.8 kV and 6 μl/min of high voltage and feeding rate, respectively. The Cu oxide/PVA nanofibers were electrospun and then calcined at 673 and 873K for 5 hrs. The Cu oxide/PVA nanofibers without calcination will be denoted as Cu-rt and the calcined Cu oxide nanofibers at 673 and 873K will be denoted as Cu-673 and Cu-873, respectively throughout this report.

The morphology of Cu oxide nanofibers were investigated with a field emission scanning electron microscopy (FE-SEM, JEOL, JSM-6700F, Japan). The crystallinity of nanofibers was analyzed with X-ray diffraction (XRD, PANalytical, X'Pert-MPD, Netherlands) with Cu Kα (λ = 1.5406 Å) radiation and a 0.02° of step size. The chemical environment of Cu oxide nanofibers was investigated with X-ray photoelectron spectroscopy (XPS, VG, ESCALab

MKII, UK). The XPS analysis was performed in a base pressure of 5.0×10^{-10} Torr. The X-ray source used in this work was Al Kα (1486.6 eV). The survey XPS spectra of Cu oxide nanofibers were taken in the range of 1200-0 eV, a scan step of 0.5 eV, and a pass energy of 50 eV with a concentric hemispherical analyzer. The high resolution XPS spectra of Cu 2p and O 1s were obtained at a scan step of 0.02 eV and a pass energy of 50 eV. The binding energies of all spectra were corrected with the binding energy of aliphatic carbon at 284.6 eV.

6.3 Results and Discussion

The morphology of Cu oxide nanofibers were examined with FE-SEM. The well aligned nanofibers were observed in Cu-rt shown in Fig. 6.1 (a). The average diameter of Cu-rt nanofibers was about 268.9 nm. After calcination of Cu-rt at 673K for 5 hrs, the morphology of Cu-673 is quite different with that of Cu-rt. In Fig. 6.1 (b), the core of Cu-673 was hollow channel and partially interconnected granules are aligned at the surface region of Cu-673 nanofibers (inset of Fig. 6.1 (b)). The decomposition temperature of pure PVA was about 579K [6.21,6.22]. Therefore PVA was decomposed during calcination of Cu-rt nanofibers. This implies that the core parts of Cu-rt mainly consisted with PVA and the outer part of Cu-rt consisted with the mixture of Cu and PVA. When the calcination temperature increased to 873K, further aggregated nanofibers without distinct hollow channel were observed in Fig. 6.1 (c). It is worthwhile to note that the hollow channel detected at Cu-673 disappeared at higher calcination temperature than 673K. A plausible explanation for this phenomenon is the rearrangement of Cu particles. Thus, the calcination temperature, 873K, is a sufficient temperature which provides energy to migrate nanoparticles resulting in aggregated nanofibers. Cu-873 was analyzed with TEM to identify the crystallinity of the nanofibers. The well aligned lattice fringes were observed and the lattice spacing was calculated to be 0.32 nm. The more detailed explanation will be given in the XRD section of this chapter. The inset in Fig. 6.1 (d) showed the selected area electron diffraction (SAED) of Cu-873. The zone axis is [233]

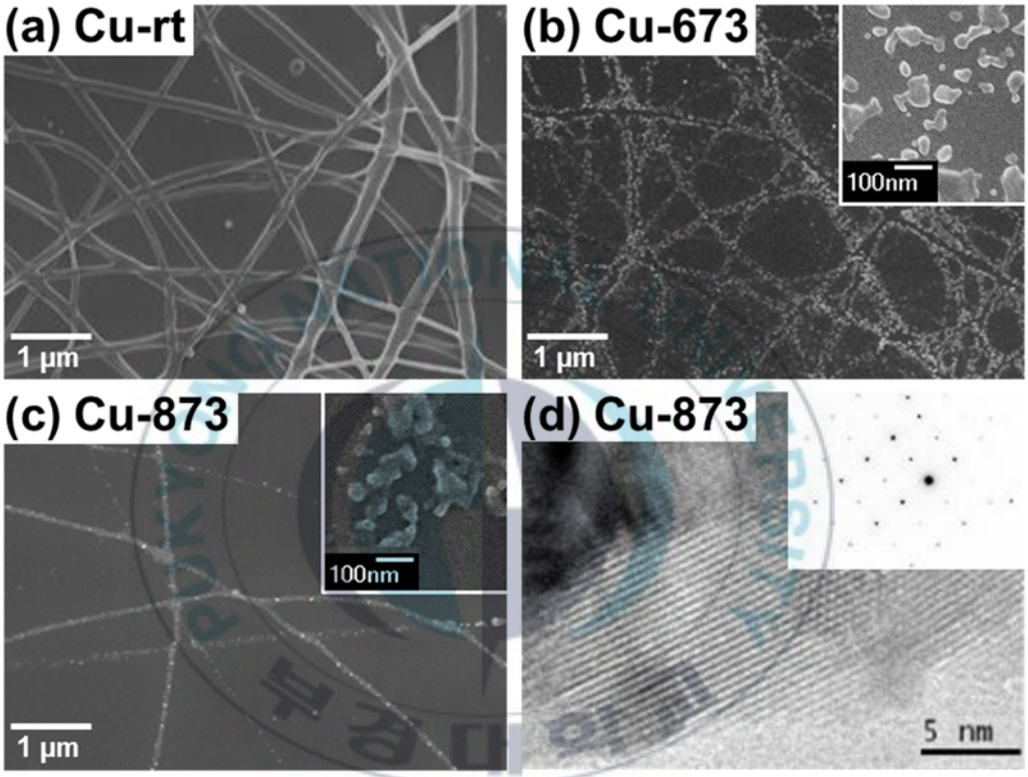

Fig. 6.1. FE-SEM images of Cu-rt in (a), Cu-673 in (b), and Cu-873 in (c). The inset images showed the morphology of magnified Cu oxide nanofibers. TEM images of Cu-873 in (d).

and it revealed that Cu -873 has a single crystal phase with high crystalline properties.

The XRD diffractograms of the Cu oxide nanofibers are shown in Fig. 6.2. Only broad peaks at around 20° are observed in Cu-rt and it is caused by PVA (101) diffraction [6.23,6.24]. Thus Cu species in Cu-rt nanofibers could be considered as an amorphous phase. At Cu-673, cubic Cu_2O peaks evolved with 13.7 nm of crystalline size calculated by Scherrer's equation (JCPDS card #78-2076). At Cu-873, more peaks were evolved. These peaks were assigned to monoclinic CuO phase (JCPDS card #80-1917) and the crystalline size increased to 27.6 from 13.7 nm comparing with Cu-673. Therefore, the phase transition occurs to monoclinic CuO through cubic Cu_2O from amorphous during calcination process.

Figure 6.3 shows the XPS survey spectra of Cu oxide nanofibers. At Cu-rt, carbon, oxygen, and copper peaks were observed and the other peaks were not detected. The formation of Cu oxide/PVA nanofibers was confirmed by XPS results. However, the peak intensity of Cu 2p was weak comparing with those of O 1s and C 1s. It implies that the surface of Cu-rt nanofibers was mainly covered with PVA. It is caused by the low percentage of Cu sulfate in electrospinning solution that was 24.2%. Thus the amount of Cu is smaller than that of PVA which caused the weak intensity of Cu from Cu-rt. After the calcination of Cu-rt nanofibers, the intensity of C 1s peak slightly decreased and that of Cu 2p peak dramatically increased and Cu Auger peaks appeared between 548-719 eV.

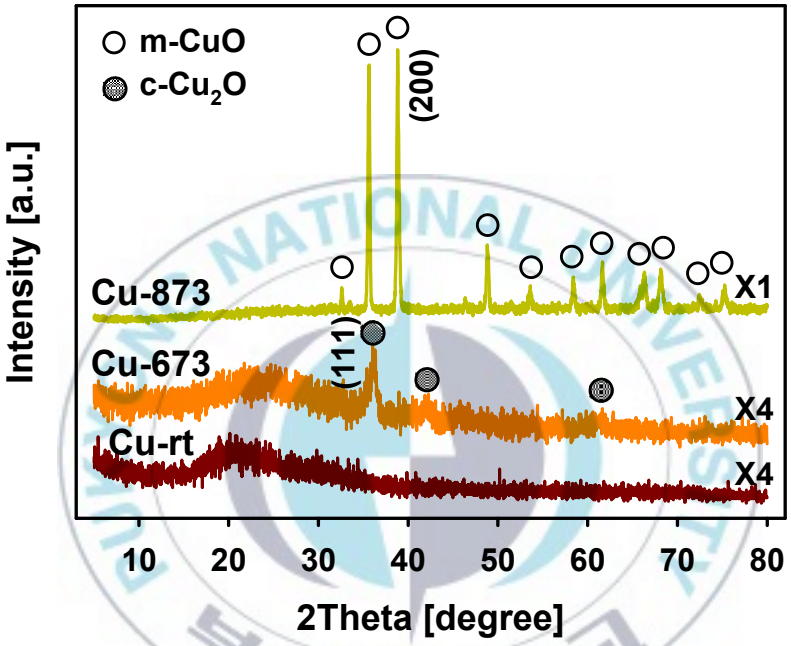

Fig. 6.2 X-ray diffractograms of Cu oxide nanofibers. The diffractograms of Cu-rt and Cu-673 were multiplied 4 times for better comparison. The filled circles represent the cubic Cu_2O phase and the hollow circles represent monoclinic CuO phase.

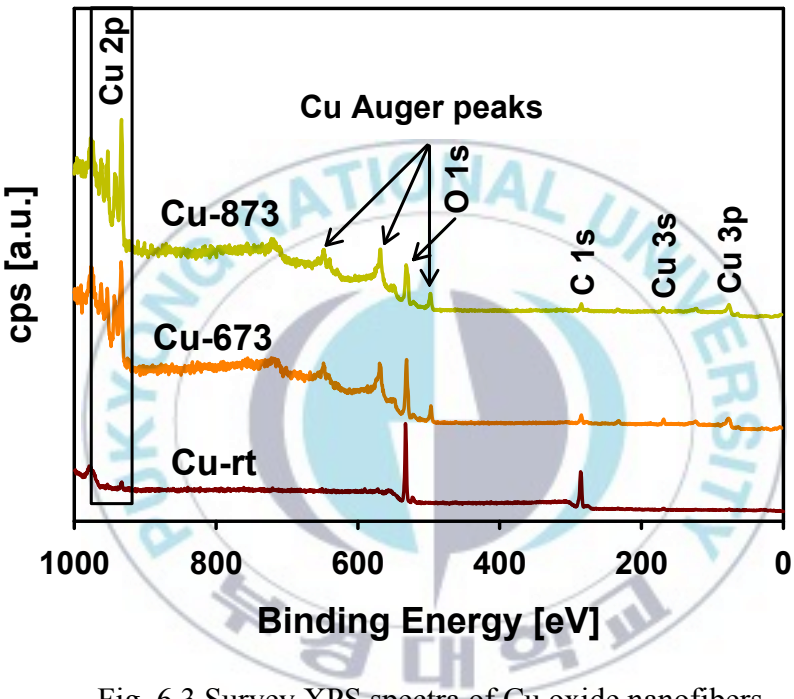

Fig. 6.3 Survey XPS spectra of Cu oxide nanofibers.

Comparing the survey spectra of Cu-673 and Cu-873, the noticeable change of peaks were not observed. For more detailed information, high resolution XPS spectra of the Cu 2p and O 1s binding energy region were analyzed.

The high resolution XPS spectra of Cu 2p and O 1s were deconvoluted to get the detailed chemical information of Cu oxide nanofibers. Deconvoluted high resolution XPS spectra of Cu $2p_{3/2}$ and O 1s are shown in Fig. 6.4 (a) and (b), respectively. At the Cu 2p region between 970-925 eV included Cu $2p_{3/2}$, Cu $2p_{1/2}$, and satellite peaks caused from Cu^{+} and Cu^{2+}. Because the peak ratio of Cu $2p_{3/2}$, Cu $2p_{1/2}$ and others are the same, Cu $2p_{3/2}$ region was deconvoluted to avoid complexity. The peak shape of Cu $2p_{3/2}$ and O 1s was asymmetric. This means that several oxidation states of Cu and O exist in Cu oxide nanofibers. Unfortunately, metallic Cu (Cu^{0}) and Cu^{+} are not distinguishable in Cu 2p region due to the final state effect [6.18]. This ambiguity can be solved through the analysis of O 1s region. Before the calcination of Cu-rt nanofibers, most of Cu species exist as Cu^{0} and Cu^{+}. As the calcination temperature increased to 673K, the relative ratio of Cu^{2+} to Cu^{0} and/or Cu^{+} increased. When the calcination temperature was increased to 873K, the ratio of Cu^{2+} is increased more than Cu-673. In Cu-rt nanofibers, two oxygen species, surface oxygen and oxygen bound with Cu^{+} were mainly detected. Because the intensity of Cu_2O is lower than that of surface oxygen, the Cu_2O phase was a minor species in Cu-rt nanofibers. Thus, we could conclude that the contribution of Cu^{0} and/or Cu^{+} (Cu^{0}/Cu^{+}) peaks in Cu $2p_{3/2}$ mainly resulted from the Cu^{0} species. After calcination of the Cu-rt

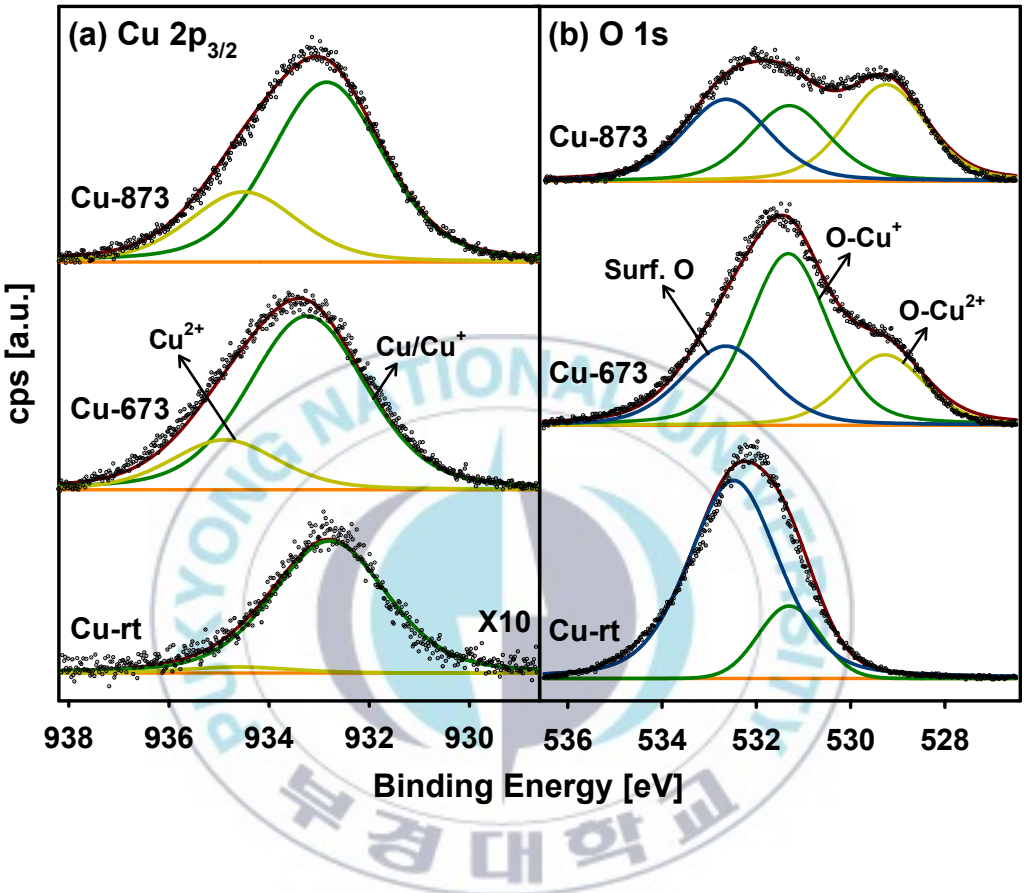

Fig. 6.4 Deconvoluted XPS spectra of Cu 2p region in (a) and that of O 1s region in (b). The dots in the spectra represent the raw data and the solid lines overlapped with the dots represent the reconstructed data of Cu and O species.

nanofibers, the ratio of oxygen bound with Cu^{+} and Cu^{2+} remarkably increased, while the ratio of surface oxygen decreased due to calcination. In Cu-673, the major Cu species was Cu^{+} shown in Fig. 6.4 (b). Further increase of calcination temperature to 873K, the portion of O-Cu^{2+} peak was increased and that of O-Cu^{+} was decreased. This result revealed that the Cu_2O phase was oxidized to CuO phase, but not fully oxidized to form CuO only by calcination of nanofibers at 873K. According to the results of the deconvoluted XPS spectra, the oxidation states of Cu species were changed to Cu^{2+} from Cu^{0} through Cu^{+} phase by calcination. This result is consistent with the change of the crystalline structure of the Cu oxide from c-Cu_2O to m-CuO described previously in the XRD section.

The relative atomic percentage of Cu and O species are deduced from the deconvoluted XPS results of Cu $2p_{3/2}$ and O 1s considering atomic sensitivity factors. As shown in Fig. 6.5 (a), the ratio of Cu^{0}/Cu^{+} was monotonically decreased while that of Cu^{2+} increased as the calcination temperature increased. This implies that the thermal oxidation of Cu proceeded. However, the ratio of O-Cu^{+} increased from 17.8% for Cu-rt to 51.2% for Cu-673 then decreased to 29.4% for Cu-873 (Fig. 6.5 (b)). The main reason for the decrease in the ratio of Cu^{0}/Cu^{+} and increase in O-Cu^{+} was caused by the oxidation of Cu species from Cu^{0} to Cu^{+} as the calcination temperature increased to 673K. When the calcination temperature increased to 873K, the major oxidation process of Cu species was from Cu^{+} to Cu^{2+}. Ultimately, the ratio of Cu^{0}/Cu^{+} decreased and CuO increased. It revealed

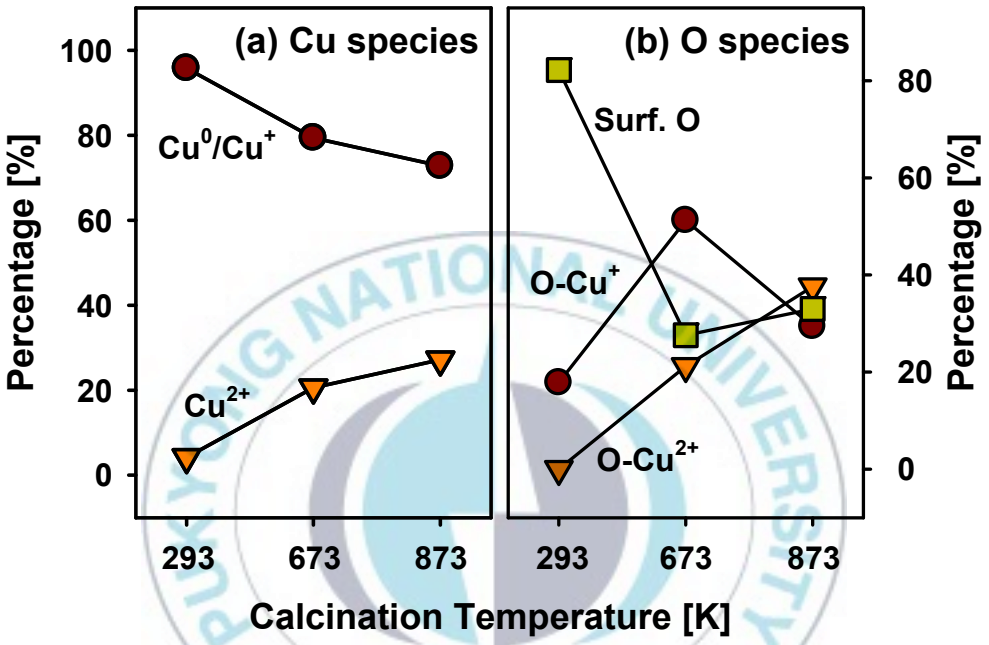

Fig. 6.5 Atomic percentage of specific species of Cu in (a) and O in (b). The circles indicate the ratio of Cu and/or Cu^{+} and the triangles indicate that of Cu^{2+} in (a). The circles represent the ratio of O bonded with Cu^{+} species, the triangles represent that of O in CuO phase, and the square represent surface oxygen in (b).

that the difference in the ratio of Cu_2O and CuO at Cu-873 are not noticeably detected. In the graph for ratio of Cu $2p_{3/2}$, the ratio of Cu/Cu^+ is 72.8% and that of Cu^{2+} is 27.2%. From the analysis for O 1s, the amount of Cu_2O and CuO are similar, the ratio of Cu^+ in Cu/Cu^+ could be considered to about 27%, and the reminder of 45% could be corresponded to metallic Cu. According to XPS and XRD results, chemical composition of nanofibers at 873K is Cu and Cu_2O as amorphous phase and monoclinic CuO phase.

6.4 Conclusion

Cu oxide nanofibers were synthesized by electrospinning technique using Cu sulfate and PVA. Before calcination of nanofibers, the average diameter of Cu oxide/PVA nanofibers was about 268.9 nm and the specific crystallinity of Cu oxide was not observed. To obtain Cu oxide nanofibers, the as-electrospun nanofibers were calcined at 673 and 873K. The crystal structure of calcined nanofibers at 673K was simple cubic Cu_2O and CuO is formed as an amorphous phase. The Cu oxide nanofibers calcined at 873K consists of amorphous Cu_2O and monoclinic CuO. It is congruent to the SAED patterns which show single crystal properties. The major oxidation mechanism of Cu species varied depending on the applied calcination temperature. Oxidation from Cu^0 to Cu^+ was dominant for Cu-673 nanofibers while the major oxidation from Cu^+ to Cu^{2+} was dominant for Cu-873 nanofibers.

CHAPTER VII. Investigation of Metal Oxide Thin Films Using Electron Emission Spectroscopy

7.1 $HfAlO_3$ Dielectric Thin Films

7.1.1 Introduction

As the field of memory devices has been growing larger and several concerns are appeared. Among the concerns, power consumption is a major problem to develop memory devices. It caused from the increase of density of memory device and this can be overcome by reducing the thickness of SiO_2 film. However, if the thickness of SiO_2 films was too thin, a large direct-tunneling current through the films is becoming a new concern. Therefore, new materials, such as HfO_2, Al_2O_3, and ZrO_2 have been investigated to replace the SiO_2 film. The important factor is the dielectric constants of high-k materials which are used for gate dielectrics. The dielectric constants are 25, 9, 25, and 3.9 and band gaps are 5.7, 8.7, 5.1, and 8.9 eV for HfO_2, Al_2O_3, ZrO_2, and Si, respectively [7.1]. Comparing these values, HfO_2 has higher dielectric constant, but lower band gap energy than Si. While Al_2O_3 has lower dielectric constant and higher band gap energy than HfO_2. Moreover, Al_2O_3 is more stable in high temperature than HfO_2. The mixed structure of Hf and Al oxide ($HfAlO_x$) has better properties to apply in memory devices than HfO_2 and Al_2O_3 alone. Zhu *et al.* reported that the

addition of Al in HfO_2 leads to increase of the crystallization temperature from 375 to 1000°C and the band gap energy increased from 5.8 to 6.5 eV [7.2]. However, new candidates must satisfy a standard processing procedure. Recently, plasma etching process has received attention because of several difficulties in the HF-based wet etching process on the high-k materials. In order to overcome this issue, an understanding about the relationship between plasma properties and etching characteristics of $HfAlO_3$ thin films is required. Until now, the effect of dry etching process on the $HfAlO_3$ thin films was not reported in our knowledge. In this study, $HfAlO_3$ thin films were synthesized by atomic layer deposition and etched using inductively coupled plasma (ICP) system at a substrate temperature of 313K with Cl_2/Ar etch gases. The etching characteristics on the $HfAlO_3$ films were analyzed by varying the gas mixing ratio, radio frequency (rf) power, direct current (dc)-bias voltage, and process pressure. The chemical reaction on the surface of the etched $HfAlO_3$ thin films was studied by X-ray photoelectron spectroscopy (XPS).

7.1.2 Experimental

$HfAlO_3$ thin films were synthesized on the SiO_2/Si substrates by atomic layer deposition. The thickness of the $HfAlO_3$ films was 50 nm. The dry etching of the $HfAlO_3$ thin films was performed using an ICP system [7.3]. The cylindrical chamber with a diameter of 26 cm was evacuated using a mechanical pump and a turbo molecular pump and the base pressure was kept below 5×10^{-7} Torr. A 3.5 turn spiral copper coil was located above

horizontal quartz window with the thickness of 24 mm at the top of the chamber. And copper coil was connected to rf power (13.56 MHz) generator and produced the ICP. Another rf power generator was connected to the substrate holder and controlled the ion energy by adjusting the dc-bias voltage. The rf power generators equipped with L type auto matching box for reducing of the power dissipation in the plasma and protect the generator. The substrate located at the bottom of the chamber was cooled down about 313K using a water flow cooling system. The distance between the topside quartz window and the bottom substrate holder was 9 cm. $HfAlO_3$ thin films were etched using Cl_2/Ar gas mixture at total gas flow rate of 20 sccm and the etch process time was 60 sec for each sample. The effect of etching on the $HfAlO_3$ thin films were investigated as functions of the gas mixing ratio, rf power, dc-bias voltage, and process pressure and the detailed description and sample notation are listed in Table 7.1. The rf power and dc-bias voltage were varied from 400 to 700 W and from −50 to −200 V, respectively. The process pressures were 0.67, 1.34, 2.00, and 2.68 Pa. The chemical composition of the etched $HfAlO_3$ thin films was analyzed using XPS (VG, Sigma Probe, UK). The monochromatic Al Kα X-ray source with 1486.6 eV at 100 W was used. Peak deconvolution was performed with XPSPEAK (ver. 4.1) program after subtraction of the background applying a Shirley model.

Table 7.1. Sample notation and different etching conditions.

sample	Cl_2/Ar gas flow rate [sccm]	rf power [W]	dc-bias [V]	pressure [Pa]
A		as-dep.		
B	16/4	500	−150	2
C	16/4	700	−150	2
D	16/4	500	−200	2

7.1.3 Results and Discussion

To analyze the change of chemical composition after etching of the $HfAlO_3$ thin films, the surfaces before and after the etching were examined by XPS. Fig 7.1 shows the survey XPS spectra obtained from the surface of the $HfAlO_3$ thin films. The characteristic peaks of Hf, C, and O atoms were observed centered at 17, 284, and 529 eV, respectively. However, those of Al and Cl atoms were not detected in the survey spectra due to the detection limit of the XPS system. The difference between before and after the etching was not significantly noticeable from all samples in the survey spectra. The position and intensity of peaks were not changed and it revealed that the etching on the surface acted uniformly regardless of the kinds of atom.

In order to obtain the detailed information of chemical states of $HfAlO_3$ films, high resolution of Hf 4f, O 1s, Al 2p, and Cl 2p XPS spectra were measured and shown in Fig. 7.2 (a), (b), (c), and (d), respectively. The peak profile of sample A is different with those of other samples. The shoulder at the higher binding energy region is decreased with applying more etching process to the $HfAlO_3$ films as shown in Fig. 7.2 (a), (b), and (c). This implies that the Hf and Al atoms are reduced to metallic form and the ratio of oxygen bonded with surface is decreased during etching the films. Thus the ratio of atoms did not affect by the etching process, however, the atomic species with different oxidation state are dependent on the etching process. The Cl 2p peak is more easily detected from sample D than from samples B and C. This means that Cl was remained in the surface region of

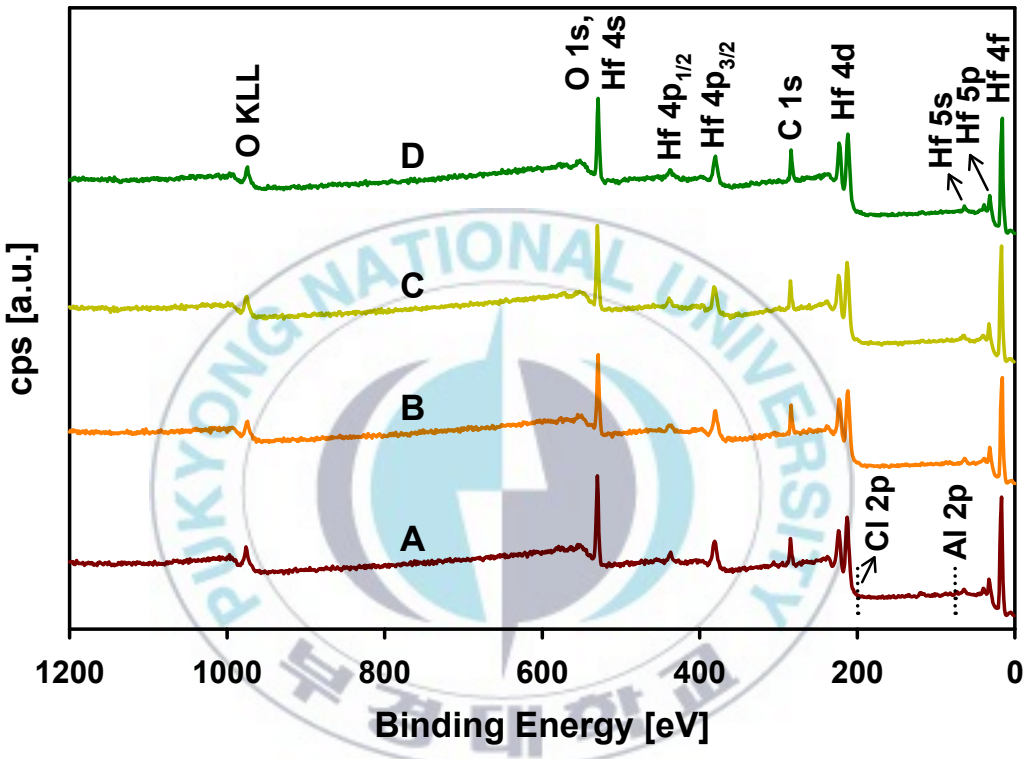

Fig. 7.1 Survey XPS spectra of $HfAlO_3$ thin films with before etching (sample A) and after etching with Cl_2/Ar gas flow rate of 16/4 sccm, rf powr of 500 W, dc-bias of −150 V, and pressure of 2 Pa (sample B), rf power of 700 W (sample C), dc bias of −200 V (sample D). Other etching conditions of sample C and D are same as sample B.

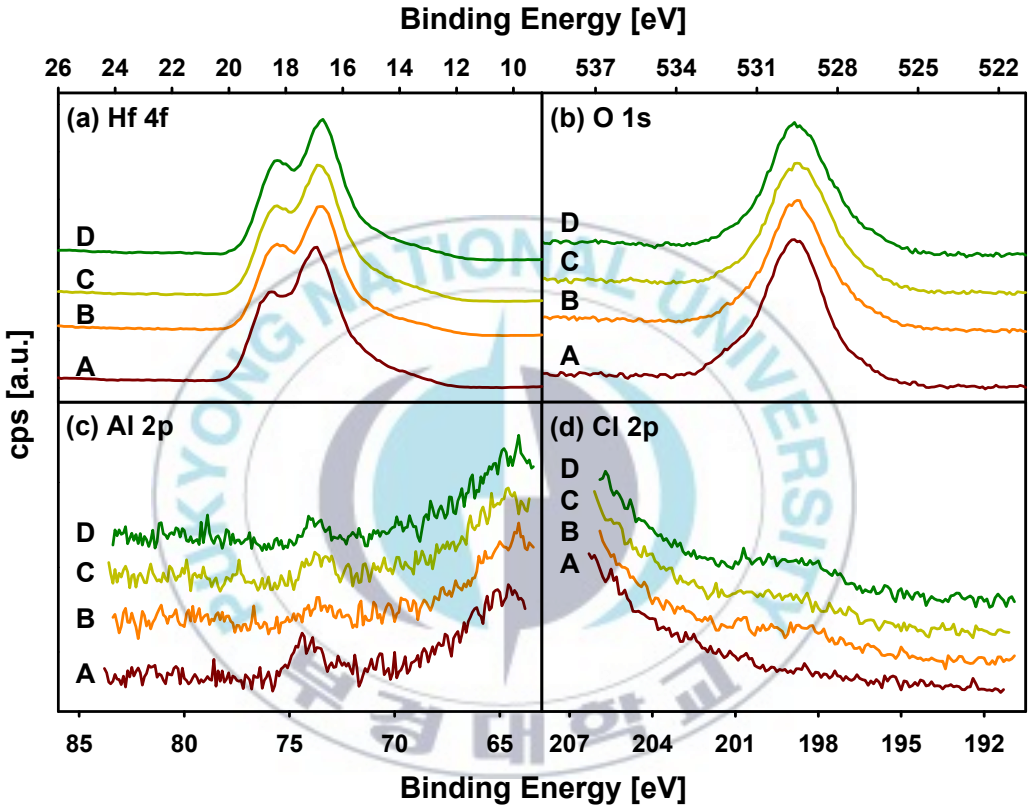

Fig 7.2 High resolution XPS spectra: (a) Hf 4f, (b) O 1s, (c) Al 2p, and (d) Cl 2p region.

$HfAlO_3$ thin films after etching with high dc-bias voltage.

Fig. 7.3 (a) shows the deconvoluted Hf 4f XPS spectra to obtain the detailed information about the change of ratio in species with different oxidation state. The XPS spectra showed doublet peaks of Hf for Hf $4f_{7/2}$ and Hf $4f_{5/2}$ with spin obit splitting (SOS) of 1.6 eV. The total Hf 4f peak can be deconvoluted into four peaks corresponding to the Hf^{4+}-O bond, $Hf^{\delta+}$-O bond, Hf-Al-O bond, and pure Hf bond. Two kinds of Hf oxides were assigned for HfO_2 and HfO_x ($0<x<2$) formed with Hf^{4+} and $Hf^{\delta+}$ species, respectively. These binding energies are shown in Table 7.2 and those are well agreed with the reported values [7.4-7.6]. It is worthy to note that the peak intensity of $Hf^{\delta+}$-O is increased by compensating Hf^{4+}-O regardless of the parameters during the etching process. The intensities of the peaks for the Hf-Al-O and Hf-Hf bonds are almost constant with increasing the amount of Cl_2, rf power, and dc-bias voltage. Fig. 7.3 (b) shows the deconvoluted high resolution O 1s XPS spectra obtained from the surface of as-deposited and the $HfAlO_3$ thin films etched at different conditions. The O 1s peak was deconvoluted into four peaks which were deemed to correspond to the oxygen and/or hydroxyl group on the surface: Surf-O bond, O-$Hf^{\delta+}$ bond, O-Hf^{4+} bond, and Hf-Al-O bond [7.7-7.9]. Similarly the result of deconvoluted Hf 4f XPS spectra, the ratio of HfO_x and HfO_2 before etching is dominated at about 43 and 30%. However, the intensity of HfO_x is increased and that of HfO_2 is decreased after etching and this phenomenon is severe in high dc-bias voltage. And the intensity of the peak centered at 528.1 eV remained nearly constant and did

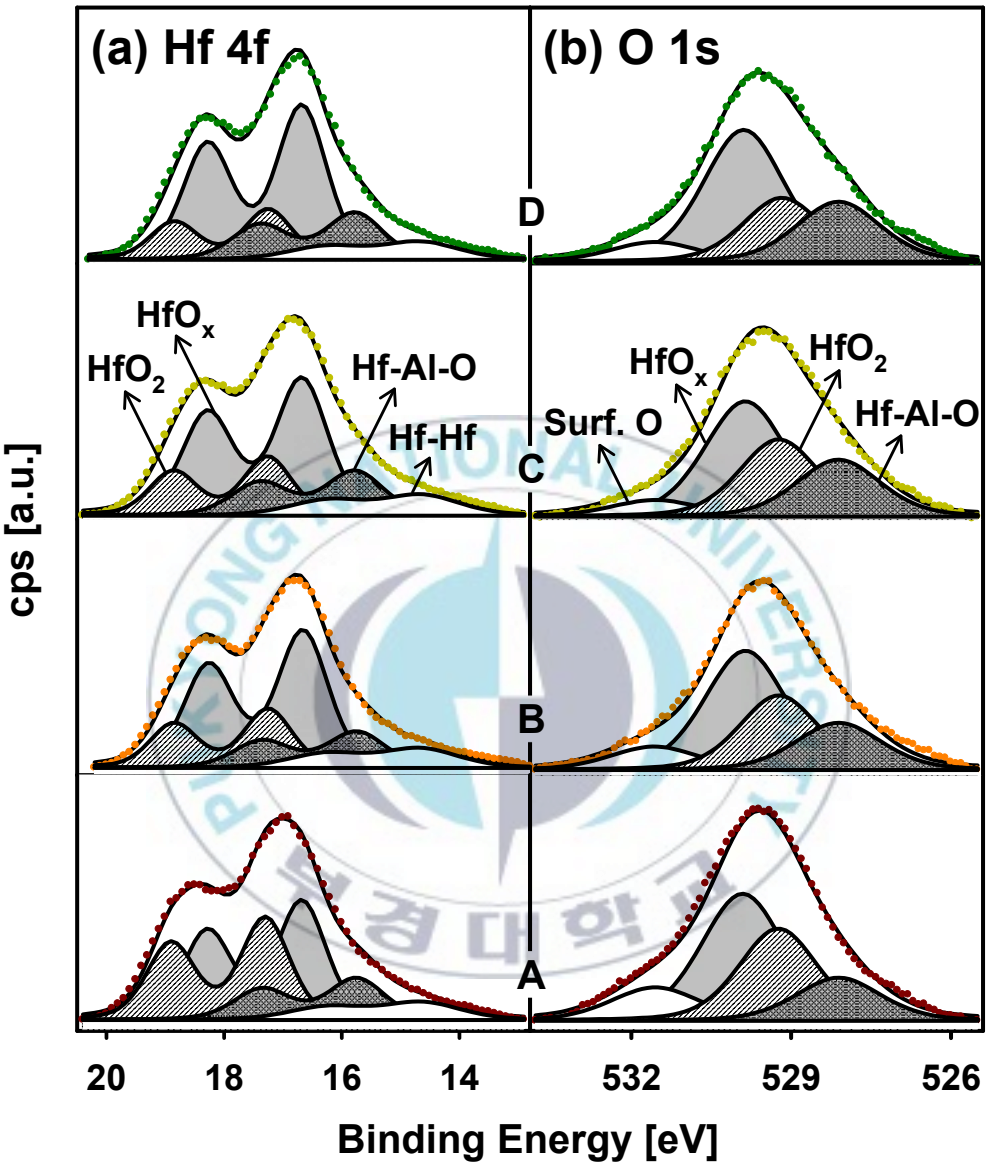

Fig. 7.3 Deconvoluted (a) Hf 4f and (b) O 1s XPS spectra.

Table 7.2 Binding energies of different chemical species of Hf 4f and O 1s. Average binding energies and standard deviations are calculated for each species of Hf 4f and O 1s.

Hf 4f	HfO_2	HfO_x	Hf-Al-O	Hf-Hf
D	17.25	16.68	15.78	14.66
C	17.26	16.68	15.78	14.64
B	17.25	16.66	15.75	14.66
A	17.30	16.68	15.75	14.64
Average	17.27	16.68	15.77	14.65
Standard Deviation	0.02	0.01	0.02	0.01
O 1s	Surf. O	HfO_x	HfO_2	Hf-Al-O
D	531.56	529.89	529.17	528.11
C	531.55	529.88	529.18	528.11
B	531.57	529.86	529.23	528.11
A	531.55	529.91	529.24	528.11
Average	531.56	529.89	529.21	528.11
Standard Deviation	0.01	0.02	0.04	0.00

not depend on the film treatment conditions. While the intensity of the Surf-O peak centered at 531.6 eV showed the significant decrease. This result means that the surface oxygen species were effectively removed by etching process as well. Therefore, the XPS data gave clear confirmation that, in the Cl_2-containing plasmas, the increase of dc-bias voltage is more effective, but remains the Cl in the surface of $HfAlO_3$ thin films, than increase of rf power.

7.1.4 Conclusion

Using inductively-coupled plasma, the etching trend of $HfAlO_3$ thin films was investigated as functions of the Cl_2/Ar gas mixing ratio, the rf power, dc-bias voltage, and process pressure. The chemical reaction on the surface of the $HfAlO_3$ thin films was investigated by using XPS analysis. According to our experimental results, the Cl_2/Ar plasma was effective to etch the $HfAlO_3$ thin films. The ratio of atoms did not affect by the etching conditions, while the ratios of chemical species, Hf and O, were affected by the etching conditions, especially dc-bias voltage.

7.2 Ga-Zn-Sn-O Thin Films

7.2.1 Introduction

Amorphous oxide semiconductors (AOSs) are attractive materials due to their superior characteristics in the field of thin film transistors (TFTs). Conventionally, amorphous Si and polycrystalline Si were applied to TFTs. Among the various amorphous oxides, amorphous oxides contained the heavy metal cations with (n-1) $d^{10}ns^0$ ($n \geq 4$) electronic configurations are focused. Despite of crystalline character, ZnO polycrystalline thin films were focused in the last few years. Because amorphous oxides exhibit a high transparency, large electron mobility, and low resistivity, amorphous In-Zn-O (a-IZO), amorphous Ga-Zn-O (a-GZO) [7.10], and amorphous Ga-In-Zn-O (a-GIZO) were intensively studied. Especially, the main point in TFTs is considered to be high channel mobility, the systems including high percentages of In is outstanding in this aspect. However, In is known as a rare metal and leads to increase in the cost, the replacement of In is necessary to synthesize cost effective TFTs. In this work, In is substituted by Sn in the amorphous Ga-Zn-Sn-O (a-GZTO) thin films.

Amorphous oxide thin films were synthesized by various techniques from the solution to vapor phase. The solution based method is versatile and cost effective method, however, the growth of amorphous oxide thin films from chemical solution is suffer to high electrical resistivity. Thus, the films are not suitable for the application TFTs in spite of its transparency. While,

the vacuum deposition process leads to the films with low electrical resistivity as well as high quality.

For the application in TFTs, it is particularly crucial to control the carrier concentration. Because the low carrier concentration contributes to good device stability and a low off-current level, this leads to a high on/off current ratio [7.11]. An appropriate addition of Ga as a carrier suppressor is known to be effective to control the carrier concentration. Because the electronegativity of Ga, Zn, Sn and In is 1.82, 1.66, 1.72, and 1.49 in Pauling scale, respectively, Ga ions are more strongly bonded with oxygen than Zn and In ions did, reducing the formation of oxygen vacancies [7.12,7.13]. And the oxygen vacancies can be modulated by post-annealing of thin films. However, the effect of Ga concentration and post-deposition annealing on the characteristic properties of GZTO films has not been reported. In this study, we have investigated the effects of Ga concentration and post-deposition annealing on the chemical properties of GZTO thin films prepared by a co-sputtering method.

7.2.2 Experimental

The GZTO films were deposited by magnetron co-sputtering method at room temperature. GZTO thin films with the thickness of 300 nm were deposited on alkali-free glass substrates (Corning Eagle 2000) using Ga-doped ZnO (GZO, 5 wt.% Ga_2O_3), SnO_2, and Ga_2O_3 targets with 4 inch in diameter each. The base pressure in the sputtering chamber was kept below 4×10^{-4} Pa

and the deposition process was carried out under a working pressure of 0.67 Pa using pure Ar gas as a sputtering gas. The applied rf power on the Ga_2O_3 target was varied as 0, 50, 75, and 100 W (denoted as GZTO-0, 50, 75, and 100), while those of the GZO and SnO_2 were fixed at 100 and 130 W, respectively. To evaluate the thermal stability of the obtained films, the prepared films were annealed in ambient condition for 1 hr at 473, 573, and 673K.

The chemical information of thin films were analyzed using an XPS (VG, MultiLab 2000, UK) with Mg Kα (1253.6 eV) X-ray source. The base pressure in the analysis chamber was maintained lower than 1×10^{-8} Pa. X-ray was generated at the high voltage of 15 kV, beam current of 15 mA, filament current of 4.2 A, a pass energy of 50 eV, dwell time of 50 ms, and energy step of 0.5 eV in constant analyzer energy (CAE) mode for survey scans. High resolution XPS spectra were obtained at pass energy of 20 eV, energy step of 0.02 eV, and other parameters were the same as applied in the survey scan. The GZTO films were electrically grounded with Ag paste, which is used for a reference peak and preventing the charge accumulation during data collection. High resolution XPS data were deconvoluted using XPSPEAK software (ver 4.1) for detailed information about the oxidation state of surface elements.

7.2.3 Results and Discussion

7.2.3.1 Effect of Ga Concentration

The composition and chemical states of GZTO films were characterized with XPS analysis. It is useful to compare the atomic ratio of each element to correlate with the changes in electrical properties of GZTO films. The survey XPS spectra of GZTO films were shown in Fig. 7.4. The detected peaks are assigned to photoelectrons or Auger electrons for Ga, Zn, Sn, and O. It means that GZTO films are successfully synthesized by rf co-sputtering method without other impurities. Interestingly, the intensity of Ga 2p was gradually increased with increasing of rf power for Ga_2O_3 target. While, that of Zn 2p was decreased, those of Sn 3d and O 1s were almost in constant level. The detailed atomic ratios of Ga, Zn, Sn, and O on the surface of GZTO films deduced after quantitative analyses with considering their atomic sensitivity factors are listed in Table 7.3. The monotonic decrease in carrier concentration of GZTO films [7.14] could be explained by the atomic ratio of Ga, which is gradually increased with the power on Ga_2O_3 target. The abundance of Ga on the surface was almost doubled up with every RF power increment of 50 W. However, the Zn/Sn ratio was almost independent with the RF power on Ga_2O_3 target over 50 W and O content in the films did not affect by the Ga doping. Therefore, it can be concluded that the decrease in carrier concentration is mainly attributed to the increase of Ga content in GZTO films.

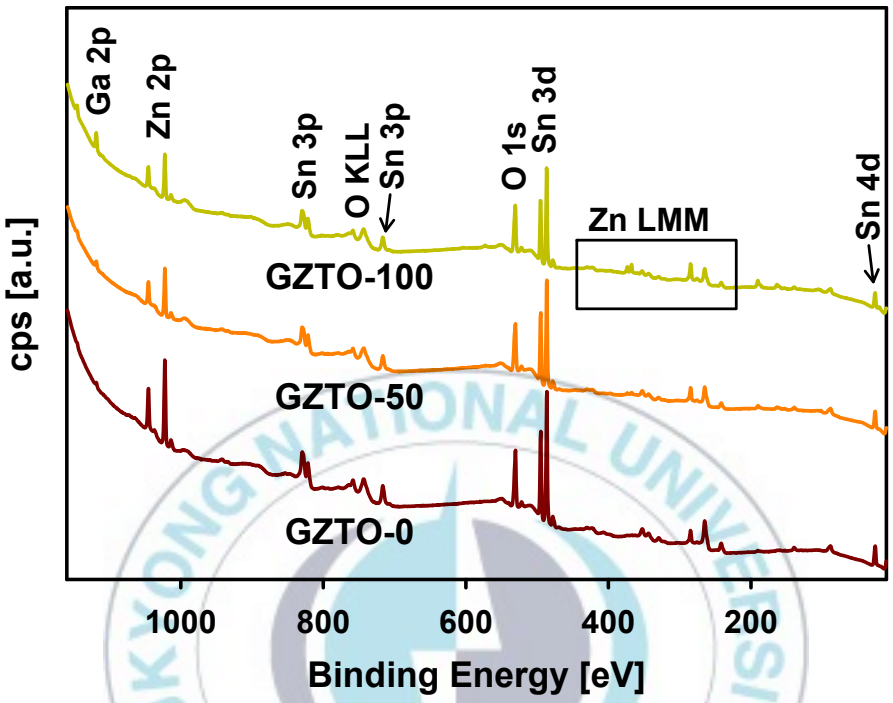

Fig. 7.4 Survey XPS spectra of GZTO films with different rf powers on Ga_2O_3 target.

Table 7.3 Atomic compositions of GZTO films determined from XPS analyses.

Sample	Ga [%]	Zn [%]	Sn [%]	O [%]
GZTO-0	0.58	15.17	30.64	53.60
GZTO-50	1.17	10.08	34.68	54.07
GZTO-100	3.08	9.52	33.44	53.96

In order to study the detailed oxidation states of Ga, Zn, Sn, and O elements, high resolution XPS spectra were taken and shown in Figs. 7.5 and 7.6. Because the SOS constants for Ga 2p, Zn 2p, and Sn 3d are large as 27.0, 23.1, and 8.5 eV, respectively, major peaks ($2p_{3/2}$ and $3d_{5/2}$) of those elements were deconvoluted to avoid complexity. Peak deconvolution was carried out after subtraction of background taken by Shirley model. Two oxidation states of Ga are assigned for Ga^{3+} and $Ga^{\delta+}$ (δ=1 or 2) centered at 1118.4 and 1117.6 eV, respectively [7.15]. There are two oxidation states of Zn (Zn^{2+} and Zn^{0}) whose binding energies are centered at 1022.6 and 1021.9 eV, respectively [7.16]. The observed oxidation states of Sn are Sn^{4+} (486.8 eV) and Sn^{2+} (486.3 eV) [7.17]. The assigned binding energies are well agreed with reported values. After deconvolution of the high resolution XPS spectra, ratios of different oxidation states for each element were determined as given in Table 7.4. Worthy of note is that the portion of high oxidation state for each cation was considerably increased with increasing Ga content (comparing GZTO-0 with GZTO-100). The increase in high oxidation state of metal cations indicates that their ionic bonds with surrounding oxygen atoms were promoted by Ga doping. This result can also be deduced from the deconvoluted high resolution XPS spectra of O 1s (Fig. 7.6). There are three oxygen species denoted as O-Surf, O-Def, and O-Met centered at 531.8, 530.8, and 530.1 eV, respectively. O-Surf represents for chemisorbed surface oxygen species including water and hydroxyl group and O-Def represents for oxygen species in the oxygen deficient region. Because the binding energies

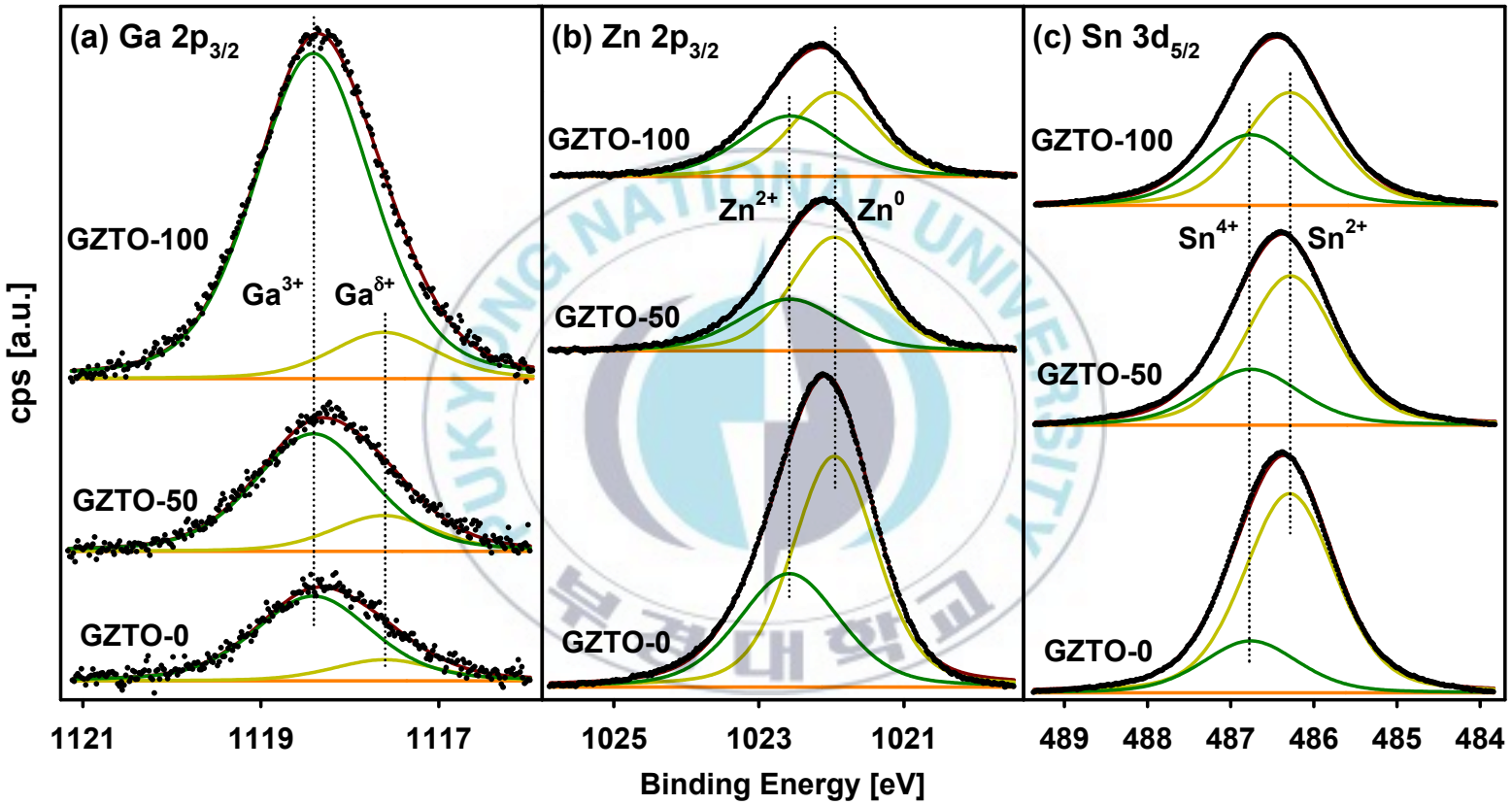

Fig. 7.5 High resolution XPS spectra of (a) Ga $2p_{3/2}$, (b) Zn $2p_{3/2}$, and (c) Sn $3d_{5/2}$. The dots represent experimental data and lines overlapped with dots represent the reconstructed data after deconvolution process.

Table 7.4 Binding energies and ratio of different oxidation states for each element in GZTO films.

Moiety	Ga $2p_{3/2}$		Zn $2p_{3/2}$		Sn $3d_{5/2}$		O 1s		
	Ga^{3+}	$Ga^{\delta+}$	Zn^{2+}	Zn^{0}	Sn^{4+}	Sn^{2+}	O-Surf	O-Def	O-Met
BE [eV]	1118.4	1117.6	1022.6	1021.9	486.8	486.3	531.8	530.8	530.1
GZTO-0	0.82	0.18	0.37	0.63	0.21	0.79	0.20	0.11	0.69
GZTO-50	0.79	0.21	0.35	0.65	0.29	0.71	0.20	0.10	0.70
GZTO-100	0.89	0.11	0.46	0.54	0.40	0.60	0.20	0.09	0.71

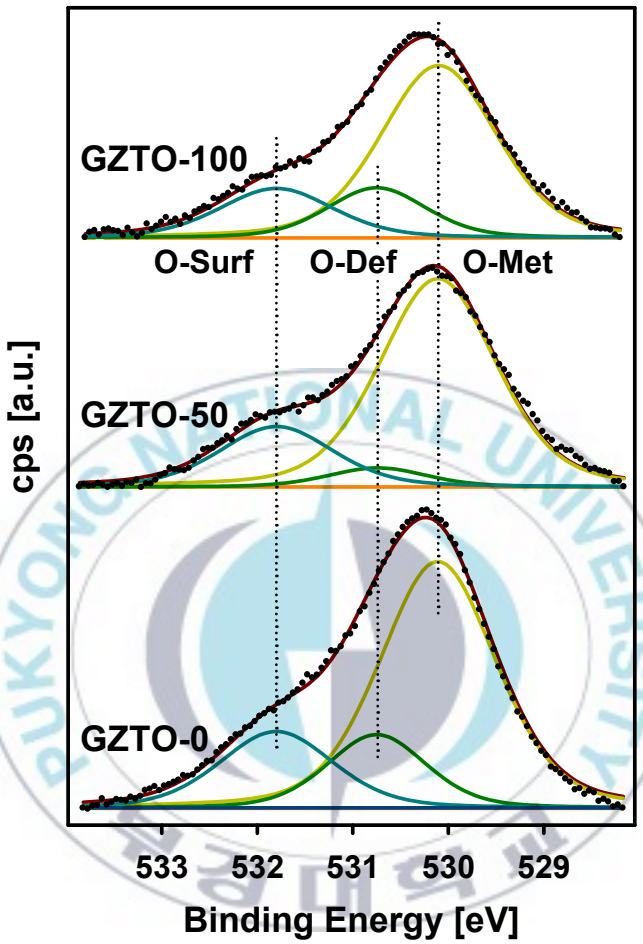

Fig. 7.6 High resolution O 1s XPS spectra of GZTO thin films. The deconvolution was carried out based on O-Surf, O-Def, and O-Met, representing oxygen bound on the surface region, in oxygen deficient region, and with metal, respectively.

of O 1s in O-Zn [7.18], O-Sn [7.19], and O-Ga [7.20] are almost indistinguishable, the binding energy of O 1s bound with metals (Zn, Sn, and Ga in this study) is denoted as O-Met. The relative ratios of oxygen species are given in Table 7.4. The data reveals that there were consistent decrease in O-Def and increase in O-Met with increasing Ga content, while O-Surf did not affect. It implies that the Ga doping resulted in the reduction of oxygen vacancies, acting as the origin of charge carriers, and promoted the oxidation of metal ions. This is in accordance with the aforementioned observation on the oxidation states of metal cation species. Thus, the decrease in carrier concentration of GZTO films can be attributed to the effect of Ga as a suppressor of carrier generation in ZTO system. Nomura *et al*. suggested that Ga ions work as the carrier suppressor in IGZO system since they form strong chemical bonds with oxygen than Zn and In ions [7.12]. On the other hand, Rim *et al*. explained the cause of carrier suppression with standard electrode potential (SEP) of constituent elements. According to their report, Zr can act as an effective carrier suppressor in ZTO system because Zr has a lower SEP (−1.45 V) than Zn (−0.76 V) and Sn (−0.13 V) [7.20]. In our GZTO system, however, the effect of Ga is tough to understand with the same analogy since Ga has a higher SEP (−0.55 V) than Zn [7.21]. Thus, it is considered that the effectiveness of a suppressor element (Ga) in GZTO system is ascribed to the bond strength between metal and O; Ga-O (353.6 kJ/mol), Zn-O (270.7 kJ/mol), and Sn-O (531.8 kJ/mol). Since Ga-O has a larger binding energy than Zn-O, Ga can effectively attract oxygen atoms and

promote the oxidation of metals. Meanwhile, Sn which has the largest binding energy in this system exhibited a considerable change of its valence state from Sn^{2+} to Sn^{4+} due to the Ga doping.

7.2.3.2 Effect of Post-Annealing

The effect of post-annealing on the chemical bonding states were investigated by XPS and the peak deconvolution process was performed as the same as chapter 4.1.3.1. Representative deconvoluted high resolution XPS spectra of Ga $2p_{3/2}$ of GZTO thin films deposited at 0 and 100 W with post-annealing at different temperatures are shown in Fig. 7.7. It is noticeable that the change in the ratio of Ga species. The percentage of Ga^{3+} was 68, 92, and 94% at as-dep., 573, and 673K, respectively. It means that most of Ga cation is oxidized from $Ga^{\delta+}$ to Ga^{3+} species at 0 W. While the percentage of Ga^{3+} was decreased from 80 to 70% with increasing the post-annealing temperature. Thus, the reaction of Ga atom during post-annealing process is different on the GZTO films obtained at different rf powers on Ga_2O_3 target, even the post-annealing temperature is the same. Fig. 7.8 shows the deconvoluted Zn $2p_{3/2}$ spectra and it seems that the total intensity of Zn is increased with increasing the post-annealing temperature. The tendency of increase in the total intensities of Zn of GZTO films obtained at 0 and 100 W after post-annealing at the same temperature were similar. It implies that the diffusion of Zn from bulk to surface is occurred and it is independent with the rf power on Ga_2O_3 target. After careful comparison of the deconvoluted Zn 2p peaks, it is

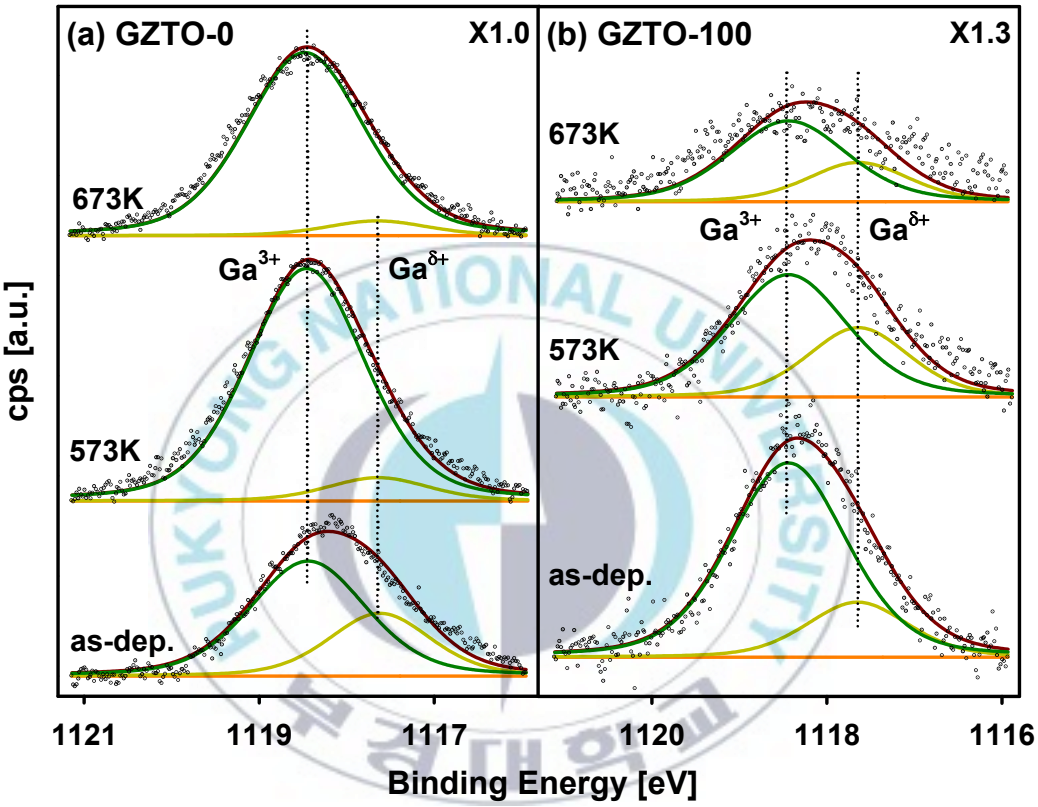

Fig. 7.7 High resolution XPS spectra of Ga $2p_{3/2}$ region. Post-annealing effect on GZTO thin films obtained at (a) 0 W and (b) 100 W of rf power for Ga_2O_3 target.

observed that the ratios of Zn^0 to Zn^{2+} are almost constant for two thin films deposited at 0 and 100 W and followed by post-annealing at as-dep. and 673K. The conversion of major species was observed from Zn^0 to Zn^{2+} state in both films. Noticeably, GZTO thin films post-annealed at 573 K shows different ratios of Zn^0 to Zn^{2+} comparing both films obtained at 0 and 100 W. The ratio of Zn^{2+}/Zn^0 is about 1.4 and 0.6 for the films obtained at 0 and 100 W, respectively. It implies that the overall reaction, oxidation of Zn with different rf power is similar, though, the ratio of Zn species could be controlled by changing the annealing temperature. And the films deposited at low rf power of Ga_2O_3 target is easily oxidized from metallic Zn to Zn^{2+} cation.

Deconvoluted high resolution Sn $3d_{5/2}$ spectra are shown in Fig. 7.9 and the spectra show the decrease of total peak intensity with increasing the post-annealing temperature. To clarify, the atomic ratio of Sn in the surface region of GZTO thin films was calculated and the values are 25.3, 19.8, and 13.7 for 0 W, 30.5, 25.3, and 12.8 for 100 W post-annealed at as-dep., 573, and 673K, respectively. It indicated that Sn atom could be diffused into bulk by post-annealing process. And the conversion of oxidation state of Sn was observed as well. Comparing the Fig. 7.9 (a) and (b), GZTO thin films without annealing process showed similar peak profile. After treated the post-annealing process, the oxidation of Sn was not severe at 100 W but it is well observed from the GZTO films at 0 W post-annealed at 573K. The ratio of Sn^{4+} of the GZTO film obtained at 100 W followed by post-annealing at

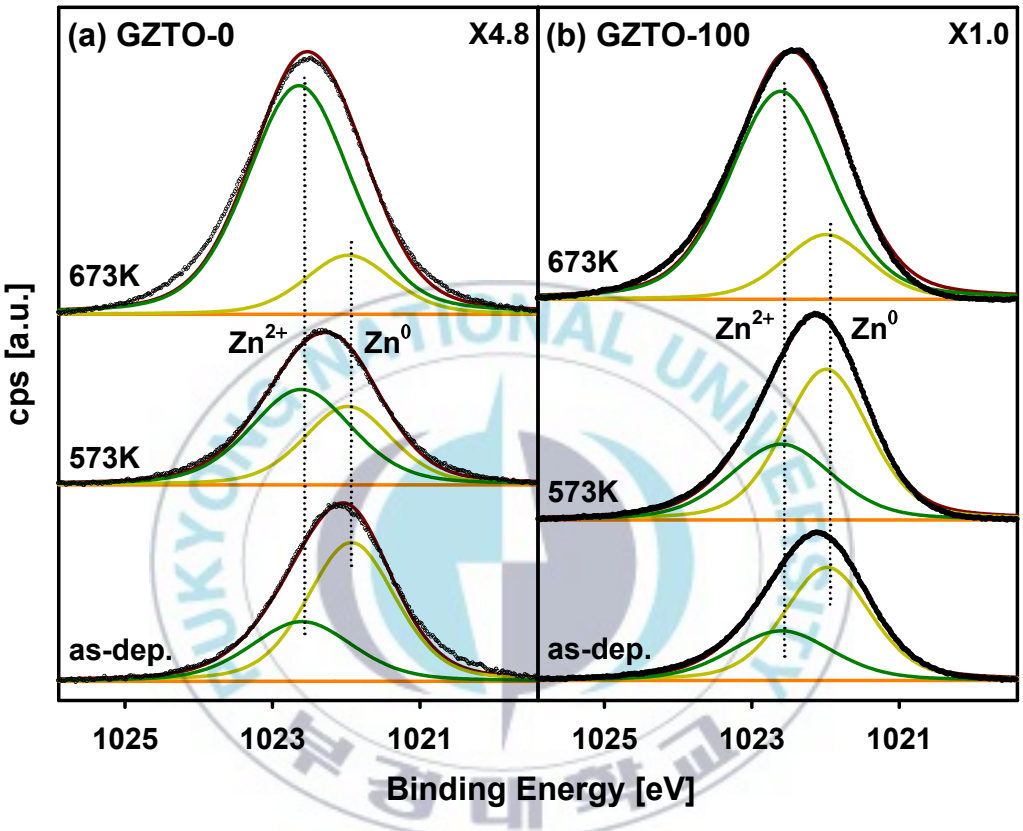

Fig. 7.8 High resolution XPS spectra of Zn $2p_{3/2}$ region. Post-annealing effect on GZTO thin films obtained at (a) 0 W and (b) 100 W of rf power for Ga_2O_3 target.

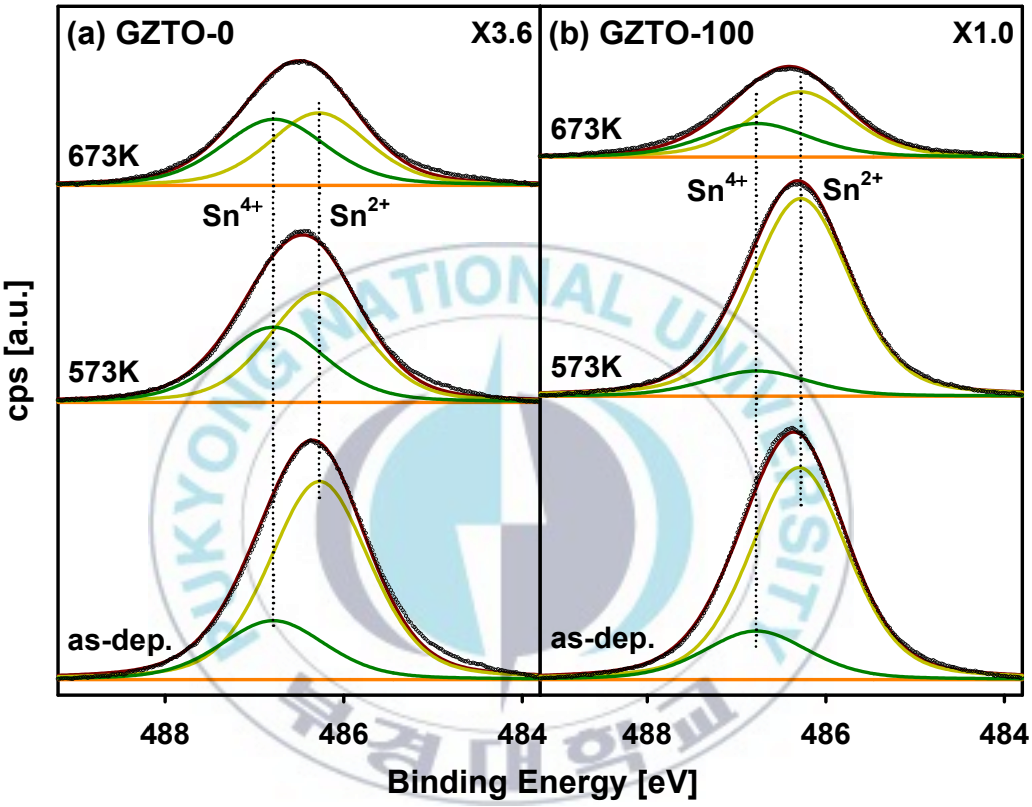

Fig. 7.9 High resolution XPS spectra of Sn $3d_{5/2}$ region. Post-annealing effect on GZTO thin films obtained at (a) 0 W and (b) 100 W of rf power for Ga_2O_3 target.

673K is lower than that at 0 W followed by post-annealing at 573K. It appears that the oxidation state of Sn is tuned by rf power and post-annealing temperature. From the results of deconvoluted XPS spectra of Ga, Zn, and Sn, the oxidation state of each atoms of GZTO thin films were altered by rf power and post-annealing process.

7.2.4 Conclusion

In summary, the effects of Ga concentration and post-annealing on the spectroscopic properties of a-GZTO films prepared by a co-sputtering method at room temperature were reported. Deconvoluted XPS spectra revealed that the carrier suppression effect of Ga ions was attributed to the decrease in oxygen vacancies along with the change of oxidation state of cations to higher species. And the post-annealing induced the transition to a higher oxidation state for each cation except for the GZTO films deposited at 100 W with post-annealing and the surface enrichment in Zn and the diffusion of Sn into bulk was occurred by post-annealing. This work suggests that a good controllability of carrier concentration and surface composition can be obtained by adjusting Ga concentration in a GZTO film, being one of promising In-free amorphous oxide semiconductors.

7.3 SnO_2:F Films

7.3.1 Introduction

Transparent conducting oxides (TCOs) are widely used materials in the industrial fields, such as low emissivity windows, electrochromic devices, gas sensors, solar cells, back contact in dye-sensitized solar cells (DSSCs), and displays [7.22-7.24]. From the introduction of CdO, tin-doped indium oxide (ITO) is one of the most important materials in TCOs. ITO has suitable characteristics for applications such as gas sensors, hole injection electrodes in polymer LEDs, front electrodes in Si solar cells, and anodes in OLED [7.25,7.26]. It is known to present a low resistance, possibility of production at low temperature, and good performance after etching process [7.27]. Despite of these benefits, it is difficult to apply ITO in DSSCs and other fields due to low chemical and mechanical durability and low thermal stability at the temperature over 500°C. To overcome these disadvantages, fluorine-doped tin oxide (FTO) is developed. Sn oxide is a semiconductor with 3.6 eV for optical band gap and rutile structure. The unit cell of Sn oxide is composed with two Sn atoms and four O atoms. While Sn oxide is transparent, the conductivity is low at room temperature. However, the conductivity of Sn oxide can be increased by dopants. In FTO, fluorine is substituted to O site and fluorine acts as an electron donor in FTO system. It is contributed to increase the carrier concentration and conductivity. Moreover, hydrogen impurities in thin films can be good attempt to increase conductivity [7.28].

Dopant, hydrogen in In_2O_3 films is located at interstitial and substitutional site and hydrogen is considered to be donors in In_2O_3 films [7.29]. And in relation to the application of solar cell, FTO films exposed to H_2 plasma is applied to tune the optical and electrical properties [7.30]. FTO is presented a highly thermal and chemical stability and good adhesive property onto glass. In this research, the intense study about the effect of H_2 plasma treatment on the FTO thin films was carried out.

7.3.2 Experimental

The commercial FTO coated soda-limed glass with a sheet resistance of 6-8 Ω/sq. (Pilkington, Ltd) was used as substrate. H_2 plasma treatment was performed on the FTO thin films in a capacitively coupled plasma chamber. Before introducing the FTO thin films in the chamber, FTO thin films were cleaned by ultrasonication with acetone and isopropyl alcohol for 10 min each and then blew with nitrogen gas. The base pressure of the chamber was lower than 1.3×10^{-4} Pa and the working pressure was about 80 Pa controlled by throttle valve with 150 sccm of flow rate of hydrogen gas. The H_2 plasma treatment was carried out 100 W of radio frequency power, 100°C for substrate temperature and performed for various treatment time in the rage of 0-60 min. The sample notation in this study, FTO-60 means that FTO films were treated with H_2 plasma for 60 min. The chemical environment of FTO thin films was investigated with X-ray photoelectron spectroscopy (XPS, VG, MultiLab 2000, UK). The XPS chamber was

equipped with a dual anode X-ray source and concentric hemispherical electron energy analyzer. In this study, Al Kα radiation (1486.6 eV) and constant analyzer energy (CAE) mode was used to obtain the XPS spectra. The deconvolution process was performed to calculate the atomic ratio of each element and to verify the oxidation state of the elements in the surface of FTO thin films.

7.3.3 Results and Discussion

In order to verify the kinds of atoms on the surface of FTO films, those were investigated by XPS and the purity of FTO films were checked by survey spectra as shown in Fig. 7.10. The characteristic XPS peaks of Sn, O, and C atoms were detected from the films without H_2 plasma treatment and other atoms were not observed from all films. After H_2 plasma treatment, the intensity of Sn 3d and C 1s was decreased and that of O 1s was gradually increased. Interestingly, the F 1s peak was appeared at FTO-60. In previous research about FTO films using XPS, the F 1s peak was detected in FTO films deposited by dc sputtering and chemical vapor deposition while that was screened with the background noise in FTO films synthesized by chemical spray pyrolysis [7.31]. Martínez *et al*. reported that the films with higher F/Sn ratio than 2% in starting solution showed the F 1s peak [7.31]. However, the atomic ratio in the surface of FTO films did not presented. The atomic ratio was calculated by peak intensities and atomic sensitivity factors of F 1s (1.0) and Sn $3d_{5/2}$ (3.2) and the F/Sn ratio is 0.3 in FTO-60.

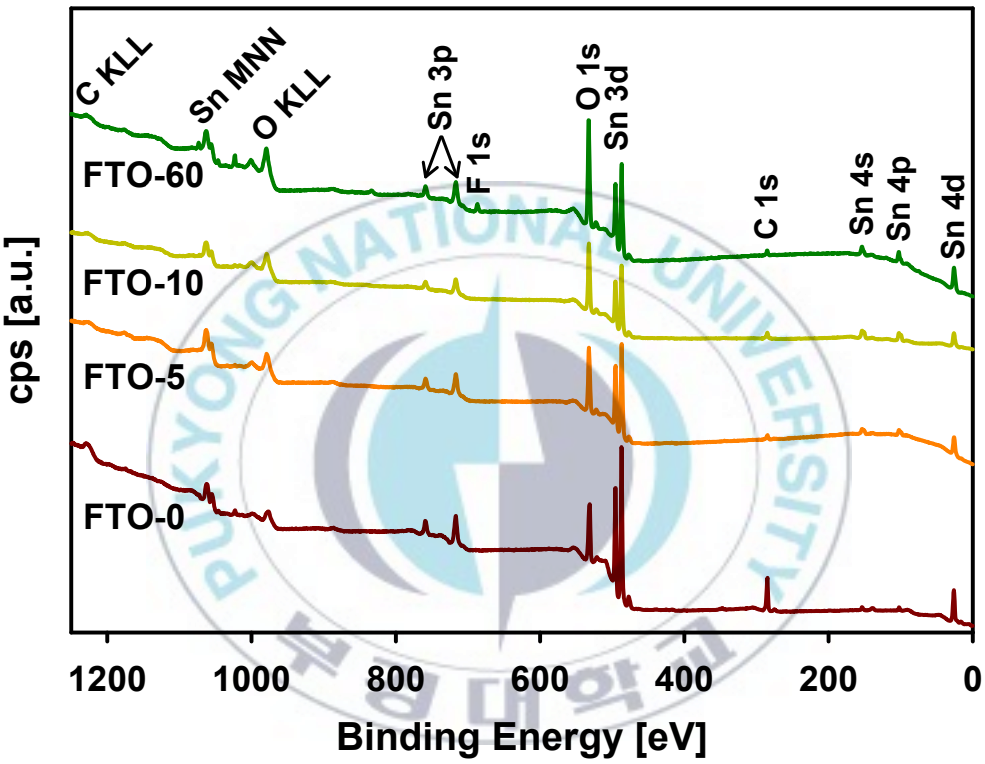

Fig. 7.10 Survey XPS spectra of FTO films.

In order to clarify the chemical environment of FTO films, such as oxidation state of surface atoms in FTO films with different time of H_2 plasma treatment, high resolution XPS spectra of Sn 3d were taken and shown in Fig. 7.11 (a). As shown in Fig 7.11 (a), the sharp doublet peak was observed in FTO-0. However, the shoulder peak at low binding energy region is grown with H_2 plasma treatment and it is clearly confirmed in FTO-60. Due to the large spin orbit splitting constant for Sn 3d (8.5 eV), Sn $3d_{5/2}$ was deconvoluted to obtain the specific information of the FTO films with a Shirley background. After peak deconvolution process, two oxidation states for Sn (Sn^0: 484.8±0.1, $Sn^{2+ \text{ and/or } 4+}$: 486.7±0.2 eV) were assigned [7.14]. As mentioned above, the high oxidation states of Sn decreased and the metallic state, Sn^0, evolved as the film of H_2 plasma treatment increased. Thus the reduction of FTO films by H_2 plasma treatment was confirmed and this phenomenon is coincident with other results [7.30].

Fig 7.12 (a) and (b) show the high resolution XPS spectra of O 1s and deconvoluted XPS spectra, respectively. The peak profiles of FTO films without and with H_2 plasma treatment is definitely different. The binding energy of peak maximum is shifted from low to high energy as the time of H_2 plasma treatment increased, it indicated that the spectra contain at least two peaks coming from two different chemical species. For accurate analysis, deconvolution process was performed and two peaks, O-Def. and O-Met. were assigned to 530. 8 and 532.3 eV, respectively [7.14]. From the result, the ratio of O-Met. (oxygen species bound with metal, Sn) was consistently

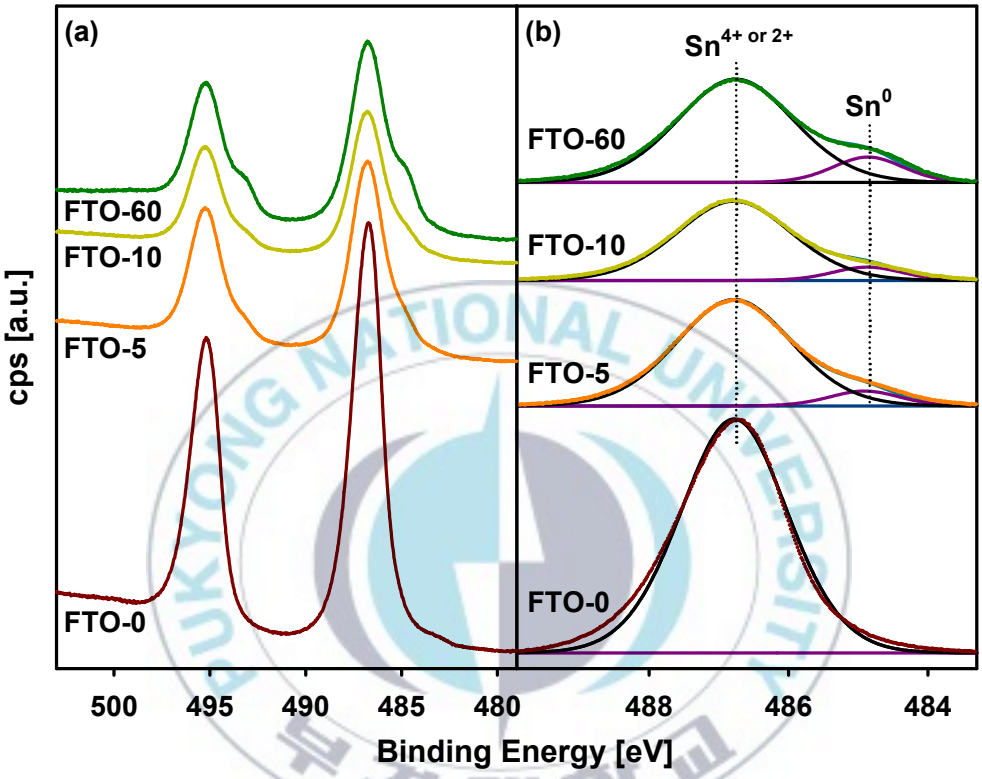

Fig. 7.11 High resolution and deconvoluted XPS spectra of Sn $3d_{5/2}$ region (a) and (b), respectively. The dotted vertical lines are inserted to clarify the peak maximum.

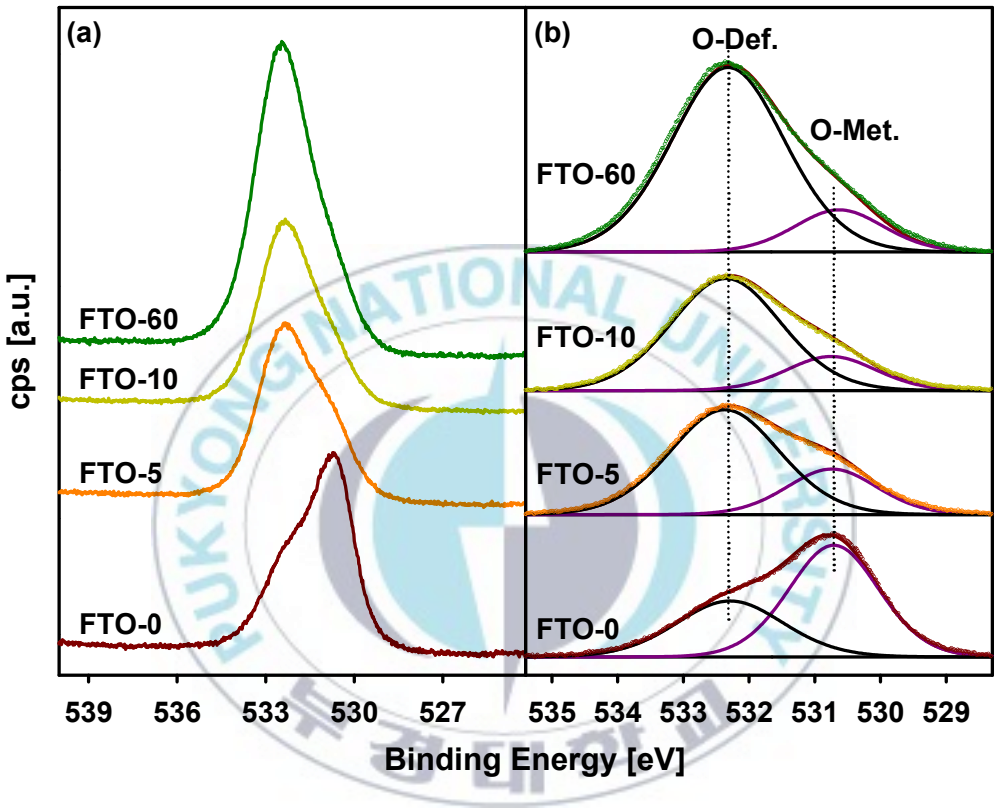

Fig. 7.12 High resolution and deconvoluted XPS spectra of O 1s region in (a) and (b), respectively.

decreased from 100 to 87% while that of O-Def. (oxygen ions in the oxygen deficient region) was increased along with the time of H_2 plasma treatment. It is well matched with the result of Sn 3d spectra.

7.3.4 Conclusion

The change in characteristic properties of FTO films by the exposure to H_2 plasma was investigated by XPS technique. XPS analysis revealed that the portion of Sn with high oxidation state decreased while that with low oxidation state, metallic Sn, increased as a function of the time of H_2 plasma treatment. Furthermore, the ratio of oxygen bound with Sn was decreased. The chemical reduction of FTO films was successfully accomplished by H_2 plasma treatment.

7.4 PEDOT:PSS Films

7.4.1 Introduction

The organic optoelectronic devices such as display, sensors, and solar cells have been interested in recent decades, especially the demand of flexible devices are gradually increased. Indium tin oxide (ITO) with good electrical and optical properties is the most commonly used material in organic optoelectronic devices. However, the application of ITO in flexible devices such as electronic papers and wearable electronic devices is difficult to prevent cracks under internal and external force [7.32-7.35]. Thus, other materials such as graphenes [7.36], carbon nanotubes [7.37], and metal nanowires [7.38-7.41] are developed. One of the promising candidates is poly(3,4-ethylenedioxythiophene) (PEDOT) which is highly conductive polymer with high work function in the range between 4.7 and 5.1 eV, high transparency in visible light region, and excellent chemical stability. The use of PEDOT as a solution phase is limited, because PEDOT is insoluble in most solvents, except for poly(styrenesulfonate) (PSS). However, doping of PSS in PEDOT causes the dramatically decrease in their conductivity below 1 S/cm, which is lower than that of ITO. Therefore, many researchers were focused to increase the conductivity of PEDOT:PSS. Addition of secondary doping solvent and dipping process are well-known methods for the purpose. First, addition of secondary doping solvent, such as sorbitol [7.42-7.44], dimethyl sulfoxide (DMSO) [7.45-7.47], and N,N-dimethylformamide [7.48] is interrupted

between PEDOT and PSS by screening effect [7.45] or changed PEDOT chains [7.49,7.50]. Second, dipping process is more effective than doping process and its mechanism is dissolving the PSS phase. In chapter 7.4.3.1, dynamic etching process is introduced for removal of PSS phase. Although dynamic etching is similar to dipping process, it is much simpler and less destructive to improve the conductivity of PEDOT:PSS. Therefore, PEDOT:PSS films without any chemical treatment, PEDOT:PSS films doped with DMSO, PEDOT:PSS films with dipping process, and PEDOT:PSS films with dynamic etching process were prepared and analyzed by XPS. For more enhancement in the conductivity of PEDOT:PSS, instead of elimination of PSS in surface region, the segregation of PEDOT and PSS phases was attempted by external force, electric field. The phenomena from this method are alignment of PSS phases in the surface region of PEDOT:PSS films. And then, the removal of PSS phase using dipping or etching process can be increase the conductivity of PEDOT:PSS because the PSS is insulating material. The effect of electric field on PEDOT:PSS films was investigated by checking the ratio of chemical composition of PEDOT and PSS and the results are described in chapter 7.4.3.2.

7.4.2 Experimental

PEDOT:PSS films deposited on glass and Si substrate were obtained by spin coating technique in ambient air condition. The glass and Si substrates were treated with oxygen and ozone plasma for 10 and 20 min,

respectively. Clevios PH 1000 (PEDOT:PSS=1:2.5 wt%), one of commercial PEDOT:PSS series was obtained from Aldrich company. PEDOT:PSS films with the thickness about 90 nm was formed with spin speed of 2000 rpm and spinning time of 40 sec. And then PEDOT:PSS films were annealed at 180°C for 10 min. To confirm the effect of dynamic etching process, four samples with different environment were prepared. PH 1000 without any chemical treatment, PH 1000 doped with DMSO solvent, PH 1000 dipping in DMSO solvent, and PH 1000 with dynamic etching process using DMSO solvent. DMSO (5 wt%) in PH 1000 solution was used to doped sample. For dipping sample, films coated with PH 1000 were dipped into DMSO solvent for 30 min and annealed. For the dynamic etching sample, 1 ml of DMSO solvent was consecutively dropped on PEDOT:PSS films during spinning process and then annealed.

For study of the effect of electric field on PEDOT:PSS films, the positive voltage was applied on the top of films and the bottom was grounded. The electric field was varied in the range from 0 to 5 kV, the distance between top and bottom was 5 mm, and the operating time was 20 min. The chemical composition in the surface and bulk PEDOT:PSS films was monitored by X-ray photoelectron spectroscopy.

7.4.3 Results and Discussion

7.4.3.1 Dynamic Etching

Fig. 7.13 shows high resolution S 2p XPS spectra. Two peaks were observed and the peak with lower binding energy increased at dipping and etching process. In PEDOT:PSS system, three S species, $PSS^- H^+$, $PSS^- Na^+$, and PEDOT were existed and deconvoluted S 2p spectra were shown in Fig 7.13 (b). Even though S 2p peak has 1.18 eV of SOS, S 2p doublet peak with high full width at half maximum (FWHM) seems to singlet peak. As mentioned above, three peaks were assigned to PEDOT (164.13±0.04 eV), $PSS^- Na^+$ (165.59±0.08 eV), and $PSS^- H^+$ (168.24±0.10 eV). The relative ratio of sulfur was listed in Table 7.5. The ratio of PEDOT was increased with introducing DMSO. Among three samples, the ratio of PEDOT is the highest in PEDOT:PSS films at etching process.

7.4.3.2 Electric Field

Fig. 7.14 shows the high resolution S 2p XPS spectra taken from PEDOT:PSS films after applying 0 and 3 kV of electric field. The bottom spectra were obtained without Ar^+ sputtering, which showed represent similar peak profile both 0 and 3 kV. It means that the topmost surface in PEDOT:PSS films is independent on the electric field. As the sputtering time increased, the peak of PEDOT region increased and that of PSS region decreased. The intensities of two peaks are almost same until 86.5 min of

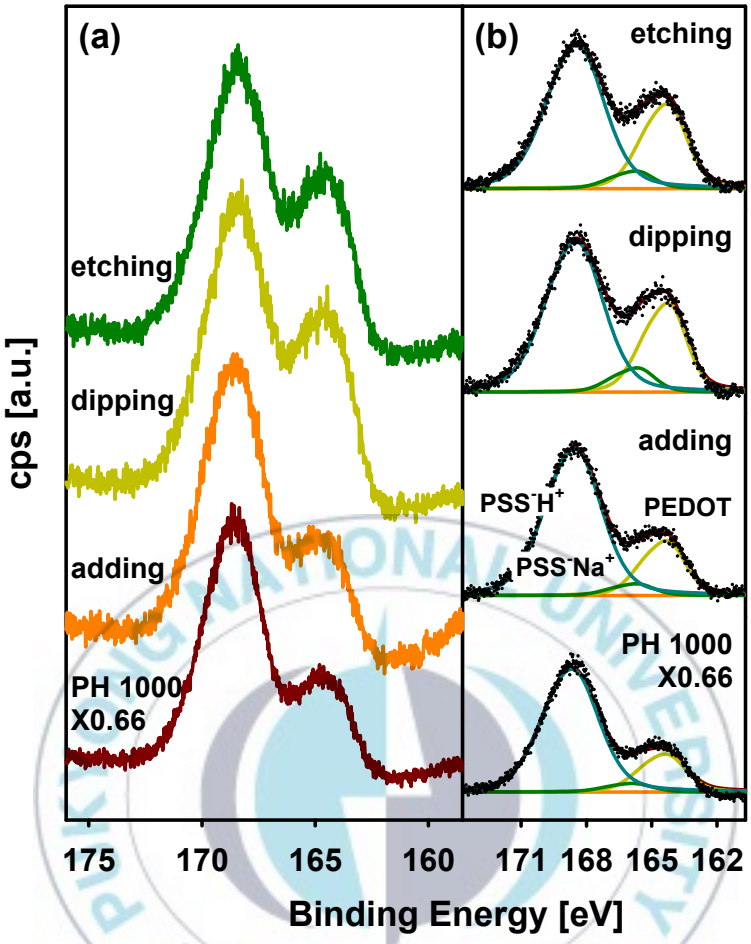

Fig. 7.13 (a) High resolution S 2p XPS spectra. (b) Deconvoluted high resolution S 2p XPS spectra of PH 1000 with different environment. The peak with lower binding energy represents PEDOT, peak with middle binding energy represents PSS^{-} Na^{+}, and peak with higher binding energy represents PSS^{-} H^{+}.

Table 7.5 Relative atomic percentage of various species of sulfur in PH 1000 with different environment.

Sample	PSS^{-} H^{+}	PSS^{-} Na^{+}	PEDOT
PH1000	76.7	4.2	19.1
adding DMSO	74.3	4.4	21.3
dipping DMSO	64.2	7.4	28.4
etching DMSO	64.7	5.8	29.5

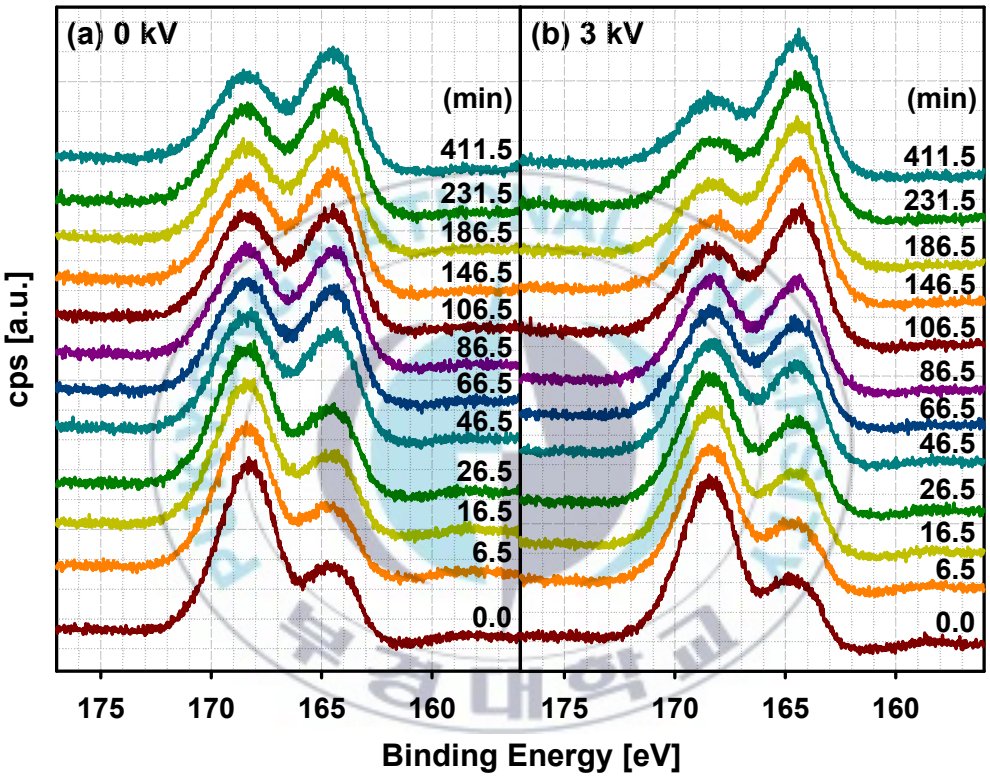

Fig. 7.14 High resolution S 2p XPS spectra for 0 kV (a) and 3 kV (b). The numbers in right side mean the sputtering time.

sputtering time and then that of PEDOT region is stronger than that of PSS region. The degree of increase of intensity of PEDOT region at 3 kV is higher than 0 kV.

To obtain the more information, deconvolution process was performed and representative deconvolution spectra are shown in Fig. 7.15. After deconvolution process, the relative percentage of PEDOT and PSS was calculated and the result is shown in Fig. 7.16. The decrease in the percentage of PSS is observed, however, the tendency is rapidly occurred in PEDOT:PSS film at 3 kV. Especially, after 100 min of Ar^+ sputtering, the percentage of PEDOT is higher than that of PSS at 3 kV.

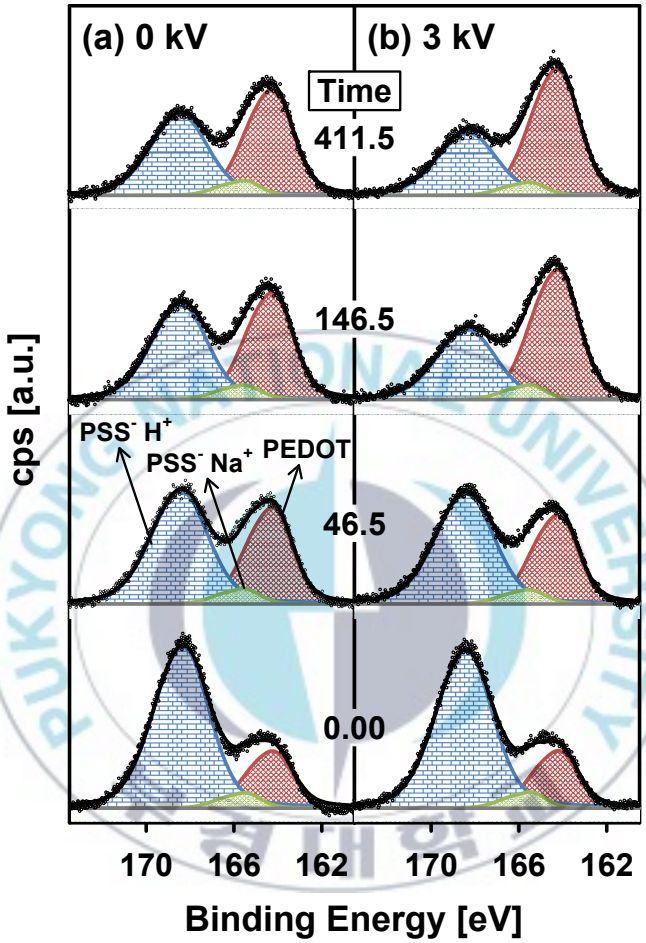

Fig. 7.15 Representative deconvoluted S 2p XPS spectra for 0 kV (a) and 3 kV (b). The peaks with diagonal cross (red), dots (green), and bricks (blue) are assigned to PEDOT, PSS^{-} Na^{+}, and PSS^{-} H^{+}, respectively. The numbers in middle of the figure indicate the sputtering time in minute.

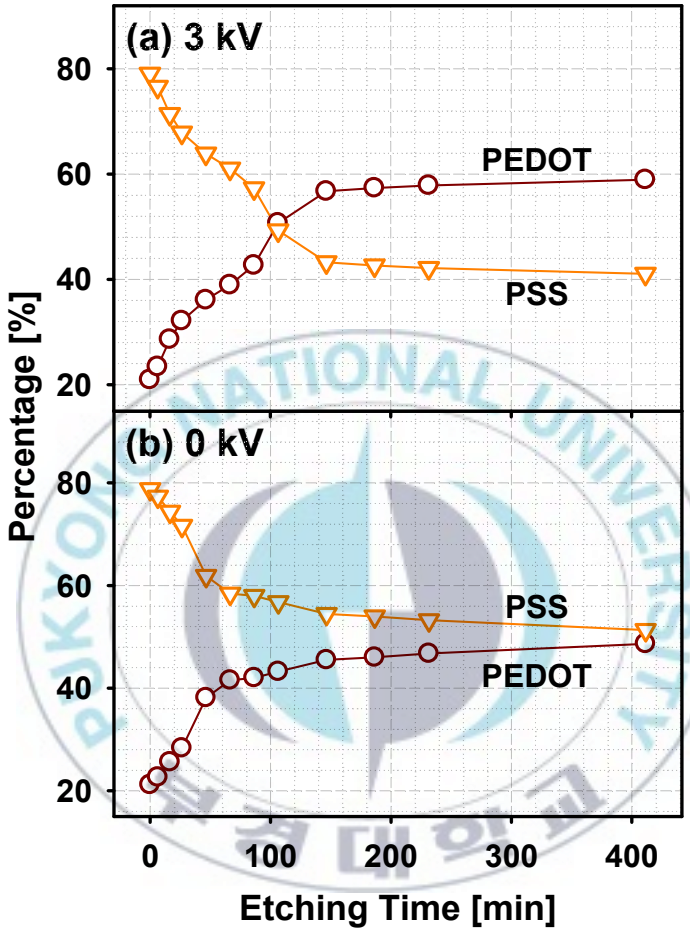

Fig. 7.16 Relative percentage of PEDOT and PSS in PEDOT:PSS films.

7.4.4 Conclusion

To apply PEDOT:PSS films in flexible devices, PEDOT:PSS films with high conductivity is required. Because the conductivity of PSS is extremely lower than PEDOT, the removal of PSS is crucial concern to many researchers. In this chapter, dynamic etching and electric field process was introduced to improve the conductivity of PEDOT:PSS films. The effect of two processes on PEDOT:PSS films was confirmed by XPS. High resolution S 2p spectra was used to distinguish the PEDOT and PSS phase and the relative ratio was calculated from the results of deconvolution of S 2p spectra. It revealed that the PEDOT phase increased after dynamic etching and applying electric filed.

7.5 Mo Oxide Thin Films

7.5.1 Introduction

Hydrogenated amorphous Si (a-Si:H) thin film solar cells are promising photovoltaic devices due to its abundance, low cost and production temperature, and feasibility of deposition on flexible substrates like plastic and stainless steel foil. Among the a-Si solar cells, p type-intrinsic-n type (p-i-n) structure is commonly adapted to construct the device having high efficiency. The results about the increase of the conductivity of a-Si were reported by Spear and Lecomber in 1975 [7.51]. They reported that mixture of some gases, such as diborane (B_2H_6) and phosphine (PH_3), were used for fabrication of p and n layers. However, these gases are toxic and need much care. These disadvantages lead to increase of the production cost. There are efforts to replace the harmful gases and to cut the cost for fabrication of devices. Many researchers reported the substitute materials, for example, a C_{60} derivative for n type a-Si:H layer [7.52]. And poly(styrenesulfonate)-doped poly(3,4-ethylene dioxythiophene) (PEDOT:PSS) [7.53] and metal oxides, for examples, tungsten oxide [7.54], vanadium oxide [7.55], molybdenum oxide (MoO_x) [7.56], and nickel oxide [7.57], are reported as p type a-Si:H layer and n type. Among them, MoO_x is an attractive material in various optoelectronic devices. It has wide optical band gap of 3.2 eV, excellent electrical conductivity, and high work function in the range of 5.8-6.9 eV. Thus, MoO_x is appropriated to use as a p type a-Si:H layer. In this study,

MoO_x thin films were fabricated by thermal evaporation and sputtering method and the chemical environment of the obtained MoO_x films was investigated with XPS.

7.5.2 Experimental

Two types MoO_x thin films were fabricated on the commercially available FTO glass substrates (Pilkington) by means of two different deposition methods. The FTO glass has a sheet resistance of about 7 Ω/sq and was cleaned twice by ultrasonication for 10 min with acetone and isopropyl alcohol and then dried with nitrogen gas. The prepared substrates were introduced into the thermal evaporation or sputtering chamber. The MoO_x thin films were deposited by thermal evaporation in high vacuum chamber with 2×10^{-6} Torr of base pressure. The sample obtained by thermal evaporation is denoted as T-MoO_x from here after and the deposition rate was achieved about 0.2 Å/s. The sample synthesized by sputtering, denoted as S-MoO_x, was obtained by a rf power of 50 W, Ar gas flow rate of 50 sccm, the working pressure of 5 mTorr, and the distance between the target and the substrate was 5 cm. The MoO_x deposition was performed without heat treatment.

7.5.3 Results and Discussion

MoO_x thin films deposited by using the different methods were characterized by XPS and high resolution XPS spectra of Mo 3d and O 1s

were observed for detailed chemical information. Charge accumulating effects in all the XPS spectra were calibrated using the binding energy of aliphatic carbon at 284.6 eV. The more specific information, such as oxidation state of Mo and O atoms and atomic ratio of Mo and O was obtained from the result of deconvolution of XPS spectra as shown in Fig. 7.17. Fig. 7.17 (a) shows different peak profiles of Mo 3d spectra. Because of the interaction between electron spin angular momentum and orbital angular momentum, Mo 3d spectra show doublet peak with spin orbit splitting constant of 3.12 eV. The bottom spectrum collected from T-MoO_x shows relatively well-defined doublet peak while the top spectrum from S-MoO_x is ill-defined. Kim *et al.* reported three Mo species with different oxidation states that three peaks positioned at 232.7, 232.0, and 230.5 eV in S-MoO_x are assigned to Mo^{6+}, Mo^{5+}, and Mo^{4+}, respectively [7.58,7.59]. After deconvolution process, Mo 3d spectrum from T-MoO_x is decomposed to two peaks, Mo^{6+} and Mo^{5+} in this study. Interestingly, the lower oxidation state of Mo was evolved from the S-MoO_x films obtained by sputtering method and the ratio of Mo^{6+} species decreased from 87.6 to 40.9%. Thus, the sputtering method was not sufficient to synthesize the fully oxidized metal oxide films, MoO_3 films in this study, comparing the MoO_x films obtained by thermal evaporation method. However, it is worthy to note that the residual oxygen in both chambers was only the source to form Mo oxide films. Fig. 7. 17 (b) shows the deconvoluted high resolution XPS spectra of O 1s region. Similarly, two and three oxygen species except for surface oxygen were

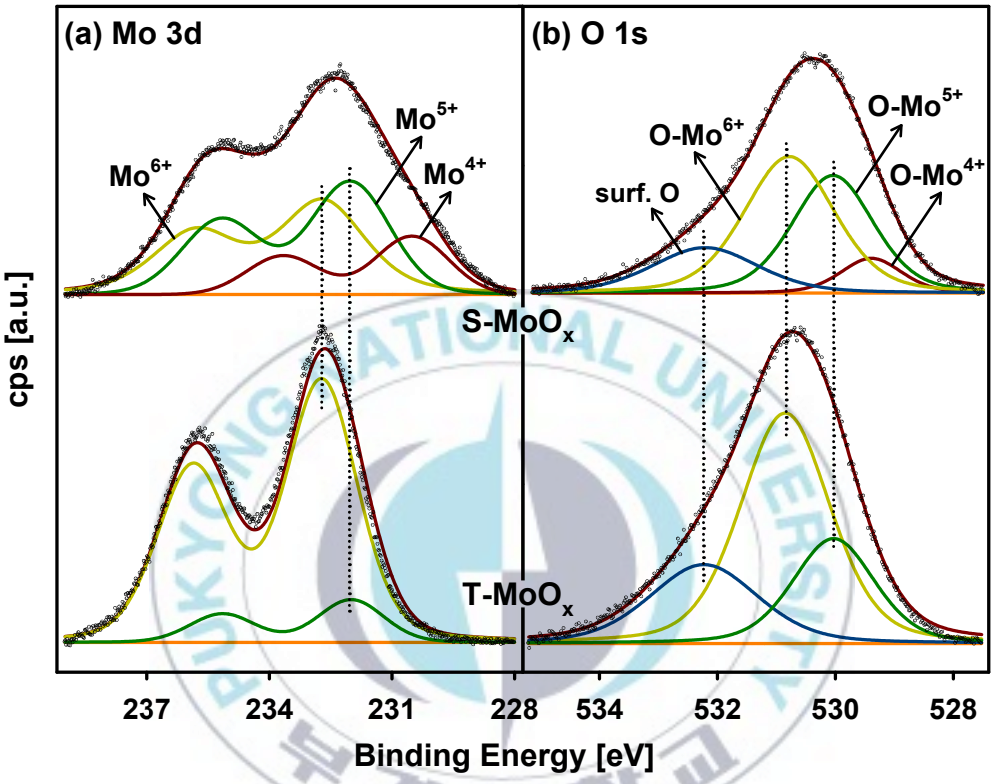

Fig. 7.17 Deconvoluted high resolution XPS spectra of Mo 3d (a) and O 1s (b). Bottom and top spectra were obtained from T-MoO_x and S-MoO_x, respectively.

existed in the T-MoO_x and S-MoO_x films, respectively. These peaks are corresponded to the oxygen bonded with Mo, 530.8, 530.1, and 529.4 eV for O-Mo^{6+}, O-Mo^{5+}, and O-Mo^{4+}, respectively. As shown in Table 7.6, the ratio of oxygen bonded with lower oxidation states of Mo is higher in S-MoO_x than that in T-MoO_x films. It is coincident with the result of Mo 3d spectra. From the deconvolution of XPS spectra, we can deduce the stoichiometric ratio of Mo oxide. The areas of Mo 3d and O 1s, especially the area excluding the surface oxygen in O 1s spectra, and their atomic sensitivity factors (ASFs) were used to deduce the concrete chemical formulas of the two types of MoO_x films. The areas of Mo and O are listed in Table 7.6 and the ASFs of Mo $3d_{5/2}$ and O 1s are 1.2 and 0.63 [7.60]. The calculated atomic ratio factors, x, are 2.95 and 2.43 for thermally evaporated and sputtered MoO_x films, respectively. As mentioned above, the stoichiometry of T-MoO_x is closer to MoO_3 than that of S-MoO_x.

Table 7.6 The area and relative atomic ratio of each species were calculated from the deconvoluted high resolution XPS spectra of Mo 3d and O 1s.

Mo 3d		T-MoOx	S-MoOx
Mo^{4+}	area	-	4353.219
	ratio	-	18.6
Mo^{5+}	area	3005.067	9459.184
	ratio	12.4	40.5
Mo^{6+}	area	21202.99	9552.306
	ratio	87.6	40.9
O 1s		T-MoOx	S-MoOx
$O\text{-}Mo^{4+}$	area	-	1621.134
	ratio	-	7.4
$O\text{-}Mo^{5+}$	area	6527.307	7273.169
	ratio	22.7	33.1
$O\text{-}Mo^{6+}$	area	15747.24	9379.857
	ratio	54.7	42.7
Surf. O	area	6508.026	3677.689
	ratio	22.6	16.8

7.5.4 Conclusion

The effect of variation of deposition methods on the surface chemistry of MoO_x thin films was investigated by XPS technique to apply p type layer in high-performance dopant-free solar cells. Mo 3d and O 1s spectra showed different peak profiles of MoO_x films obtained by thermal evaporation and rf sputtering method. From the results of deconvolution of Mo 3d and O 1s, we could confirm that Mo atoms are more oxidized in MoO_x films synthesized by thermal evaporation than that synthesized by rf sputtering method.

7.6 Tungsten Oxide Films

7.6.1 Introduction

SnO_2 is one of the semiconducting materials and it is applied as optical, electrical, and chemical devices [7.61-7.63]. To synthesize the SnO_2 nanowires, metal nanoparticles or films, catalysts, such as Au, Ni, and Cu, are needed [7.64-7.66]. However, these catalysts caused the unexpected effects by residues of metal. Thus, the self-catalytic growth [7.67,7.68] was developed to grow impurity free SnO_2 nanowires. In this study, WO_x thin films played a role of catalytic material for the growth of SnO_2 nanowires. Tungsten oxides (WO_x) are known as wide band gap semiconductor and used in electrochromic, photocatalyst, and active layer in gas sensors [7.69,7.70]. WO_x films are synthesized by various techniques, such as thermal oxidation, thermal evaporation, and chemical vapor deposition [7.69]. In a variety of WO_x films, most WO_x are non-stoichiometric with mixture of WO_3 and WO_y ($y<3$). The structural and electrical properties of WO_x are considerably affected by their chemical composition [7.69]. Thus the growth of SnO_2 can be affected by the quality of WO_x films, furthermore, SnO_2 devices can be also dependent on the WO_x substrate. Therefore the analysis of chemical composition in WO_x films deposited by rf sputtering were performed by X-ray photoelectron spectroscopy in this study.

7.6.2 Experimental

WO_x thin films were deposited on substrates by rf magnetron sputtering. The substrates were SiO_2 layers with thickness of 300 nm thermally coated on the p-type Si(100). During the deposition of WO_x thin films, the substrate temperature was kept at room temperature. The rf power was 50 W and Ar gas was used with a flow rate of 50 sccm and working pressure of 50 mTorr. The deposited films were analyzed by X-ray photoelectron spectroscopy (XPS) to verify the chemical composition of WO_x thin films. The XPS system was evacuated to ultrahigh vacuum with several pumps. And the X-ray source was Mg Kα (1253.6 eV) and the details are described in Chapter 2.1.

7.6.3 Results and Discussion

Fig. 7.18 (a) shows the survey XPS spectra for the WO_x thin films. The characteristic XPS peaks of W, O, C, and N atoms and the Auger lines of O atom represented as O KLL were detected. Because nitrogen did not deal with the deposition process, the peak of nitrogen could be arose from the impurity in the sputter chamber. To obtain the chemical information of WO_x thin films, high resolution XPS spectra in the binding energy regions of W 4f and O 1s were observed as shown in Fig. 7.18 (b) and (c), respectively. Although the W 4f spectra have doublet peak with spin orbit splitting energy of 2.15 eV, three peaks were detected. Thus, at least two oxidation states of W are existed in the surface of WO_x thin films. After deconvolution process,

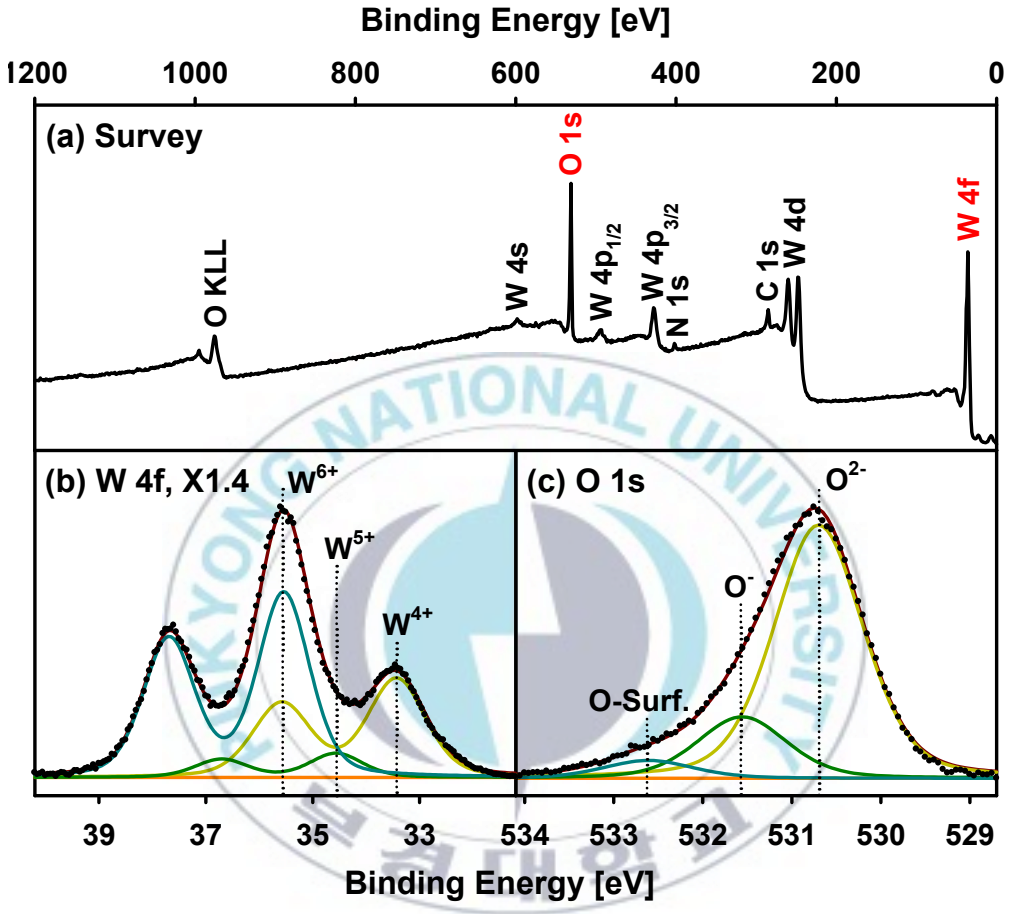

Fig. 7.18 Survey XPS spectra (a) and high resolution XPS spectra of W 4f (b) and O 1s (c). The inserted lines are indicated the binding energy of each peak maximum.

W 4f spectra were decomposed to three peaks, W^{4+} (33.43 eV), W^{5+} (34.56 eV), and W^{6+} (35.54 eV). The ratio of each peaks are 34.6, 7.7, and 57.7 % from low to high oxidation states of Mo. The deconvoluted XPS spectra of O 1s are revealed the existence of O with three different oxidation state. These peaks are corresponded to O^{2-} (530.70 eV), O^{-} (531.56 eV), and surface O (O-Surf., 532.61 eV). From the results of deconvolution, the chemical composition considering with peak area and atomic sensitivity factors for W 4f of 2.000 and O 1s of 0.640 was obtained as $WO_{2.74}$.

7.6.4 Conclusion

WO_x thin films were deposited on SiO_2 coated Si(100) substrate by rf magnetron sputtering. The chemical state of WO_x thin films were analyzed by X-ray photoelectron spectroscopy. Three species, W^{4+}, W^{5+}, and W^{6+} were detected in W 4f spectra and O^{2-}, O^{-}, and surface oxygen were observed in O 1s spectra. The chemical composition of WO_x thin films was calculated to x = 2.74.

7.7 $Ba_3P_4O_{13}$_Eu

7.7.1 Introduction

In the phosphorous materials, controlling the ratio of Eu^{2+} to Eu^{3+} is important to apply in industrial application. Most of studies about phosphorous materials have been focused on the photoluminescence properties, a few papers reported the oxidation state of Eu atom investigated by X-ray photoelectron spectroscopy (XPS) [7.71-7.73]. XPS is widely used technique to obtain the chemical information, such as, oxidation state of metal, surrounding environment of atoms, qualitative and relatively quantitative analysis of surface. In this research, XPS analysis of $Ba_3P_4O_{13}$_Eu samples were performed and obtained the relative ratio of Eu^{2+} with different Eu concentration in air condition.

7.7.2 Experimental

The chemical environment of $Ba_3P_4O_{13}$_Eu samples was analyzed by X-ray photoelectron spectroscopy (XPS, VG, ESCALAB MKII, UK) with a concentric hemispherical analyzer (CHA). The $Ba_3P_4O_{13}$_Eu samples were introduced into load-lock chamber and pumped with a rotary vane (RP) and a turbo molecular pump (TMP) during overnight. The purity of $Ba_3P_4O_{13}$_Eu was confirmed by survey scan with Al Kα X-ray source (1486.6 eV) with beam current of 20 mA, filament current of 5.2 A, high voltage of 9 kV,

energy step of 0.5 eV, dwell time of 100 ms, and channeltron voltage of 3100 V. The base pressure of XPS chamber was about 5.0×10^{-10} Torr and the working pressure was maintained below 5.0×10^{-9} Torr. High resolution XPS spectra were obtained at the step size of 0.02 eV and other parameters were consistent with those used for survey spectra. The obtained XPS spectra were deconvoluted using XPSPEAK program (ver. 4.1) and the ratio of Gaussian to Lorentzian function for each peak was set to 70 and 30%. The charge accumulation effect was eliminated by shift of spectra based on the result of deconvoluted C 1s spectra.

7.7.3 Results and Discussion

To identify the oxidation state of Ba, Eu, and P atoms, XPS technique was applied on $Ba_3P_4O_{13}$_Eu samples. Fig. 7.19 shows the deconvoluted high resolution XPS spectra of Ba 3d region with respect to Eu concentration. In this section, the sample notation A-0.02 means that the sample was synthesized with 0.02 mol% of Eu in air condition. The Ba 3d spectra showed that no significant difference in binding energy as well as intensity were observed with increasing Eu concentration. Ba 3d spectra were well consistent with 1 doublet peak with 15.4 eV of spin obit splitting (SOS) and it was assigned to Ba^{2+} (780.2±0.1 eV) [7.74,7.75]. It implies that Eu concentration did not affect on the chemical state of Ba atom. The highest peak intensity about Eu atom in the XPS spectra was Eu 3d region which is positioned at ~1136 eV for Eu $3d_{5/2}$ and ~1165 eV for Eu $3d_{3/2}$.

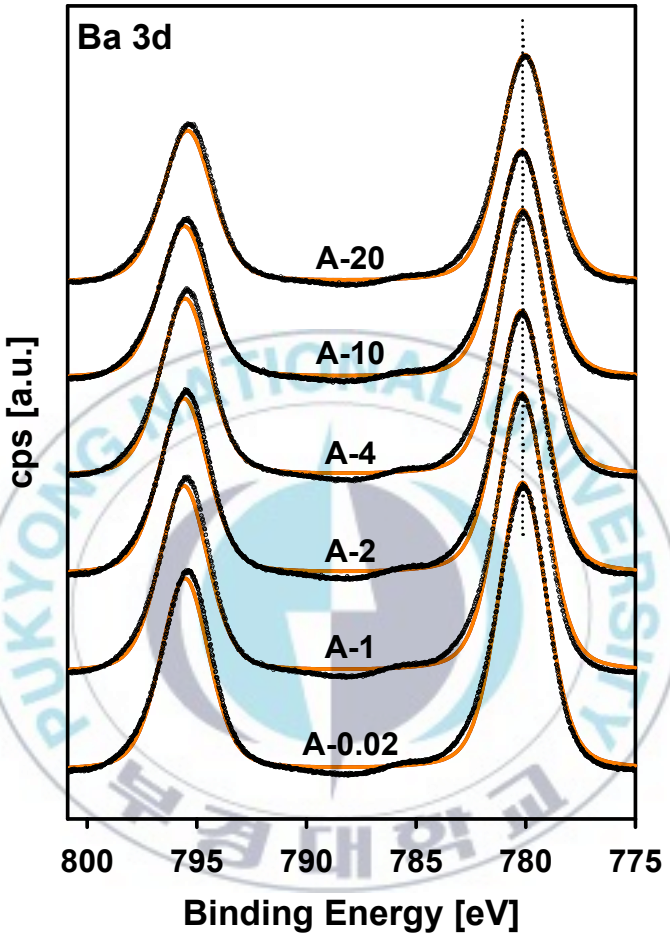

Fig. 7.19 High resolution XPS spectra of Ba 3d region with different Eu concentration. The dotted line is inserted to easily detect the peak position.

In $Ba_3P_4O_{13}$_Eu sample, the binding energy of Eu $3d_{5/2}$ was overlapped with that of Ba $3p_{1/2}$ at ~1137 eV. Thus, Lu *et al.* studied Eu 4d spectra instead of Eu 3d to identify the oxidation state of Eu atom in $Ba_{1-x}Eu_xTiO_3$ samples [7.71]. Unfortunately in our sample, the peak position of Eu 4d also approaches that of P 2p positioned at ~135 eV. Therefore, the analysis of Eu atom was conducted as the deconvolution of Eu $3d_{3/2}$ region. The high resolution XPS spectra of Ba $3p_{1/2}$ and Eu 3d region were shown in Fig. 7.20 (a). It indicates that the Eu $3d_{3/2}$ peak at ~1165 eV evolved after 1% of Eu concentration and gradually increased with increasing the Eu concentration. However, the peak at ~1155 eV appeared regardless of Eu concentration. The Eu $3d_{3/2}$ region without Ba effect was deconvoluted and representative spectra are shown in Fig. 7.20 (b). After the deconvolution process, we could mention that two Eu species with different oxidation states, Eu^{2+} (1155.3±0.1 eV) and Eu^{3+} (1164.4±0.1 eV), were detected from all samples [7.73]. When the Eu concentration increased, the intensity of Eu^{2+} was almost constant while that of Eu^{3+} gradually increased. The percentage of Eu species was deduced by deconvolution of Eu $3d_{3/2}$ and shown in Fig. 7.21. It clearly showed that the oxidation state of Eu changed with different Eu concentration. The calculated Eu^{2+} percentage is close to 70% for A-0.02 and then dramatically decreased to ~50% with increasing the Eu concentration. Finally Eu^{2+} percentage was reached to ~25% for A-20.

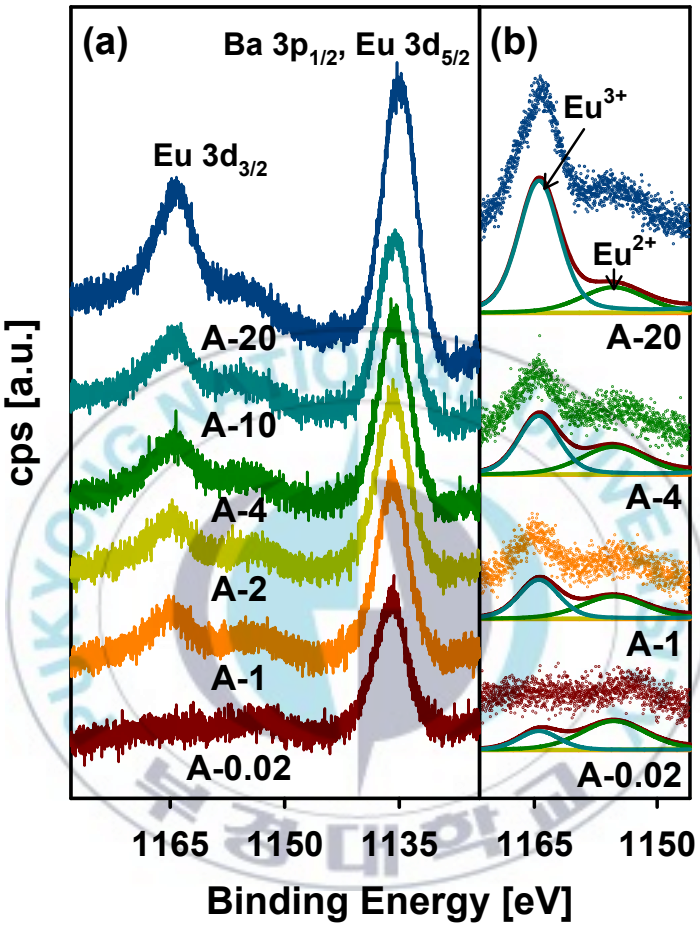

Fig. 7.20 (a) High resolution Ba $3p_{1/2}$ and Eu 3d XPS spectra (b) Deconvoluted high resolution Eu $3d_{3/2}$ XPS spectra.

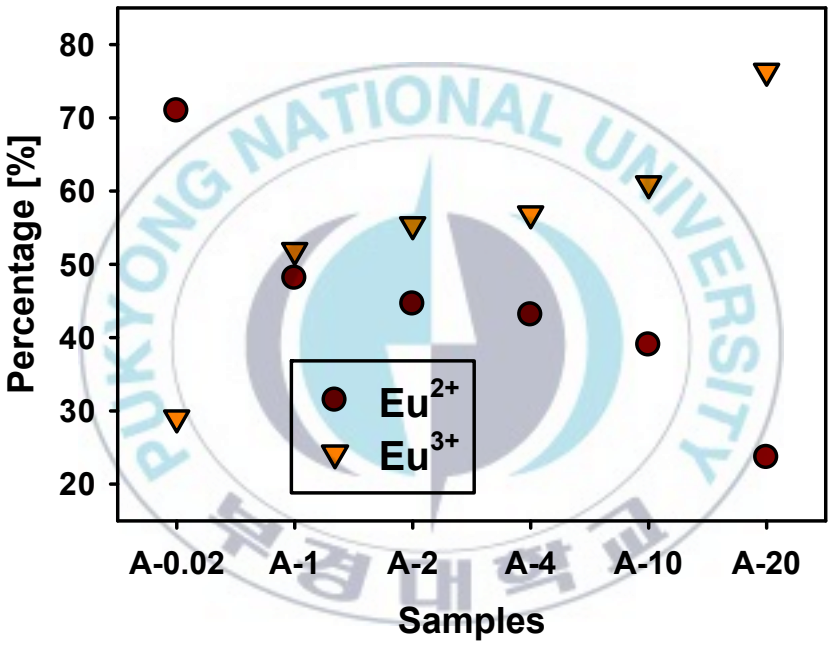

Fig. 7.21 Relative ratio of Eu species, Eu^{2+} and Eu^{3+} with different Eu concentration.

7.7.4 Conclusion

One of the phosphorous materials, $Ba_3P_4O_{13}$_Eu were synthesized and XPS studies was conducted. XPS analysis revealed that the mixture of Eu^{2+} and Eu^{3+} species are detected and the relative ratio of Eu^{2+} is gradually decreased with higher Eu concentration. The oxidation state of Ba did not affect by the concentration of Eu.

7.8 ZnO Thin Films

7.8.1 Introduction

ZnO is considered as a n-type semiconducting material with a direct wide band gap of 3.3 eV [7.76] which has a hexagonal wurtzite structure [7.77], a chemical stability, a superior electrical conductivity and transparency, and a large exciton binding energy of 60 meV [7.78]. From these properties, ZnO is used for an electron transfer layer (ETL) in organic solar cell [7.79]. In solar cell industry, energy band diagram of ZnO is crucial to increase in the efficiency of solar cell. If the conduction band minimum (CBM) of ETL is higher than that of active layer, energy barrier from active layer to ETL is occurred and the efficiency of solar cell becomes low. On the other hand it is relatively easy to synthesize ZnO with various shapes, such as nanoparticles (NPs) [7.77], nanorods (NRs) [7.80], and nanopencils [7.81]. The shape of ZnO can effect on the energy band alignment, such as CBM, valence band maximum (VBM), and Fermi level. In this chapter, two types of ZnO thin films consisted with NPs and NRs are prepared and the energy band diagram was estimated by applying several techniques.

7.8.2 Experimental

ZnO NPs and NRs are prepared by the method of Beek *et al.* [7.80]. Zinc acetate dihydrate (Sigma-Aldrich, 2.95 g, 13.4 mmol) and potassium

hydroxide (Sigma-Aldrich, 1.48 g, 23 mmol) were dissolved in 125 and 65 ml of methanol at 62°C and room temperature, respectively. Potassium hydroxide solution was added into zinc acetate solution for 10 min under stirring. The precipitation of zinc hydroxides is occurred, however it dissolved. After 5 min, the solution became slightly transparent. After 2 hrs, ZnO NPs precipitated and the solution became turbid. ZnO NPs were obtained by centrifugation and washed twice with methanol. To synthesize the ZnO thin films, ZnO NPs were dispersed in the mixed solvent consisting of 50 ml of chlorobenzene and 50 ml of isopropyl alcohol. Dispersed solution of ZnO NPs is almost transparent and stable for more than 6 months without any treatment. The synthesis of ZnO NRs was started at the end of the precipitation ZnO NPs. Instead of centrifugation, the solution was stirring until the volume was reduced to 1/10 and then heated for 4 hrs at 60°C. And the cleaning and dispersion process were performed as the same as ZnO NPs. Finally, ZnO NR solution was translucent and stable until two months. Before fabrication of ZnO thin films, ITO/glass substrates were ultrasonicated by several solvents: trichloroethylene, acetone, isopropyl alcohol, and distilled water for 10 min. And the substrates were blew by nitrogen. The ZnO NPs and NRs thin films were deposited by spin coating method under 1000 rpm for 30 sec. The deposited films were annealed with 150°C for 10 min in glove box.

The VBM spectra are analyzed by XPS (VG, ESCALab MKII, UK) with Mg Kα X-ray source. The X-ray source was operated with the high

voltage of 9 kV and the current of 20 mA. The spectra were collected with a pass energy of 50 eV and energy step of 0.02 eV in constant analyzer energy (CAE) mode. The UPS spectra are taken from He I source with a filament voltage of 0.54 kV and a filament current of 56 mA. During UPS experiment, the working pressure was maintained at about 1.1×10^{-7} Torr. To distinguish the peak between sample and detector, sample bias was applied to 7 V. The other parameters were the same as VBM spectra.

7.8.3 Results and Discussion

To obtain the energy band diagram, VBM and work function (WF) were obtained by XPS and UPS technique, respectively. Fig. 7.22 shows valence band spectra of Zn NPs and NRs. The charge accumulation on the sample was corrected by shifting to aliphatic carbon at 284.6 eV. The sharp peak at about 10 eV was assigned to Zn 3d spectra and the broad peak, density of state (DOS) from 7 to 3 eV was also observed from the samples. From the DOS, VBM was calculated [7.82-7.84]. The intersection point of two linear lines obtained by using a least square method is VBM and the values of VBM are 2.47 and 2.75 eV for ZnO NPs and NRs, respectively. Fig. 7.23 shows the UPS spectra of ZnO NPs and NRs. UPS spectra can plot two axes, binding energy and kinetic energy and UPS spectra in this figure presented the intensity versus kinetic energy. Thus the region at low kinetic energy possesses the information of secondary cutoff and that at high kinetic energy indicates Fermi level. The values of secondary cutoff and Fermi level were

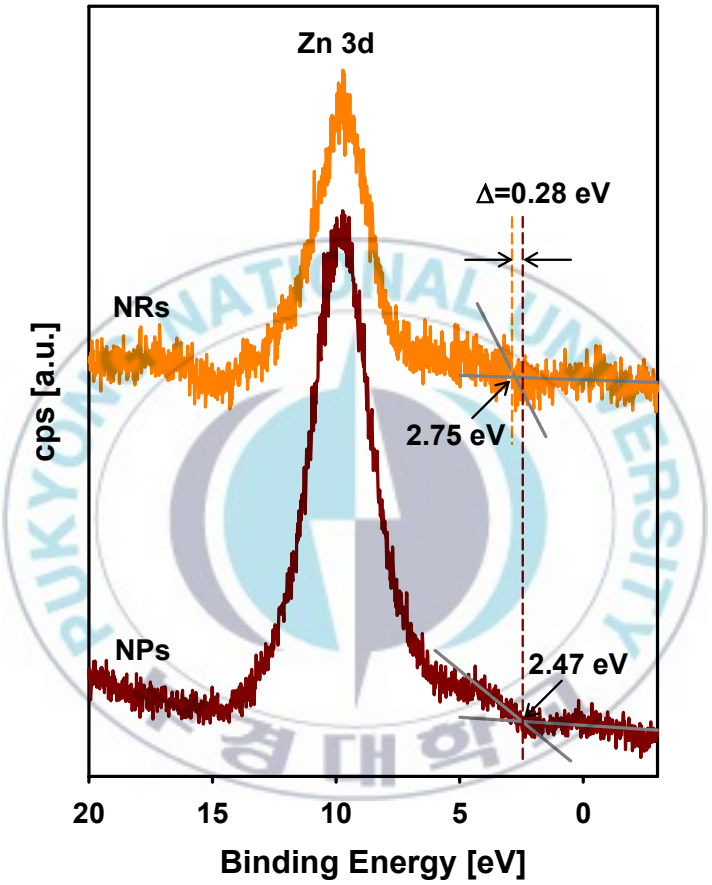

Fig. 7.22 Valence band spectra of ZnO NPs and NRs. Red and orange lines indicated the VBM of NPs and NRs, respectively.

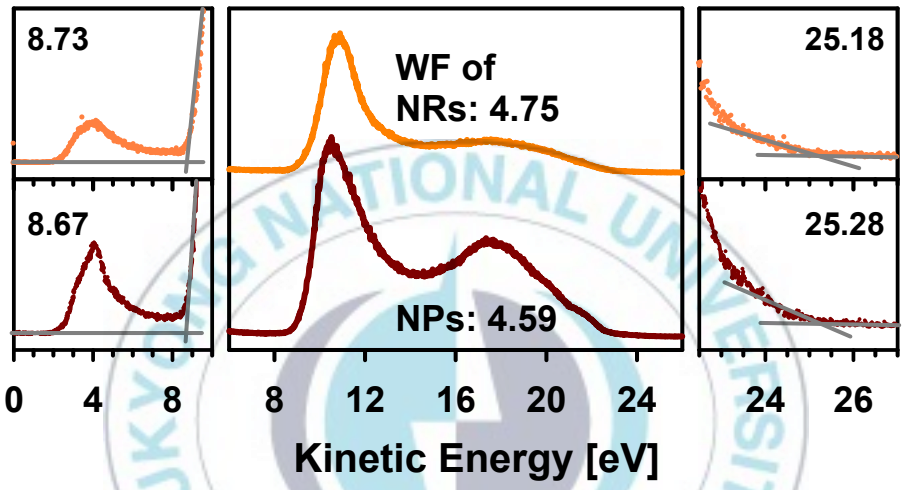

Fig. 7.23 UPS spectra of ZnO NPs and NRs. Left and right graphs show the secondary edge and the Fermi level region, respectively. The middle graph shows the entire spectra and the value of work function. The numbers have scale of eV.

calculated by the same method as VBM. The secondary cutoff and Fermi level of ZnO NPs were 8.67 and 25.28 eV and those of ZnO NRs were 8.73 and 25.18 eV, respectively. The work function is calculated by following equation,

$$\phi_{sample} = h\nu - (\text{Fermi edge - Secondary edge}).$$

Thus, the determined work functions are 4.59 and 4.75 eV for ZnO NPs and NRs. The obtained VBM and WF are used to determine the energy band diagram as shown in Fig. 7.24. The Fermi level, VBM, and conduction band minimum (CBM) were calculated by using the value of work function, VBM, and band gap. The band gap is obtained by UV-vis spectroscopy and the obtained values are 3.47 and 3.28 eV for ZnO NPs and NRs (not shown here). The starting point of energy band diagram is the assumption of E_V equals zero. For example, in ZnO NPs, the value of Fermi level, 4.59 eV was confirmed by work function. The VBM in the energy band diagram, 7.06 eV was calculated by adding VBM (2.47 eV) to Fermi level (4.59 eV) [7.85]. Finally, band gap, 3.47 eV was subtracted from the value of VBM in the energy band diagram (7.06 eV) is CBM (3.59 eV) [7.85]. From this energy band diagram, the values of CBM and VBM in ZnO NRs are lower than those of NPs. It means that different shape of ZnO can adjust the energy band of ZnO.

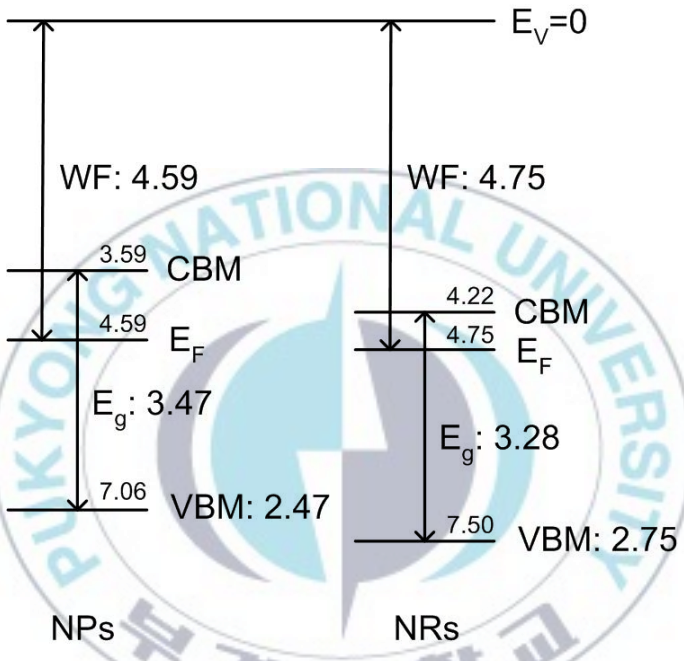

Fig. 7.24 Energy band diagram of ZnO NPs and NRs. The numbers have scale of eV.

7.8.4 Conclusion

In this chapter, the energy band diagram of ZnO NPs and NRs are calculated by using three different techniques. The VBM, work function, and band gap were obtained by XPS, UPS, and UV-vis spectroscopy, respectively. The Fermi level was verified by work function and then VBM in the energy band diagram was obtained using Fermi level and VBM from XPS. Finally, CBM was confirmed by VBM in the energy band diagram and band gap. From this process, we can determine the energy band diagram of two types of ZnO and verified the difference, VBM and CBM of ZnO NPs and NRs.

REFERENCES

CHAPTER I

[1.1] K.A. Lim, J.Y. Park, R.D. Ramsier, D.G. Kim, J.W. Kang, Y.C. Kang, *Appl. Surf. Sci.* 258 (2012) 4097.

[1.2] K.A. Lim, J.Y. Park, D.G. Kim, J.K. Kim, J.W. Kang, Y.C. Kang, *Appl. Surf. Sci.* 258 (2012) 9054.

[1.3] J.Y. Park, T.H. Kwon, S.W. Koh, Y.C. Kang, *Bull. Korean Chem. Soc.* 32 (2011) 1331.

[1.4] J.Y. Park, S.Y. Seo, S.W. Koh, Y.C. Kang, *J. Vac. Sci. Technol. B* 32 (2014) 04E104-1.

[1.5] J.Y. Park and Y.C. Kang, *Met. Mater. Int.* 19 (2013) 55.

[1.6] J.H. Yang, H.H. Jung, J.H. Seo, K.D. Kim, D.H. Kim, D.C. Lim, S.G. Park, J.W. Kang, M.K Song, M.S. Choi, J.D. Kwon, K.S. Nam, Y.S. Jeong, S.H. Kwon, Y.C. Park, Y.C. Kang, K.B. Chung, C.S. Kim, K.S. Lim, S.Y. Ryu, *J. Phys. Chem. C* 117 (2013) 23459.

[1.7] J.C. Woo, T.K. Ha, D.S. Um, J.Y. Park, Y.C. Kang, C.I. Kim, *Thin Solid Films* 520 (2011) 1141.

[1.8] H.R. Kim, J.Y. Park, S.H. Lee, G.H. Lee, P.G. Song, Y.C. Kang, D.H. Kim, *Electrochem. Solid-State Lett.* 14 (2011) H411.

[1.9] D.H. Kim, H.R. Kim, J.D. Kwon, G.H. Lee, J.Y. Park, Y.C. Kang, *J. Non-Cryst. Solids* 358 (2012) 2616.

[1.10] M.-S. Choi, Y.-J. Lee, J.-D. Kwon, Y. Jeong, J.Y. Park, Y.-C. Kang, P.-K. Song, D.-H. Kim, *Curr. Appl. Phys*. 13 (2013) 1589.

[1.11] K.A. Lim, S.H. Jung, S.H. Lee, J.H. Heo, J.Y. Park, J.W. Kang, Y.C. Kang, D.G. Kim, *Org. Electron.* 15 (2014) 1849.

[1.12] Y. Nakano, S. Saeki, T. Morikawa, *Appl. Phys. Lett.* 94 (2009) 022111.

[1.13] H. Kbayashi, T. Nakamura, N. Takahashi, *Mater. Chem. Phys.* 106 (2007) 292.

[1.14] S.C. Ray *Sol. Energy Mater. Sol. Cells* 68 (2001) 307.

[1.15] B.S. Li, K. Akimoto, A. Shen, *J. Crystal Growth* 311 (2009) 1102.

[1.16] G.K. Paul, R. Ghosh, S.K. Bera, S. Bandyopadhyay, T. Sakurai, K. Akimoto, *Chem. Phys. Lett.* 463 (2008) 117.

[1.17] B. Balamurugan, B.R. Mehta, *Thin Solid Films* 396 (2001) 90.

[1.18] N. Miyata, S. Akiyoshi, *J. Appl. Phys.* 58 (1985) 1651.

[1.19] T.S. Sian, G.B. Reddy, *J. Appl. Phys*. 98 (2005) 026104.

[1.20] T. Tsunoda, T. Hayakawa, Y. Imai, T. Kameyama, K. Takehira, K. Fukuda, *Catal. Today* 25 (1995) 371.

[1.21] B.F. Bartlett, H. Molero, W. T. Tysoe, *J. Catal.* 167 (1997) 470.

[1.22] S. Boyadzhiev, V. Lazarova, K. Makita, Y. Kotani, I. Yordanova, Y. Matsumura, M. Rassovska, *e-J. Surf. Sci. Nanotech.* 7 (2009) 796.

[1.23] D. Briggs, M.P. Seah, Practical Surface Analysis (2nd Ed.), Vol. 1, Auger and X-ray photoelectron spectroscopy, pp. 52, Wiley, Chichester (1990).

[1.24] J.T. Yates, Jr., Experimental Innovations in Surface Science, pp. 604-613, AIP Press, New York (1997).

CHAPTER II

[2.1] D. Briggs, M.P. Seah, Practical Surface Analysis (2nd Ed.), Vol. 1, Auger and X-ray photoelectron spectroscopy, pp. 52, Wiley, Chichester (1990).

[2.2] X-ray Source RS 40B1 Operating Manual, Ver. 01, pp. 20, Prevac (2012).

[2.3] D. Briggs, M.P. Seah, Practical Surface Analysis (2nd Ed.), Vol. 1, Auger and X-ray photoelectron spectroscopy, pp. 61, Wiley, Chichester (1990).

[2.4] D. Briggs, M.P. Seah, Practical Surface Analysis (2nd Ed.), Vol. 1, Auger and X-ray photoelectron spectroscopy, pp. 62, Wiley, Chichester (1990).

[2.5] LEG200 Electron Gun Operating Instructions, pp. 18, VG (1987).

[2.6] S. Zhong, J.Q. Zhong, H.Y. Mao, J.L. Zhang, J.D. Lin, W. Chen, Phys. Chem. Chem. Phys. 14 (2012) 14127.

CHAPTER III

[3.1] Y. Nakano, S. Saeki, T. Morikawa, *Appl. Phys. Lett.* 94 (2009) 022111.

[3.2] H. Kbayashi, T. Nakamura, N. Takahashi, *Mater. Chem. Phys.* 106 (2007) 292.

[3.3] S.C. Ray, *Sol. Energy Mater. Sol. Cells* 68 (2001) 307.

[3.4] B.S. Li, K. Akimoto, A. Shen, *J. Crystal Growth* 311 (2009) 1102.

[3.5] G.K. Paul, R. Ghosh, S.K. Bera, S. Bandyopadhyay, T. Sakurai, K. Akimoto, *Chem. Phys. Lett.* 463 (2008) 117.

[3.6] B. Balamurugan, B.R. Mehta, *Thin Solid Films* 396 (2001) 90.

[3.7] A. Mittiga, E. Salza, F. Sarto, M. Tucci, R. Vasanthi, *Appl. Phys. Lett.* 88 (2006) 163502.

[3.8] T. Serin, S. Horzum, Y. Celik, *Semicond. Sci. and Technol.* 20 (2005) 398.

[3.9] W.-Y. Yang, S.-W. Rhee, *Appl. Phys. Lett.* 91 (2007) 232907.

[3.10] Y. Yoshida, S. Tanaka, Y. Fujita, I. Hiromitsu, *J. Appl. Phys.* 106 (2009) 064510.

[3.11] J. Deuermeier, J. Gassmann, J. Brotz, A. Klein, *J. Appl. Phys.* 109 (2011) 113704.

[3.12] T.D. Golden, M.G. Shumsky, Y. Zhou, R.A. VanderWerf, R.A. Van Leeuwen, J.A. Switzer, *Chem. Mater.* 8 (1996) 2499.

[3.13] S.C. Ray, *Sol. Energy Mater. Sol. Cells* 68 (2001) 307.

[3.14] A. Chen, H. Long, X. Li, Y. Li, G. Yang, P. Lu, *Vacuum* 83 (2009) 927.

[3.15] N. Serin, T. Serin, S. Horzum, Y. Celik, *Semicond. Sci. Technol.* 20 (2005) 398.

[3.16] T.S. Nair, L. Guerrero, O.L. Arenas, P.K. Nair, *Appl. Surf. Sci.* 150 (1999) 143.

[3.17] M. Ottosson, J.O. Carlsson, *Surf. Coat. Technol.* 78 (1996) 263.

[3.18] K. Santra, C.K. Sarkar, M.K. Mukheriee, B. Ghosh, *Thin Solid Films* 213 (1992) 226.

[3.19] A.E. Rakhshani, *Solid-State Electron.* 29 (1986) 7.

[3.20] S. Izhizuka, S. Kato, T. Maruyama, K. Akimoto, *Jpn. J. Appl. Phys.* 40 (2001) 2765.

[3.21] K. Lim, J. Park, R.D. Ramsier, D.-G. Kim, J.-W. Kang, Y.-C. Kang, *Appl. Surf. Sci.* 258 (2012) 4097.

[3.22] K. Lim, J. Park, D.-G. Kim, J.-K. Kim, J.-W. Kang, Y.-C. Kang, *Appl. Surf. Sci. 258* (2012) 9054.

[3.23] A.H. Jayatissa, K. Guo, A.C. Jayasuriya, *Appl. Surf. Sci.* 255 (2009) 9474.

[3.24] JCPDS card No. 85-1326.

[3.25] JCPDS card No.78-2076.

[3.26] JCPDS card No. 80-1917.

[3.27] I. Espitia-Cabrera, H.D. Orozco-Hernandez, P. Bartolo-Perez, M.E. Contreras-Garcia, *Surf. Coat. Technol.* 203 (2008) 211.

[3.28] H.J. Li, X.Y. Jiang, W.M. Huang, X.M. Zheng, *Energy Fuels* 23 (2009) 2967.

[3.29] C.L. Chu, H.C. Lu, C.Y. Lo, C.Y. Lai, Y.U. Wang, *Physica B* 404 (2009) 4831.

[3.30] Z. Ai, L. Zhang, S. Lee, W. Ho, *J. Phys. Chem. C* 113 (2009) 20896.

[3.31] S.Y. Lee, M.N. Nguyen, Y.M. Sun, J.M. White, *Appl. Surf. Sci.* 206 (2003) 102.

[3.32] J.Y. Park, T.H. Kwon, S.W. Koh, Y.C. Kang, *Bull. Korean Chem. Soc.* 32 (2011) 1331.

[3.33] F. Shi, C. Cui, *Inorg. Mater.* 46 (2010) 565.

[3.34] K.H. Yoon, W.J. Choi, D.H. Kang, *Thin Solid Films* 372 (2000) 250.

[3.35] G. Papadimitropoulos, N. Vourdas, V. Em Davazoglou, D. Vamvakas, *Thin Solid Films* 515 (2006) 2428.

[3.36] M.F. Al-Kuhaili, *Vacuum* 82 (2008) 623.

[3.37] S. Venkataraj, O. Kappertz, Ch. Liesch, R. Detemple, R. Jayavel, M.

Wuttig, *Vacuum* 75 (2004) 7.

[3.38] S.H. Mohamed, S. Venkataraj, *Vacuum* 81 (2007) 636.

[3.39] C.D. Wagner, W.M. Riggs, L.E. Davis, J.F. Moulder, G.E. Muilenberg, Handbook of X-ray Photoelectron Spectroscopy, Perkin-Elmer Corp., Minnesota, USA, 1979.

[3.40] J. Morales, L. Sánchez, F. Martín, J.R. Ramos-Barrado, M. Sánchez, *Thin Solid Films* 474 (2005) 133.

[3.41] T. Miyamura, J. Koike, *Mater. Sci. Eng. A* 445-446 (2007) 620.

[3.42] L.M. Wong, S.Y. Chiam, J.Q. Huang, S.J. Wang, J.S. Pan, W.K.J. *Chim, Appl. Phys.* 108 (2010) 033702.

[3.43] A. Marmur, *Langmuir* 19 (2003) 8343.

[3.44] F. Lin, Y. Zhang, J. Xi, Y. Zhu, N. Wang, F. Xia, L. Jiang, *Langmuir* 24 (2008) 4114.

[3.45] User Manual for Model L116C Ellipsometer, Gaertner Scientific Corporation, Illinois, USA.

[3.46] F. Yakuphanoglu, A. Cukurovali, İ. Yilmaz, *Opt. Mater.* 27 (2005) 1363.

[3.47] J.I. Pankove, Optical Processes in Semiconductors, Prentice-Hall, New Jersey, USA, 1971.

[3.48] M.S. Hossain, R. Islam, K.A. Khan, *Chalcogenide Lett.* 7 (2010) 21.

[3.49] A.F. Qasrawi, *Cryst. Res. Technol.* 40 (2005) 610.

[3.50] V. Figueiredo, E. Elangovan, G. Gonçalves, P. Barquinha, L. Pereira, N. Franco, E. Alves, R. Martins, E. Fortunato, *Appl. Surf. Sci.* 254 (2008) 3949.

[3.51] J.P. Zhang, L.D. Zhang, L.Q. Zhu, Y. Zhang, M. Liu, X.J. Wang, *J. Appl. Phys.* 102 (2007) 114903.

[3.52] S.C. Roy, G.L. Sharma, M.C. Bhatnagar, *Solid State Commun.* 141 (2007) 243.

CHAPTER IV

[4.1] S.Y. Kim, D.H. Han, J.N. Kim, J.J. Lee, *J. Power Sources* 193 (2009) 570.

[4.2] M.-H. Chan, F.-H. Lu, *Thin Solid Films* 517 (2009) 5006.

[4.3] A. Rizzo, M.A. Signore, L. Mirenghi, A. Cappello, L. Tapfer, *Surf. Coat. Technol.* 204 (2010) 2019.

[4.4] M.A. Signore, A. Rizzo, L. Tapfer, E. Piscopiello, L. Capodieci, A. Cappello, *Thin Solid Films* 518 (2010) 1943.

[4.5] M. Grafouté, C. Petitjean, C. Rousselot, J.F. Pierson, J.M. Grenèche, *J. Phys.: Condens. Matter* 19 (2007) 226207.

[4.6] N. Miyata, S. Akiyoshi, *J. Appl. Phys.* 58 (1985) 1651.

[4.7] T.S. Sian, G.B. Reddy, *J. Appl. Phys.* 98 (2005) 026104.

[4.8] T. Tsunoda, T. Hayakawa, Y. Imai, T. Kameyama, K. Takehira, K. Fukuda, *Catal. Today* 25 (1995) 371.

[4.9] B.F. Bartlett, H. Molero, W. T. Tysoe, *J. Catal.* 167 (1997) 470.

[4.10] S. Boyadzhiev, V. Lazarova, K. Makita, Y. Kotani, I. Yordanova, Y. Matsumura, M. Rassovska, *e-J. Surf. Sci. Nanotech.* 7 (2009) 796.

[4.11] J. Danroc, A. Aubert, R. Gilet, *Thin Solid Films* 153 (1987) 281.

[4.12] A. Fan, L. Qin, L. Tian, B. Tang, *J. Wuhan Univ. Technol.-Mat. Sci. Edit.* 23 (2008) 358.

[4.13] Y. He, J.Y. Feng, *J. Cryst. Growth* 263 (2004) 203.

[4.14] H.J. Lee, J.-C. Choi, C.W. Colling, M.S. Mudholkar, L.T. Thompson, *Appl. Surf. Sci.* 89 (2005) 121.

[4.15] H. Abe, A.T. Bell, *J. Catal.* 142 (1993) 430.

[4.16] Y. G. Shen, Y. -W. Mai, *Mater. Sci. Eng. B-Solid State Mater. Adv. Technol.* 95 (2002) 222.

[4.17] L. Cunha, L. Rebouta, F. Vaz, M. Staszuk, S. Malara, J. Barbosa, P. Carvalho, E. Alves, E. Le Bourhis, Ph. Goudeau, J. P. Rivière, *Vacuum* 82 (2008) 1428.

[4.18] Y.-H. Yang, I.-W. Lyo, S.-J. Park, D.-S. Lim, Y.-S. Oh, *Korean J. Met. Mater.* 50 (2012) 549.

[4.19] J.H. Bihn, J.Y. Park, Y.C. Kang, *J. Korean Phys. Soc.* 58 (2011) 509.

[4.20] D.-C. Tsai, Y.-L. Huang, S.-R. Lin, S.-C. Liang, F.-S. Shieu, *Appl. Surf. Sci.* 257 (2010) 1361.

[4.21] J.-R. Xiao, X.-H. Li, Z.-X. Wang, *Trans. Nonferrous Met. Soc. China* 19 (2009) 1551.

[4.22] H. Jehn, P. Ettmayer, *J. Less-Common Met.* 58 (1978) 85.

[4.23] J. Barbosa, L. Cunha, L. Rebouta, C. Moura, F. Vaz, S. Carvalho, E. Alves, E. Le Bourhis, Ph. Coudeau, J.P. Rivière, *Thin Solid Films* 494 (2006) 201.

[4.24] M. Yamada, J. Yasumaru, M. Houalla, D.M. Hercules, *J. Phys. Chem.* 95 (1991) 7037.

[4.25] T. Bécue, J.-M. Manoli, C. Potvin, G. Djéga-Mariadassou, *J. Phys. Chem. B* 101 (1997) 6429.

[4.26] P. Perez-Rome, C. Potvin, J.-M. Manoli, M.M. Chehimi, G. Djéga-

Mariadassou, *J. Catal.* 208 (2002) 187.

[4.27] M.A. Hasan, M.I. Zaki, L. Pasupulety, K. Kumari, *Appl. Catalysis A: General* 181 (1999) 171.

[4.28] S. Agouram, F. Bodart, G. Terwagne, *Surf. Coat. Technol.* 180-181 (2004) 164.

CHAPTER V

[5.1] R. Bichsel, P. Buffat, and F. Lévy, *J. Phys. D: Appl. Phys.* 19 (1986) 1575.

[5.2] T. Kubart, T. Polcar, L. Kopecký, R. Novák, and D. Nováková, *Surf. Coat. Technol.* 193 (2005) 230.

[5.3] W. Lauwerens, J. Wang, J. Navratil, E. Wieërs, J. D'haen, L.M. Stals, J.P Celis, and Y. Bruynseraede, *Surf. Coat. Technol.* 131 (2000) 261.

[5.4] H.-D. Wang, B.-S. Xu, J.-J. Liu, and D.-M. Zhuang, *Mater. Chem. Phys.* 91 (2005) 494.

[5.5] K.F. Mark, C. Lee, J. Hene, J. Shan, and T.F. Heinz, *Phys. Rev. Lett.* 105 (2010) 136805.

[5.6] K.K. Kam and B.A. Parkinson, *J. Phys. Chem.* 289 (1982) 463.

[5.7] Q.H. Wang, K. Kalantar-Zadeh, A. Kis, J.N Coleman, and M.S. Strano, *Nat. Nanotechnol.* 7 (2012) 699.

[5.8] A.K. Geim, *Science*, 324 (2009) 1530.

[5.9] F. Schwierz, *Nat. Nanotechnol.* 5 (2010) 487.

[5.10] K.F. Mark, C. Lee, J. Hene, J. Shan, and T.F. Heinz, *Phys. Rev. Lett.* 105 (2010) 136805.

[5.11] S. Najmaei, Z. Liu, P.M. Ajayan, and J. Lou, *Appl. Phys. Lett.* 100 (2012) 013106.

[5.12] H. Vrubel and X. Hu, *ACS Catal.* 3 (2013) 2002.

[5.13] C. Yim, M. O'Brien, N. McEvoy, S. Winters, I. Mirza, J.G. Lunney, and G.S. Duesberg, *Appl. Phys. Lett.* 104 (2014) 103114.

[5.14] J. Tao, J.W. Chai, Z. Zhang, J.S. Pan, and S.J. Wang, *Appl. Phys. Lett.* 104 (2014) 232110.

[5.15] V. Weiss, W. Bohne, J. Röhrich, E. Strub, U. Bloeck, I. Sieber, K. Ellmer, R. Mientus, and F. Porsch, *J. Appl. Phys.* 95 (2004) 7665.

[5.16] R. Bichsel and F. Lévy, *J. Phys. D: Appl. Phys.* 19 (1986) 1809.

[5.17] J.K. Seo, K.-H. Ko, H.J. Cho, W.S. Choi, M. Park, K.-H. Seo, Y. Park, and D.-G. Lim, *Trans. Electr. Electron. Mater.* 11 (2010) 29.

[5.18] M. Farooq and Z.H. Lee, *J. Korean Phys. Soc.* 40 (2012) 511.

[5.19] J. Park and Y.-C. Kang, *Met. Mater. Int.* 19 (2013) 55.

[5.20] D. Kim, S.V. Kagwade, and C.R. Clayton, *Surf. Interface Anal.* 26 (1998) 155.

[5.21] G.-T. Kim, T.-K. Park, H. Chung, Y.-T. Kim, M.-H. Kwon, and J.-G. Choi, *Appl. Surf. Sci.* 152 (1999) 35.

[5.22] M.B. Casu, W. Braun, K.R. Bauchspie, S. Kera, B. Megner, C. Heske, R. Thull, and E. Umbach, *Surf. Sci.* 602 (2008) 1599.

[5.23] X. Li, W. Zhang, Y. Wu, C. Min, and J. Fang, *ACS Appl. Mater. Interfaces* 5 (2013) 8823.

[5.24] T. Young, *Philos. Trans. R. Soc. Lond.* 95 (1805) 65.

[5.25] N.B. Vargaftik, B.N. Volkov, and L.D. Voljak, *J. Phys. Chem. Ref. Data* 12 (1983) 817.

[5.26] C. Jho and M. Carreras, *J. Colloid Interface Sci.* 99 (1984) 543.

[5.27] D.K. Owens and R.C. Wendt, *J. Appl. Polym. Sci.*13 (1969) 1741.

[5.28] F.M. Fowkes, *J. Phys. Chem.* 66 (1962) 382.

CHAPTER VI

[6.1] C.H. Xu, C.H. Woo, S.Q. Shi, *Superlattices Microstruct*. 36 (2004) 31.

[6.2] X. Jiang, T. Herricks, Y. Xia, *Nano Lett*. 2 (2002) 1333.

[6.3] S.R. Chun, W.A. Sasangka, M.Z. Ng, Q. Liu, A. Du, J. Zhu, C.M. Ng, Z.Q. Liu, S.Y. Chiam, C.L. Gan, *Small* 9 (2013) 2546.

[6.4] H. Bai, Z. Liu, D.D. Sun, *J. Am. Ceram. Soc*. 96 (2013) 942.

[6.5] B. Wang, S. Gu, Y. Ding, Y. Chu, Z. Zhang, X. Ba, Q. Zhang, X. Li, *Analyst* 138 (2013) 362.

[6.6] W.H. Jung, N.-S. Kwak, T.S. Hwang, K.B. Yi, *Appl. Surf. Sci*. 261 (2012) 343.

[6.7] H. Hu, W. Jiang, F. Lan, X. Zeng, S. Ma, Y. Wu, Z. Gu, *RSC Adv*. 3 (2013) 879.

[6.8] T.T.T. Nguyen, C. Ghosh, S.G. Hwang, N. Chanunpanich, J.S. Park, *Int. J. Pharm*. 439 (2012) 296.

[6.9] C.-H. Huang, C.-Y. Chi, Y.-S. Chen, K.-Y. Chen, P. -L. Chen, C.-H. Yao, *Mater. Sci. Eng. C* 32 (2012) 2476.

[6.10] C.-T. Hsieh, J.-M. Chen, H.-H. Lin, H.-C. Shih, *Appl. Phys. Lett*. 82 (2003) 3316.

[6.11] Y. Li, P. Kuai, P. Huo, C.-J. Liu, *Mater. Lett*. 63 (2009) 188.

[6.12] C. Li, R. Chen, X. Zhang, S. Shu, J. Xiong, Y. Zheng, W. Dong, *Mater. Lett*. 65 (2011) 1327.

[6.13] K. Garg, G. L. Bowlin, *Biomicrofluidics* 5 (2011) 013403.

[6.14] W.E. Teo, S. Ramakrishna, *Nanotechnology* 17 (2006) R89.

[6.15] J. Ghijsen, L.H. Tjeng, J. van Elp, H. Eskes, J. Westerink, G.A. Sawatzky, M.T. Czyzyk, *Phys. Rev. B* 38 (1988) 322.

[6.16] J.Y. Park, T.H. Kwon, S.W. Koh, Y.C. Kang, *Bull. Korean Chem. Soc*. 32 (2011) 1331.

[6.17] A.V. Korshunov, A.P. Il'in, *Russ. J. Appl. Chem*. 82 (2009) 1164.

[6.18] K. Lim, J.Y. Park, D.-G. Kim, J.-K. Kim, J.-W. Kang, Y.-C. Kang, *Appl. Surf. Sci*. 258 (2012) 9054.

[6.19] L.S. Huang, S.G. Yang, T. Li, B.X. Gu, Y.W. Du, Y.N. Lu, S.Z. Shi *J. Cryst. Growth* 260 (2004) 130.

[6.20] Y.-K. Hsu, C.-H. Yu, H.-H. Lin, Y.-C. Chen, Y.-G. Lin, *J. Electroanal. Chem*. 704 (2013) 19.

[6.21] B. Rannou, F. Velasco, S. Guzmán, V. Kolarik, F. Pedraza, *Mater. Chem. Phys*. 134 (2012) 360.

[6.22] M. Mohsin, A. Hossin, Y. Haik, *Mater. Sci. Eng., A* 528 (2011) 925.

[6.23] S.N. Bhad, V.S. Sangawar, *Chem. Sci. Trans*. 1 (2012) 653.

[6.24] S. Gupta, T.J. Webster, A. Sinha, *J. Mater. Sci.-Mater. Med*. 22 (2011) 1763.

CHAPTER VII

[7.1] J.-C. Woo, T.-K. Ha, D.-S. Um, J. Park, Y.-C. Kang, C.-I. Kim, *Thin Solid Films* 520 (2011) 1141.

[7.2] W.J. Zhu, T. Tamagawa, M. Gibson, T. Furukawa, T.P. Ma, *IEEE Electron Device Lett*. 23 (2002) 649.

[7.3] J.-C. Woo, Y.-S. Chun, C.-I. Kim, *Appl. Surf. Sci*. 292 (2014) 915.

[7.4] E. Jud, M. Tang, Y.-M. Chiang, *J. Appl. Phys*. 103 (2008) 114108.

[7.5] H. Jin, U.K. Oh, H.J. Kang, S.W. Lee, Y.S. Lee, K.Y. Lim, *J. Korean Phys. Soc*. 46 (2005) S52.

[7.6] R. Tan, Y. Azuma, I. Kojima, *Appl. Surf. Sci*. 241 (2005) 135.

[7.7] L.-P. Feng, Z.-T. Liu, Y.-M. Shen, *Vacuum* 83 (2009) 902.

[7.8] L. Zhang, S.-Y. Terauchi, Y. Azuma, T. Fujimoto, *Surf. Interface Anal.* 40 (2008) 1701.

[7.9] X. Cheng, L. Wan, Z. Song, Y. Yu, D. Shen, *Appl. Phys. Lett*. 90 (2007) 152910.

[7.10] A.E. Rakhshani, A. Bumajdad, J. Kokaj, S. Thomas, *Appl. Phys. A* 97 (2009) 759.

[7.11] K. Nomura, A. Takagi, T. Kamiya, H. Ohta, M. Hirano, H. Hosono, *Jpn. J. Appl. Phys*. 45 (2006) 4303.

[7.12] K. Nomura, H. Ohta, A. Takagi, T. Kamiya, M. Hirano, H. Hosono, *Nature* 432 (2004) 488.

[7.13] K.-K. Kim, H.-S. Kim, D.-K. Hwang, J.-H. Lim, S.-J. Park, *Appl. Phys. Lett*. 83 (20003) 63.

[7.14] H.-R. Kim, J. Park, S.-H. Lee, G.-H. Lee, P.-G. Song, Y.-C. Kang, D.-H. Kim, *Electrochem. Solid-State. Lett.* 14 (2011) H411.

[7.15] J.L. Chung, J.C. Chen, C.J. Tseng, *Appl. Surf. Sci.* 255 (2008) 2494.

[7.16] C.D. Wagner, W.M. Riggs, L.E. Davis, J.F. Moulder, G.E. Muilenberg, Handbook of X-ray Photoelectron Spectroscopy, pp. 82, Perkin-Elmer Corp., Minnesota (1979).

[7.17] J.M. Themlin, M. Chtaib, L. Henrard, P. Lambin, J. Darvile, J. M. Gilles, *Phys. Rev. B* 46 (1992) 2460.

[7.18] D.-H. Cho, S. Yang, C. Byun, J. Shin, M.K. Ryu, S.-H.K. Park, C.-S. Hwang, S.M. Chung, W.-S. Cheong, S.M. Yoon, H.-Y. Chu, *Appl. Phys. Lett*. 93 (2008) 142111.

[7.19] Z. Stýhal, J. Pavlík, S. Novák, A. Macková, V. Peina, K. Veltruská, *Vacuum* 67 (2002) 665.

[7.20] Y.S. Rim, D.L. Kim, W.H. Jeong, H.J. Kim, *Appl. Phys. Lett*. 97 (2010) 233502.

[7.21] D.R. Lide, CRC Handbook of Chemistry and Physics, Internet Version, pp. 8-25, CRC Press, Florida (2005).

[7.22] P.R. Ohodnicki Jr., M. Andio, C. Wang *J. Appl. Phys*. 116 (2014) 024309.

[7.23] N. Chantarat, Y.-W. Chen, C.-C. Lin, M-C. Chiang, S.-Y. Chen, *Inorg. Chem*. 49 (2010) 11077.

[7.24] D.S. Ginley, Handbook of Transparent Conductors, pp. 1-25, Springer US (2011).

[7.25] A. Andersson, N. Johansson, P. Bröms, N. Yu, D. Lupo, W.R. Salaneck, *Adv. Mater.* 10 (1998) 859.

[7.26] H.Y. Yu, X.D. Feng, D. Grozea, Z.H. Lu, R.N.S. Sodhi, A.-M. Hor, H.

Aziz, *Appl. Phys. Lett*. 78 (2001) 2595.

[7.27] C.-K. Song, C.-Y. Kim, S.-H. Huh, D.-H. Riu, Y.-H. Choa, Kor. *J. Mater. Res.* 17 (2007) 376.

[7.28] S. Luo, S. Kohiki, K. Okada, A. Kohno, T. Tajiri, M. Arai, S. Ishii, D. Sekiba, M. Mitome, F. Shoji, *ACS Appl. Mater. Interfaces* 2 (2010) 663.

[7.29] S. Limpijumnong, P. Reunchan, A. Janotti, C.G. Van de Valle, *Phys. Rev. B* 80 (2009) 193202.

[7.30] S. Major, S. Kumar, M. Bhatnagar, K.L. Chopra, *Appl. Phys. Lett*. 49 (1986) 394.

[7.31] A.I. Martínez, L. Huerta, J.M.O-Rueda de León, D. Acosta, O. Malik, M. Aguilar, *J. Phys. D: Appl. Phys*. 39 (2006) 5091.

[7.32] B. Cotterell, W. Wang, Z. Chen, *Eng. Fract. Mech*. 69 (2002) 597.

[7.33] Y. Leterrier, L. Médico, F. Demarco, J.-A.E. Månson, U. Betz, M.F. Escolà, M. Kharrazi Olsson, F. Atamny, *Thin Solid Films* 460 (2004) 156.

[7.34] D.R. Cairns, R.P. Witte Il, D.K. Sparacin, S.M. Sachsman, D.C. Paine, G.P. Crawford, *Appl. Phys. Lett*. 76 (2000) 1425.

[7.35] S.H. Choa, C.K. Cho, W.J. Hwang, K.T. Eun, H.K. Kim, *Sol. Energy Mater. Sol. Cells* 95 (2011) 3442.

[7.36] M.W. Rowell, M.A. Topinka, M.D. McGehee, H.J. Prall, G. Dennler, N.S. Sariciftci, L. Hu, G. Gruner, *Appl. Phys. Lett*. 88 (2006) 233506.

[7.37] L. Gomez de Arco, Y. Zhang, C.W. Schlenker, K. Ryu, M.E. Thompson, C. Zhou, *ACS Nano* 4 (2010) 2865.

[7.38] S. De, T.M. Higgins, P.E. Lyons, E.M. Doherty, P.N. Nirmalraj, W.J. Blau, J.J. Boland, J.N. Coleman, *ACS Nano* 3 (2009) 1767.

[7.39] L. Hu, H.S. Kim, J.Y. Lee, P. Peumans, Y. Cui, *ACS Nano* 4 (2010) 2955.

[7.40] C.H. Liu, X. Yu, *Nanoscale Res. Lett*. 6 (2011) 1.

[7.41] J. Ajuria, I. Ugarte, W. Cambarau, I. Etxebrria, R. Tena-Zaera, R. Pacios, *Sol. Energy Mater. Sol. Cells* 102 (2012) 148.

[7.42] S.K.M. Jönsson, J. Birgerson, X. Crispin, G. Greczynski, W. Osikowic, A.W.D. Van de Con, W.R. Salaneck, M. Fahlman, *Synth. Met*. 139 (2003) 1.

[7.43] A.M. Nardes, R.A.J. Janssen, M. Kemerink, *Adv. Funct. Mater*. 18 (2008) 865.

[7.44] A.M. Nardes, J. Kemerink, M.M. de Kok, E. Vinken, K. Maturova, R.A.J. Janssen, *Org. Electron*. 9 (2008) 727.

[7.45] J.Y. Kim, J.H. Jung, D.E. Lee, J. Joo, *Synth. Met*. 126 (2002) 311.

[7.46] J.H. Huang, D. Kekuda, C.W. Chu, K.C. Ho, *J. Mater. Chem*. 19 (2009) 3704.

[7.47] S.K. Hau, H.L. Yip, J. Zou, A.K.Y. Jen, *Org. Electron.* 10 (2009) 1401.

[7.48] K.J. Kim, Y.S. Kim, W.S. Kang, B.H. Kang, S.H. Yeom, D.E. Kim, J.H. Kim, S.W. Kang, *Sol. Energy Mater. Sol. Cells* 94 (2010) 1303.

[7.49] J. Ouyang, C.W. Chu, F.C. Chen, Q. Xu, Y. Yang, *Adv. Funct. Mater*. 15 (2005) 203.

[7.50] J. Ouyang, Q. Xu, C.W. Ch, Y. Yang, G. Li, J. Shinar, *Polymer* 45 (2004) 8443.

[7.51] A. Luque, S. Hegedus, Handbook of Photovoltaic Science and Engineering, 2nd Edition, pp. 506, Wiley, Chichester (2010).

[7.52] R.C. Mahadevapuram, V.L. Dalal, S. Chaudhary, *Nanomaterials and*

Energy 2 (2013) 186

[7.53] E.L. Williams, G.E. Jabbour, Q. Wang, S.E. Shaheen, D.S. Ginley, E.A. Schiff, *Appl. Phys. Lett.* 87 (2005) 223504-1.

[7.54] S.J. Kang, J.-W. Jeon, S.J. Baik, K.S. Lim, *Appl. Phys. Lett*. 103 (2013) 153903

[7.55] V. Shrotriya, G. Li, Y. Yao, C.W. Chu, Y. Yang, *Appl. Phys. Lett*. 88 (2006) 073508-1.

[7.56] H. Choi, B. Kim, M.J. Ko, D.K. Lee, H. Kim, S.H. Kim, K. Kim, *Org. Electron*. 13 (2012) 959.

[7.57] M.D. Irwin, D.B. Buchholz, A.W. Hains, R.P.H. Chang, T.J. Marks, *Proc. Natl. Acad. Sci*. 105 (2008) 2783.

[7.58] M. Yamada, J. Yasumaru. M. Houalla, D.M. Hercules, *J. Phys. Chem*. 95 (1991) 7037.

[7.59] D. Kim, S.V. Kagwade, C.R. Clayton, *Surf. Interface Anal*. 26 (1998) 155.

[7.60] C.D. Wagner, W.M. Riggs, L.E. Davis, J.F. Moulder, G.E. Muilenberg, Handbook of X-ray Photoelectron Spectroscopy, Perkin-Elmer Corp., Minnesota, USA, 1979.

[7.61] E.N. Dattoli, Q. Wan, W. Guo, Y. Chen, X. Pan, W. Lu, *Nano Lett*. 7 (2007) 2463.

[7.62] S. Ju, P. Chen, C. Zhou, Y. Ha, A. Facchetti, T.J. Marks, S.K. Kim, S. Mohammadi, D.B. Janes, *Appl. Phys. Lett*. 92 (2008) 243120.

[7.63] A. Kolmakov, Y. Zhang, G. Cheng, M. Moskovits, *Adv. Mater*. 15 (2003) 997.

[7.64] A.M. Morales, C.M. Lieber, *Science*, 279 (1998) 208.

[7.65] C. Chèze, L. Geelhaar, O. Brandt, W.M. Weber, H. Riechert, S. Münch, R. Rothemund, S. Reitzenstein, A. forchel, T. Kehagias, P. Komninou, G.P. Dimitrakopulos, T. Karakostas, *Nano Res*. 3 (2010) 528.

[7.66] H.-Y. Tuan, A. Ghezelbash, B.A. Korgel, *Chem. Mater*. 20 (2008) 2306.

[7.67] Y. Chen, X. Cui, K. Zhang, D. Pan, S. Zhang, B. Wang, J.G. Hou, *Chem. Phys. Lett* 369 (2003) 16.

[7.68] Y.X. Chen, L.J. Campbell, W.L.Zhou, *J. Cryst. Growth* 270 (2004) 505.

[7.69] K. Senthil, K. Yong, *Nanotechnology* 18 (2007) 395604.

[7.70] S.H. Mohamed and A. Anders, *Surf. Coat. Technol*. 201 (2006) 2977.

[7.71] D.-Y. Lu, M. Sugano, X.-Y. Sun, W.-H. Su, *Appl. Surf. Sci*. 242 (2005) 318.

[7.72] W.B. Im, J.H. Kang, D.C. Lee, S. Lee, D.Y. Jeon, Y.C. Kang, K.Y. Jung, *Solid State Commun*. 133 (2005) 197

[7.73] K. Lim, S. Jung, S. Lee, J. Heo, J. Park, J.-W. Kang, Y.-C. Kang, D.-G. Kim, *Org. Electron*. 20 (2012) 17119.

[7.74] X.L. Li, H.B. Lu, M. Li, Z. Mai, H. Kim, Q.J. Jia, *Appl. Phys. Lett*. 92 (2008) 012902.

[7.75] S. Kumar, V.S. Raju, T.R.N. Kutty, *Appl. Surf. Sci*. 206 (2003) 250.

[7.76] S. Ashtaputre, S. Marathe, S. Kulkarni, *J. Mater. Sci*. 42 (2007) 9990.

[7.77] L.-J. Meng, C.P. Moreira de Sá, M.P. dos Santos, *Appl. Surf. Sci*. 78 (1994) 57.

[7.78] O. Lupan, L. Chow, L.K. Ono, B.R. Cuenya, G. Chai, H. Khallaf, S. Park, A. Schulte, *J. Phys. Chem. C* 114 (2010) 12401.

[7.79] K.C. Choi, E.J. Lee, M.J. Kim, Y.K. Beak, P.W. Shin, Y.D. Kim, Y.K. Kim, *Korean J. Met. Mater*. 52 (2013) 813.

[7.80] W.J.E. Beek, M.M. Wienk, M.Kemerink, X. Yang, R.A.J. Janssen, *J. Phys. Chem. B* 109 (2005) 9505.

[7.81] A. Moulahi, F. Sediri, *Mater. Res. Bull*. 48 (2013) 3723.

[7.82] G.W. Cong, W.Q. Peng, H.Y. Wei, X.X. Han, J.J. Wu, X.L. Liu, Q.S. Zhu, Z.G. Wang, J.G. Lu, Z.Z. Ye, L.P. Zhu, H.J. Qian, R. Su, C.H. Hong, J. Zhong, K. Ibrahim, T.D. Hu, *Appl. Phys. Lett*. 88 (2006) 062110.

[7.83] A.G. Joshi, S. ÖSahai, N. Gandhi, Y.G. Radha Krishna, D. Haranath, *Appl. Phys. Lett*. 96 (2010) 123102.

[7.84] J.D. Hwang, Y.L Lin, C.Y. Kung, *Nanotechnology*, 24 (2013) 115709.

[7.85] V. Diesen, C.W. Dunnill, E. Österberg, I.P. Parkin, M. Jonsson, *Dalton Trans*. 43 (2014) 344.

APPENDICES

Appendix A: Procedure for Baking the EES Chamber

- Whenever the EES chamber was vented to atmosphere, the EES chamber should be baked by heating up to ~200°C using halogen lamps and heating tapes until the pressure is steady state.

- Baking procedure should be started at the pressure of 10^{-7} Torr range.

1. Take samples (carbon tape used) out.
2. Connect the digital multimeter with the K-type thermocouple to read the temperature of the EES chamber.
3. Drain the D.W. from X-ray source and target of rf sputter.
4. Remove all cables (electron gun for AES, UV, Ar sputter guns for cleaning and depth profile, CHA, AES/LEED, QMS, convectron gauge, bias line for UPS, N_2 gas line for vent, cooling lines for X-ray source and rf sputter target) and a magnet of rf sputter except the cables of IPs and TSPs.
5. Lower the setting temperature of chiller for TMP down to 12°C.
6. Open the MGV between sample transferring part and sample load-lock part in sample preparation chamber.
7. Wrap the EES chamber with heat resistant blankets.
8. Connect the power of halogen lamps and heating tapes with voltage transformers using multitaps. Distribute the power evenly for safety.
9. Plug the multitaps to wall power.

10. Set the power of transformers given as following.
    A. Heating tapes for IP (720 L/s, 2 ea): 220 V
    B. Heating tapes for IP (360 L/s, 1 ea): 140 V
    C. Heating tapes for TSP (main, 1 ea): 220 V
    D. Heating tapes for CHA (1 ea): 170 V
    E. Heating tapes for elbow at IP (720 L/s, 1 ea): 170 V
    F. Heating tapes for TMP (2 ea): 160 V
    G. Halogen lamps (3 ea): 100 V
11. Record the pressure and temperature of the EES chamber periodically.
12. Finish the baking when the pressure is in steady state (~3.0×10^{-7} Torr).
    A. Turn off the transformers.
    B. Take off the blankets.
    C. Wait to cool down the EES chamber before degassing the filaments.

Appendix B: Procedure for Degassing the Equipment

- Degas the filaments of the equipment or pumps after baking process as following sequence.

B-1: Titanium Sublimation Pump (TSP)

Sublimation Pump Supply SPS6

1. Check the pressure of the EES chamber (~1.0×10^{-8} Torr).
2. Check the [**SUPPLY**] button is on.
3. Push the [**MODE**] button (yellow) in [**STATUS**]. Yellow and green lights will be on and the filament current will be increased. First time of ON/OFF should be instant and then increased the ON/OFF time.
4. Select other Ti filaments using the selector and follow the steps as given above.

B-2: Ion Pump (IP)

VIPC4200: CH1 for IP (720 L/s) and CH2 for IP (360 L/s)

IPC-200: IP at rf-sputter chamber

1. Check the pressure of the EES chamber (~1.0×10^{-8} Torr).
2. Turn on the power.
3. Push the [**HV**] button and then push [**ST**] button. The pressure will be dramatically increased. First time of ON/OFF should be instant and then increased the ON/OFF time. This process should be performed until the pressure is in steady state.

B-3: UV Lamp

UV Lamp Control Unit

1. Check the pressure of the EES chamber (~1.0×10^{-9} Torr).
2. Connect the cable: black - up and red - down.
3. Turn on the power using [**MAINS**] switch.

   → The voltage and current will be increased.

B-4: Quadrupole Mass Spectrometer (QMS)

RGA program

1. Check the pressure of the EES chamber (~1.0×10^{-9} Torr).
2. Mount the QMS control box to QMS head at EES chamber.
   A. Connect the RGA200 cable with the QMS port.
   B. Tighten the RGA200 cable using knobs.
3. Connect the power and RS232 and ground cables.
4. Turn on the power.
5. Open the RGA program.
6. Click the [**Utilities**] and then click the [**RS232 Setup**].
   A. Check the COM Port: [**COM1**].
   B. Click the [**Connect**] button.
7. Click the [Head] and then click the [**Degas**].
8. After finishing the degassing, click the [**Utilities**], [**RS232 Setup**], and [**Disconnect**].

9. Close the RGA program.

10. Turn off the power.

B-5: Argon Ion Sputtering Gun

Iom Gun Power Supply 86 79 11

1. Check the pressure of the EES chamber (~1.0×10^{-9} Torr).

2. Push the power button.

3. Turn the knob to [**DEGAS**] in [**FUNCTION**].

4. After finishing the degassing, red lights will be blinking.

5. Turn the knob to [**0**] and push the power button.

B-6: Argon Ion Depth Gun

400X Gun Supply

1. Check the pressure of the EES chamber (~1.0×10^{-9} Torr).

2. Push the power button. Yellow light will be on and the filament current will be increased.

3. Wait for ~5 min.

4. Decrease the filament current slowly and push the power button.

B-7: Electron Flood Gun

Flood Gun Supply Unit 401

1. Check the pressure of the EES chamber (~1.0×10^{-9} Torr).

2. Push the power button.
3. Increase the filament current slowly using knob up to 2.2 A. 0.2 A of increment is recommended. The emission current will be increased after 2.0 A of filament current.
4. Wait for ~5 min.
5. Decrease the filament current slowly and push the power button.

B-8: Electron Source for AES

Gun Supply

1. Check the pressure of the EES chamber (~1.0×10^{-9} Torr).
2. Change the toggle switch of power to [**ON**].
3. Increase the filament current slowly using knob up to 2.1 A. 0.2 A of increment is recommended.
4. Wait for ~5 min.
5. Decrease the filament current slowly.
6. Change the toggle switch of power to [**OFF**].

B-9: X-ray Source for EES

XRCB-01, XRHV01-PS, XR40B-EC

1. Check the pressure of the EES chamber (~1.0×10^{-9} Torr).
2. Chiller (HX-20H and XRCB-01).
   A. Turn on the power.
   B. Check the setting temperature of chiller. If the temperature

setting is not 18°C, push the [**MENU**] button and set the temperature at 18°C using arrow buttons.

3. X-ray source (XRHV01-PS and XR40B-EC).

   A. Turn on the power of two controllers. The display and green light of POWER will be on.

   B. Push the [**STBY**] button. Green light of OPERATE will be on.

   C. Check the arrow in panel is located at filament voltage.

   D. Increase the high voltage up to 14. 0 kV using knob. 1 kV of increment is recommended. Watch the pressure and adjust the increasing speed.

   E. Push the [**U/Ie**] button to select the filament current.

   F. Increase current to 20 mA for Mg and 30 mA for Al source using knob. 0.5 mA of increment is recommended.

   G. Wait for ~5 mins.

   H. Decrease the current slowly, push the [**U/Ie**] button, decrease the voltage slowly, and then push the [**STBY**] button.

   I. Change the anode type.

      i. Push the [**MENU**] button.

      ii. Check the ANODE TYPE and push the [**OK**] button.

      iii. Select the anode type, Aluminium or Magnesium, using [**ARROW**] button and then push the [**OK**] button.

      iv. Push the [**ESC**] button.

   J. Degas other anode as follow step B~H.

   K. Turn off the power of two controllers.

4. Turn of the chiller after 1 hr.

B-10: X-ray Source for SAM

362 Spectrometer Control Unit, 360 and 367C X-ray source

1. Check the pressure of the EES chamber (~1.0×10^{-9} Torr).
2. Turn on the chiller (HX-20H).
3. Set the spectrometer control unit.
   A. Push the [**POWER**] button.
   B. Move the [**ENERGY**] knob to Al B.E. or Mg B.E. to select Al or Mg anode. Two anodes are need to degas.
4. Set the X-ray source
   A. Change the toggle switch to [**MAINS ON**]. Red light will be on.
   B. Move the knob to [**START**].
   C. Push the [**ON**] button (green) in MAINS. Filament current will be increased ~5 A.
   D. Increase the anode volts using the knob in ANODE VOLTS until emission reads to 20 mA.
   E. Move the knob to [**5 mA**] and slightly increase the volts.
   F. Move the knob to [**10 mA**] and slightly increase the volts.
   G. Move the knob to [**20 mA**] and increase the volts until emission reads to 20 mA.
   H. Wait for ~5 min.
   I. Move the knob to [**10 mA**] and then [**5 mA**].

J. Decrease the volts.

K. Move the knob to [**START**].

L. Drop the voltage down to zero.

M. Push the [**OFF**] button (red) in MAINS.

5. Wait for ~5 min.
6. Change the anode by step 3.B.
7. Degas the anode.
8. Push the [**POWER**] button in the spectrometer control unit.
9. After 1 hr, turn off the chiller.

B-11: LEED/AES

Spectraleed Control Unit

- Description below is that we are doing **Auger Electron Spectroscopy**.
- If you want to do **LEED** experiment, change the cable at the back panel of the Spectraleed Control Unit.

1. Check the pressure of sample preparation chamber (~1.0×10^{-9} Torr).
2. Push the [**MAINS**] button.
3. Check the selection is [**AUGER**] instead of [**LEED**].
4. Push the [**I FIL**] button.
5. Increase the filament current slowly up to 1.25 A. 0.1 A of increment is recommended. Watch the pressure and adjust the increasing speed.

6. Push the [**E**] button.
7. Increase the high voltage slowly up to 3 kV. 0.2 kV of increment is recommended. Watch the pressure and adjust the increasing speed.
8. Wait for ~5 min.
9. Decrease the high voltage slowly.
10. Push the [**I FIL**] button and decrease the filament current slowly.
11. Push the [**MAINS**] button.

Appendix C: Procedure for Loading and Unloading Samples

- Think before doing anything (assume that what you are doing is wrong and needs to be rethought).

- Check the valves before opening or closing anything.

- Remember to wheel tracks back before shutting valves between chambers.

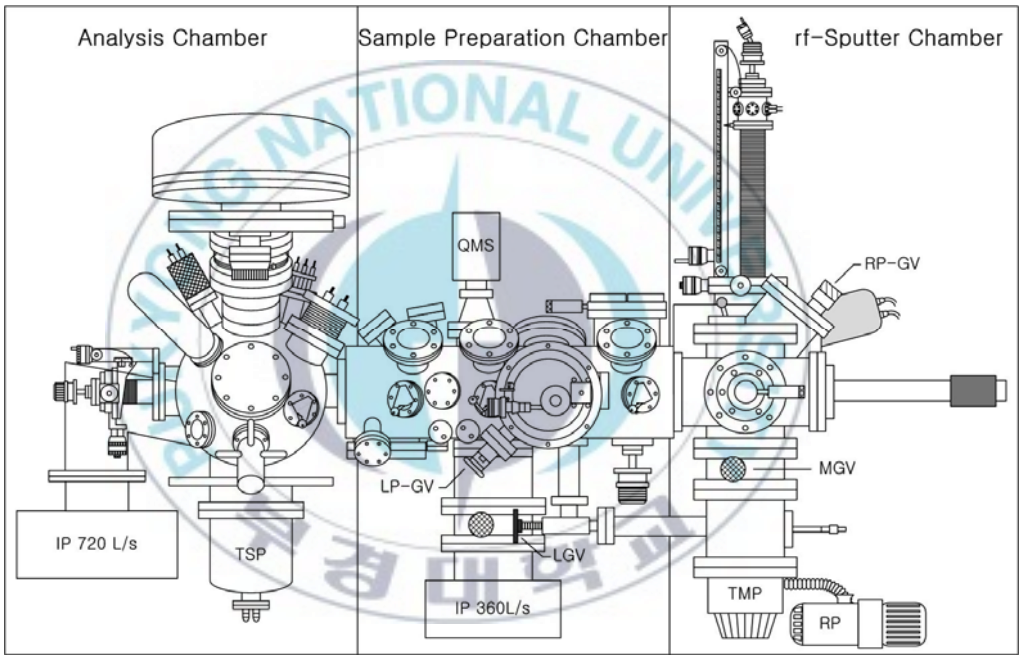

1. Move the sample to load-lock chamber.

   A. Pump the load-lock chamber.

      i. Close the MGV and then open the LGV.

      ii. Wait at least 1 hr.

   B. Close the LGV and then open the MGV.

   C. Open the LP-GV slowly. Watch the pressure and adjust the

opening speed.

D. Put the rail into the sample preparation chamber.

E. Move samples into load-lock chamber using wobble sticks.

F. Take the rail out of the sample preparation chamber.

G. Close the LP-GV valve.

H. Pump the sample preparation chamber for ~10 min.

2. Vent the load-lock chamber and change the sample.

A. Close the MGV and check that the LP-GV and LGV are closed.

B. Turn off TMP.

i. Push the [**START/STOP RESET**] button and check the PUMP READY: PUSH START BUTTON in panel.

ii. Wait at least 1 hr.

C. Recheck that the LP-GV, LGV, and MGV are closed.

D. Open the valve of N_2 gas cylinder counterclockwise.

E. Open the nupro vent valve counterclockwise.

F. At 760 mTorr, open the door, load samples, and close the door.

3. Pump the load-lock chamber.

A. Close the vent valve and the valve for N_2 gas cylinder.

B. Turn on the hood.

C. Open the LGV slowly and wait until the pressure is about ~20 mTorr.

D. Turn on TMP.

i. Push the [**START**] button and check the NORMAL

OPERATION in panel.

ii. Overnight pumping is preferred.

4. Move the sample to sample preparation chamber.

A. Close the LGV and then open the MGV.

B. Open the LP-GV slowly. Watch the pressure and adjust the opening speed.

C. Put the rail into the sample preparation chamber.

D. Move samples into load-lock chamber using wobble sticks.

E. Take the rail out of the sample preparation chamber.

F. Close the LP-GV valve.

* Manipulator Settings for Various Techniques (in black scale).

	XPS	AES	UPS	ISE 5	EX05
X	10.70	9.62	13.50	9.70	14.50
Y	11.30	15.70	15.00	21.50	12.30
Z	19.50	15.70	17.75	17.75	19.50
θ	210°	190°	175°	305°	160°

Appendix D: Procedure for XPS

D-1: XPS at EES Chamber

- Don't use liquid samples.
- Make sure equipment is not running while loading or unloading samples.
- Don't touch wires when high voltage is on.

1. Set the sample position for XPS experiment.

   X: 10.70

   Y: 11.30

   Z: 19.50

   θ: 210°

   (All numbers are on black scales)

2. X-ray source (XRCB-01, XRHV01-PS, and XR40B-EC).

   A. Turn on the power of chiller (HX-20).

   B. Check the setting temperature of chiller. If the temperature setting is not 18°C, push the [**MENU**] button and set the temperature at 18°C using arrow buttons.

   C. Turn on XRCB-01.

   D. Turn on the power of two controllers. The display and green light of POWER will be on.

   E. Check the anode type in panel. If the change of anode type is needed, follow the steps as below.

i. Push the [**MENU**] button.

ii. Check the ANODE TYPE and push the [**OK**] button.

iii. Select the anode type, Aluminium or Magnesium, using [**ARROW**] button and then push the [**OK**] button.

iv. Push the [**ESC**] button.

F. Push the [**STBY**] button. Green light of OPERATE will be on.

G. Check the arrow in panel is located at filament voltage.

H. Increase the high voltage up to 14.0 kV using knob. 1 kV of increment is recommended. Watch the pressure and adjust the increasing speed.

I. Push the [**U/Ie**] button to select the filament current.

J. Increase current to 20 mA for Mg and 30 mA for Al source using knob. 0.5 mA of increment is recommended.

3. 340/361 Lock-in amplifier.

   Pull the power button.

4. 363 Spectrometer indicator.

   A. Turn on [**MAINS**] switch.

   B. Check the [**SCINTILLATOR**] is off.

   C. Check the switch to ESCA.

5. 362 Spectrometer control unit.

   A. Push the [**POWER**] button.

   B. Check the energy selection knob to Al B.E.

6. 434 Electron multiplier.

A. Push the [**POWER**] button.

B. Turn on the toggle switch in the channeltron voltage panel.

7. 454 ESCA lens power supply.

A. Push the [**POWER**] button.

B. Push the [**HIGH VOLTAGE**].

8. Open the XPS program: XPS-Survey, XPS-narrow.

9. Change the settings as necessary.

Condition	Survey	Narrow
Analyzer transmission	CAE 100 eV	CAE 50 eV or 20 eV
Dwell time [ms]	100	100
Step [eV]	0.5	0.05
Sweeps	4	9

10. Run the XPS program.

11. After finishing the measurement, follow the step as above inversely.

D-2: XPS at SAM Chamber

1. Set the sample position for XPS experiment.

2. 367C X-ray source.

A. Turn on the power of chiller (HX-20).

B. Check the setting temperature off chiller. If the temperature setting is not 18°C, push the [**MENU**] button and set the temperature at 18°C using arrow buttons.

C. Move the toggle switch to MAINS ON. Red light will be on.

D. Selection knob to **[START]**.

E. Push the **[ON]** button (Green) in **[MAINS]**.

F. Increase the anode volts until emission reads to 20 mA.

G. Move the knob to 5 mA and slightly increase the anode volts.

H. Move the knob to 10 mA and slightly increase the anode volts.

I. Move the knob to 20 mA.

J. Increase the anode volts until emission reads to 20 mA.

K. Anode Volts stays about 9.0 kV and filament current stays between 4 and 5 A.

3. 340/361 Lock-in amplifier.

   Pull the power button.

4. 363 Spectrometer indicator

   A. Turn on [**MAINS**] switch.

   B. Check the [**SCINTILLATOR**] is off.

   C. Check the switch to ESCA.

5. 362 Spectrometer control unit

   A. Push the [**POWER**] button.

   B. Check the energy selection knob to Al B.E. or Mg B.E.

6. 434 Electron multiplier

   A. Push the [**POWER**] button.

7. 454 ESCA lens power supply

   A. Push the [**POWER**] button.

B. Turn on the toggle switch in the channeltron voltage panel.

8. 454 ESCA lens power supply.

   A. Push the [**POWER**] button.

   B. Push the [**HIGH VOLTAGE**]

9. Open the XPS program: XPS-Survey, XPS-narrow.

10. Change the settings as necessary.

Condition	Survey	Narrow
Analyzer transmission	CAE 100 eV	CAE 50 eV or 20 eV
Dwell time [ms]	100	100
Step [eV]	0.5	0.05
Sweeps	4	9

11. Run the XPS program.

12. After finishing the measurement.

   A. Turn off the electron multiplier and ESCA lens power supply.

   B. Selection knob to 10 mA and then 5 mA.

   C. Lower anode volts down slowly.

   D. Selection knob to start.

   E. Lower the voltage down to zero.

   F. Turn off [**MAINS**] switch.

   G. Turn off other controllers.

Appendix E: Procedure for AES

1. Set the sample position for AES experiment.
2. 432 Gun Supply.
   A. Change the toggle switch of power to [**ON**].
   B. Increase the filament current slowly using knob up to 2.1 A. 0.2 A of increment is recommended.
   C. Check the beam current is positioned at indicator.
   D. Change the toggle switch of HV to [**ON**].
   E. Increase the HV slowly using knob up to 3 kV.
3. 340/361 Lock-in amplifier.

   Pull the power button.
4. 363 Spectrometer indicator
   A. Turn on [**MAINS**] switch.
   B. Check the [**SCINTILLATOR**] is off.
   C. Check the switch to ESCA.
5. 362 Spectrometer control unit
   A. Push the [**POWER**] button.
   B. Check the energy selection knob to Al B.E. or Mg B.E.
6. 434 Electron multiplier
   A. Push the [**POWER**] button.
7. 454 ESCA lens power supply

A. Push the [**POWER**] button.

B. Turn on the toggle switch in the channeltron voltage panel.

8. 454 ESCA lens power supply.

A. Push the [**POWER**] button.

B. Push the [**HIGH VOLTAGE**].

9. Open the AES program: DATAuger.

10. Change the settings as necessary.

11. Run the AES program.

12. After finishing the measurement, follow the step as above inversely.

Appendix F: Procedure for UPS

ON Process

1. Set the sample position for UPS experiment.
2. Close GVs for IPs.
3. Turn off the IG of analysis chamber.
4. Open MGV (two and half turns).
5. 232 UV Lamp Control Unit
   A. Check that RP and TMP for UPS are on and lamp lines are pumped. If the pumps are off, turn on the pumps and do not open the valve, just pump the lines (at least 1 hr).
   B. Just open the RP valve and fully open the TMP valve.
   C. Turn on mains. The voltage will be immediately increased. The current will be increased when the UV light appeared.
   D. Check the knob to [**MAX**].
   E. Open the He gas cylinder.
   F. Open the nupro valve (green) of He.
   G. Slowly open the leak valve of He until UV light appeared. The pressure must be lower than 1.5×10^{-7} Torr (by IG of sample preparation chamber).
   H. Open the MGV fully.
   I. Close the leak valve until ~1.5×10^{-7} Torr.
6. 340/361 Lock-in amplifier.

Pull the power button.

7. 363 Spectrometer indicator

   A. Turn on [**MAINS**] switch.

   B. Check the [**SCINTILLATOR**] is off.

   C. Check the switch to ESCA.

8. 362 Spectrometer control unit

   A. Push the [**POWER**] button.

   B. Check the energy selection knob to Al B.E. or Mg B.E.

9. 434 Electron multiplier

   Push the [**POWER**] button.

10. 454 ESCA lens power supply

   A. Push the [**POWER**] button.

   B. Turn on the toggle switch in the channeltron voltage panel.

11. Sample bias (Farnell D30 2T)

   A. Connect the power supply lines: black-sample and red-chamber.

   B. Push the [**INPUT**] and then [**AMP OUTPUT**] buttons.

   C. Increase the voltage using knob (normally 10 V).

12. Open the UPS program.

13. Change the settings as necessary.

Condition	UPS
Scan range [eV]	0 ~ 40
Analyzer transmission	CAE 20 eV
Dwell time [ms]	100
Step [eV]	0.02

Sweeps	9

14. Run the UPS program.

15. After finishing the measurement,

    A. Close the leak valve.

    B. Open the GV of pumping.

    C. Close the nupro valve and Ar cylinder.

    D. Turn off the electron multiplier and ESCA lens power supply.

    E. Turn off other controllers.

    F. Turn off sample bias.

    G. Open the GVs of IPs at $\leq 1.5\times10^{-9}$ Torr (wait for ~1 hr).

Appendix G. Procedure for Electron Flood Gun

- Use the electron flood gun during XPS and AES experiment.

1. Push the power button.
2. Increase the filament current slowly using knob up to 2.2 A. 0.2 A of increment is recommended. The emission current will be increased after 2.0 A of filament current.
3. After finishing the measurement, decrease the filament current slowly and push the power button.

Appendix H. Procedure for Ar Ion Sputtering

1. Set the sample position for Ar Ion Sputtering (ISE 5 and EX05).
2. Close the GVs for IPs.
3. Close the MGV until the gate is touched.
4. Open the Ar cylinder.
5. Open the nupro valve for Ar.
6. Attach the magnet.
7. Take X-ray source back.
8. Slowly open the leak valve to introduce the Ar into the analysis chamber and adjust the pressure (~1.0×10^{-5} Torr).

For ISE 5

9. Push the power button.
10. Increase the beam energy using knob.
11. Record the pressure, target current, and sputtering time.
12. After finishing the sputtering, decrease the beam energy and turn off the power.

For EX05

9. Push the power button and check the [**ION ENERGY**] (≥3 keV).
10. Move the knob to [**OPERATE**].

11. Record the pressure, target current, and sputtering time.
12. After finishing the sputtering, move the knob to [**0**] and then turn off the power.

13. Close the leak valve.
14. Open the GV of pumping.
15. Close the nupro valve and Ar cylinder.
16. Open the GVs of IPs at $\leq 1.5\times10^{-9}$ Torr (wait for ~1 hr).

Appendix I. Procedure for Depth Profile

1. Set the sample position for depth profile (400X).
2. Close the GVs for IPs.
3. Close the MGV until the gate is touched.
4. Open the Ar cylinder.
5. Open the nupro valve for Ar.
6. Attach the magnet.
7. Take X-ray source back.
8. Slowly open the leak valve to introduce the Ar into the analysis chamber and adjust the pressure (~1.0×10^{-5} Torr).
9. Push the power button. Yellow light will be on and the filament current will be increased.
10. Move the toggle switch to [**HT**] from [**STANDBY**].
11. Move the toggle switch to [**ON**]. The sputter will be operated.
12. After finishing the sputtering, move the toggle switches to [**OFF**], [**STANDBY**], and turn off the power.
17. Close the leak valve.
18. Open the GV of pumping.
19. Close the nupro valve and Ar cylinder.
20. Open the GVs of IPs at ≤ 1.5×10^{-9} Torr (wait for ~1 hr.)

Appendix J: Procedure for Quadrupole Mass Spectrometer (QMS)

1. Turn on the power.
2. Open the RGA program.
3. Connect QMS with RGA program.
   A. Click the [**Utilities**] and then click the [**RS232 Setup**].
   B. Check the COM Port: [**COM1**].
   C. Click the [**Connect**] button.
4. Turn on the filament.

Click the [**Head**] and then click the [**Filament On**].

5. Turn on the electron multiplier.
   A. Click the [**Channel Electron Multiplier**]
   B. Click the [**On**] in Channel Electron Multiplier panel.
   C. Click the [**OK**].
6. After finishing the measurement, turn off the electron multiplier and filament, and disconnection.
7. Close the RGA program.
8. Turn off the power.

Appendix K: Procedure for rf Sputtering in UHV

1. Load the substrate on the precision 5-axis manipulator. Use the wobble sticks with caution.
2. Adjust the sample position for rf sputtering. Refer the guide lines on the Z-axis of the manipulator.
3. Turn on the power of chiller (HX-20). Check the setting temperature and the water valves are opened.
4. Pre-pumping the gas line then fill up the gas line with desired gases.
5. Deposit the film.
   A. Checklist before deposit the film.
      i. Close the RP-GV.
      ii. Turn off the IP and IG.
      iii. Turn on the chiller.
      iv. Close the target shield.
   B. Adjust the rf power to desired value (depending on the target and 100 W is normally used to starting point).
   C. Adjust the working pressure to ~25 mTorr (by convectron gauge) using GV.
   D. After the pre-sputtering, sputter the target as the shield open. The time of pre-sputtering and sputtering is normally 5 and 10 min, respectively.

Appendix L: Procedure for rf co-Sputtering

1. Cleaning substrate

   - Never touch the surface of substrate with bare hands.

   A. Wear gloves and using tweezers.

   B. Wipe the substrate (glass or Si wafer) with acetone.

   C. Attach the kapton tape at the end of substrate (2 mm) for thickness measurement.

2. Install substrate

   - For all toggle switches, upside is on and downside is off.

   - [**V**] means valve and it needs few seconds for fully operation. Please wait until no more air leaking sound.

   - Never touch the switch of [**TURBO**] (red light) and [**RP**] (green light) in power & schematic diagram panel. A turbo molecular pump (TMP) and a rotary vane pump (RP) must be always working.

   A. Off [**MV**]. Orange light is off.

   B. Vent the chamber: On [**HLV**]. You can check the pressure using convectron gauge from 0.0 mTorr to 780 Torr.

   C. Open the lid: On [**CHAMBER**].

   D. Install the substrate at desired position using a clean screw driver.

   E. Check the cleanliness of the inside of the chamber and target at the bottom of chamber.

F. Off [**CHAMBER**] and [**HLV**].

G. Pumping by RP: Off [**FV**] and then On [**RV**].

H. Pumping by RP and TMP: Off [**RV**] and then On [**FV**] and [**MV**]. The pressure will be reach ~0.0 mTorr by a convectron gauge.

3. Measure pressure

A. Check the pressure using convectron gauge (0.0 mTorr is minimum).

B. Open the gate valve of ion gauge (IG).

C. Read the pressure by IG.

i. Open the gate valve.

ii. Select IG by pushing [**CHAN**] button until OFF sign on the display.

iii. Push [**EMIS**] for IG and read the base pressure.

D. Turn off IG and close MGV.

4. Set temperature

A. Change [**Prog/PV**] switch to [**Prog**].

B. Push [**Shift**] + [**Seg/Check**] together to change mode until LEVL appears.

C. Change the temperature by using side and up arrows.

D. Restore the temperature by pushing [**Ent/End**] button.

E. Turn on the [**TP**] switch to heating.

F. Change [**Prog/PV**] switch to [**PV**].

G. Start heating by pushing [**Run/Step**] button.

H. Adjust the [**volume**] knob to get desired temperature.

I. Push [**Hold**] button to maintain at the target temperature when the SV value reached just below the target temperature.

J. After finishing the experiment, push [**Shift**] + [**Seg/Check**] together.

5. Deposit film

A. Close MGV until feels the door touched.

B. Set the mass flow controller (MFC).

i. Turn on the power switch. Red number is real flow value and yellow number is set value.

ii. On [**GMV**] toggle switch.

iii. On [**CH-1**] for Ar and [**CH-2**] for O_2/N_2, if needed. These are toggle switches.

iv. Set MFC to desired value using knob (normally P(Ar) = 20 sccm).

C. Turn on the rf generators and matching boxes.

D. Increase the rf power slowly while watching the view port whether plasma generated or not. When the plasma is generated, measure time.

E. Adjust working pressure to ~45 mTorr (by convectron gauge) using MGV.

F. Finish the pre-sputtering, turn on the switch for the target shield (S1, S2, and S3) in turbo power supply panel. Normally, the time of pre-sputtering and sputtering is 10 min).

G. After sputtering.

i. Turn off the rf power and then decrease the rf power.

ii. Turn off [**CH-1**], [**CH-2**], [**MGV**], and power of MFC.

iii. Open MGV.

6. See the step 1 and 2 for next experiment.

Appendix M: Procedure for Kelvin probe (KP)

- Make sure the surroundings are quite and lights are blocked before KP measurement.

1. Turn on the power of KP6500 and computer.
2. Open the KP6500 program.
3. Sampling

   Put the sample on the sample holder and connect between the sample and sample holder using clip.
4. Set the probe characterization.

   A. Retract the probe tip away from the sample.

   B. Click the [**CONFIGURATION**] and then [**PROBE CHARACTERIZATION**]. Amplitude will be set to 0.

   C. [**KP500 CONTROL**]

      i. Probe Controls

      Frequency: 260, Amplitude: 20, DC Offset: 0.000

      ii. Backing Potential Controls

      Upper BP (V): 1.00, Lower BP (V): -1.00, Scan Steps: 1

      iii. Data Acquisition Controls

      Trigger Delay: 68, A/D points: 1000, A/D Rate: 3332, D/A Delay: 0

      iv. Series Controls

      Number: 0, Average over: 1, Interval (s): 0.0

D. [**PROBE CHARACTERIZATION**]

i. Start: 50, End: 500, Step: 5

ii. Click the [**START**]

E. Determinate the value of frequency with low amplitude.

5. KP500 Control

A. Probe Controls

Frequency: 260, Amplitude: 50, DC Offset: 0.000

B. Backing Potential controls

Upper BP (V): 1.00, Lower BP (V): -1.00, Scan Steps: 1

C. Data Acquisition Controls

Trigger Delay: 68, A/D points: 1000, A/D Rate: 3332, D/A Delay: 0

D. Series Controls

Number: 0, Average over: 1, Interval (s): 0.0

E. Click the [**GO**].

F. Move the probe tip close to the sample. The raw signal will be changed.

G. Reduce the data points in Raw Signal panel.

i. Click the mouse button twice in Raw Signal panel.

ii. Select the [**Raw signal Customization**].

iii. Change the value to 100 in Points-Points to Graph.

iv. Click the [**OK**]. If you can see the sine wave, tip is getting close to the sample. When the gradient is 1.0 in the Latest

Reading panel, click the [**STOP**].

6. Tracking Mode

   Set point gradient: 0.300, Step Size: 0.001, Max Gradient Deviation: 0.001.

7. Click the [**BEGIN**] and then [**GO**].

8. Read the valves of CPD and Gradient when the value of Gradient is closed to that of setting point gradient.

9. After finishing the measurement, click the [**STOP**] in menu bar.

10. Enter the [**0**] at DC Offset.

11. Retract the probe tip away from the sample.

12. Close the KP6500 program and turn off the controller and computer.

Appendix N: Procedure for Alpha Step

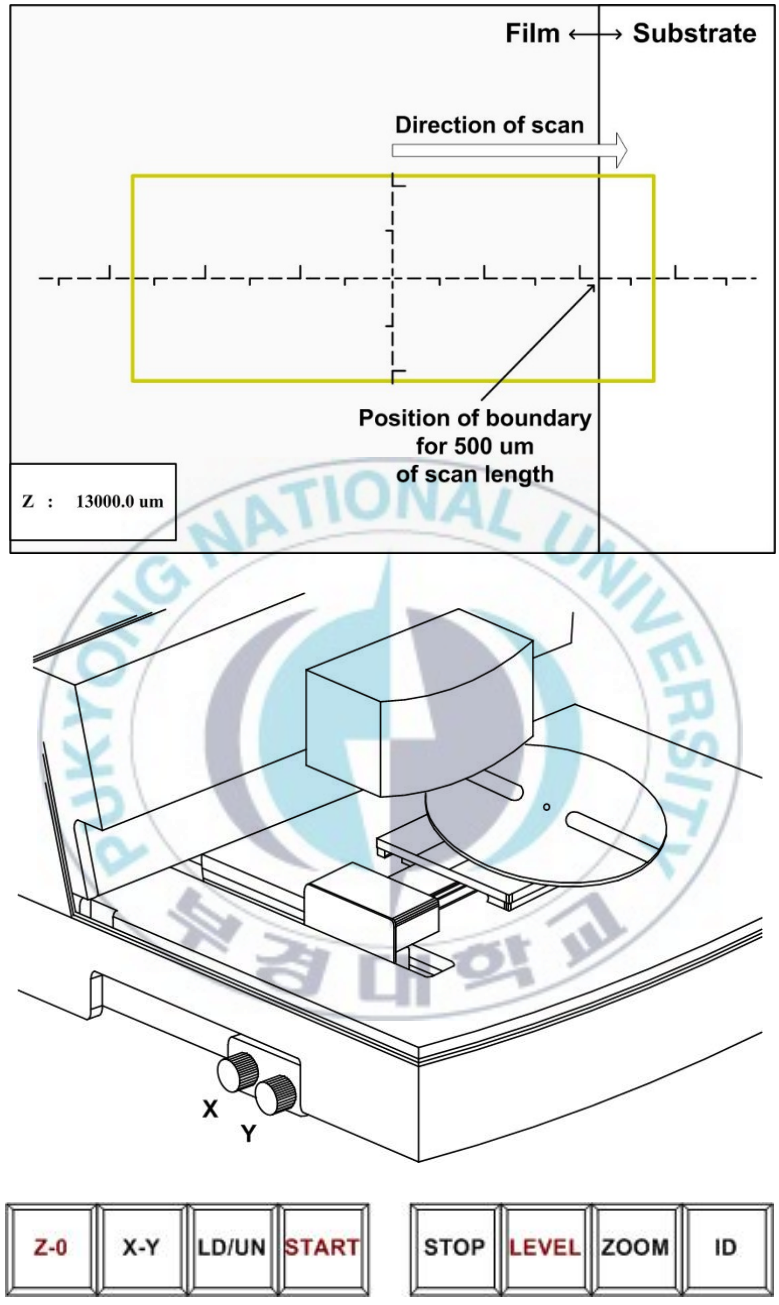

1. Push the power button and turn on the monitor.

2. Push the [**ESC**] key in the keyboard.

3. Push the [**ENTER**] key in the keyboard.
4. Set the save mode.
   A. Go to [**CONFIG**] and select [**SETTING**] using arrow keys.
   B. Change to enable from disable in the save data in ASCII using arrow in keyword.
   C. Press the [**F2**] key.
   D. Go to [**CONFIG**] and select [**DISK PATH**].
   E. Choose the [**A:**] in Export To/Import From.
   F. Press the [**F3**] key.
5. Set the scan condition.
   A. Go to [**RECIPE**] and select [**VIEW/MODIFY**].
   B. Change the scan length and speed. Normally, 500 μm of scan length and 20 μm/s of scan speed are suitable to measure the film thickness.
   C. Press the [**F4**] key in the keyboard.
6. Put the sample on the middle of stage.
7. Press the [**Z-0**] key in the keyboard.
8. Keep the downwards arrow key pressed before the tip shows the monitor.
9. Put the tip on the middle of sample using X and Y knobs.
10. Press the downwards arrow until the tip is reflected on the sample.
11. Adjust the position of sample to start the measurement.
12. Press the [**START**] key in the keyboard. Keep the quiet during scan.

13. Level the graph.

    A. Press the [**LEVEL**] key in the keyboard. Two red lines are appeared.

    B. Press the space bar to switch the left and right red lines.

    C. Set the left red line at the left of substrate and the right red lines at the right of substrate using arrows.

    D. Press the [**LEVEL**]. The modified graph will be shown in monitor.

14. Set the left blue line at the film and the right blue line at the substrate.

15. Read the thickness.

16. Move the stage using X and Y knobs. The 10 measurements are normal for one sample.

17. After finishing the measurement, press the upwards arrow key. For the measurement of other samples, see the step 18. For stop the measurement, see the step 19.

18. For the measurement of other samples, change the sample and follow the step 7.

19. For stop the measurement, take off the sample and follow the steps as below.

    A. Go to [**EXIT**] and select the [**SHUTDOWN**].

    B. Press the [**F2**] key.

    C. Push the power button of computer.

Appendix O. Procedure for 4-point Probe

1. Mount the sample on the Si wafer of sample holder (1.33 inch blank flange).
2. Remove the cover (petri dish) of probe.
3. Open the controller (MCP-T600).
4. Turn on the power at the backside of controller.
5. Set the thickness of film.
   A. Select MEAS. CONDITION using arrow button in the controller and then push the [**ENT**] button in the controller.
   B. Check the MEAS. POSI. FILE and then push the [**ENT**] button.
   C. Check the CONSTANT RCF and then push the [**ENT**] button.
   D. Select the THICKNESS using arrow button, enter the thickness of films using number buttons, and then push the [**ENT**] button.
   E. Push the [**ESC**] button 3 times.
6. Set the sample for measurement.
   A. Move the probe stage to the lowest level using the knob of microscope.
   B. Check the lens is the shortest one (27780).
   C. Set up the sample holder on the probe stage. Sample is downside.
   D. Switch the lens of microscope from the shortest one (27780) to the middle one (19698).

E. Move the probe stage to the highest level carefully.

7. Measure the electrical properties.

A. Select the MEASUREMENT using arrow button and then push the [**ENT**] button.

B. Push [**START/HOLD**] button to start the measurement.

C. Push the [**START/HOLD**] button to stop the measurement.

D. Record the values having different units (S/cm, Ω, Ω/sq., and Ω·cm) by pushing the [**UNIT**] button in the controller.

8. Change the sample.

A. Move the probe stage to the lowest level.

B. Switch the lens of microscope from the middle one (19698) to the shortest one (27780).

C. Take off the sample holder, change the sample and then set up the sample holder.

D. Start to the step 6.D.

9. Finish the measurement.

A. Push the [**ESC**] button.

B. Turn off the power of controller.

C. Close the controller.

Appendix P: Procedure for Measurement of Contact Angle

1. Check that the magnification of camera lens is 5X (lens: red line, 105323).
2. Mount the camera.
   A. Remove the lens of camera.
   B. Mount the camera on the eyepiece of the microscope.
3. Mount the sample on the mark of the sample holder.
4. Turn on the backlight.
5. Find the proper position of sample using camera. Careful movement is required.
6. Drop the droplet (2 μL) at the end of surface using micropipet and take a picture immediately. Distilled water (DW) and ethylene glycol (EG) are normally used as the test solution.
7. After finishing the measurement, turn off the backlight and take the camera off the microscope.
8. Analyze the data using [**Motic Images Plus 2.0**] program.

Appendix Q: Procedure for Measurement of Viscosity

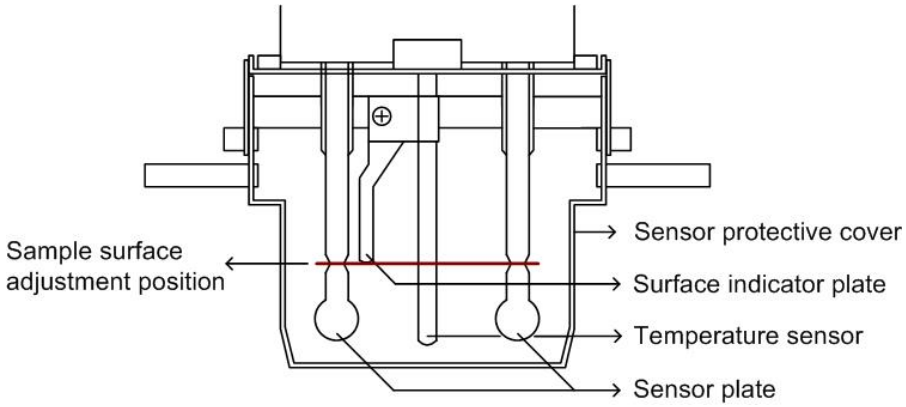

1. Fill the solution into the sample cup until its surface reaches at the level gauges.
2. Put the sample cup on the table and then fix the sample cup using two guides.
3. Pull the sensor protective cover to front direction.
4. Hold the sensor unit until the number 7.
5. Lean back the level at the supporting post.
6. Pinch grips and then move gently the sensor unit. It is enough to touch the sensor plate with the sample surface. Do not move too close.
7. Pull the level at the supporting post.
8. Adjust the remained distance using the knob at the lap-jack. The appropriate level is shown in figure.
9. Push the [**ON/OFF**] button of viscometer.
10. Push the [**START**] button to measure the viscosity of the sample.

11. Record the viscosity and temperature in the stable state.
12. Push the [**STOP**] button.
13. Press the [**ON/OFF**] button.
14. Down the table using the knob.
15. Hold the sensor unit, lean back the level, Pinch grips, move the sensor unit, and pull the level.
16. Clean the 4 plates using tissue paper. Move the tissue paper downward to remove the sample.
17. Put the sensor protective cover back.
18. For electrospinning, add the solution into the syringe.
19. Clean the sample cup.

Appendix R: Procedure for Electrospinning

- Check the ground of the equipment.

- Record the temperature and humidity.

- Do not touch wires when high voltage is on.

1. Make a electrospinning solution (mixture solution of polymer and inorganic material).
2. Check the viscosity using viscometer. To measure the viscosity, the volume of solution is at least 10 ml.
3. Setting of drum collector.
   A. Wrap drum collector with Al foil.
   B. Check the ground is connected.
   C. Control the collector real rpm at 100.
      i. Push the [**MODE**] button until SET is on display.
      ii. Set the real RPM is almost 100 by pushing the arrow buttons.
      iii. Push the [**MODE**] button to see the real rpm.
4. Setting of syringe pump.
   A. Transfer the solution to syringe.
   B. Attach the syringe needle (normally 21 gauge).
      i. Cut the needle flat with a scissors.
      ii. Smooth the flat surface with a sand paper.
      iii. Clean the needle in ethanol for 10 min using the ultrasonication.

C. Measure the distance between the end of needle and collector.

D. Connect the HV (+) lead at the end of the needle.

E. Set the conditions.

i. Turn on the power at the backside of controller (The power of syringe pump controller, KD scientific, is 110 V).

ii. Push the [**ENTER**] button until Vol. is on display.

iii. Push the [**SELECT**] button.

iv. Input the value of solution volume and then push the [**SELECT**] button.

v. Adjust the pumping speed.

vi. Push the [**ENTER**] button.

5. Collect the fiber.

A. Turn on the high voltage power supply.

B. Set the high voltage using the knob. The proper feed speed and high voltages make fiber.

6. Check the fiber using an optical microscope.

Appendix S: Procedure for Furnace

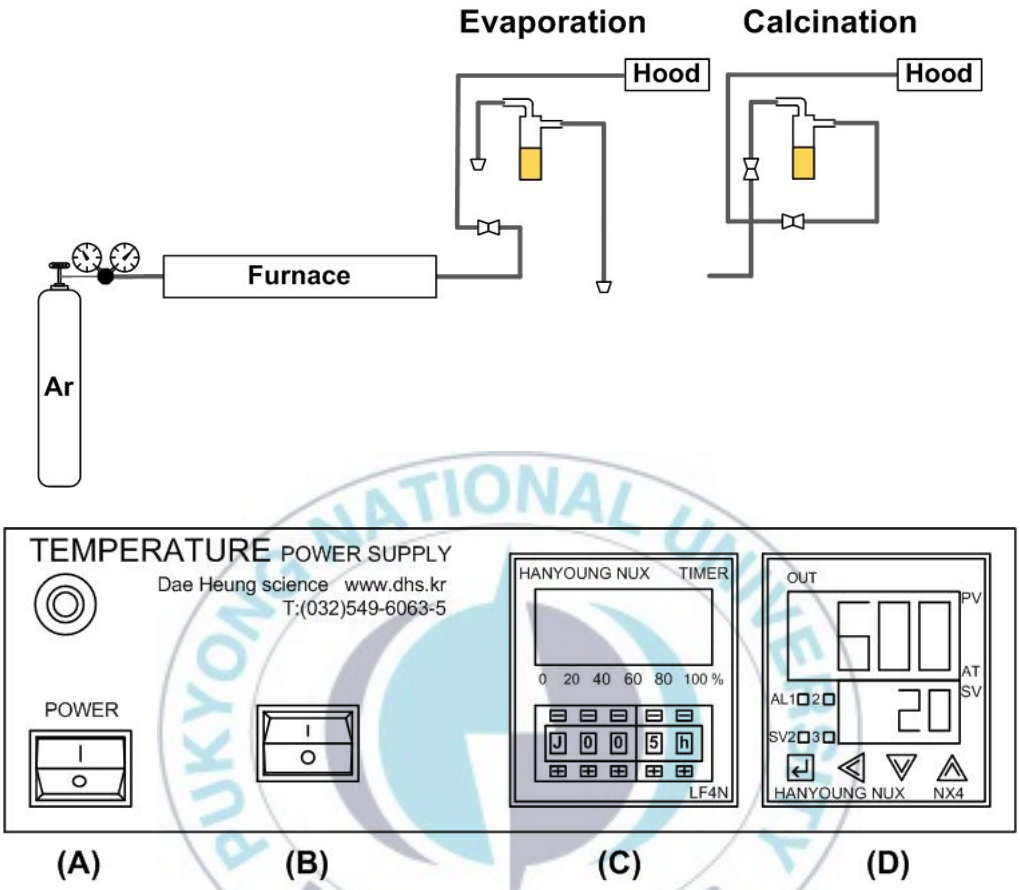

1. Put the sample in the crucible.
2. Open the screw anticlockwise.
3. Open the lid of the furnace.
4. Move the sample to the center of sensor using a bar.
5. Close the lid and screw.
6. Turn on the chiller. The power button is located at the back side of chiller. Do not touch the power button of front side. It is always on.
7. Set the vent lines. There are two modes, one is evaporation of

solvent and the other is calcination at high temperature. The setting of vent lines is shown in following figure and refer to the figure.

8. Turn on the power in the region (A) of controller.
9. Check the mode J, heating time, and unit in the region (C). Commonly the heating time is 5 hrs.
10. Set the temperature.
    A. Enter the number using arrow buttons in the region (D). The setting temperature is bottom number. The upper number indicates the real temperature. At the first time, the setting temperature should be lower than the wanted temperature. Repeat the A and B steps in the number 10 with increasing the setting temperature. When the setting temperature is reached to the wanted temperature, go to the number 11.
    B. Push the enter button in the region (D). Heating of sample is started and the real temperature will be increased.
11. Turn on the button (B). The timer is operated and the progress is appeared in region (C).
12. When the time is over, the tick sound is occurred.
13. Wait the temperature is down.
14. Open the screw anticlockwise and then open the lid.
15. Take out the sample.
16. Clean the tube using brush (stainless steel) and paper towel.
17. Close the lid and screw.
18. Turn off the power of controller and chiller.

Appendix T: XPS Line Positions Obtained from Mg Ka X-rays

Z		Photoelectron Lines												Auger Lines						
		1s	2s	$2p_{1/2}$	$2p_{3/2}$	3s	$3p_{1/2}$	$3p_{3/2}$	$3d_{3/2}$	$3d_{5/2}$	4s	$4p_{1/2}$	$4p_{3/2}$	KL_1 L_1	KL_1 L_{23}	$KL_{23}L_{23}$[b)]				
1	H																			
2	He																			
3	Li	**56**																		
4	Be	**113**																		
5	B	**191**														**1082**				
6	C	**287**														**993**				
7	N	**402**														**875**				
8	O	**531**	23											779	764	**743**				
9	F	**686**	30											645	626	**599**				
10	Ne	**863**	41	14										491	468	**435**				
11	Na	**1072**	64	31										332	303	**264**				
12	Mg		**90**	51																
13	Al		119	**74**																
14	Si		153	103	**102**															
15	P		191	134	**133**	14														

Z		Photoelectron Lines												Auger Lines						
		1s	2s	$2p_{1/2}$	$2p_{3/2}$	3s	$3p_{1/2}$	$3p_{3/2}$	$3d_{3/2}$	$3d_{5/2}$	4s	$4p_{1/2}$	$4p_{3/2}$	$L_3M_{23}M_{23}$[C]	$L_2M_{23}M_{23}$[C]	$L_3M_{23}M_{45}$ ^1P	$L_3M_{23}M_{45}$ ^3P	$L_2M_{23}M_{45}$ ^1P	$L_3M_{45}M_{45}$[d]	$L_2M_{45}M_{45}$
16	S		229	166	**165**	17								**1103**						
17	Cl		270	201	**199**	17								**1071**						
18	Ar		319	243	**241**	22								1037	**1035**					
19	K		378	296	**293**	33	17							1005	**1003**					
20	Ca		439	350	**347**	44	25							964	**961**					
21	Sc		501	407	**402**	53	31							**920**		892				
22	Ti		565	464	**458**	62	37							873		**839**				
23	V		630	523	**515**	69	40							822		**784**				
24	Cr		698	586	**577**	77	46	45						767		**729**				
25	Mn		770	652	**641**	83	49	48						715		**670**			620	
26	Fe		847	723	**710**	93	56	55						659		608			**553**	
27	Co		927	796	**781**	103	63	61						604	597	546	541		**483**	468
28	Ni		1009	873	**855**	112	69	67						548	542	482	476		**410**	393
29	Cu		1098	954	**934**	124	79	77						486	479	416	408	396	**337**	317
30	Zn		1196	1045	**1022**	140	92	89	10					429	422	352	343	329	**265**	242
31	Ga			1144	**1117**	160	108	105	20					368	361	284	275	257	**189**	162
32	Ge					184	128	124	32	**31**				305	297	215	205	184	**113**	82
33	As					207	148	143	45	**44**										
34	Se					232	169	163	58	**57**										
35	Br					256	189	182	70	**69**										
36	Kr					287	216	208	89	**88**	22									
37	Rb					322	247	238	111	**110**	29		14							

Z		Photoelectron Lines												Auger Lines						
		1s	2s	$2p_{1/2}$	$2p_{3/2}$	3s	$3p_{1/2}$	$3p_{3/2}$	$3d_{3/2}$	$3d_{5/2}$	4s	$4p_{1/2}$	$4p_{3/2}$	$L_3M_{23}M_{23}$[C)]	$L_2M_{23}M_{23}$[C)]	$L_3M_{23}M_{45}$ ^1P	$L_3M_{23}M_{45}$ ^3P	$L_2M_{23}M_{45}$ ^1P	$L_3M_{45}M_{45}$[d)]	$L_2M_{45}M_{45}$
38	Sr					358	280	269	135	**133**	37		20							
39	Y					395	313	301	160	**158**	45		25							
40	Zr					431	345	331	183	**181**	51		29							

		3s	$3p_{1/2}$	$3p_{3/2}$	$3d_{3/2}$	$3d_{5/2}$	4s	$4p_{1/2}$	$4p_{3/2}$	$4d_{3/2}$	$4d_{5/2}$	$4f_{5/2}$	$4f_{7/2}$	5s	$5p_{1/2}$	$5p_{3/2}$	$M_{45}N_{23}V$	$M_5N_4{}_5N_{45}$[d)]	$M_4N_4{}_5N_{45}$[d)]
41	Nb	470	379	364	209	**206**	59	35										**1088**	1056	
42	Mo	508	413	396	233	**230**	65	38										**1068**	1033	
43	Tc	544	445	425	257	**253**	68	39										1047	**1008**	
44	Ru	587	485	463	286	**282**	77		45[e)]									1025	**981**	
45	Rh	629	522	498	314	**309**	83		49[e)]									1002	**954**	
46	Pd	673	561	534	342	**337**	88		54[e)]									979	**928**	
47	Ag	718	604	573	374	**368**	97		58[e)]										903	**897**
48	C	772	652	618	412	**405**	109		68[e)]	11									889	**872**
49	In	828	704	666	453	**445**	123		79[e)]	19									853	**846**
50	Sn	884	757	715	494	**486**	137		91[e)]	26	25								827	**819**
51	Sb	946	814	768	539	**530**	155		105[e)]	35	34								803	**794**
52	Te	1009	873	822	585	**575**	171		114[e)]	44	43			14					775	**765**
53	I	1071	930	874	630	**619**	186		123[e)]	52	50			16					748	**737**
54	Xe	1144	997	936	685	**672**	209		141[e)]	65	63			19					724	**711**
55	Cs		1064	997	738	**724**	230	170	158	77	75			24					698	**684**
56	Ba		1137	1062	795	**780**	254	192	179	92	90			23					671	**657**
57	La			1126	851	**834**	274	210	195	104	101			34	17				632	

Z		Photoelectron Lines															Auger Lines			
		3s	$3p_{1/2}$	$3p_{3/2}$	$3d_{3/2}$	$3d_{5/2}$	4s	$4p_{1/2}$	$4p_{3/2}$	$4d_{3/2}$	$4d_{5/2}$	$4f_{5/2}$	$4f_{7/2}$	5s	$5p_{1/2}$	$5p_{3/2}$	$M_{45}N_{23}V$	M_5N_{45}	M_4N_{45}	
58	Ce			1184	900	**882**	290	222	207	112	108			37	18			594		
59	Pr				950	**930**	305	237	218	114[f]				38	20			555		
60	Nd				1001	**980**	318	248	227	120[f]				38	23			519		

		$3d_{3/2}$	$3d_{5/2}$	4s	$4p_{1/2}$	$4p_{3/2}$	$4d_{3/2}$	$4d_{5/2}$	$4f_{5/2}$	$4f_{7/2}$	5s	$5p_{1/2}$	$5p_{3/2}$	$M_{45}N_{23}V$	M_5N_{45}	M_4N_{45}	$M_{45}N_{45}V$	M_5VV	M_4VV
61	Pm	1060	**1034**	337	264	242	129				38	22			481				
62	Sm	1110	**1083**	349	283	250	132				41	20			440				
63	Eu	1166	**1136**	366	289	261	136				34	24			402				
64	Gd		**1186**	380	301	270	141				36	21			362				
65	Tb			398	317	284	150				42	28							
66	Dy			412	329	293	154				63	26							
67	Ho			431	345	306	**161**				51	20							
68	Er			451	362	320	**169**				61	25							
69	Tm			470	378	333	**180**				54	32	26						
70	Yb			483	392	342	194	**185**			55	33	26						
71	Lu			507	412	359	207	**197**			58	34	27						
72	Hf			537	437	382	224	213	19	**17**	64	37	30						
73	Ta			566	464	403	241	229	27	**25**	71	45	37						
74	W			594	491	425	257	245	36	**34**	77	47	37						
75	Re			628	521	449	277	263	45	**43**	81	44	33						
76	Os			657	549	475	294	279	55	**52**	86	60	48						

Z		Photoelectron Lines															Auger Lines			
		4s	$4p_{1/2}$	$4p_{3/2}$	$4d_{3/2}$	$4d_{5/2}$	$4f_{5/2}$	$4f_{7/2}$	5s	$5p_{1/2}$	$5p_{3/2}$	$5f_{5/2}$	$5f_{7/2}$	6s	$6p_{1/2}$	$6p_{3/2}$	N_7O_4 $_5O_{45}$	N_6O_4 $_5O_{45}$	N_{67} $O_{45}V$	
77	Ir	692	579	497	313	297	65	**62**	98	65	53									
78	Pt	726	610	521	333	316	76	**73**	105	69	54						**1192**			
79	Au	763	643	547	354	336	89	**85**	110	75	57						**1184**			
80	Hg	803	681	577	379	359	104	**100**	127	84	65						**1176**	1173		
81	Tl	845	721	608	406	385	122	**118**	137	100	76	15	13				**1169**			
82	Pb	893	762	645	435	413	143	**138**	148	107	84	22	19				**1162**	1159		
83	Bi	942	807	681	467	443	164	**159**	161	120	94	29	26				**1155**	1151		
90	Th		1168	968	714	677	344	**335**	290	226	179	94	87	43	26	18	1100		**1005**	
92	U			1046	781	739	391	**380**	325	262	197	104	96	46	29	19	1064		**970**	
93	Np			1086	816	771	414	**402**			206		101		29	18				
94	Pu			1121	850	802	439	**427**			216		105		31	18				
95	Am				883	832	463	**449**	351		216	119	109		31	18				
96	Cm				919	865	487	**473**			232		113		32	18				
97	Bk				959	901	514	**498**			246		120		34	18				
98	Cf				994	933	541	**523**					124		35	19				

[a] Lines as bold are the most intense and are the most suitable for use of line energies in identifying chemical states.
[b] Includes KVV designation when L_{23} is not a core level.
[c] Designation is oversimplified
[d] Includes LVV when M levels are not in core and MVV when N levels are not in core
[e] No simple $4p_{1/2}$ line exists for this group of elements.
[f] The 4d doublet for these elements is complex and is variable with chemical state because of multiplet splitting and multielectron processes.

Appendix U: XPS Line Positions Obtained from Al Ka X-rays

Z		Photoelectron Lines												Auger Lines						
		1s	2s	$2p_{1/2}$	$2p_{3/2}$	3s	$3p_{1/2}$	$3p_{3/2}$	$3d_{3/2}$	$3d_{5/2}$	4s	$4p_{1/2}$	$4p_{3/2}$	KL_1 L_1	KL_1 L_{23}	$KL_{23}L_{23}$[b)]				
1	H																			
2	He																			
3	Li	**56**																		
4	Be	**113**														**1315**				
5	B	**191**														**1226**				
6	C	**287**														**1108**				
7	N	**402**												1012	997	**976**				
8	O	**531**	23											878	859	**832**				
9	F	**686**	30											724	701	**668**				
10	Ne	**863**	41	14										565	536	**497**				
11	Na	**1072**	64	31										384	350	**305**				
12	Mg	**1305**	90	51												100[g)]				
13	Al		119	**74**																
14	Si		153	103	**102**															
15	P		191	134	**133**	14														

Z		Photoelectron Lines												Auger Lines						
		1s	2s	$2p_{1/2}$	$2p_{3/2}$	3s	$3p_{1/2}$	$3p_{3/2}$	$3d_{3/2}$	$3d_{5/2}$	4s	$4p_{1/2}$	$4p_{3/2}$	$L_3M_{23}M_{23}$[c]	$L_2M_{23}M_2$[c]	$L_3M_{23}M_{45}$ ^1P	$L_3M_{23}M_{45}$ ^3P	$L_2M_{23}M_{45}$ ^1P	$L_3M_{45}M_{45}$[d]	$L_2M_{45}M_{45}$
16	S		229	166	**165**	17								**1336**						
17	Cl		270	201	**199**	17								**1304**						
18	Ar		319	243	**241**	22								**1270**	**1268**					
19	K		378	296	**293**	33	17							**1238**	**1236**					
20	Ca		439	350	**347**	44	25							**1197**	**1194**					
21	Sc		501	407	**402**	53	31							**1153**		1125				
22	Ti		565	464	**458**	62	37							1106		**1072**				
23	V		630	523	**515**	69	40							1055		**1017**				
24	Cr		698	586	**577**	77	46	45						1000		**962**				
25	Mn		770	652	**641**	83	49	48						948		**903**			853	
26	Fe		847	723	**710**	93	56	55						892		841			**786**	
27	Co		927	796	**781**	103	63	61						837	830	779	774		**716**	701
28	Ni		1009	873	**855**	112	69	67						781	775	715	709		**643**	626
29	Cu		1098	954	**934**	124	79	77						719	712	649	641	629	**570**	550
30	Zn		1196	1045	**1022**	140	92	89	10					662	655	585	576	562	**498**	475
31	Ga		1299	1144	**1117**	160	108	105	20					601	594	817	508	490	**422**	395
32	Ge			1250	**1219**	184	128	124	32	31				538	530	448	438	417	**346**	315
33	As				**1326**	207	148	143	45	44						376	365	341	**266**	232
34	Se					232	169	163	58	**57**						300	288	259	**184**	143
35	Br					256	189	182	70	**69**										
36	Kr					287	216	208	89	**88**	22									
37	Rb					322	247	238	111	**110**	29		14							

Z		Photoelectron Lines												Auger Lines						
		1s	2s	$2p_{1/2}$	$2p_{3/2}$	3s	$3p_{1/2}$	$3p_{3/2}$	$3d_{3/2}$	$3d_{5/2}$	4s	$4p_{1/2}$	$4p_{3/2}$	$L_3M_{23}M_{23}$	$L_2M_{23}M_{23}$	$L_3M_{23}M_{45}$ ^1P	$L_3M_{23}M_{45}$ ^3P	$L_2M_{23}M_{45}$ ^1P	$L_3M_{45}M_{45}$	$L_2M_{45}M_{45}$
38	Sr					358	280	269	135	**133**	37		20							
39	Y					395	313	301	160	**158**	45		25							
40	Zr					431	345	331	183	**181**	51		29							

		3s	$3p_{1/2}$	$3p_{3/2}$	$3d_{3/2}$	$3d_{5/2}$	4s	$4p_{1/2}$	$4p_{3/2}$	$4d_{3/2}$	$4d_{5/2}$	$4f_{5/2}$	$4f_{7/2}$	5s	$5p_{1/2}$	$5p_{3/2}$	$M_{45}N_{23}V$	$M_5N_4{}_5N_{45}$	$M_4N_4{}_5N_{45}$
41	Nb	470	379	364	209	**206**	59	35										**1321**	1289	
42	Mo	508	413	396	233	**230**	65	38										**1301**	1266	
43	Tc	544	445	425	257	**253**	68	39										1280	**1241**	
44	Ru	587	485	463	286	**282**	77	45[e]										1258	**1214**	
45	Rh	629	522	498	314	**309**	83	49[e]										1235	**1187**	
46	Pd	673	561	534	342	**337**	88	54[e]										1212	**1161**	
47	Ag	718	604	573	374	**368**	97	58[e]											1136	**1130**
48	C	772	652	618	412	**405**	109	68[e]	11										1112	**1105**
49	In	828	704	666	453	**445**	123	79[e]	19										1086	**1079**
50	Sn	884	757	715	494	**486**	137	91[e]	26	25									1060	**1052**
51	Sb	946	814	768	539	**530**	155	105[e]	35	34									1036	**1027**
52	Te	1009	873	822	585	**575**	171	114[e]	44	43				14					1008	**998**
53	I	1071	930	874	630	**619**	186	123[e]	52	50				16					981	**970**
54	Xe	1144	997	936	685	**672**	209	141[e]	65	63				19					957	**944**
55	Cs	1216	1064	997	738	**724**	230	170	158	77	75			24					931	**917**
56	Ba	1292	1137	1062	795	**780**	254	192	179	92	90			23					904	**890**
57	La		1207	1126	851	**834**	274	210	195	104	101			34	17				865	

Z		Photoelectron Lines															Auger Lines			
		3s	$3p_{1/2}$	$3p_{3/2}$	$3d_{3/2}$	$3d_{5/2}$	4s	$4p_{1/2}$	$4p_{3/2}$	$4d_{3/2}$	$4d_{5/2}$	$4f_{5/2}$	$4f_{7/2}$	5s	$5p_{1/2}$	$5p_{3/2}$	$M_{45}N_{23}V$	$M_5N_4{}_5N_{45}$	$M_4N_4{}_5N_{45}$	
58	Ce		**1271**	1184	900	882	290	222	207	112	108			37	18			827		
59	Pr		**1337**	1242	950	930	305	237	218	114[f]				38	20			788		
60	Nd			1299	1001	980	318	248	227	120[f]				38	23			752		

		$3d_{3/2}$	$3d_{5/2}$	4s	$4p_{1/2}$	$4p_{3/2}$	$4d_{3/2}$	$4d_{5/2}$	$4f_{5/2}$	$4f_{7/2}$	5s	$5p_{1/2}$	$5p_{3/2}$	$M_{45}N_{23}V$	$M_5N_4{}_5N_{45}$	$M_4N_4{}_5N_{45}$	$M_{45}N_{45}V$	M_5VV	M_4VV	
61	Pm	1060	**1034**	337	264	242	129				38	22			714					
62	Sm	1110	**1083**	349	283	250	132				41	20			673					
63	Eu	1166	**1136**	366	289	261	136				34	24			635					
64	Gd	1219	**1186**	380	301	270	141				36	21			595					
65	Tb	1279	**1244**	398	317	284	150				42	28			568		426	**265**	235	
66	Dy	1334	**1295**	412	329	293	154				63	26			527		375	**195**	155	
67	Ho			431	345	306	**161**				51	20			490		325	**142**	100	
68	Er			451	362	320	**169**				61	25			454		273	**99**	56	
69	Tm			470	378	333	**180**				54	32	26							
70	Yb			483	392	342	194	**185**			55	33	26							
71	Lu			507	412	359	207	**197**			58	34	27							
72	Hf			537	437	382	224	213	19	**17**	64	37	30							
73	Ta			566	464	403	241	229	27	**25**	71	45	37							
74	W			594	491	425	257	245	36	**34**	77	47	37							
75	Re			628	521	449	277	263	45	**43**	81	44	33							
76	Os			657	549	475	294	279	55	**52**	86	60	48							

Z		Photoelectron Lines															Auger Lines			
		4s	$4p_{1/2}$	$4p_{3/2}$	$4d_{3/2}$	$4d_{5/2}$	$4f_{5/2}$	$4f_{7/2}$	5s	$5p_{1/2}$	$5p_{3/2}$	$5f_{5/2}$	$5f_{7/2}$	6s	$6p_{1/2}$	$6p_{3/2}$	N_7O_4 $_5O_{45}$	N_6O_4 $_5O_{45}$	N_{67} $O_{45}V$	
77	Ir	692	579	497	313	297	65	**62**	98	65	53									
78	Pt	726	610	521	333	316	76	**73**	105	69	54						**1425**			
79	Au	763	643	547	354	336	89	**85**	110	75	57						**1417**			
80	Hg	803	681	577	379	359	104	**100**	127	84	65						**1409**	1406		
81	Tl	845	721	608	406	385	122	**118**	137	100	76	15	13				**1402**			
82	Pb	893	762	645	435	413	143	**138**	148	107	84	22	19				**1395**	1392		
83	Bi	942	807	681	467	443	164	**159**	161	120	94	29	26				**1388**	1384		
90	Th	1330	1168	968	714	677	344	**335**	290	226	179	94	87	43	26	18	1333		**1238**	
92	U		1274	1046	781	739	391	**380**	325	262	197	104	96	46	29	19	1297		**1203**	
93	Np		1327	1086	816	771	414	**402**			206		101		29	18				
94	Pu			1121	850	802	439	**427**			216		105		31	18				
95	Am				883	832	463	**449**	351		216	119	109		31	18				
96	Cm				919	865	487	**473**			232		113		32	18				
97	Bk				959	901	514	**498**			246		120		34	18				
98	Cf				994	933	541	**523**					124		35	19				

[a] Lines as bold are the most intense and are the most suitable for use of line energies in identifying chemical states.
[b] Includes KVV designation when L_{23} is not a core level.
[c] Designation is oversimplified
[d] Includes LVV when M levels are not in core and MVV when N levels are not in core
[e] No simple $4p_{1/2}$ line exists for this group of elements.
[f] The 4d doublet for these elements is complex and is variable with chemical state because of multiplet splitting and multielectron processes.
[g] Often observable, induced by Bremsstrahlung.

Appendix V: Atomic Sensitivity Factors for XPS

Z	Element	Line	Sensitivity		
			Wagner	Scofield Mg anode	Scofield Ag anode
1	H				
2	He				
3	Li	1s	0.020	0.06	0.06
4	Be	1s	0.059	0.20	0.19
5	B	1s	0.130	0.49	0.19
6	C	1s	0.250	1.00	1.00
		2p	-	0.00	0.05
7	N	1s	0.420	1.77	1.80
		2p	-	0.01	0.01
8	O	1s	0.660	2.85	2.93
		2s	0.025	0.14	0.14
		2p	-	0.02	0.02
9	F	1s	1.000	4.26	4.43
		2s	0.040	0.20	0.21
		2p	-	0.05	0.10
10	Ne	1s	1.500	5.95	6.30
		2s	0.070	0.28	0.30
11	Na	1s	2.300	7.99	8.52
		2s	0.130	0.39	0.42
		2p	-	0.21	0.19
12	Mg	2s	0.200	0.52	0.57
		2p	0.120	0.36	0.11
		1s	3.500	11.18	11.18
13	Al	2s	0.230	0.68	0.75
		2p	0.185	0.57	0.22
14	Si	2s	0.260	0.86	0.96
		2p	0.270	0.86	0.82
		3s	-	0.07	0.08
		3p	-	0.01	0.01
15	P	2s	0.290	1.05	1.18
		2p	0.390	1.25	1.19
16	S	2s	0.330	1.25	1.43
		2p	0.540	2.14	1.68
17	Cl	2s	0.370	1.48	1.69
		2p	0.730	2.36	0.78
18	Ar	2s	0.400	1.71	1.97
		2p	0.960	3.13	3.04

Z	Element	Line	Sensitivity		
			Wagner	Scofield Mg anode	Scofield Ag anode
19	K	2s	0.430	1.95	2.27
		$2p_{1/2}$	0.410	1.37	1.35
		$2p_{3/2}$	0.830	2.67	2.62
		2p	1.240	-	-
		3s	-	0.25	0.29
		3p	-	0.36	0.36
20	Ca	2s	0.470	2.21	2.59
		$2p_{1/2}$	0.530	1.74	1.72
		$2p_{3/2}$	1.050	3.39	3.35
		2p	1.580	-	-
		3s	-	0.31	0.35
		3p	-	0.50	0.51
21	Sc	2s	0.500	2.46	2.91
		$2p_{1/2}$	0.550	2.18	2.17
		$2p_{3/2}$	1.100	4.24	4.21
		2p	1.650	-	-
		3s	-	0.36	0.41
		3p	-	0.64	0.65
22	Ti	2s	0.540	2.72	3.24
		$2p_{1/2}$	0.600	2.68	2.69
		$2p_{3/2}$	1.200	5.22	5.22
		2p	1.800	-	-
		3s	-	0.41	0.47
		3p	0.210	0.79	0.81
23	V	2s	-	2.98	3.57
		$2p_{1/2}$	0.650	3.26	3.29
		$2p_{3/2}$	1.300	6.33	6.37
		2p	-	0.46	0.54
		3s	0.950	-	-
		3p	0.210	0.96	1.00
24	Cr	2s	-	3.23	3.91
		$2p_{1/2}$	0.800	3.92	3.98
		$2p_{3/2}$	1.500	7.60	7.69
		2p	2.300	-	-
		3s	-	0.51	0.60
		3p	0.210	1.12	1.17

Z	Element	Line	Sensitivity		
			Wagner	Scofield Mg anode	Scofield Ag anode
25	Mn	2s	-	3.48	4.23
		$2p_{1/2}$	0.900	4.63	4.74
		$2p_{3/2}$	1.700	8.99	9.17
		2p	2.600	-	-
		3s	-	0.57	0.67
		3p	0.220	1.35	1.42
26	Fe	2s	-	3.70	4.57
		$2p_{1/2}$	1.000	5.43	5.60
		$2p_{3/2}$	2.000	10.54	10.82
		2p	3.000	-	-
		3s	-	0.63	0.74
		3p	0.260	1.58	1.31
27	Co	2s	-	3.92	4.88
		$2p_{1/2}$	1.300	6.28	6.54
		$2p_{3/2}$	2.500	12.20	12.62
		2p	3.800	-	-
		3s	-	0.69	0.82
		3p	0.350	1.81	1.93
28	Ni	2s	-	4.16	5.16
		$2p_{1/2}$	1.500	7.18	7.57
		$2p_{3/2}$	3.000	13.92	14.61
		2p	4.500	-	-
		3s	-	0.75	0.82
		3p	0.500	2.06	2.22
29	Cu	2s	-	4.38	5.46
		$2p_{1/2}$	2.100	8.18	8.66
		$2p_{3/2}$	4.200	15.87	16.73
		2p	6.300	-	-
		3s	-	0.81	0.96
		3p	0.650	2.28	0.85
30	Zn	2s	-	4.55	5.76
		$2p_{1/2}$	-	9.29	9.80
		$2p_{3/2}$	4.800	18.01	18.92
		3s	-	0.87	1.04
		3p	0.750	2.58	2.83
		3d	-	0.90	0.81

Z	Element	Line	Sensitivity		
			Wagner	Scofield Mg anode	Scofield Ag anode
31	Ga	$2p_{1/2}$	-	10.56	11.09
		$2p_{3/2}$	5.400	20.47	21.40
		3s	-	0.94	1.13
		$3p_{1/2}$	-	0.99	1.10
		$3p_{3/2}$	-	1.92	2.11
		3p	0.840	-	-
		3d	0.310	1.19	1.09
32	Ge	$2p_{1/2}$	-	10.95	12.52
		$2p_{3/2}$	6.100	21.22	24.15
		3s	-	1.02	1.23
		$3p_{1/2}$	-	1.11	1.24
		$3p_{3/2}$	-	2.15	2.39
		3p	0.920	-	-
		3d	0.380	1.55	1.42
33	As	$2p_{1/2}$	-	14.07	14.07
		$2p_{3/2}$	6.800	27.19	27.19
		3s	-	1.10	1.32
		$3p_{1/2}$	0.970	1.24	1.39
		$3p_{3/2}$	-	2.40	2.68
		3d	0.530	1.97	1.82
34	Se	3s	-	1.18	1.43
		$3p_{1/2}$	-	1.37	1.55
		$3p_{3/2}$	-	2.65	2.98
		3p	1.050	-	-
		3d	0.670	2.46	2.29
35	Br	3s	-	1.26	1.53
		$3p_{1/2}$	-	1.50	1.72
		$3p_{3/2}$	-	2.92	3.31
		3p	0.140	-	-
		3d	0.830	3.04	2.84
36	Kr	3s	-	1.35	1.64
		$3p_{1/2}$	0.390	1.64	1.89
		$3p_{3/2}$	0.820	3.20	3.65
		3p	1.230	-	-
		3d	-	3.69	3.48
		4s	-	0.18	0.21

Z	Element	Line	Sensitivity		
			Wagner	Scofield Mg anode	Scofield Ag anode
37	Rb	3s	-	1.43	1.75
		$3p_{1/2}$	0.430	1.79	2.07
		$3p_{3/2}$	0.870	3.48	4.00
		3p	1.300	-	-
		3d	1.230	4.20	4.21
		4s	-	0.21	0.25
		$4p_{1/2}$	-	0.50	0.21
38	Sr	3s	-	1.52	1.85
		$3p_{1/2}$	0.460	1.93	2.25
		$3p_{3/2}$	0.920	3.78	4.37
		3p	1.380	-	-
		3d	1.480	5.29	5.05
		4s	-	0.24	0.29
		4p	-	0.68	0.78
39	Y	3s	-	1.61	1.98
		$3p_{1/2}$	0.590	2.08	2.44
		$3p_{3/2}$	0.980	4.09	4.75
		3p	1.470	-	-
		$3d_{3/2}$	-	2.54	2.44
		$3d_{5/2}$	-	3.70	3.54
		3d	1.760	-	-
		4s	-	0.27	0.33
		4p	-	0.79	0.91
		4d	-	0.03	0.03
40	Zr	3s	-	1.70	2.10
		$3p_{1/2}$	0.530	2.24	2.64
		$3p_{3/2}$	1.040	4.40	5.14
		3p	1.560	-	-
		$3d_{3/2}$	2.100	2.97	2.87
		$3d_{5/2}$	-	4.43	4.17
		4s	-	0.31	0.37
		4p	-	0.90	1.05
		4d	-	0.09	0.08
41	Nb	3s	-	1.79	2.22
		$3p_{1/2}$	-	2..39	2.84
		$3p_{3/2}$	1.100	4.71	5.53
		$3d_{3/2}$	0.960	3.45	3.35
		$3d_{5/2}$	1.440	5.01	4.86
		3d	2.400	-	-
		4s	-	0.33	0.40
		4p	-	1.00	1.16

Z	Element	Line	Sensitivity		
			Wagner	Scofield Mg anode	Scofield Ag anode
42	Mo	3s	-	1.89	2.34
		$3p_{1/2}$	-	2.54	3.04
		$3p_{3/2}$	1.170	5.03	5.94
		$3d_{3/2}$	1.090	3.97	3.88
		$3d_{5/2}$	1.660	5.77	5.62
		3d	2.750	-	-
		4s	-	0.36	0.44
		4p	-	1.12	1.31
43	Tc	3s	-	1.98	2.45
		$3p_{1/2}$	-	2.69	3.23
		$3p_{3/2}$	1.240	5.36	6.36
		$3d_{3/2}$	1.260	4.54	4.46
		$3d_{5/2}$	1.890	6.60	6.47
		3d	3.150	-	-
		4s	-	0.40	0.48
		4p	-	1.24	1.45
44	Ru	3s	-	2.07	2.57
		$3p_{1/2}$	-	2.84	3.44
		$3p_{3/2}$	1.300	5.68	6.78
		$3d_{3/2}$	1.450	5.17	5.10
		$3d_{5/2}$	2.150	7.51	7.39
		3d	3.600	-	-
		4s	-	0.43	0.52
		4p	-	1.36	1.59
45	Rh	3s	-	2.15	2.70
		$3p_{1/2}$	-	2.98	3.64
		$3p_{3/2}$	1.380	6.00	7.21
		$3d_{3/2}$	1.700	8.48	8.39
		$3d_{5/2}$	2.400	-	-
		3d	4.100	0.46	0.56
		4s	-	1.48	1.75
		4p	-		
46	Pd	3s	-	2.24	2.81
		$3p_{1/2}$	-	3.12	3.83
		$3p_{3/2}$	1.430	6.33	7.63
		$3d_{3/2}$	1.900	6.58	6.56
		$3d_{5/2}$	2.700	9.54	9.48
		3d	4.600	-	-
		4s	-	0.49	0.60
		4p	-	1.60	1.88

Z	Element	Line	Sensitivity		
			Wagner	Scofield Mg anode	Scofield Ag anode
47	Ag	3s	-	2.33	2.93
		$3p_{1/2}$	-	3.25	4.03
		$3p_{3/2}$	1.520	6.64	8.06
		$3d_{3/2}$	2.100	7.36	7.38
		$3d_{5/2}$	3.100	10.68	10.66
		3d	5.200	-	-
		4s	-	0.53	0.64
		$4p_{1/2}$	-	0.59	0.70
		$4p_{3/2}$	-	1.15	1.36
		4d	-	1.50	1.55
48	Cd	3s	-	2.40	3.04
		$3p_{1/2}$	-	3.39	4.22
		$3p_{3/2}$	1.600	6.96	8.50
		$3d_{3/2}$	-	8.22	8.27
		$3d_{5/2}$	3.500	11.91	11.95
		4s	-	0.57	0.69
		4p	-	1.90	2.25
		4d	-	1.82	1.89
49	In	3s	-	2.48	3.16
		$3p_{1/2}$	-	3.51	4.40
		$3p_{3/2}$	1.680	7.27	8.93
		$3d_{3/2}$	-	9.13	9.22
		$3d_{5/2}$	3.900	13.23	13.32
		4s	-	0.61	0.74
		4p	-	2.06	2.45
		4d	-	2.18	2.27
50	Sn	3s	-	2.54	3.26
		$3p_{1/2}$	-	3.62	4.58
		$3p_{3/2}$	1.770	7.58	9.35
		$3d_{3/2}$	-	10.09	10.25
		$3d_{5/2}$	4.300	14.63	14.80
		4s	-	0.65	0.79
		4p	-	2.22	2.67
		4d	-	2.56	2.70

Z	Element	Line	Sensitivity		
			Wagner	Scofield Mg anode	Scofield Ag anode
51	Sb	3s	-	2.60	3.36
		$3p_{1/2}$	-	3.71	4.76
		$3p_{3/2}$	-	7.86	9.77
		$3d_{3/2}$	-	11.13	11.35
		$3d_{5/2}$	4.800	16.13	16.39
		4s	-	0.70	0.85
		4p	-	2.40	2.88
		4d	1.000	2.98	3.14
52	Te	3s	-	2.67	3.46
		$3p_{1/2}$	-	3.79	4.92
		$3p_{3/2}$	-	8.14	10.21
		$3d_{3/2}$	-	12.21	12.52
		$3d_{5/2}$	5.400	17.70	18.06
		4s	-	0.74	0.90
		4p	-	2.59	3.11
		4d	1.230	3.41	3.59
53	I	3s	-	2.75	3.53
		$3p_{1/2}$	-	3.87	5.06
		$3p_{3/2}$	-	8.37	10.62
		$3d_{3/2}$	-	13.33	13.77
		$3d_{5/2}$	6.000	19.33	19.87
		4s	-	0.79	0.96
		4p	-	2.77	3.34
		4d	1.440	3.87	4.13
54	Xe	3s	-	2.83	3.62
		$3p_{1/2}$	-	3.95	5.20
		$3p_{3/2}$	-	8.64	10.99
		$3d_{3/2}$	-	14.55	15.10
		$3d_{5/2}$	6.600	21.08	21.79
		4s	-	0.83	1.02
		4p	-	2.96	3.58
		4d	1.720	4.35	4.68

Z	Element	Line	Sensitivity		
			Wagner	Scofield Mg anode	Scofield Ag anode
55	Cs	3s	-	2.84	3.73
		$3p_{1/2}$	-	4.04	5.29
		$3p_{3/2}$	-	8.97	11.38
		$3d_{3/2}$	-	15.80	16.46
		$3d_{5/2}$	7.200	22.93	23.76
		4s	-	0.88	1.08
		$4p_{1/2}$	-	1.03	1.27
		$4p_{3/2}$	-	2.12	2.56
		$4d_{3/2}$	-	1.99	2.15
		$4d_{5/2}$	-	2.88	3.10
		4d	2.000	-	-
56	Ba	$3p_{1/2}$	-	4.10	5.42
		$3p_{3/2}$	-	9.26	11.71
		$3d_{3/2}$	-	17.04	17.92
		$3d_{5/2}$	7.800	24.75	25.84
		4s	-	0.92	1.13
		$4p_{1/2}$	-	1.09	1.34
		$4p_{3/2}$	-	2.26	2.73
		4d	2.350	2.21	5.86
57	La	$3p_{1/2}$	-	4.06	5.55
		$3p_{3/2}$	-	9.52	12.11
		$3d_{3/2}$	-	18.25	19.50
		$3d_{5/2}$	-	26.49	28.12
		3d	10.000	-	-
		4s	-	0.97	1.19
		$4p_{1/2}$	-	1.15	1.42
		$4p_{3/2}$	-	2.40	2.91
		4d	2.000	5.97	6.52
58	Ce	$3p_{3/2}$	-	9.67	12.53
		$3d_{3/2}$	-	19.67	21.12
		$3d_{5/2}$	-	28.57	30.50
		3d	10.000	-	-
		4s	-	1.00	1.24
		$4p_{1/2}$	-	1.18	1.47
		$4p_{3/2}$	-	2.49	3.03
		4d	2.000	6.32	6.93
59	Pr	3d	9.000	-	-
		4d	2.000	-	-

Z	Element	Line	Sensitivity		
			Wagner	Scofield Mg anode	Scofield Ag anode
60	Nd	$3d_{3/2}$	-	22.66	24.27
		$3d_{5/2}$	-	32.96	35.29
		3d	7.000	-	-
		4s	-	1.07	1.33
		$4p_{1/2}$	-	1.27	1.59
		$4p_{3/2}$	-	2.71	3.31
		4d	2.000	7.24	8.03
		5s	-	0.20	0.25
		5p	-	0.58	0.71
61	Pm	3d	9.000	-	-
		4d	2.000	-	-
62	Sm	$3d_{3/2}$	5.000	26.12	27.96
		$3d_{5/2}$	-	37.90	40.37
		4s	-	1.14	1.42
		$4p_{1/2}$	2.000	1.34	1.70
		$4p_{3/2}$	-	2.91	3.59
		4d	-	8.15	9.16
63	Eu	$3d_{3/2}$	-	28.20	29.91
		$3d_{5/2}$	-	40.87	43.24
		3d	5.000	-	-
		4s	-	1.17	1.46
		$4p_{1/2}$	-	1.37	1.75
		$4p_{3/2}$	-	3.01	3.72
		4d	2.000	8.60	10.73
		5s	-	0.22	0.27
		5p	-	0.63	0.77
64	Gd	$3d_{3/2}$	-	24.35	31.98
		$3d_{5/2}$	3.000	43.43	46.23
		4s	-	1.20	1.51
		$4p_{1/2}$	-	1.41	1.80
		$4p_{3/2}$	-	3.13	3.88
		4d	2.000	9.14	10.40
		5s	-	0.23	0.29
		5p	-	0.69	0.85
65	Tb	$3d_{5/2}$	3.000	20.80	49.42
		4s	-	1.22	1.54
		$4p_{1/2}$	-	1.43	1.84
		$4p_{3/2}$	-	3.21	3.99
		4d	2.000	9.49	8.45
		5s	-	0.23	0.28
		5p	-	0.65	0.80

Z	Element	Line	Sensitivity		
			Wagner	Scofield Mg anode	Scofield Ag anode
66	Dy	4d	2.000	-	-
		$4p_{3/2}$	0.600	-	-
67	Ho	4d	2.000	-	-
		$4p_{3/2}$	0.600	-	-
68	Er	4s	-	1.29	1.64
		$4p_{1/2}$	-	1.49	1.95
		$4p_{3/2}$	0.600	3.48	4.37
		4d	2.000	10.70	12.56
		5s	-	0.24	0.30
		5p	-	0.68	0.89
69	Tm	4s	-	1.31	1.67
		$4p_{1/2}$	-	1.50	1.98
		$4p_{3/2}$	0.600	3.56	4.48
		4d	2.000	11.18	9.86
		5s	-	0.24	0.30
		5p	-	0.69	0.86
		4f	-	4.98	4.64
70	Yb	4s	-	1.32	1.70
		$4p_{1/2}$	-	1.51	2.00
		$4p_{3/2}$	0.600	3.64	4.60
		$4d_{3/2}$	2.000	4.72	5.61
		$4d_{5/2}$	-	6.85	8.07
		5s	-	0.25	0.31
		5p	-	0.70	0.88
		4f	-	5.96	5.58
71	Lu	4s	-	1.34	1.73
		$4p_{1/2}$	-	1.52	2.03
		$4p_{3/2}$	0.600	3.73	4.74
		$4d_{3/2}$	-	4.91	5.87
		$4d_{5/2}$	-	7.13	8.45
		4d	2.000	-	-
		5s	-	0.26	0.33
		5p	-	0.76	0.95
		4f	-	6.92	6.50

Z	Element	Line	Sensitivity		
			Wagner	Scofield Mg anode	Scofield Ag anode
72	Hf	4s	-	1.66	1.76
		$4p_{1/2}$	-	1.53	2.06
		$4p_{3/2}$	-	3.83	4.88
		$4d_{3/2}$	0.930	5.10	6.13
		$4d_{5/2}$	1.420	7.42	8.84
		4d	2.350	-	-
		5s	-	0.28	0.34
		$5p_{1/2}$	-	0.25	0.32
		$5p_{3/2}$	-	0.56	0.70
		4f	2.050	8.00	7.52
73	Ta	4s	-	1.38	1.79
		$4p_{1/2}$	-	1.54	2.08
		$4p_{3/2}$	-	3.93	5.02
		$4d_{3/2}$	1.000	5.29	6.40
		$4d_{5/2}$	1.500	7.71	9.24
		4d	2.500	-	-
		5s	-	0.29	0.36
		$5p_{1/2}$	-	0.27	0.35
		$5p_{3/2}$	-	0.61	0.75
		4f	2.400	9.00	8.62
74	W	4s	-	1.39	1.81
		$4p_{1/2}$	-	1.55	2.10
		$4p_{3/2}$	-	4.03	5.16
		$4d_{3/2}$	1.030	5.48	6.68
		$4d_{5/2}$	1.570	8.01	9.65
		4d	2.600	-	-
		$4f_{5/2}$	-	4.52	4.32
		$4f_{7/2}$	-	5.75	5.48
		4f	2.750	-	-
75	Re	4s	-	1.41	1.84
		$4p_{1/2}$	-	1.55	2.12
		$4p_{3/2}$	-	4.13	5.30
		$4d_{3/2}$	1.090	5.67	6.95
		$4d_{5/2}$	1.660	8.31	10.06
		4d	2.750	-	-
		$4f_{5/2}$	3.100	5.08	4.88
		$4f_{7/2}$	-	6.46	6.20

Z	Element	Line	Sensitivity		
			Wagner	Scofield Mg anode	Scofield Ag anode
76	Os	4s	-	1.42	1.86
		$4p_{1/2}$	-	1.55	2.13
		$4p_{3/2}$	-	4.24	5.45
		$4d_{3/2}$	0.850	5.86	7.23
		$4d_{5/2}$	1.750	8.60	10.48
		4d	2.900	-	-
		5s	-	0.34	0.42
		$4f_{5/2}$	-	5.67	5.48
		$4f_{7/2}$	-	7.22	6.96
		4f	3.500	-	-
77	Ir	4s	-	1.43	1.88
		$4p_{1/2}$	-	1.55	2.14
		$4p_{3/2}$	-	4.34	5.59
		$4d_{3/2}$	-	6.05	7.51
		$4d_{5/2}$	1.840	8.90	10.90
		5s	-	4.00	0.44
		$4f_{5/2}$	1.700	6.30	6.12
		$4f_{7/2}$	2.250	8.03	7.78
		4f	3.950	-	-
78	Pt	4s	-	1.44	1.90
		$4p_{1/2}$	-	1.54	2.14
		$4p_{3/2}$	-	4.45	5.74
		$4d_{3/2}$	-	6.24	7.78
		$4d_{5/2}$	1.920	9.20	11.32
		5s	-	1.50	0.46
		$4f_{5/2}$	1.850	6.97	6.81
		$4f_{7/2}$	2.550	8.89	8.65
		4f	4.400	-	-
		$5p_{3/2}$	-	0.83	1.04
79	Au	$4p_{1/2}$	-	1.53	2.14
		$4p_{3/2}$	-	4.55	5.89
		$4d_{3/2}$	-	6.42	8.06
		$4d_{5/2}$	2.050	9.50	11.74
		$4f_{5/2}$	2.150	7.68	7.54
		$4f_{7/2}$	2.800	9.79	9.58
		4f	4.950	-	-
		$5p_{1/2}$	-	0.35	0.46
		$5p_{3/2}$	-	0.88	1.10

Z	Element	Line	Sensitivity		
			Wagner	Scofield Mg anode	Scofield Ag anode
80	Hg	$4p_{1/2}$	-	1.52	2.14
		$4p_{3/2}$	-	4.65	6.04
		$4d_{3/2}$	-	6.60	8.33
		$4d_{5/2}$	2.15	9.79	12.17
		5s	-	0.40	0.50
		$4f_{5/2}$	3.150	8.431	8.32
		$4f_{7/2}$	2.350	10.75	10.57
		4f	5.500	-	-
		$5p_{1/2}$	-	0.37	0.48
		$5p_{3/2}$	-	0.94	1.17
		5d	-	1.70	2.08
81	Tl	4s	-	1.46	1.95
		$4p_{1/2}$	-	1.50	2.13
		$4p_{3/2}$	-	4.75	6.19
		$4d_{3/2}$	-	6.78	8.60
		$4d_{5/2}$	-	10.08	12.60
		$4f_{5/2}$	2.650	9.22	9.14
		$4f_{7/2}$	3.500	11.77	11.62
		4f	6.150	-	-
		$5p_{1/2}$	-	0.38	0.50
		$5p_{3/2}$	-	1.00	1.25
		5d	0.900	1.44	2.38
82	Pb	4s	-	1.46	1.96
		$4p_{1/2}$	-	1.47	2.12
		$4p_{3/2}$	-	4.86	6.33
		$4d_{3/2}$	-	6.94	8.87
		$4d_{5/2}$	2.350	10.37	13.02
		$4f_{5/2}$	2.950	10.05	10.01
		$4f_{7/2}$	3.850	12.83	12.73
		4f	6.700	-	-
		5p	-	1.40	1.86
		5d	1.000	1.29	3.95

Z	Element	Line	Sensitivity		
			Wagner	Scofield Mg anode	Scofield Ag anode
83	Bi	4s	-	1.45	1.96
		$4p_{1/2}$	-	1.45	2.10
		$4p_{3/2}$	-	4.96	6.48
		$4d_{3/2}$	-	7.11	9.14
		$4d_{5/2}$	2.500	10.64	13.44
		$4f_{5/2}$	3.150	10.93	10.93
		$4f_{7/2}$	4.250	13.95	13.90
		4f	7.400	-	-
		$5p_{1/2}$	-	0.41	0.55
		$5p_{3/2}$	-	1.13	1.41
		5d	1.100	1.44	3.00
85	At	4s	-	1.44	1.96
		$4p_{1/2}$	-	1.38	2.04
		$4p_{3/2}$	-	5.15	6.77
		$4d_{3/2}$	-	7.42	9.65
		$4d_{5/2}$	-	11.20	14.29
		4f	-	29.15	29.36
		5s	-	0.48	0.60
		$5p_{1/2}$	-	0.44	0.58
		$5p_{3/2}$	-	1.26	1.58
		5d	-	2.92	3.63
86	Rn	4s	-	1.44	1.95
		$4p_{1/2}$	-	1.34	2.00
		$4p_{3/2}$	-	5.24	6.92
		$4d_{3/2}$	-	7.56	9.90
		$4d_{5/2}$	-	11.46	14.70
		4f	-	31.43	14.00
		5s	-	0.49	17.81
		$5p_{1/2}$	-	0.45	0.45
		$5p_{3/2}$	-	1.33	1.33
		5d	-	3.17	3.17
88	Ra	4s	-	1.41	1.95
		$4p_{1/2}$	-	1.26	1.26
		$4p_{3/2}$	-	5.42	1.91
		$4d_{3/2}$	-	7.82	7.20
		$4d_{5/2}$	-	11.95	10.40
		4f	-	36.20	37.04
		5s	-	0.52	0.66
		$5p_{1/2}$	-	0.47	0.63
		$5p_{3/2}$	-	1.48	1.86
		5d	-	3.69	4.61

Z	Element	Line	Sensitivity		
			Wagner	Scofield Mg anode	Scofield Ag anode
90	Th	$4p_{3/2}$	-	5.59	7.46
		$4d_{3/2}$	-	8.05	10.82
		$4d_{5/2}$	3.500	12.45	16.31
		$4f_{5/2}$	-	18.21	18.81
		$4f_{7/2}$	7.800	23.30	23.94
		5s	-	0.55	0.70
		$5p_{1/2}$	-	0.9	0.66
		$5p_{3/2}$	-	1.63	2.05
		$5d_{3/2}$	0.600	1.70	2.15
		$5d_{5/2}$	0.900	2.52	3.15
		5d	1.500	-	-
92	U	$4d_{3/2}$	-	8.20	11.25
		$4d_{5/2}$	3.850	12.80	17.05
		$4f_{5/2}$	-	20.60	21.50
		$4f_{7/2}$	9.000	26.30	247.36
		$5d_{3/2}$	0.600	2.40	2.36
		$5d_{5/2}$	1.000	3.46	3.46
		5d	1.600	-	-

전자 방출 분광기를 이용한 금속산화물 박막과 나노섬유의 연구

박주연

일반대학원, 화학과

부경대학교

초록

이 학위 논문은 구리 산화물, 몰리브데넘 산화질화물, 몰리브데넘 황화물, 그리고 다양한 금속 산화물 박막을 전자 방출 분광기를 이용하여 분석한 결과에 대해 서술하고 있다. 박막의 표면 특성을 연구하기 위해 전자 방출 분광기와 스퍼터 챔버를 설치하고 수정하였다. 전자 방출 분광기 챔버는 X-선 광전자 분광기, 오제이 전자 분광기, 그리고 자외선 광전자 분광기를 구비하고 있다. 박막 내 원소의 산화 상태는 피크 분리 과정을 통해 결정하였다. 이를 통해 다른 산화 상태를 가지는 화학종의 비율이 박막의 성질에 큰 영향을 끼친다는 것을 확인하였다.